DOE/BC/14899-17
Distribution Category UC-122

MODIFICATION OF CHEMICAL AND PHYSICAL FACTORS IN STEAMFLOOD TO INCREASE HEAVY OIL RECOVERY

Annual Report for the Period
October 1992 to September 1993

by
Y. C. Yortsos

October 1994

Work Performed Under Contract No. DE-FG22-93BC14899

Prepared for
U.S. Department of Energy
Assistant Secretary for Fossil Energy

Thomas B. Reid, Project Manager
Bartlesville Project Office
P.O. Box 1398
Bartlesville, OK 74005

Prepared by
Department of Chemical Engineering
Petroleum Engineering Program
University of Southern California
Los Angeles, CA 90089-1211

DISCLAIMER

Contents

List of Figures

List of Tables

ACKNOWLEDGMENTS

The research reported in this volume was supported by the U.S. Department of Energy under contract FG22-90BC14600, subcontracted from Stanford University. We would like to express our gratitude to Tom Reid, our DOE Project Manager, for his steady support and commitment. Thanks are also due to Prof. Bill Brigham and Dr. Louis Castanier of SUPRI for their continuing interest and for their invaluable help in administering the subcontract. Part of the work on heterogeneity was also supported by the USC Center for Study of Fractured Reservoirs, sponsored by Aramco, Mineral Management Services, the State Lands Commision of California and Unocal. All these sources of support are greatfully acknowledged.

ABSTRACT

Thermal methods, and particularly steam injection, are currently recognized as the most promising for the efficient recovery of heavy oil. Despite significant progress, however, important technical issues remain open. Specifically, still inadequate is our knowledge of the complex interaction between porous media and the various fluids of thermal recovery (steam, water, heavy oil, gases, and chemicals). While, the interplay of heat transfer and fluid flow with pore- and macro-scale heterogeneity is largely unexplored.

The objectives of this contract are to continue previous work and to carry out new fundamental studies in the following areas of interest to thermal recovery: displacement and flow properties of fluids involving phase change (condensation-evaporation) in porous media; flow properties of mobility control fluids (such as foam); and the effect of reservoir heterogeneity on thermal recovery. The specific projects are motivated by and address the need to improve heavy oil recovery from typical reservoirs as well as less conventional fractured reservoirs producing from vertical or horizontal wells.

This report covers work performed in the past year in these three areas. In the area of vapor-liquid flow, we present the continuation of work on the pore network modeling of bubble growth in porous media driven by the application of a prescribed heat flux or superheat. The scaling of bubble growth in porous media is also discussed. In another study we study the problem of steam injection in fractured systems using visualization in micromodels. The interplay of drainage, imbibition and bubble growth problems is discussed. Two aspects of effects of heterogeneity are analysed: One pertains to the capillary properties of displacement in anisotropic media, where it is shown that the capillary pressure curve in such systems also depends on the direction of displacement. The other addresses a numerical problem in the simulation of unstable displacement processes. Finally, the report concludes with two studies on non-Newtonian behavior in porous media. The first study considers the displacement of a Bingham plastic, using both numerical simulation and experiments in Hele-Shaw cells. The second study in this topic is a continuation of our work on foam flow in porous media, where we discuss aspects of the solution of some recently proposed equations and we also continue in the development of a pore network model.

1 PORE NETWORK MODELS FOR BOILING AND BUBBLE GROWTH IN POROUS MEDIA

C. Satik and Y. C. Yortsos

1.1 INTRODUCTION

Vapor-liquid flow in porous media, driven by temperature and pressure gradients, is involved in a wide variety of processes, such as geothermal systems [8, 95, 102, 110], solution gas-drive oil reservoirs [119], thermal oil recovery [86], nuclear waste disposal [11, 27, 105], porous heat pipes [38, 81], boiling [18, 25, 29] and drying [99]. These processes share the common aspects of phase change and its interplay with fluid flow, heat (or mass) transfer and capillarity.

As in other flow processes in porous media, vapor-liquid flows can be described at three different levels: the pore level, where the emphasis is on the mechanisms of nucleation and local interface growth; the pore network level, where the collective action of an ensemble of interacting pores is considered; and the macroscopic or continuum level, where information of the average behavior only is relevant. In the past, the overwhelming majority of theoretical and experimental studies have addressed the continuum level. Continuum approaches make use of Darcy's law extended to multi-phase flow with saturation-dependent relative permeabilities and capillary pressure functions (borrowed from isothermal, immiscible displacement processes) which assume capillary control at the pore level (low Capillary and Bond numbers). These approaches ignore the underlying pore microstructure and require restrictions on scale-dependent viscous and gravity forces. Due to these limitations, continuum approaches may not be fully adequate to describe these vapor-liquid flows. To obtain a better understanding of the process over a very large range of operating conditions, a microscopic approach in which the pore microstructure is acknowledged must be used. A network model approach, in which the porous medium is represented as a two- or three-dimensional network of interconnected simple geometrical shapes of pores (pore bodies or throats), is one such approach. Pore network models have emerged as very convenient and useful discrete alternatives that provide a better understanding of microscopic pore level phenomena and have been frequently used to simulate immiscible displacement processes in porous media [33, 53, 63, 100, 103]. In the context of solution gas-drive, Li [69] recently studied the diffusion-driven isothermal bubble growth in porous

media and developed experimental and numerical pore network models. That study achieved a significant improvement in understanding bubble growth processes. Heat transfer-driven and diffusion-driven bubble growth have similarities although the heat transfer in the solid, the much faster growth process and the possible importance of inertia are important differences.

Bubble growth begins with the onset of at least one nucleation event and is driven by a liquid-to-vapor temperature gradient created by a superheat imposed in liquid. Depending on the pore surface roughness, a number of nucleation centers may exist. Therefore, growth may occur from a multitude of separate clusters. While the latter is important, the simpler problem of single-bubble growth is poorly understood. Two important steps of bubble growth have been identified: pressurization and pore filling steps. During a pressurization step, all interfaces reside in converging pore geometries, where they are stable, due to the strong capillary barrier. Liquid and vapor pressures are spatially uniform. Thus, the volume generated due to phase change contributes only to increase of the vapor pressure (and temperature). This step continues until the capillary barrier is exceeded at a point on the bubble perimeter. Then, pore filling step takes place. Simultaneous penetration of multiple pore bodies is also possible depending on the parameter values. At the moment of penetration, the pressure in the vapor phase relaxes to the adjacent liquid pressure due to immediate expansion, thus the previous vapor phase volume is now redistributed among the old vapor-occupied and the newly-penetrated pore bodies. This step ends when all newly-penetrated pore bodies are completely filled by vapor.

Contrary to growth in the bulk [84, 97, 107], or in a Hele-Shaw cell [70], bubble growth patterns in porous media are disordered and not compact. As in related immiscible displacement processes, these patterns reflect the underlying pore micro structure. In external drive drainage processes (displacement of a wetting fluid by a non-wetting fluid), the flow regimes depend on the parameter values [63]. Flow regimes are of the percolation type when the viscous pressure drop across the interface between the two fluids is smaller than the capillary pressure drop. In this regime, the displacement follows the well known invasion percolation [111]. As viscous pressure drop increases, viscous forces dominate over capillary forces and the displacement evolves to non-local regimes, such as viscous fingering. We expect similar behavior in the case of bubble growth.

To understand key features of heat transfer-driven bubble growth in porous media, we developed experimental and numerical pore level models. We have used glass micromodels to visualize pore

Table 1: Properties of the liquid used in the experiments.

T_b	=	78.5 °C
L_v	=	$1.9496 * 10^9$ J/kg
λ	=	0.169 W/m − K
ρ	=	787.3 kg/m^3
μ	=	$1.074 * 10^{-3}$ N − s/m^2
C_p	=	$2.44 * 10^3$ J/kg − K
M	=	46.069 kmol/kg
γ	=	0.022 N/m

level mechanisms such as nucleation, phase change and phase growth during vapor-liquid flow in porous media. Glass micromodels as alternative to other transparent models have been very useful in the past and widely used in pore level visualization studies of fluid flow and immiscible displacement in porous media [26, 54, 62, 63, 75]. Recently, Yousfi et al. [63], Danesh et al. [12] and Li [69] used micromodels to study nucleation and bubble growth processes in solution gas-drive systems, which have some similarities with our problem.

This chapter is organized as follows: First, we briefly describe our experimental apparatus and the experimental results. Next, we describe the numerical pore network model and its application to two different cases. Effects of various parameters on the growth patterns are discussed. The boundary between percolation and non-percolation regimes, which we shall refer as the "percolation boundary", is analyzed. In particular, we investigate effects of solid conduction, liquid convection and transient heat transfer.

1.2 EXPERIMENTAL

The experimental apparatus (details of which are given in [93]) consists of a glass micromodel, two variant power controllers, a vacuum pump, a 12-channel temperature scanner, a video camera, a microscope, a VCR and a monitor. Figure 1 shows a schematic of the apparatus. Ethyl alcohol was used to study a bubble growth process. Typical properties of which are given in Table 1 [46]. In the

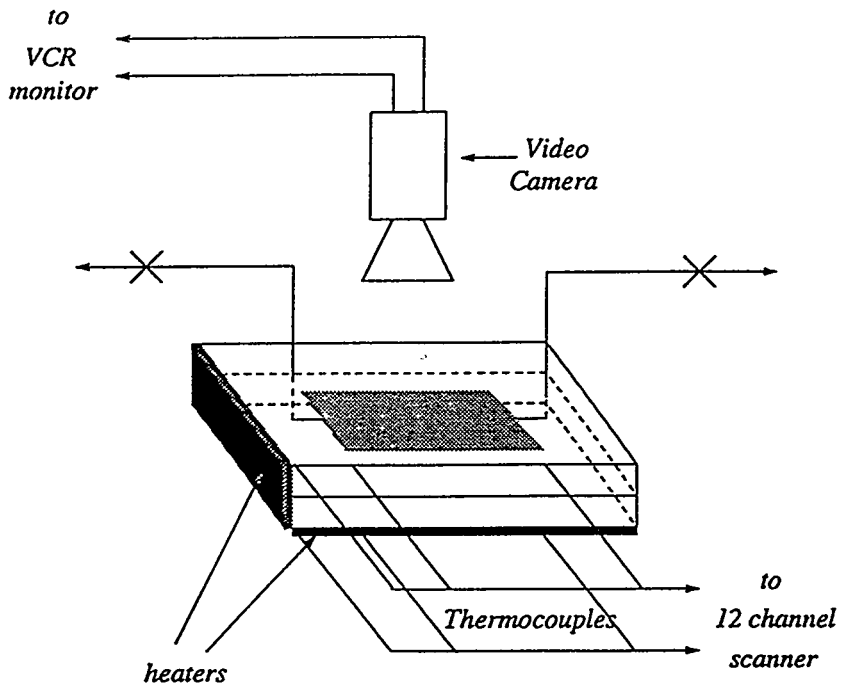

Figure 1: Schematic of experimental apparatus.

Table, T_b, L_v, λ, ρ, μ, C_p, M and γ denote boiling temperature, latent heat of evaporation, thermal conductivity, density, viscosity, specific heat, molecular weight and interfacial tension, respectively (at 25 °C).

The procedure for a typical experiment was as follows:

(1) Mix ethyl alcohol with a proper dye.

(2) Deaerate ethyl alcohol by vacuuming.

(3) Fill the micromodel with ethyl alcohol.

(4) Connect heaters to power controllers and thermocouples to temperature scanner.

(5) Start heating from the bottom heater to increase the system temperature.

(6) Start heating from the side heater to impose the desired heat flux.

(7) Turn on the recording system when the first bubble forms.

Visualization experiments for boiling and bubble growth in micromodels were carried out to get a better understanding of the phenomena occurring at the microscopic pore level. Because a heating process is involved, carrying out this type of experiments is by no means an easy task.

Micromodels fabricated for the experiments were made of ordinary glass. Provided that spatial temperature gradients do not exist, they can withstand temperatures of as high as 100 °C. The

alternative solution of pyrex glasses, which can withstand very high temperatures, was not considered because of the difficulties in micromodel fabrication. Another alternative is to use liquids which have sufficiently low boiling temperature. Ethyl alcohol, which has a boiling temperature of 78.5 °C, is a good candidate.

Removal of possible dissolved-air from the liquid ethyl alcohol is necessary to avoid any solution gas coming out when the pressure of the system is lowered below the saturation pressure. Before every experiment, the dissolved-air was removed by using a vacuum pump.

To control heating and heat losses, we use two heater mats: one at the bottom of the micromodel provides a spatially uniform heating to the desired temperature; the other, placed at one of the vertical sides closer to the inlet or outlet ports of the micromodel, provides a temperature gradient along the micromodel. To eliminate heat losses, we covered all sides of the micromodel with silicon rubber, except for the top surface to allow visualization of the pore network. This surface was covered by a glass plate.

1.2.1 Nucleation

Nucleation is the first stage of bubble growth in porous media. Homogeneous nucleation can be discarded because of its restrictive conditions of perfectly smooth and liquid wet surface, the absence of trapped gases, and the unrealistically high superheat requirements. Heterogeneous nucleation, in which pore surface irregularities (cracks, scratches and pits etc.) that are not liquid wet and contain pre-existing or trapped gases which act as nucleation sites, is the mechanism likely to dominate. Recently, Li [69] reported visualization experiments for nucleation events following bubble growth in porous media in the context of solution gas-drive systems. He also suggested that the nucleation mechanism is heterogeneous, although nucleation events are not likely to be reproducible experimentally.

During one of our visualization experiments, we observed vapor phase growth in a pore body, following a nucleation event. Shown in Figure 2 are consecutive snapshots of this event spanning two minutes and ten seconds. The vapor phase first formed on the pore wall at the onset of nucleation. The shape of the evolving bubble is quite spherical (Figure 2a,b,c and d) before it encounters the effects of the constraining pore geometry. Then, the bubble elongates accordingly (Figure 2f,g and h) until the complete filling of the pore body (Figure 2i).

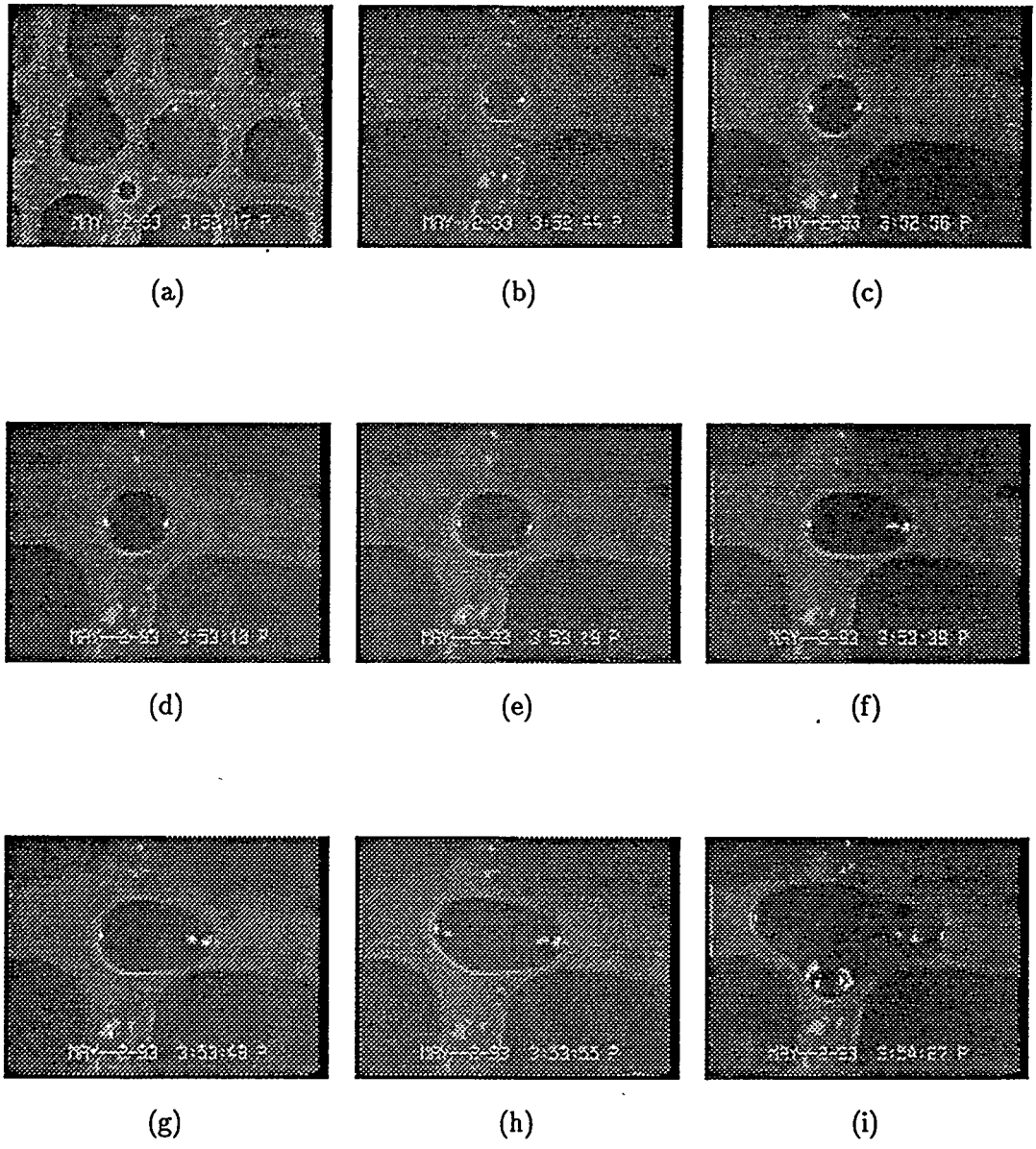

Figure 2: Observation of vapor phase growth in a pore body, following a nucleation event.

1.2.2 Bubble Growth

Following nucleation, the growth of the bubble continues until the pore body is completely filled with vapor phase. When this is completed, the bubble cannot grow any larger because of the capillary pressure barrier induced by the constraining pore walls. During this stage, the pressure in the vapor phase increases due to the continuous phase change at the liquid-vapor interfaces. We refer this stage as the "pressurization step". It continues until the capillary pressure barrier is exceeded, which occurs when the difference between the pressures in the vapor and the surrounding liquid phases becomes equal to the capillary pressure. When this condition is achieved, an immediate jump of the interface takes place from one pore body to another, and the existing vapor phase volume is redistributed among the previously vapor-occupied and newly-penetrated pore bodies. The bubble readjusts its shape by retreating its interfaces from all bonds (Figure 3). In typical immiscible displacements, this event is known as a "rheon" Immediately following this stage, the previously completely-occupied and newly-penetrated pore bodies become partially-occupied by the vapor phase. The next stage is a "pore-filling step", during which bubble growth continues until full occupancy is achieved in all pore bodies. During a bubble growth process, these two stages are repeated continuously.

It was also observed that the bubble growth process follows two different modes. The first one is a "one-site-at-a-time" mode, where a pore-filling step strictly follows a pressurization step and only one perimeter bond is penetrated at each time. Shown in Figure 4 are our experimental results to illustrate "one-site-at-a-time" growth mode. In the second mode, instantaneously multiple bond penetrations over the bubble perimeter are possible.

Figure 5 shows bubble growth patterns obtained during one experiment. As shown in this figure, bubble growth patterns obtained are ramified and not compact, contrary to the growth in the bulk. These patterns reflect the underlying pore microstructure. All these observations will be used next to develop a pore network model that describes bubble growth in pore networks.

1.3 PORE NETWORK MODEL

To study bubble growth in a porous medium, we modelled the porous medium as an equivalent two-dimensional network of interconnected pore bodies and pore throats randomly distributed. The growth from a single vapor bubble in a horizontal sample of a finite size was studied.

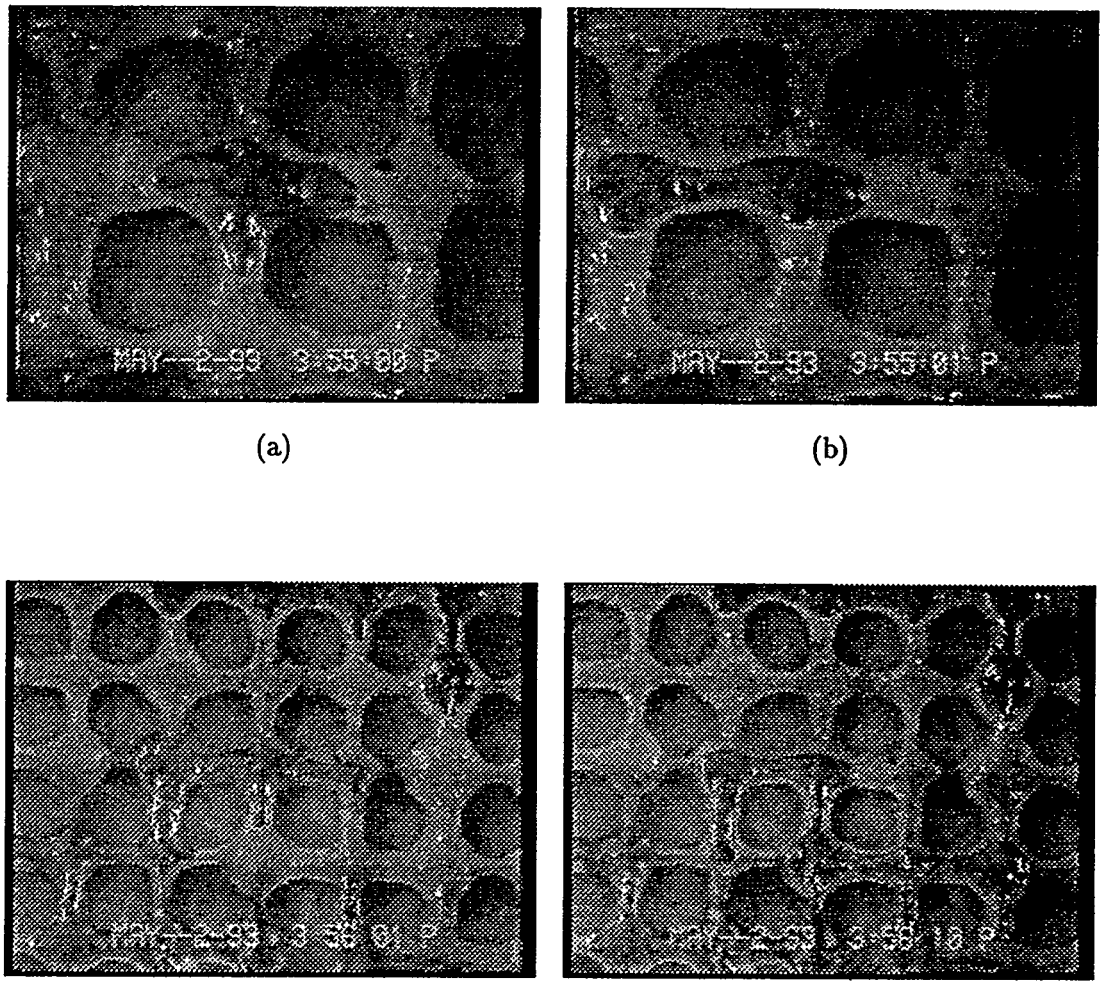

Figure 3: Observation of a "rheon" event in a pore network.

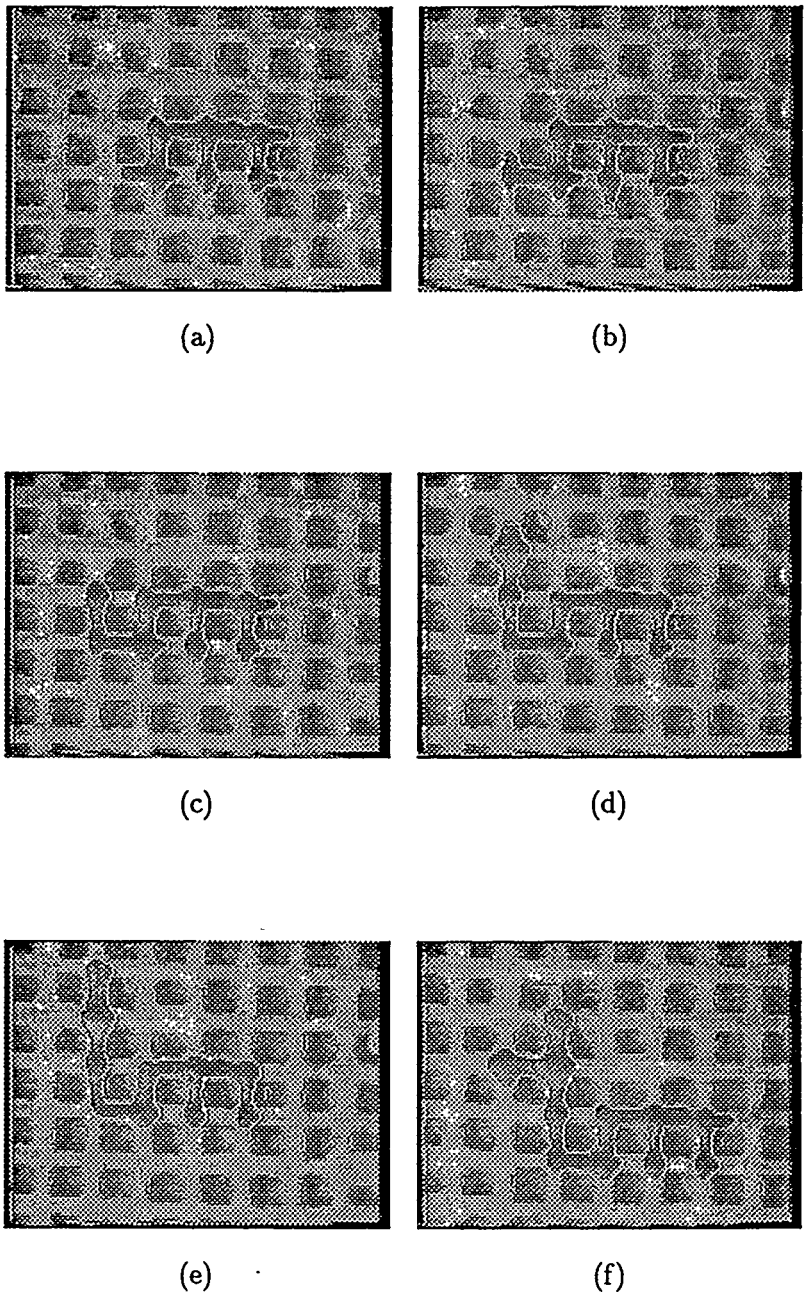

Figure 4: Illustration of "one-site-at-a-time" bubble growth mode.

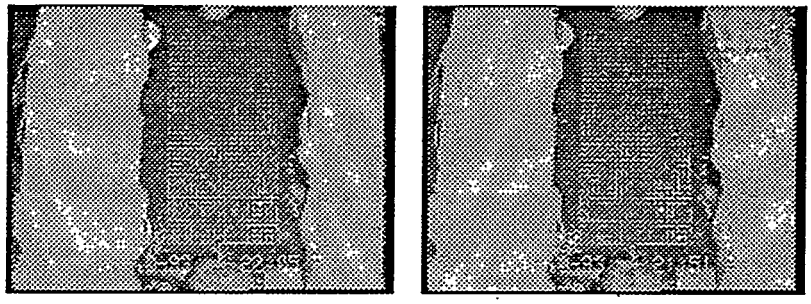

(a) (b)

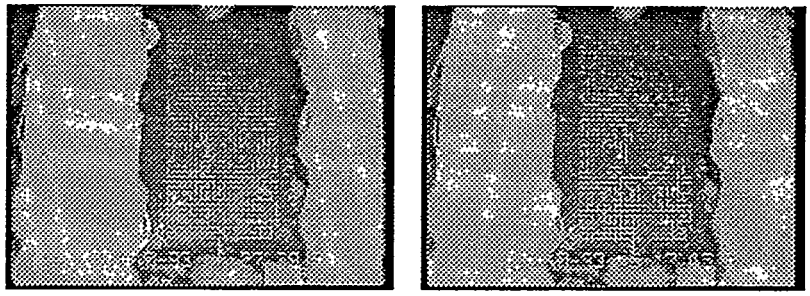

(c) (d)

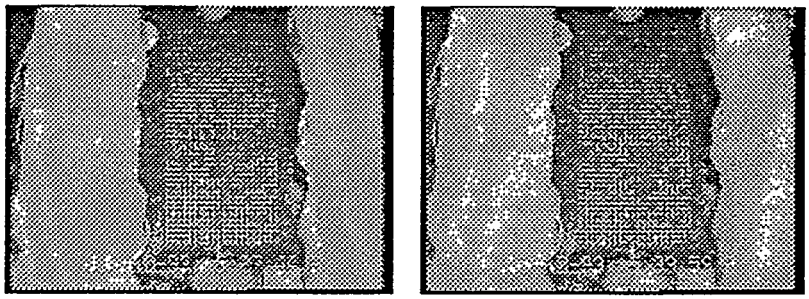

(e) (f)

Figure 5: Bubble growth patterns.

To model bubble growth in porous media, we postulated the following:

(i) Pore bodies may contain both vapor and liquid phases, while interconnecting bonds contain only one phase (either vapor or liquid).

(ii) Pressure drops occur only in the connections (bonds) between pore bodies, while the bulk of the volume of either phase (vapor or liquid) is in a pore body only.

(iii) The vapor phase is non-viscous, no pressure gradients exist in the vapor-occupied pore space.

(iv) The liquid phase is incompressible.

(v) The vapor phase is at saturated conditions while the liquid phase is superheated. The pressure of the vapor phase is obtained by using the Clausius-Clapeyron equation

$$P_v = P_{vo}(T_v) \tag{1}$$

(vi) Ideal gas law applies, such that changes in the total mass of the vapor phase (Δm) during time increment Δt are calculated as

$$\Delta m = \frac{M}{R}\left(\frac{P_v^{n+1}}{T_v^{n+1}}\Delta V + \frac{P_v^n V^n}{T_v^{n+1}}\left(\frac{\Delta P}{P_v^n} - \frac{\Delta T}{T_v^n}\right)\right) \tag{2}$$

where,

$$\Delta P = P_v^{n+1} - P_v^n, \tag{3}$$

$$\Delta T = T_v^{n+1} - T_v^n, \tag{4}$$

$$\Delta V = V^{n+1} - V^n \tag{5}$$

and P_v, T_v, V, M and R denote vapor pressure, vapor temperature, vapor volume, molecular weight and the ideal gas constant, respectively. Superscripts n and $n+1$ indicate time levels separated by an increment Δt. The change in the total mass of the vapor phase, Δm, is related to the total heat flow rate from liquid to vapor

$$\Delta m = \frac{\sum Q}{L_v}\Delta t, \tag{6}$$

where Q, L_v and Δt are heat flow rate, latent heat of evaporation and time increment, respectively, and the summation is over the perimeter of the vapor bubble.

(vii) The capillary pressure drop across interfaces between vapor and liquid phases in the pore body is neglected (flat interface) when pore bodies are partially occupied by vapor and liquid, and

are inversely proportional to the radii connecting pore bodies when they are completely occupied by the vapor phase. Thus, the condition for an interface to move from a completely vapor-occupied pore j to a neighboring completely liquid-occupied pore i is

$$P_v^j - (P_l^i - \frac{1}{\rho_l L_v}\frac{G^{ji}}{g^{ji}}(T_l^i - T_v^j)) \geq \frac{2\gamma}{R_b^{ji}} \tag{7}$$

where P_l^i, T_l^i, ρ_l, G^{ji}, g^{ji}, γ and R_b^{ji} are liquid pressure, temperature, density, heat conductance, flow conductance, surface tension and radius of the connection between pore bodies j and i, respectively. In the above equation, the second term on LHS represents liquid pressure at the interface, which differs from P_l^i due to the mass transport towards the latter, induced by evaporation.

(viii) The liquid phase may be trapped. The volume of liquid in the trapped pores does not change during bubble growth, since the ratio of liquid to vapor densities is large, but the heat flow from the trapped liquid to the vapor bubble is included in the total heat flow when calculating the total mass involved in phase change.

As observed in the experiments, we use two different steps during bubble growth: (a) Pressurization step and (b) Pore body-filling step. In the first step, the capillary pressure is larger than the viscous pressure drop, all menisci of the vapor bubble are static and the total vapor volume is constant. All pores at the perimeter are completely filled, except for those containing trapped liquid. The vapor pressure at the end of this step is calculated from equations (2) and (6). This step continues until the capillary condition in (7) is satisfied across an interface. Then, the capillary pressure difference is set to zero across such interfaces. The next step involves filling of the pore body invaded, during which time liquid is displaced from the pore body, while the vapor phase occupies it as dictated by the evaporation rate. During this step, both the total volume of the vapor bubble and the pressure (and temperature) change. At the end of this step, the pore body is completely filled with the vapor phase. If the capillary condition is not satisfied, the pressurization step begins, otherwise menisci jump may occur elsewhere and other pore bodies are filled with vapor.

The appropriate mass, momentum and energy balances and the numerical algorithm are described in detail in Satik [93]. Here, we shall simply summarize important results obtained.

During bubble growth, two dimensionless numbers control the growth regime: The Jacob number, Ja, and the modified capillary number, Ca^*. Ja is related to the initial imposed superheat.

For the bubble growth in a uniform initial superheat problem, it is defined as

$$Ja = \frac{\rho_l C_{pl} \Delta T}{\rho_v L_v} \tag{8}$$

$$\Delta T = T_{init} - T_{vo}(P_{init}) \tag{9}$$

where ρ_v, ΔT, T_{init} and $T_{vo}(P_{init})$ denote vapor density, initial superheat imposed, initial temperature of liquid and saturation temperature of liquid at the initial pressure, respectively. For the problem of bubble growth with a prescribed heat flux, the Jacob number is defined as

$$Ja = \frac{\rho_l C_{pl} L_b q_h}{\rho_v L_v \lambda_l} \tag{10}$$

where q_h is prescribed heat flux. The modified capillary number is expressed as

$$Ca^* = \frac{\lambda_l \mu_l L_b}{\rho_l C_{pl} R_b^{*2} \gamma} Ja \tag{11}$$

where R_b^* is average bond radius.

1.4 RESULTS AND DISCUSSION

We used the simulator to examine two different cases: (i) Bubble growth with a uniform superheat imposed initially, and (ii) Bubble growth with a prescribed heat flux at one boundary. In the first case, the pore space is completely filled with a superheated liquid. Initial temperatures in the liquid and solid of the porous medium are spatially constant. The geometry of the porous medium is square and all four boundaries are open to a constant (atmospheric) pressure. The pressure in the liquid-occupied pore space is initially constant and at atmospheric pressure. In the second case, the geometry of the medium is rectangular. A heat flux is imposed on one side of the medium. No-heat flux boundary conditions are imposed at the remaining boundaries. A constant pressure (atmospheric) boundary condition is imposed on the left-hand side boundary, while no-flux boundary conditions are imposed on all other boundaries of the medium. The initial nucleation site is located at the center of the medium in the first case and at the center of the side where the heat flux is imposed in the second case.

Depending on system parameters, bubble growth may reach two states. In the first state, the bubble grows until it touches the outer boundaries. In the second state, the superheat in the system is completely depleted so that the bubble cannot grow further. At this (steady) state,

bubble growth stops and temperature and pressure in the network stabilize to a spatially constant value. In our simulation results, the final growth stage is reached when the vapor bubble reaches either of the two states.

1.4.1 Bubble Growth in a Uniform Initial Superheat

For this case, we used a square lattice (31x31). Throat (bond) sizes were randomly assigned from a uniform distribution, while pore body (site) sizes were kept constant. Initial temperature and pressure were set to 104.44 °C and 1.0133x10^5 N/m^2, respectively, and the amount of the superheat imposed was 4.4 °C. Other typical parameters used are shown in Table 2. In the table d^*, d^*_{tf}, R^*_s, P_{ref} and T_{ref} are dimensionless parameters for solid-to-liquid and solid-to-thin liquid film heat transfer coupling, average pore body sizes and reference pressure and temperature values, respectively. All parameters given in Table 2 are at reference conditions (P_{ref}, T_{ref}).

Fluid distributions at three different stages of bubble growth for the typical parameters given in Table 2 are shown in Figure 6. Corresponding time values for these stages are 2.45, 2.89 and 7.42 seconds, respectively. Many other simulation results with different parameter values and larger network sizes showed that the time spend to reach the final stage is in fact very small (order of a few seconds), implying that heat transfer driven bubble growth of this type is very fast. In the figure, white or black colors represent liquid only or vapor only occupancy, respectively, while gray color denotes partial liquid occupancy. The growth regimes for the first two stages are of the percolation type, during which the two steps (pressurization and pore-filling steps) discussed above follow one another and penetration of single interface occurs at the end of each pressurization step with no further interface penetration. All three fluid distributions shown in the Figure are at the end of a pore-filling step. Therefore, for the first two stages, pore bodies are occupied with vapor- or liquid-only. However, in a regime other than percolation, penetration of multiple interfaces may occur during both pressurization and pore filling steps, hence some of the pore bodies may be partially liquid-occupied, as shown in Figure 6c.

Fluid temperature and pressure and solid temperature distributions corresponding to these are shown in Figures 7, 8 and 9, respectively. In the Figures, black or white colors denote maximum or minimum values, respectively. As described above, all pore bodies in the network are initially filled with a superheated liquid and initial temperatures in both pore bodies and solid are spatially

Table 2: Typical parameter values.

ρ_l	=	$960.85\ \mathrm{kg/m^3}$
C_{pl}	=	$4.2092 * 10^3\ \mathrm{J/kg-K}$
λ_l	=	$0.6808\ \mathrm{W/m-K}$
μ_l	=	$2.4799 * 10^{-4}\ \mathrm{N-s/m^2}$
L_v	=	$2.2568 * 10^6\ \mathrm{J/kg}$
γ	=	$0.0584\ \mathrm{N/m}$
ρ_v	=	$0.5886\ \mathrm{kg/m^3}$
ρ_s	=	$2082.40\ \mathrm{kg/m^3}$
C_{ps}	=	$8.3732 * 10^2\ \mathrm{J/kg-K}$
λ_s	=	$6.808\ \mathrm{W/m-K}$
d^*	=	1
d^*_{tf}	=	0.01
M	=	$18\ \mathrm{kmol/kg}$
R	=	$8.315\ \mathrm{kJ/kmol-K}$
L_b	=	$1320\ \mu\mathrm{m}$
R^*_b	=	$450\ \mu\mathrm{m}$
R^*_s	=	$601\ \mu\mathrm{m}$
P_{init}	=	$1.0133 * 10^5\ \mathrm{N/m^2}$
$T_{vo}(P_{init})$	=	$100\ ^\circ\mathrm{C}$
P_{ref}	=	$1.0133 * 10^5\ \mathrm{N/m^2}$
T_{ref}	=	$100\ ^\circ\mathrm{C}$

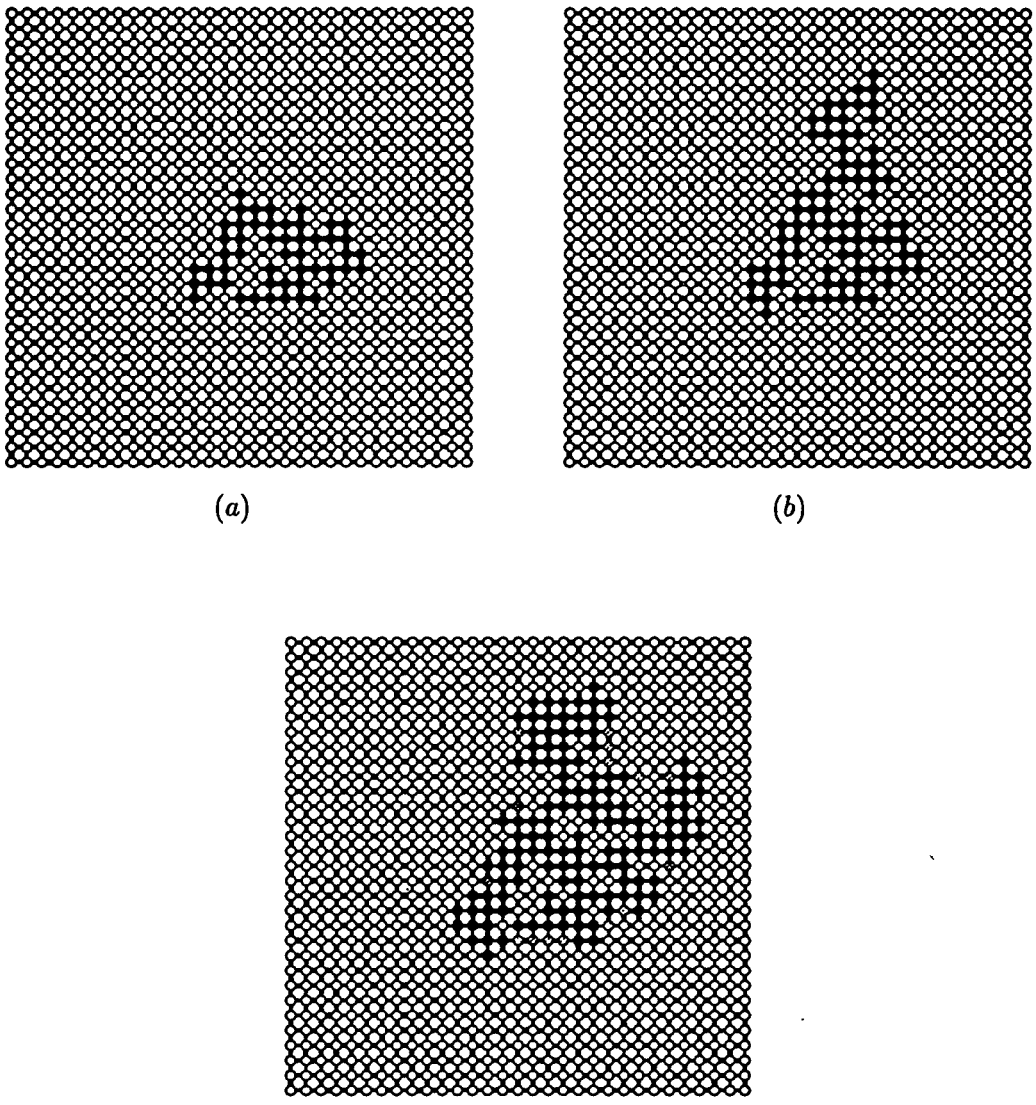

Figure 6: Fluid distributions at three stages of bubble growth in a uniform initial superheat.

constant. At the completion of a nucleation event, bubble growth process begins and a liquid-to-vapor temperature gradient forms since the vapor is at the saturation temperature which is lower than the surrounding liquid temperatures. With the existence of such a gradient, heat transfer (both conduction and convection) takes place towards the bubble, which drives the phase change process at all liquid-vapor interfaces. The fluid temperatures in Figure 7 show a good agreement with the above argument. In the Figure, fluid temperatures are constant in the liquid-occupied pore space except in a boundary layer where a liquid-to-vapor temperature gradient exists. For this particular parameter values, a very sharp gradient is observed.

Solid temperatures, shown in Figure 8, are coupled with liquid temperatures. The measure of coupling between the two fields is provided by a dimensionless parameter d^*, defined as

$$d^* = \frac{\alpha^*}{G^*} \tag{12}$$

where

$$G^* = \frac{\lambda_l \pi (R_b^*)^2}{L_b} \tag{13}$$

and α^* is a characteristic thermal conductance for heat transfer between liquid and solid phases. The thermal interaction between solid and liquid increases as d^* increases. We also allow for another coupling between the solid and vapor-occupied pore space in order to account for possible thin liquid films. The solid temperature fields shown in the Figure are almost uniform. Due to the coupling with fluid temperatures, a very small gradient, similar to the liquid-to-vapor temperature gradient in the pore space, is present.

Finally, fluid pressure distributions in Figure 9 show that the highest pressure is in the bubble, the lower pressures being in the liquid, thus indicating displacement of liquid by vapor. This is expected because the total increase in vapor volume due to phase change is significantly larger than the actual volume of liquid evaporated, since the ratio of liquid and vapor densities is very large ($O(10^3)$).

1.4.2 Effect of Initial Superheat

The initial superheat is the driving force for bubble growth. As the initial superheat increases, evaporation rates will increase and more vapor will be generated in a given time. During growth, the vapor displaces some liquid out of the pore bodies due to expansion. Liquid is displaced at

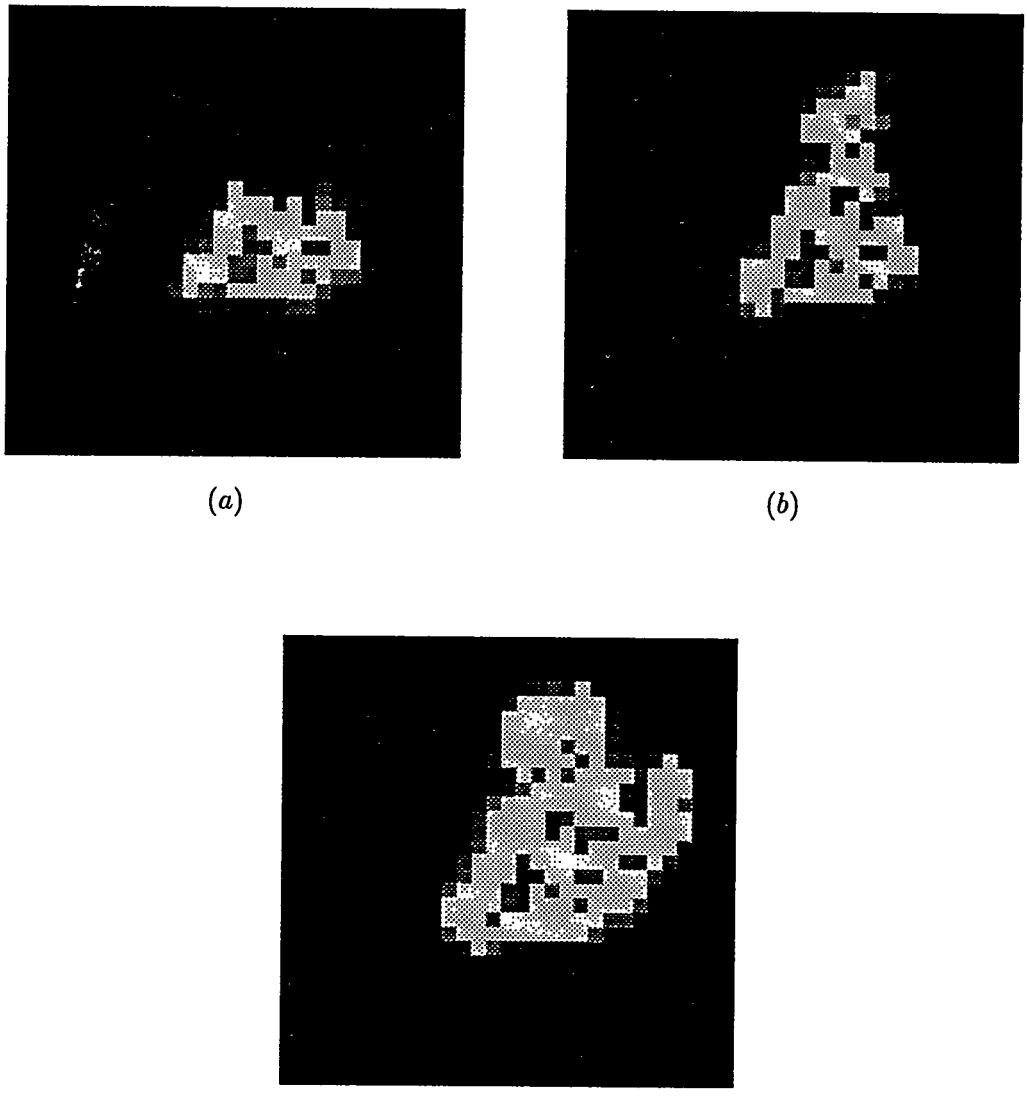

(a) (b)

(c)

Figure 7: Fluid temperature distributions at three stages of bubble growth in a uniform initial superheat. Minimum and maximum values in °C are (a) 100.01 and 104.48, (b) 100.02 and 104.51, and (c) 100.00 and 104.44, respectively.

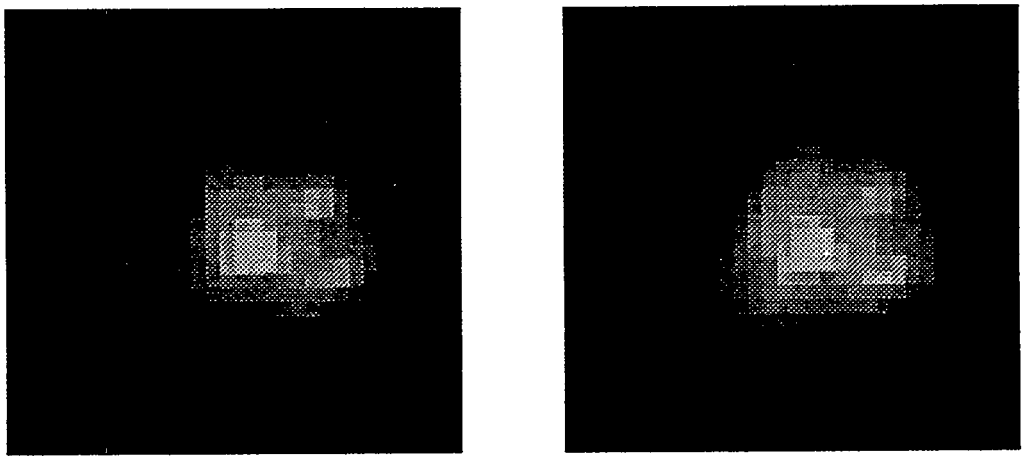

(a) (b)

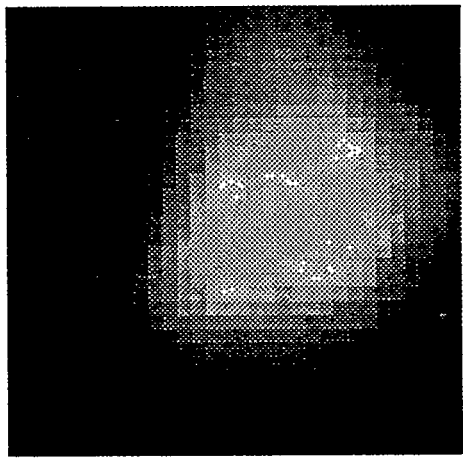

(c)

Figure 8: Solid temperature distributions at three stages of bubble growth in a uniform initial superheat. Minimum and maximum values in °C are (a) 104.38 and 104.44, (b) 104.37 and 104.44, and (c) 104.30 and 104.44, respectively.

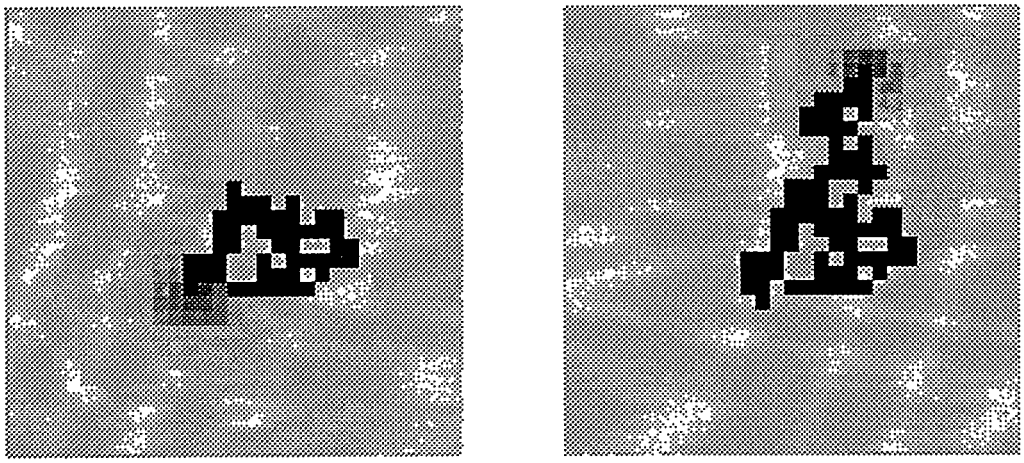

(a) (b)

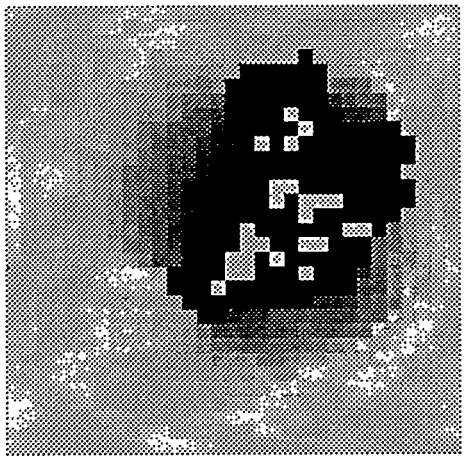

(c)

Figure 9: Fluid pressure distributions at three stages of bubble growth in a uniform initial superheat. Minimum and maximum values in psi are (a) 14.696 and 14.7014, (b) 14.696 and 14.7041, and (c) 14.696 and 14.69609, respectively.

Table 3: Ja, Ca^* and t_f values corresponding to the initial superheat values used in the sensitivity analysis.

ΔT, °C	Ja	Ca^*	t_f, s
0.28	0.8458	1.6923×10^{-4}	105.1
4.44	13.53	2.7072×10^{-3}	15.92
21.10	64.28	1.2861×10^{-2}	16.99
76.67	233.40	4.6701×10^{-2}	3.878

faster rates when the initial superheat increases. As a result, larger pressure drops will be induced, which affect the competition between capillary and viscous forces. From equation (8), Ja and Ca^* are directly related to the initial superheat, ΔT, thus as ΔT increases both Ja and Ca^* will increase. At sufficiently small initial superheats, both Ja and Ca^* are small, such that capillary forces are likely to dominate over the viscous forces, thus the growth pattern is expected to be of the percolation type. On the other hand, as the initial superheat (and also Ja and Ca^*) increases, viscous forces become stronger and bubble growth patterns deviate from percolation. Eventually, at sufficiently large initial superheats, both Ja and Ca^* are large enough for viscous forces to dominate the flow regime and the growth pattern will be more like viscous fingering, which is sensitive to boundary conditions and the underlying lattice.

Figure 10 shows the final growth patterns obtained at four different initial superheats with parameter values shown in Table 3. Here, t_f denotes the time elapsed to reach the final growth pattern. The growth pattern is of the percolation type in Figure 10a, but deviates from percolation and takes different patterns when the initial superheat is increased (Figure 10b, c and d). As seen from the Figure, the growth pattern at the maximum ΔT value (76.7 °C), is not a purely viscous fingering. We found that the initial superheat required to obtain a viscous fingering type growth to be unrealisticly high for these simulations. On the other hand, by changing a parameter value included in the Ca^*, e.g. by increasing the liquid viscosity, viscous fingering patterns can be obtained at a realistic initial superheat.

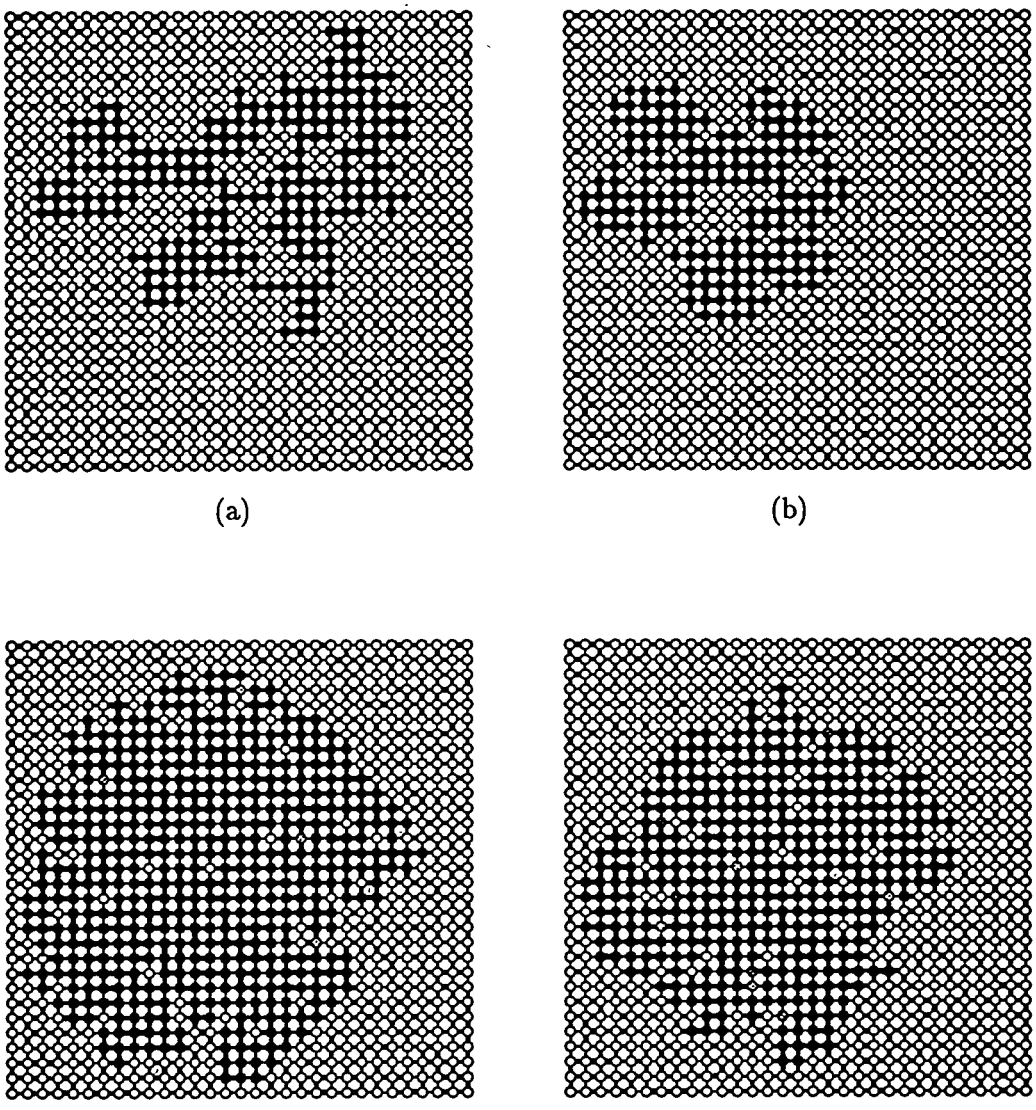

Figure 10: Final growth patterns at four different initial superheat values; (a) ΔT= 0.28 °C, (b) ΔT= 4.44 °C, (c) ΔT= 21.10 °C, (d) ΔT= 76.67 °C.

Table 4: Ja, Ca^* and t_f values corresponding to the liquid viscosity values used in the sensitivity analysis.

μ_l, N-s/m^2	Ja	Ca^*	t_f, s
2.4799x10^{-5}	13.53	2.7072x10^{-4}	6.924
2.4799x10^{-4}	13.53	2.7072x10^{-3}	15.92
2.4799x10^{-3}	13.53	2.7072x10^{-2}	56.46
2.4799x10^{-1}	13.53	2.7072	30.89

1.4.3 Effect of Liquid Viscosity

The liquid viscosity influences the liquid pressure field in the network, thus the competition between viscous and capillary forces are affected, the growth regime changing from capillary control (percolation pattern) to viscous control (viscous fingering pattern).

The final growth patterns obtained at four different liquid viscosity values are shown in Figure 11 with parameter values corresponding to each simulation given in Table 4. At μ_l= 2.4799x10^{-5} N-s/m^2, we obtain a percolation pattern (Figure 11a). As μ_l increases the growth pattern deviates from percolation (Figure 11b and c), and eventually reaches a viscous fingering type pattern at μ_l= 2.4799x10^{-1} N-s/m^2 (Figure 11d). These results are expected. Because the liquid viscosity controls the rate at which liquid phase is being displaced the larger the liquid viscosity, the slower the process (Table 4).

1.4.4 Effect of Interfacial Tension

Figure 12 shows the final growth patterns obtained at four different interfacial tension values with parameter values shown in Table 5. The pattern is percolation for γ= 5.9833x10^{-2} N/m (Figure 12a). As this value decreases, the growth pattern deviates from percolation (Figure 12b and c), and eventually reaches a viscous fingering type pattern (Figure 12d) at γ= 5.9833x10^{-6} N/m.

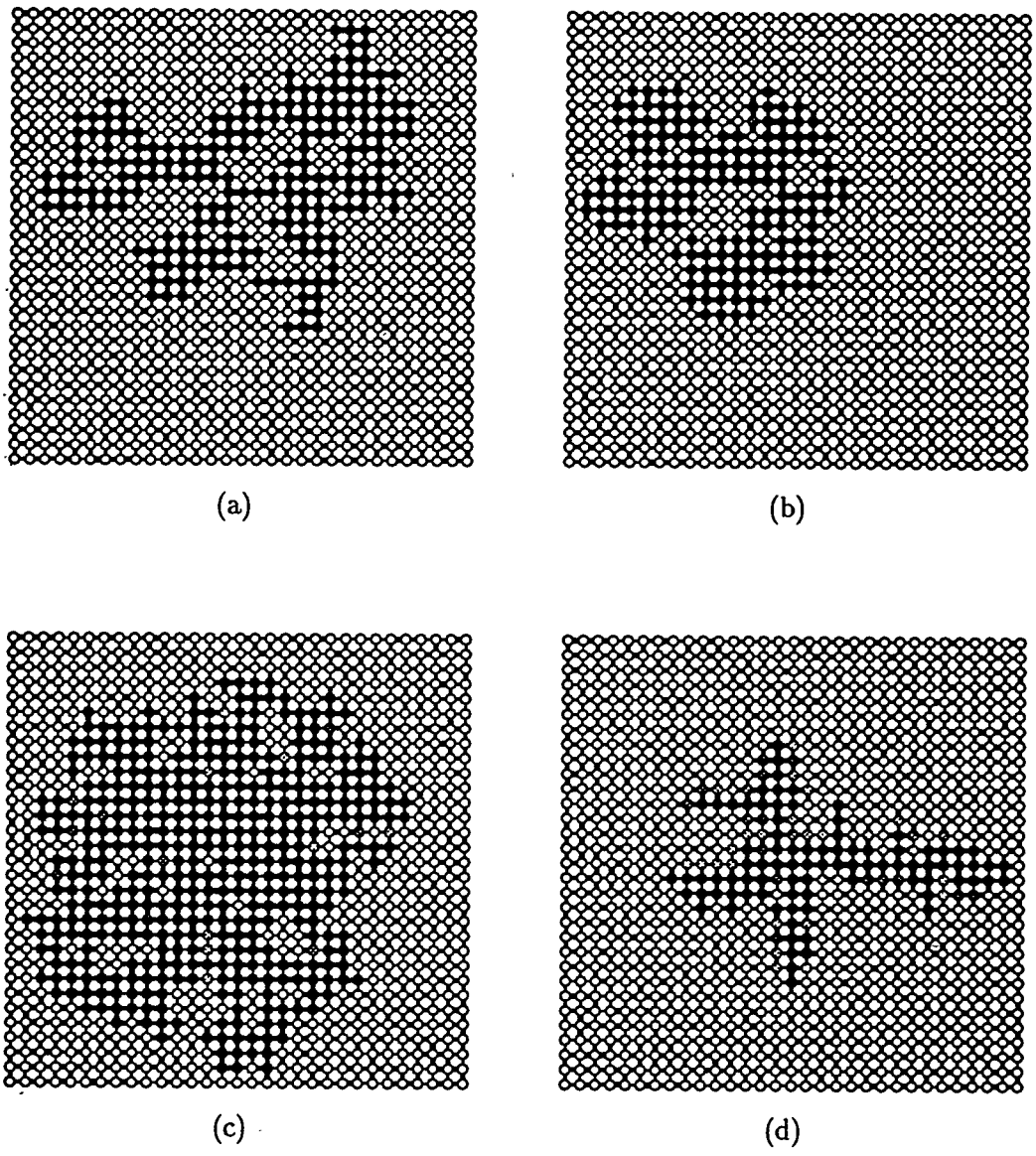

Figure 11: Final growth patterns at four different liquid viscosity values; (a) μ_l= 2.4799x10^{-5} N-s/m^2, (b) μ_l= 2.4799x10^{-4} N-s/m^2, (c) μ_l= 2.4799x10^{-3} N-s/m^2, (d) μ_l= 2.4799x10^{-3} N-s/m^2.

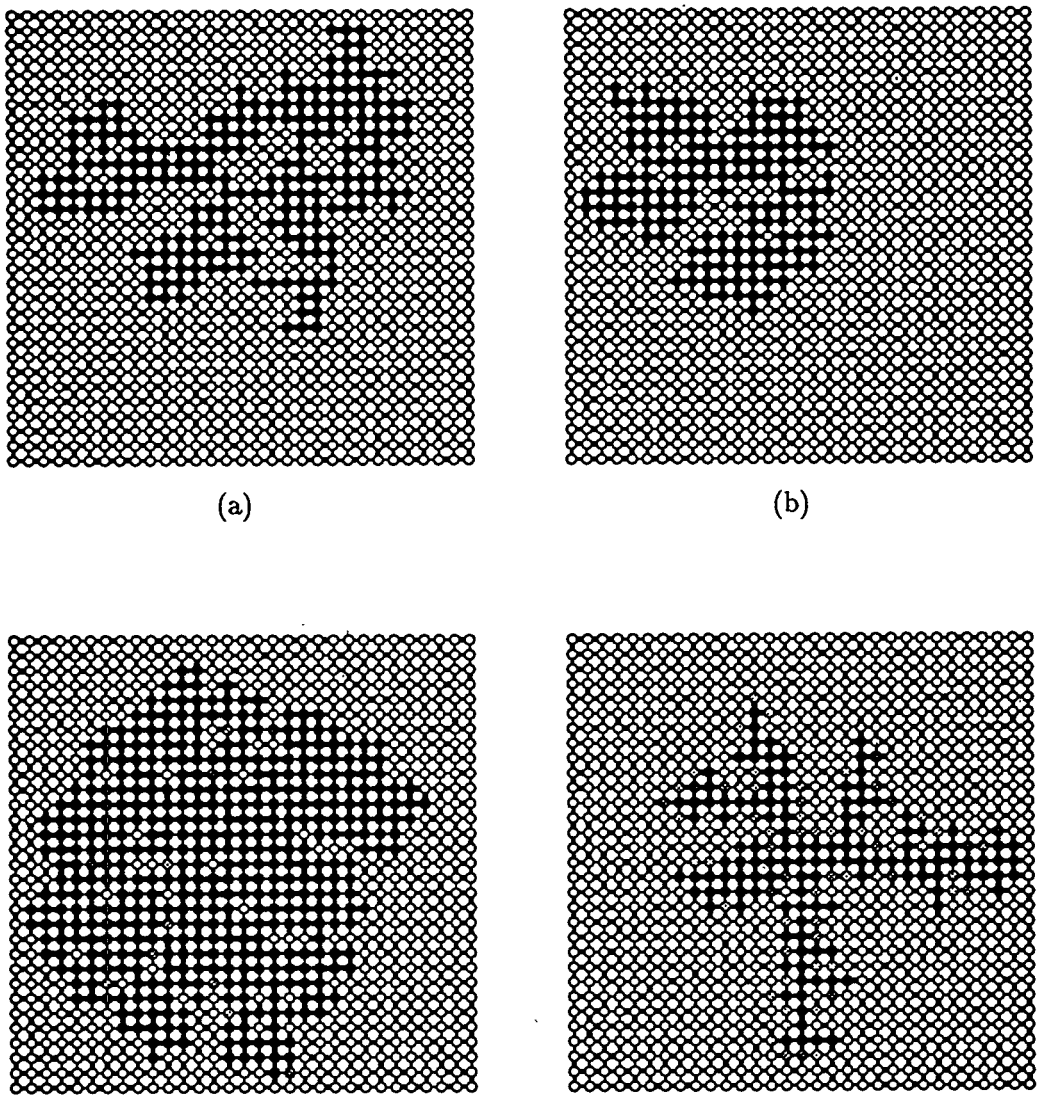

Figure 12: Final growth patterns at four different interfacial tension values; (a) $\gamma = 5.9833 \times 10^{-2}$ N/m, (b) $\gamma = 5.9833 \times 10^{-3}$ N/m, (c) $\gamma = 5.9833 \times 10^{-4}$ N/m, (d) $\gamma = 5.9833 \times 10^{-6}$ N/m.

Table 5: Ja and Ca^* values corresponding to the interfacial tension values used in the sensitivity analysis.

γ, N/m	Ja	Ca^*
5.9833×10^{-2}	13.53	2.7072×10^{-4}
5.9833×10^{-3}	13.53	2.7072×10^{-3}
5.9833×10^{-4}	13.53	2.7072×10^{-2}
5.9833×10^{-6}	13.53	2.7072

Table 6: Ja, Ca^* and t_f values corresponding to the liquid conductivity values used in the sensitivity analysis.

λ_l, W/m-K	Ja	Ca^*	t_f, s
0.06808	13.53	2.7072×10^{-4}	69.10
0.6808	13.53	2.7072×10^{-3}	7.702
6.8080	13.53	2.7072×10^{-2}	5.443
680.80	13.53	2.7072	3.141

1.4.5 Effect of Liquid Conductivity

The liquid conductivity controls the rate by which heat conduction in liquid occurs. The larger the liquid conductivity, the faster the heat conduction, thus the smaller the time required for a given volume to be occupied by the vapor and the larger the viscous pressure drop needed, since the same volume of liquid has to be displaced. Therefore, as the liquid conductivity increases, the growth patterns will change from a percolation to a viscous fingering type.

Shown in Figure 13 are the final growth patterns obtained at four different liquid conductivity values given in Table 6. At λ_l= 0.06808 W/m-K, a percolation pattern is obtained (Figure 13a). As λ_l increases, the growth pattern deviates from percolation (Figure 13b and c), and eventually reaches a viscous fingering type pattern at λ_l= 680.8 W/m-K (Figure 13d). Also given in Table 6 are t_f values obtained from each simulation. As seen from the table, t_f decreases from 69.10 s to

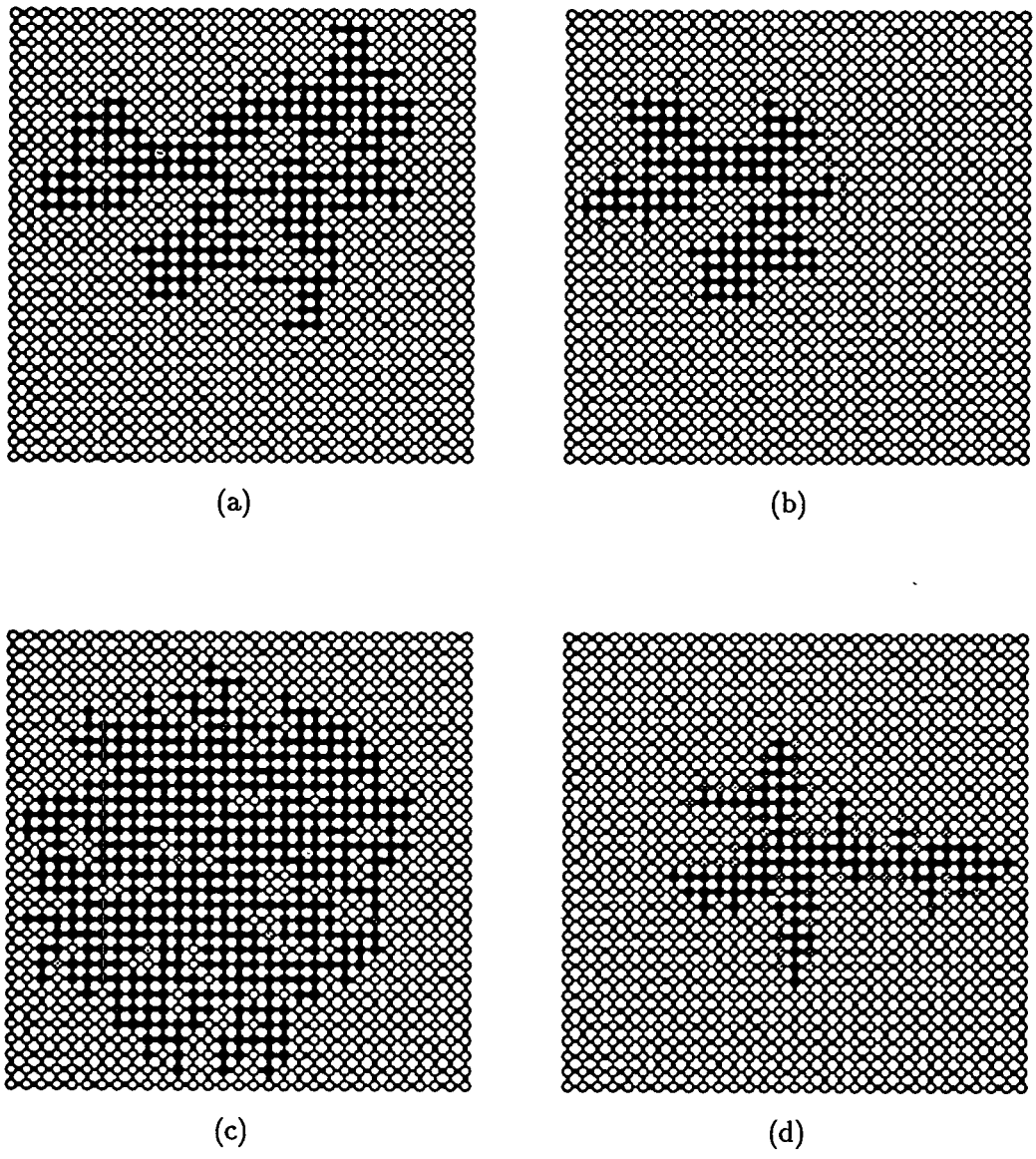

Figure 13: Final growth patterns at four different liquid conductivity values; (a) λ_l= 0.06808 W/m-K, (b) λ_l= 0.6808 W/m-K, (c) λ_l= 6.808 W/m-K, (d) λ_l= 680.8 W/m-K.

Table 7: Ja, Ca^* and t_f values corresponding to the latent heat of evaporation values used in the sensitivity analysis.

L_v, J/kg	Ja	Ca^*	t_f, s
2.2568×10^{10}	0.01489	2.9793×10^{-3}	2.176×10^{8}
1.1283×10^{9}	0.2977	5.9567×10^{-2}	1.389×10^{6}
2.2568×10^{8}	1.489	2.9793×10^{-1}	789.6
2.2568×10^{6}	148.90	2.9793×10^{1}	4.097

3.141 s when λ_l increases 10^4 times, indicating faster growth as λ_l increases.

1.4.6 Effect of Latent Heat

The latent heat of evaporation directly controls the rate by which energy is consumed for phase change at liquid-vapor interfaces. The larger the latent heat, the more energy is required for a given mass of vapor to be generated by phase change. Therefore, the process will be slower and viscous pressure drops will be smaller.

In Figure 14, we show the final growth patterns obtained at four different latent heat of evaporation values. At $L_v = 2.2568 \times 10^{10}$ J/kg, we obtain a percolation pattern (Figure 14a). As it decreases, the growth pattern deviates from percolation (Figure 14b and c), and eventually reaches a viscous fingering type pattern at $L_v = 2.2568 \times 10^{6}$ J/kg (Figure 14d).

As discussed above, the latent heat of evaporation affects evaporation rates at the interfaces over the bubble perimeter. Hence, as it increases growth will be slower, implying an increase in t_f. t_f values for the patterns shown in Figure 14 are given in Table 7. These results also show that t_f values decrease significantly when L_v is decreased.

1.4.7 Effect of Solid Conductivity

Finally, we considered the effect of solid conductivity which controls the rate by which heat transfer (conduction) takes place through the solid. Since solid and liquid temperature fields are coupled, a change in the solid conductivity will also affect liquid temperature field.

Shown in Figure 15 are the final growth patterns obtained at four different solid conductivity

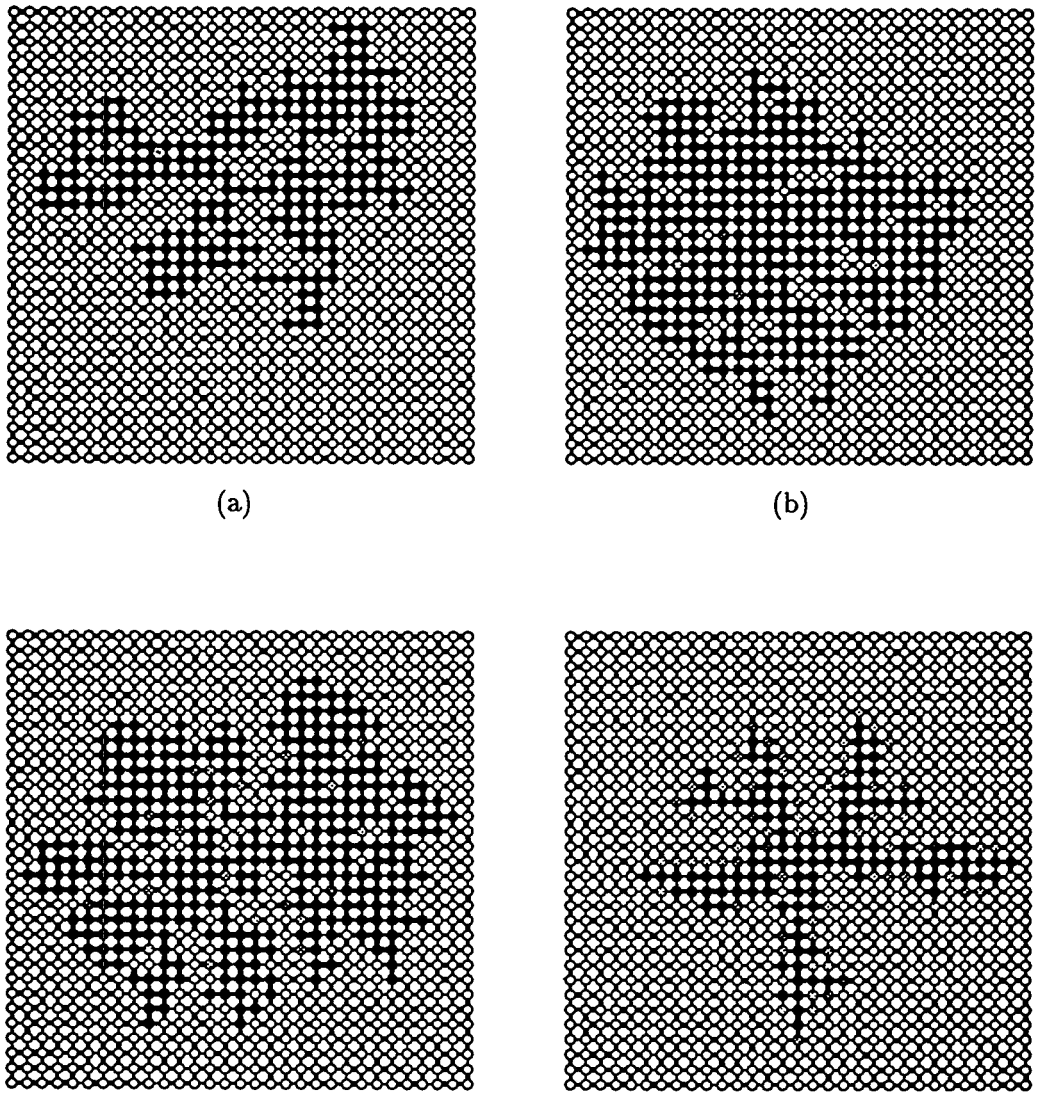

Figure 14: Final growth patterns at four different latent heat of evaporation values; (a) L_v= 2.2568x10^{10} J/kg, (b) L_v= 1.1283x10^{9} J/kg, (c) L_v= 2.2568x10^{8} J/kg, (d) L_v= 2.2568x10^{6} J/kg.

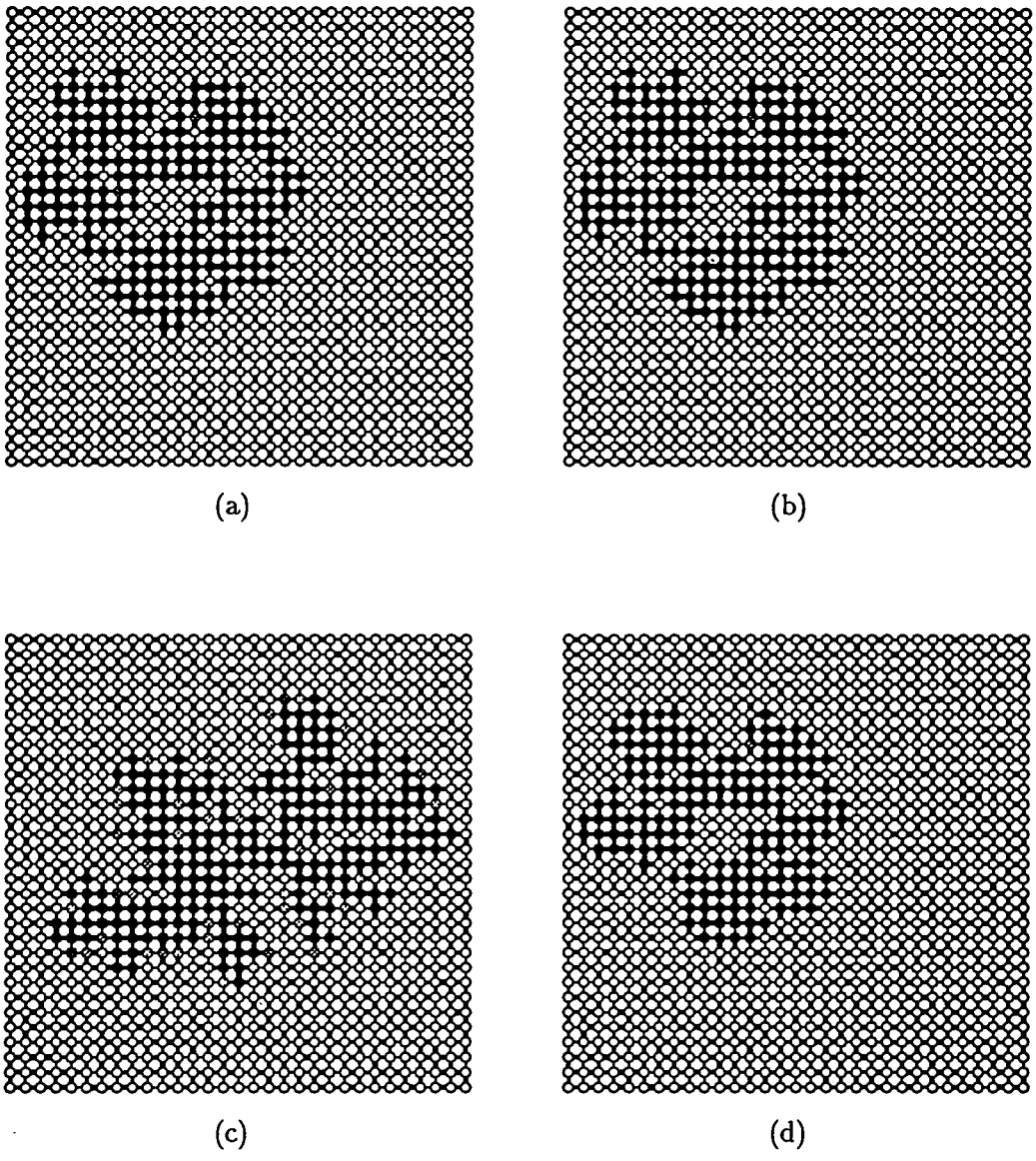

Figure 15: Final growth patterns at four different solid conductivity values; (a) λ_s= 0.06808 W/m-K, (b) λ_s= 0.6808 W/m-K, (c) λ_s= 6.808 W/m-K, (a) λ_s= 68.08 W/m-K.

values (λ_s= 0.06808, 0.6808, 6.808 and 68.08 W/m-K). As seen from the Figure, the growth patterns change and take different shapes as λ_s increases. However, neither percolation nor viscous fingering type growth patterns are obtained, which indicates that effects of solid heat transfer on the growth may be different than expected.

1.4.8 Bubble Growth with a Prescribed Heat Flux

The other case considered involved a prescribed heat flux. To model this process, we used a square lattice (21x42) network with the same bond and site distributions as in the previous case. Now, initial liquid and solid temperatures are the same, while a heat flux (q_h) is imposed over the first column of the network. Initial liquid temperature and pressure were set to 100 °C and 1.0133x10^5 N/m^2, respectively. The initial nucleation site was arbitrarily located at the node (11,1). Onset of nucleation takes place when the temperature of the node (11,1) reaches the nucleation temperature.

Fluid distributions at three different stages of bubble growth for typical parameters given in Table 2 are shown in Figure 16. For this particular run, the onset of nucleation took place at 39.673 seconds, while the corresponding times for the stages of Figure 16 are 42.37, 52.99 and 60.80 seconds, respectively. As in the previous case, fast growth dynamics are observed with partially liquid-occupied pores present, since all three stages are at a regime other than percolation.

The corresponding solid temperature, fluid temperature and pressure fields are shown in Figures 17, 18 and 19. The important differences between this and the previous case are due to the existence of a prescribed heat flux in the solid temperature field. This flux generates a temperature gradient along the solid body of the porous medium, which also brings about a gradient in the fluid temperature as both are coupled (Figures 17 and 18). As a result, the liquid phase in the pore spaces becomes superheated, providing a driving force for bubble growth. Fluid pressure fields (Figure 19) are similar to the ones obtained in the previous case.

We investigated effects of some important parameters on the bubble growth. The effect of μ_l, γ, λ_l, L_v and λ_s is expected to be similar to the previous case. The present problem, however, involves one additional parameter, the prescribed heat flux.

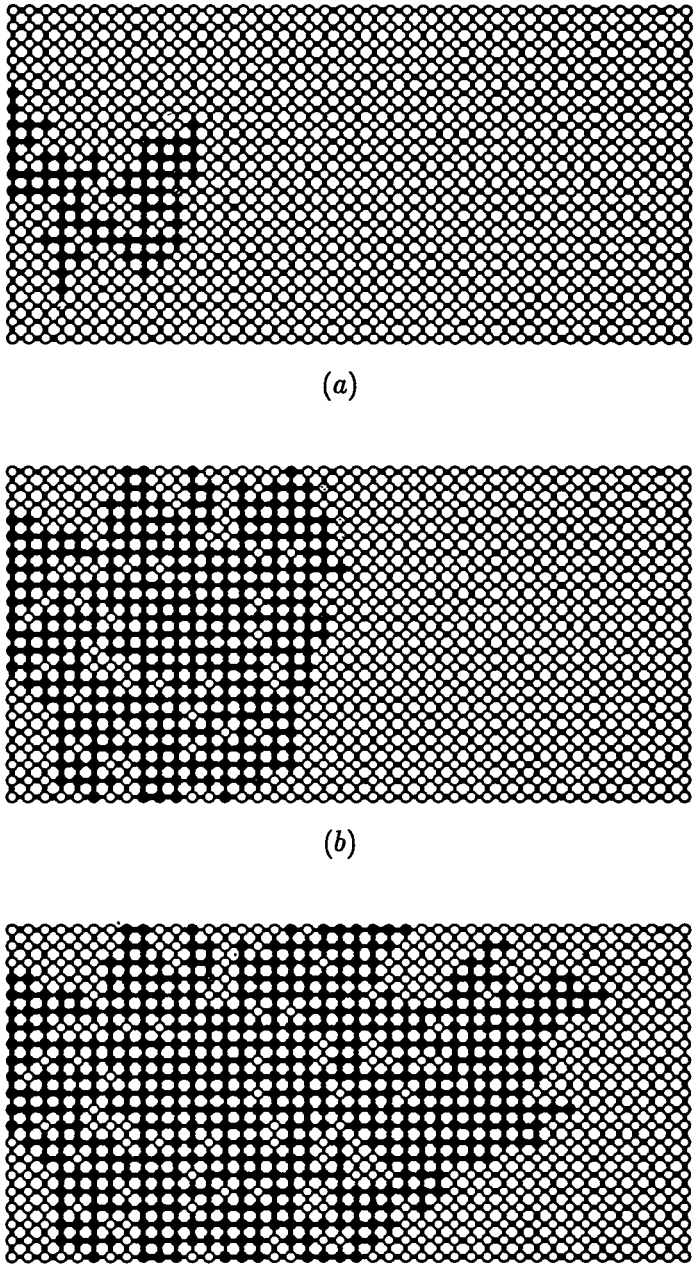

Figure 16: Fluid distributions at three stages of bubble growth with a prescribed heat flux.

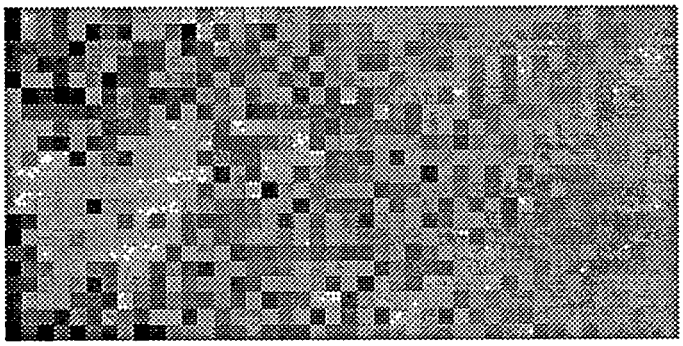

(*a*)

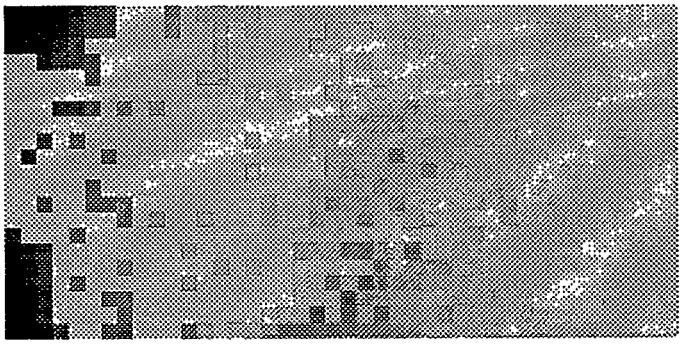

(*b*)

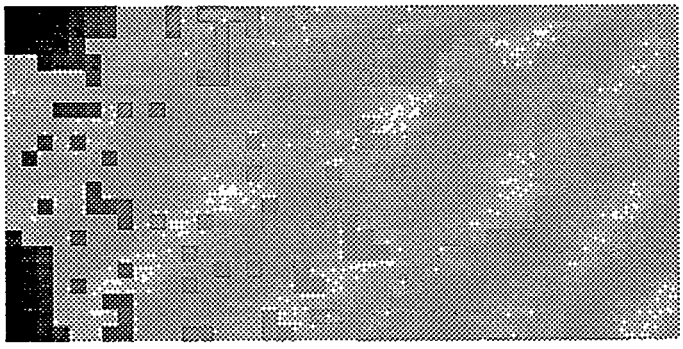

(*c*)

Figure 17: Fluid temperature fields at three stages of bubble growth with a prescribed heat flux. Minimum and maximum values in °C are (a) 91.56 and 127.35, (b) 99.78 and 107.77, and (c) 100.03 and 107.98, respectively.

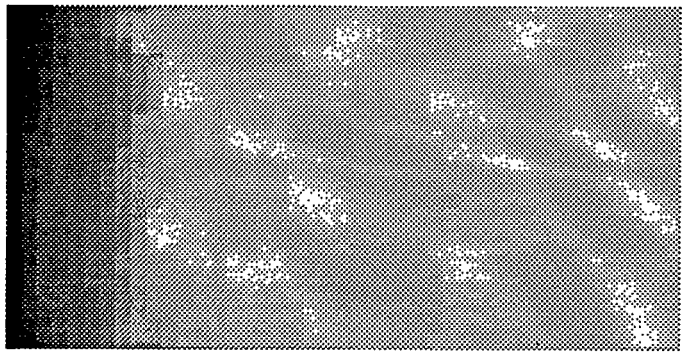

(*a*)

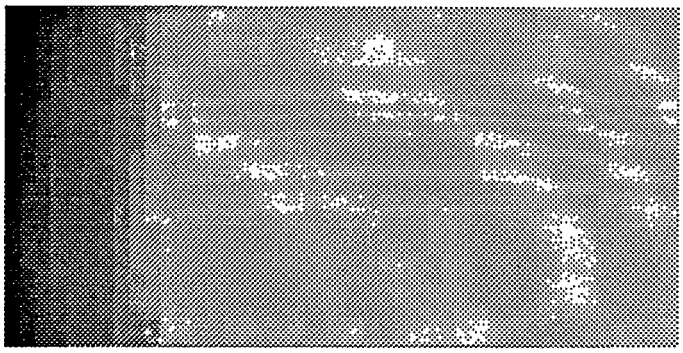

(*b*)

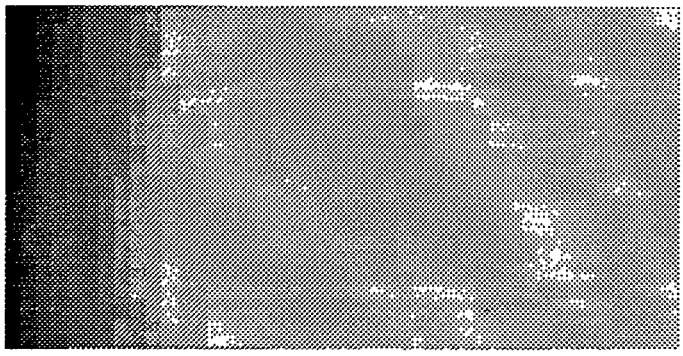

(*c*)

Figure 18: Solid temperature fields at three stages of bubble growth with a prescribed heat flux. Minimum and maximum values in °C are (a) 99.99 and 107.16, (b) 100.07 and 108.29, and (c) 100.25 and 108.69, respectively.

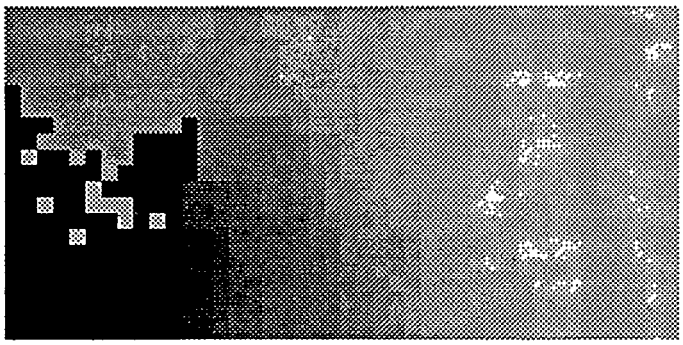

(*a*)

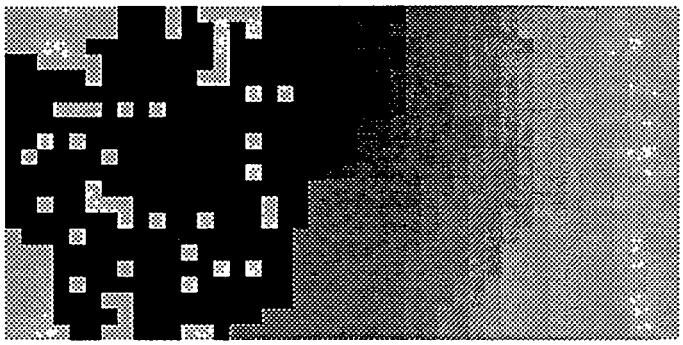

(*b*)

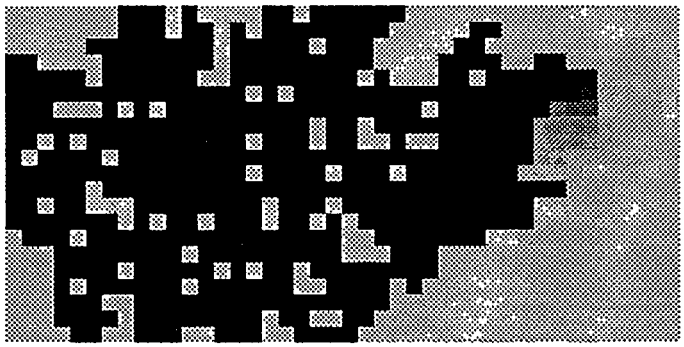

(*c*)

Figure 19: Fluid pressure fields at three stages of bubble growth with a prescribed heat flux. Minimum and maximum values in psi are (a) 14.696 and 14.701, (b) 14.696 and 14.70563, and (c) 14.696 and 14.7096, respectively.

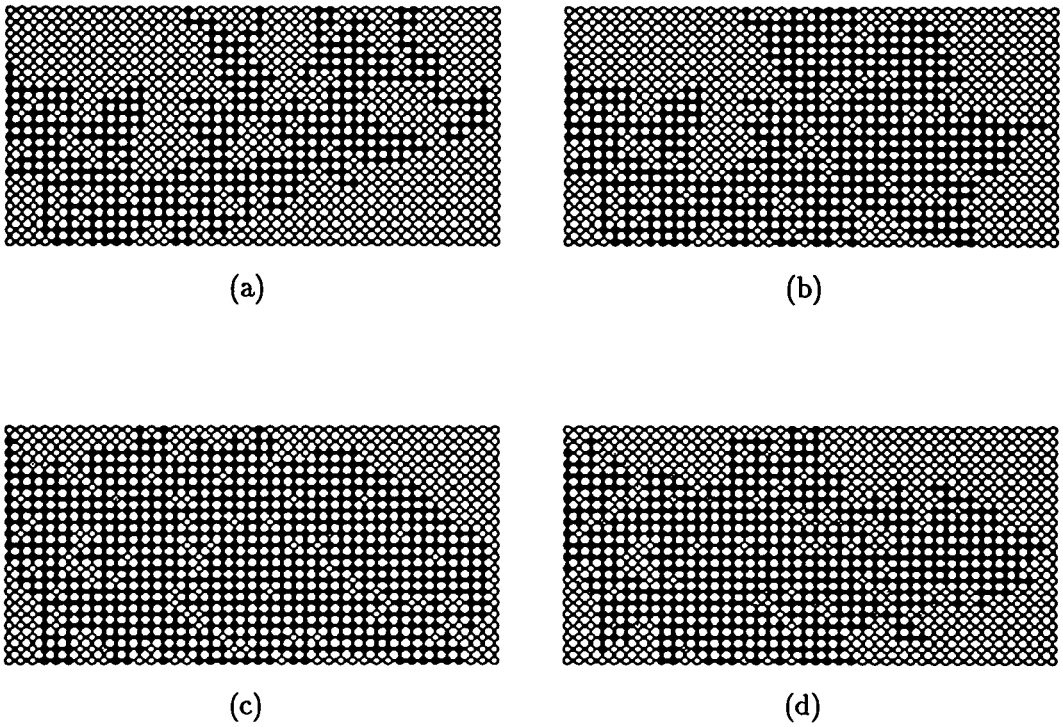

Figure 20: Final growth patterns at four different heat flux values; (a) q_h= 9.4607x10^2 W/m^2, (b) q_h= 9.4607x10^3 W/m^2, (c) q_h= 9.4607x10^4 W/m^2, (d) q_h= 9.4607x10^5 W/m^2.

1.4.9 Effect of Heat Flux

The prescribed heat flux controls both solid liquid temperatures. The larger the heat flux imposed, the larger the superheat in liquid, and the driving force for bubble growth will be greater. As a result, more vapor will form for a given time, thus more liquid will be displaced out of the pore bodies, which will increase viscous pressure drops in the liquid.

Figure 20 shows the final growth patterns obtained at four different heat flux values (q_h= 9.4607x10^2, 9.4607x10^3, 9.4607x10^4 and 9.4607x10^5 W/m^2), for the parameter values given in Table 2 with the nucleation parameter β equal to 0.1. The growth pattern in Figure 20a is of the percolation type since q_h is sufficiently small. However, the pattern deviates from percolation and takes various shapes as q_h is increased (Figure 20b,c and d). We have been unable to obtain viscous fingering type growth at the largest q_h value used (Figure 20d), however, we conjecture that at sufficiently large q_h the growth will be viscous controlled, yielding viscous fingering patterns.

1.4.10 Percolation Boundary

The previous sensitivity study shows that bubble growth pattern follows an invasion percolation pattern when viscous forces are small compared to capillary forces (sufficiently small Ca^*). During this regime, perimeter bonds are penetrated "one-at-a-time", such that the largest available bond is always penetrated first and there exists only one partially vapor-occupied pore during any pore filling step. These results are consistent with the experimental observations. The rules are the same with invasion percolation in drainage, except that here invasion occurs from an internal, rather than an external source. When viscous forces become dominant over capillary forces, the vapor pressure will be sufficiently large for multiple bond penetration over the bubble perimeter to occur, thus the bubble growth pattern deviates from percolation. At this stage, there may exist more than one partially vapor-occupied pore bodies at any pore-filling step. The number of partially vapor-occupied pore bodies determine whether the growth regime is of the percolation type or not. When this limit is reached, we shall denote the size of the bubble as the percolation boundary. To quantify the bubble size, we use the radius of gyration (R_g) of the cluster [35]

$$R_g^2 = \frac{1}{2N^2} \sum_{i,j} (r_i - r_j)^2 \tag{14}$$

where N and $(r_i - r_j)$ denote the number of vapor-occupied pore bodies and the distance between pore bodies i and j, respectively. The radius of gyration (R_g) is simply the root mean square radius of the vapor bubble measured from its center of gravity.

A detailed scaling of the conditions to estimate the percolation boundary is given in the next chapter. Here, we focus on the numerical sensitivity of the latter to various parameters, such as Ja, Ca^*, liquid heat convection, transient heat transfer and solid heat conduction. Figure 21 shows four different vapor clusters at the percolation boundary for the same parameter values used to obtain the patterns of Figure 11 except that the liquid viscosity takes the values of 2.4799x10^{-5}, 1.1408x10^{-4}, 2.4799x10^{-4} and 2.4799x10^{-3} N-s/m^2, respectively. Ca^* and R_g values values corresponding to the patterns shown in the Figure are 2.7076x10^{-4}, 1.2456x10^{-3}, 2.7076x10^{-3} and 2.7076x10^{-2}, and 7.88, 6.42, 5.0 and 1.82, respectively. As Ca^* increases, R_g decreases, which implies an earlier deviation from percolation. This is expected because viscous forces becomes dominant over capillary forces as Ca^* increases. Plotted in Figure 22 is a log-log plot of R_g vs. Ca^* at the percolation boundary, for the same parameter values used in Figure 21. The plot shows that the flow regime is

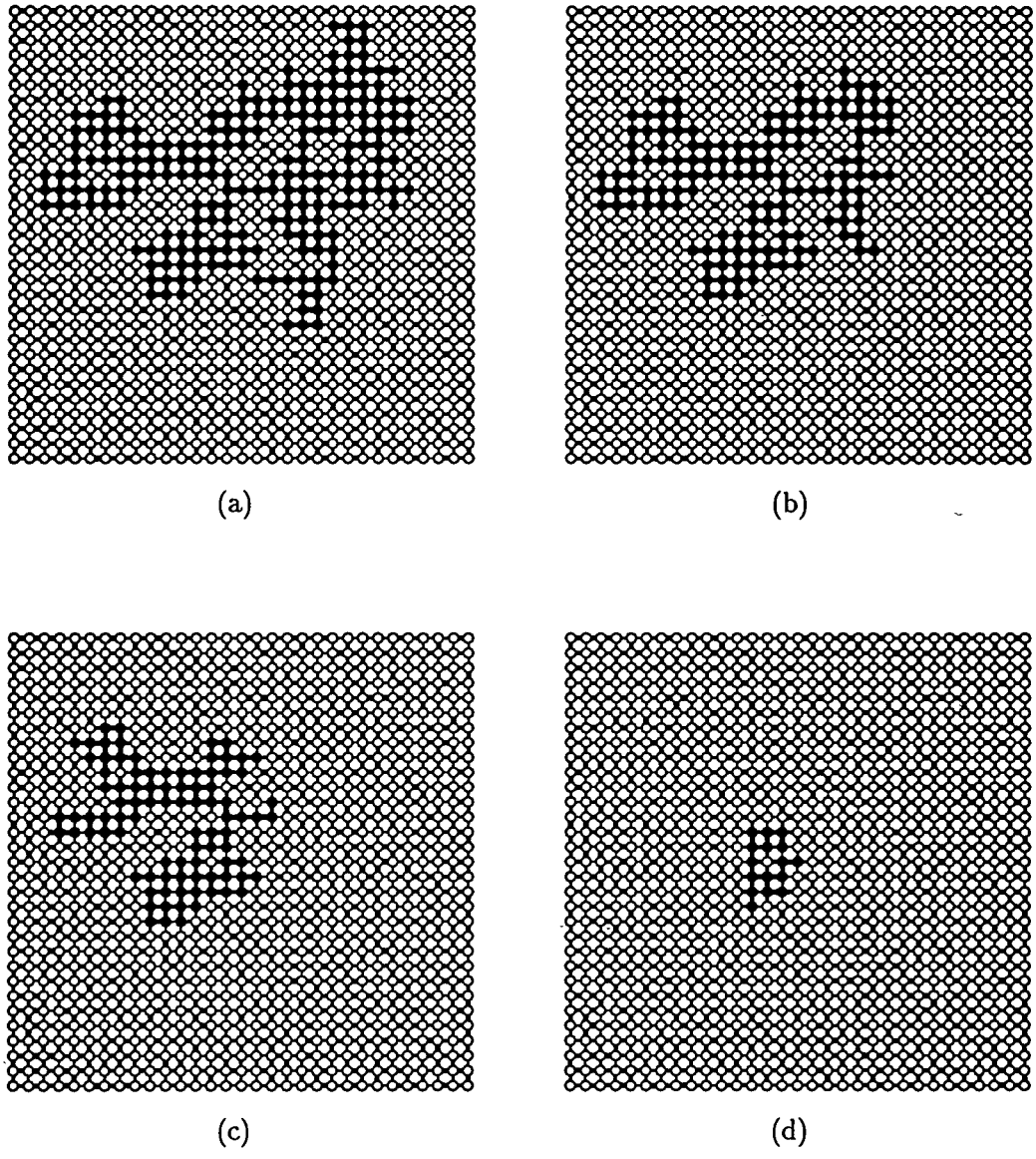

Figure 21: Bubble growth patterns at the percolation boundary.

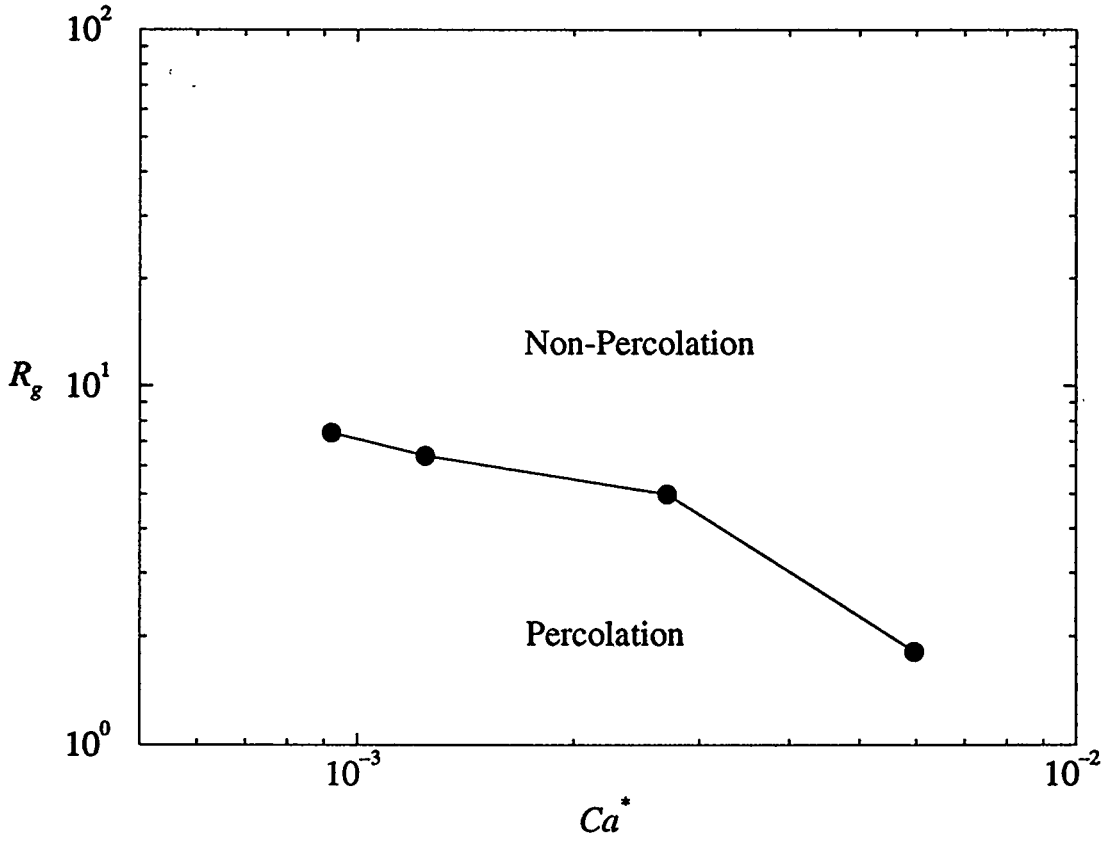

Figure 22: Percolation boundary obtained by varying liquid viscosity.

percolation as long as R_g and Ca^* are sufficiently small (below the curve). For a given Ca^* value, the bubble growth pattern is percolation at sufficiently small radius and deviates from it as the radius becomes large enough.

The effect of Ja is shown in Figure 23 (three different Ja values (0.1353, 1.353 and 13.53)). A log-log plot of R_g vs. Ca^*/Ja shows that different percolation boundaries are obtained when Ja changes (Figure 23a). However, all data collapse on the same curve when the log-log plot of R_g vs. Ca^* is used (Figure 23b), implying that percolation boundaries are insensitive to the value of Ja.

Effects of liquid heat convection and transient terms in the energy balance on the percolation boundary are illustrated in Figure 24. In the Figure, filled circles, squares and triangles denote data points corresponding to growth under the following conditions: both transient and liquid heat convection are neglected (quasi-static conditions), only liquid heat convection is neglected, and both transient and liquid heat convection are included in the liquid energy balance, respectively. As seen from the Figure, under quasi-static conditions, the percolation boundary is reached at values of R_g larger than in the other two cases. Under quasi-static conditions ($Ja \ll 1$), both transient and convection terms are negligible compared to the heat conduction terms in the energy balance. Here, the liquid temperature field, which is independent of time, is determined by solving the Laplace equation. Since the times involved in bubble growth are quite small, larger liquid-to-vapor temperature gradients form around the bubble, which in turn lead to an increase in evaporation rates over the perimeter. Therefore, an earlier deviation from percolation is expected. When both transient and convective terms are included, the gradients in the temperature field becomes larger than previously. As a result, an earlier deviation from percolation also occurs.

To examine effects of solid heat transfer, we show in Figures 25 and 26 percolation boundaries obtained at three different values of the solid thermal conductivity (λ_s= 0.6808, 6.808 and 68.08 W/m-K) and at three different values of the dimensionless parameter for heat transfer between solid and liquid phases (d^*= 19, 1900 and 19000), respectively. Our results suggest that the effect of solid heat transfer on the percolation boundary is not very pronounced.

1.5 CONCLUSIONS

In this chapter, we discussed the visualization of boiling and bubble growth in pore networks and presented a pore network model that describes bubble growth in porous media due to a temper-

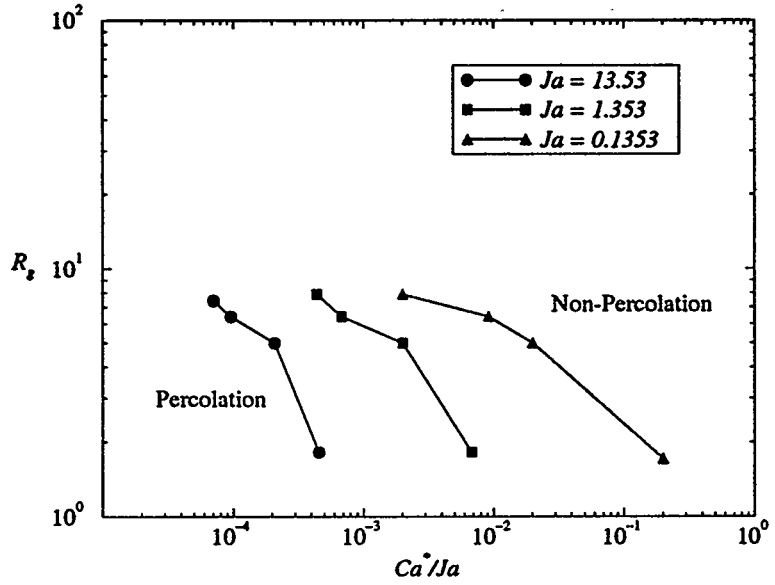

(a)

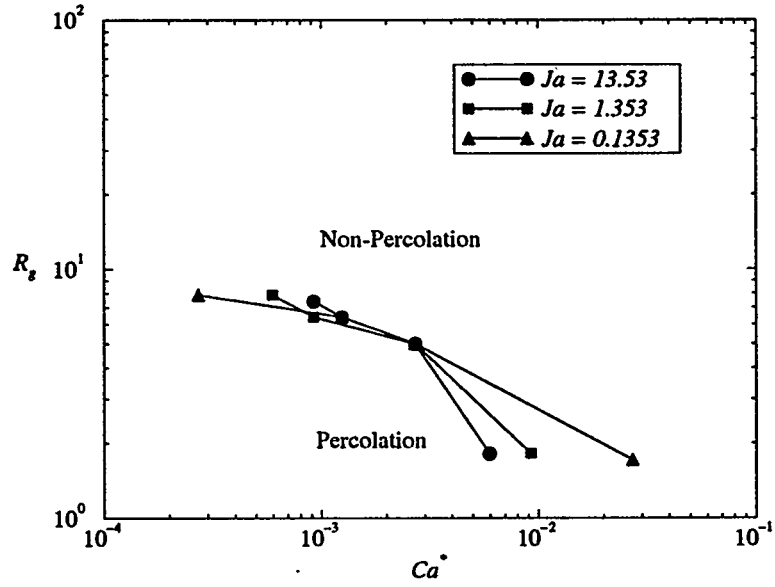

(b)

Figure 23: Percolation boundaries obtained by varying liquid viscosity at three different Ja values.

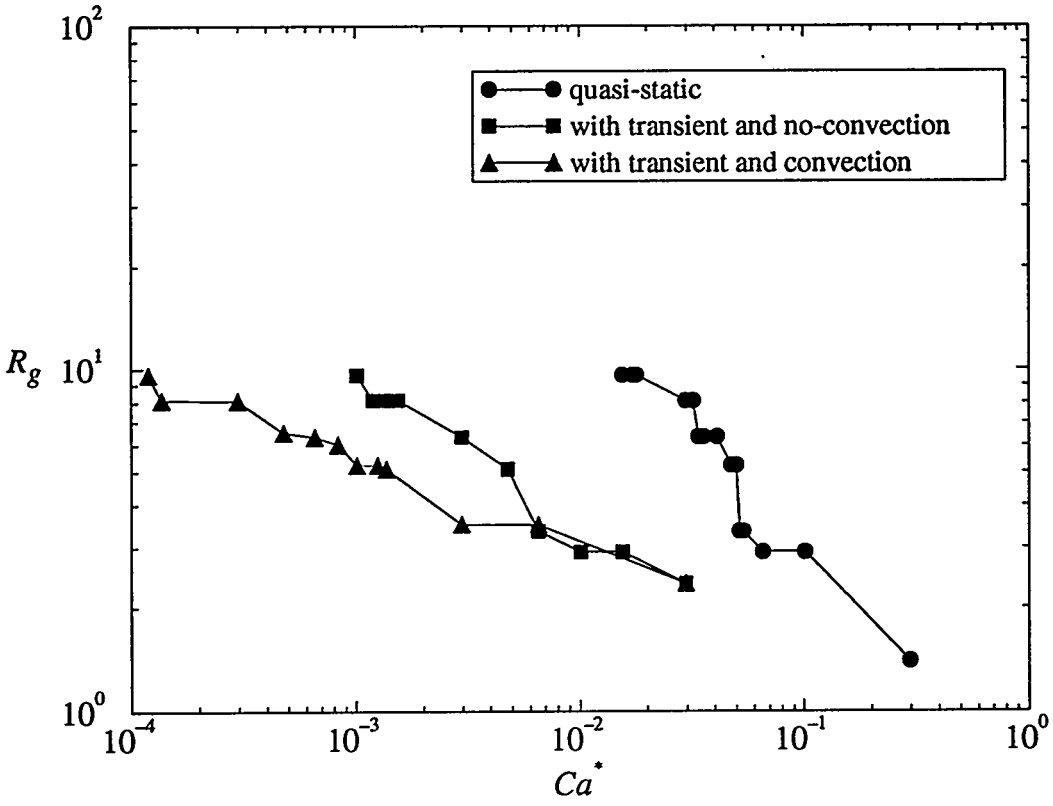

Figure 24: Effects of heat convection and transient terms in the liquid energy balance on the percolation boundary.

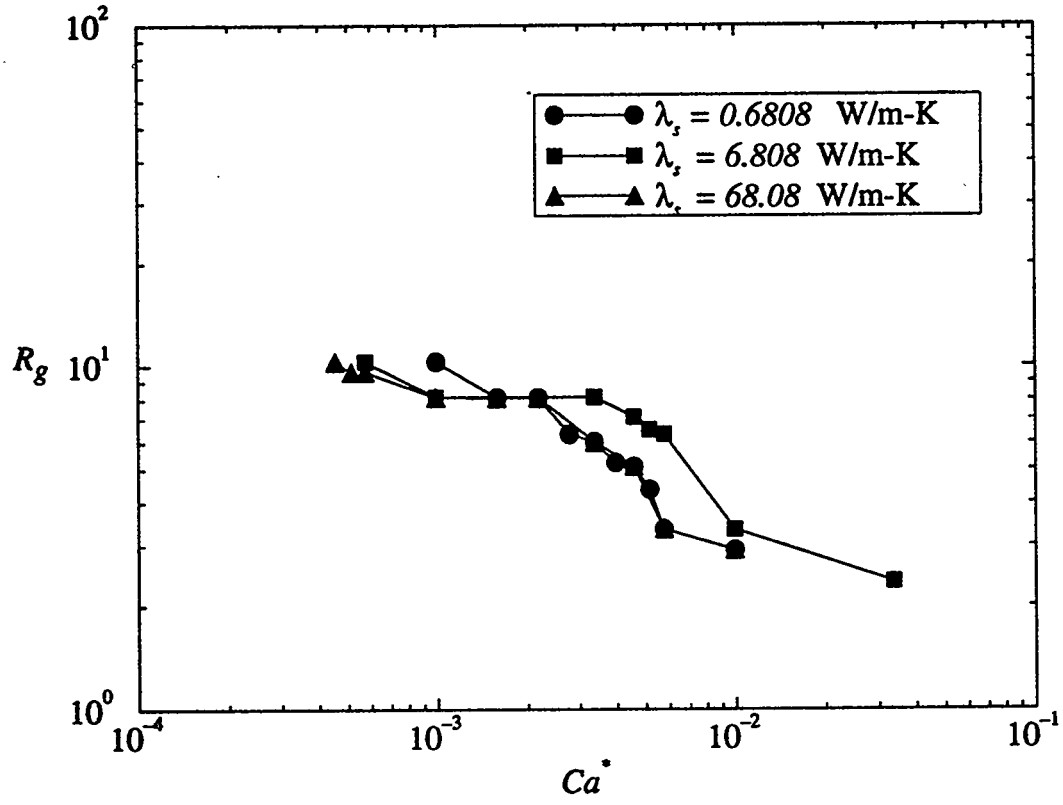

Figure 25: Percolation boundaries obtained at three solid thermal conductivity values.

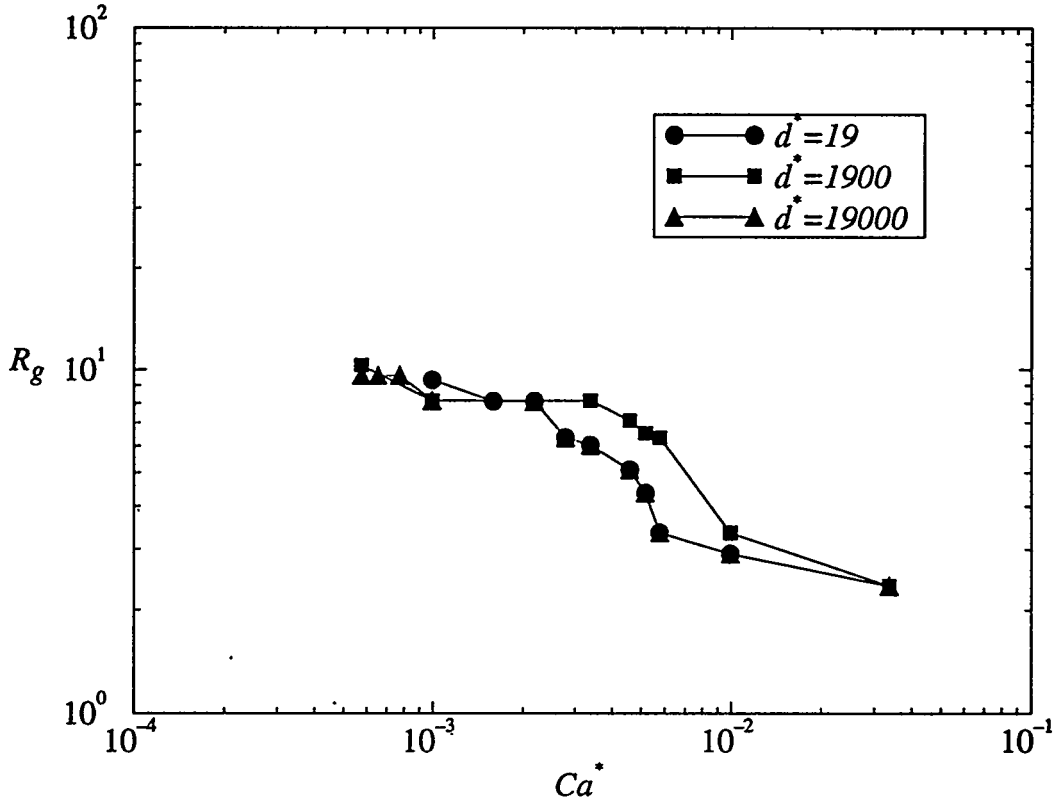

Figure 26: Percolation boundaries obtained at three d^* values.

ature supersaturation. Visualization experiments of boiling of ethyl alcohol in horizontal glass micromodels were conducted. We observed the growth of a microscopic bubble formed at the onset of a nucleation event. We found that, during bubble growth process, two stages are repeatedly followed: pore-filling and pressurization stages. During the pore-filling stage, the vapor phase is filling a pore body while the liquid is being displaced. During pressurization, the occupancy of all vapor-occupied pore bodies is complete, the bubble volume does not change significantly, the vapor pressure increases until the capillary pressure barrier is exceeded. Then, a sudden jump of the interface occurs during which interfaces located at all bonds are retreated and the bubble readjusts its shape. We identified two different modes of bubble growth. In the first mode, which is referred as "one-site-at-a-time' mode, a pore filling step strictly follows a pressurization step, while only one of the perimeter bonds are penetrated at a time. Whereas, in the second mode, instantaneous multiple bond penetrations over the bubble perimeter are possible.

The numerical model accounts for heat convection in the liquid and heat conduction in the solid, in addition to heat conduction in the liquid. We have analyzed two different types of bubble growth: (i) Bubble growth with a uniform superheat initially imposed, and (ii) Bubble growth with a constant heat flux imposed. In both cases, the final stages of the growth are reached at very small time values (order of a few second), indicating fast growth. During the bubble growth process, a liquid-to-vapor temperature gradient exist in the fluid temperature fields and this gradient drives the growth. Due to the coupling between liquid and solid temperatures, a similar gradient also exists in the solid temperature fields.

Using the pore network model, we carried out a numerical sensitivity analysis to examine effects of various parameters on the growth of vapor bubble. In bubble growth in a uniform initial superheat, we examined effects of initial superheat, liquid viscosity, interfacial tension, liquid conductivity, latent heat of evaporation and solid conductivity on the growth patterns. We showed that, at parameter values yielding sufficiently small Ca^*, the growth regime is capillary-controlled and the growth pattern is percolation. The pattern deviates from percolation according to the competition between capillary and viscous forces, as Ca^* increases. At parameter values with sufficiently large Ca^*, the regime is viscous-controlled and the growth pattern becomes viscous fingering. We identified the percolation boundary where the transition from a percolation to a non-percolation regime takes place. We showed that the bubble growth regime will be percolation as long

as the bubble size is sufficiently small not to exceed the percolation boundary. Our results suggest that liquid heat convection and transient effects change the percolation boundary significantly, while effects of solid heat transfer are minimal.

2 SCALING OF BUBBLE GROWTH IN A POROUS MEDIUM

C. Satik, X. Li and Y.C. Yortsos

2.1 INTRODUCTION

Processes involving liquid-to-gas phase change in porous media are routinely encountered, for example in the recovery of oil, geothermal processes, nuclear waste disposal or enhanced heat transfer [23, 45, 102, 108]. They involve diffusion (and convection) in the pore space, driven by an imposed supersaturation in pressure or temperature. Phase change proceeds by nucleation and phase growth. Depending on pore surface roughness, a number of nucleation centers exist, thus phase growth occurs from a multitude of clusters [121]. Contrary to growth in the bulk or in a Hele-Shaw cell [70, 84, 97], however, growth patterns in porous media are disordered and not compact. As in immiscible displacements [64, 111], they reflect the underlying pore microstructure. The competition between multiple clusters is also different from the bulk. For example, cluster growth may be controlled by a combination of diffusion (e.g. Laplace equation in the quasi-static case) with percolation. Novel growth patterns are expected from this competition [73].

While multiple cluster growth is important, the simpler problem of single-bubble growth is still not well understood. In this section, we focus on the growth of a single bubble, subject to a fixed far-field supersaturation (e.g. by lowering the pressure in a supersaturated solution or by raising the temperature in a superheated liquid). Our emphasis is on deriving a scaling theory for growth at conditions of quasi-static diffusion, guided by recent experimental observations.

Visualization of bubble growth in model porous media was recently conducted [71, 72] using 2-D etched-glass micromodels. Fig. 27 shows a typical CO_2 cluster evolving from carbonated water, initially saturated at 50 *psi*, the pressure of which was subsequently reduced to 14.7 *psi*. The non-compact nature of the cluster is apparent. The cluster grows in a manner similar to external drainage: gas-liquid interfaces are stable in the converging portion of a pore throat, but rapidly move to occupy an adjacent pore (in an event known as a "rheon"), once the capillary pressure barrier of that throat was exceeded. During the early stages, the growth occurs "one-site-at-a-time", which is a mode of interface advance typical of invasion percolation.

To model this problem, we developed a pore network simulation of multiple cluster growth (Li

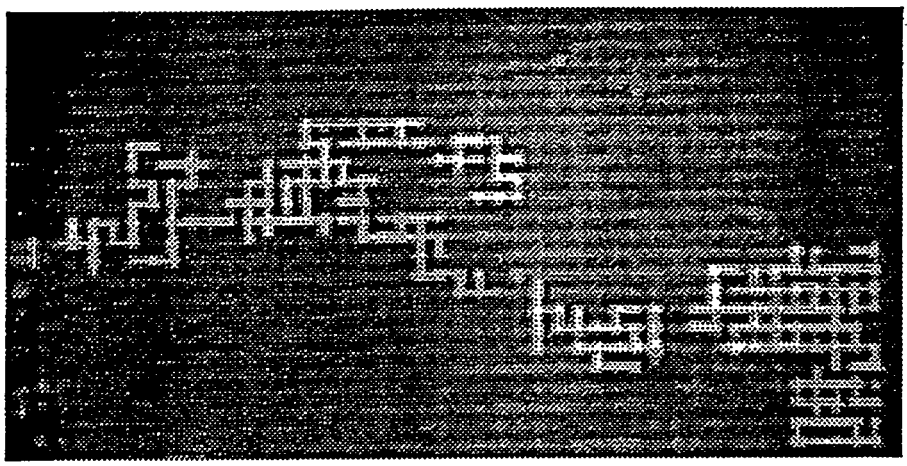

(a)

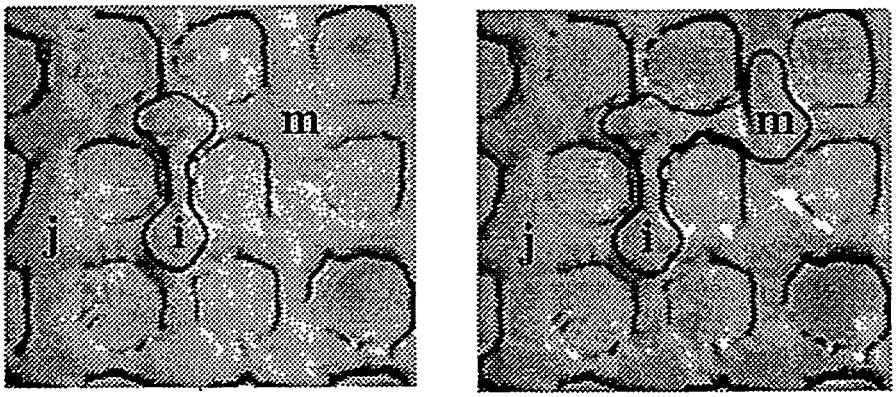

(b)

Figure 27: Experimental snapshots of gas cluster growth from carbonated water in a glass micromodel: (a) Large scale; (b) Pore scale sequence.

and Yortsos [73]) and a scaling theory for single-bubble growth when mass transfer is diffusion-controlled. This quasi-static limit is described below. We consider the initial conditions $C = C_0$, $P_l = P_0$, and the far-field conditions $C = C_0$, $P_l = P_\infty < P_0 \equiv KC_0$, where C is solute concentration, P_l is liquid pressure and K is a solubility constant. Equivalently, the supersaturation can be expressed with the Jacob number, $Ja = \frac{P_0 - P_\infty}{P_0}$. At low supersaturations ($Ja \ll 1$) the concentration field in the liquid is quasi-static and satisfies the Laplace equation $D\nabla^2 C = 0$, where D is the solute diffusivity. We consider a porous medium model in terms of an equivalent network of bonds (throats) and sites (pores). The gas-liquid interface consists of menisci residing on the cluster perimeter sites. We take the gas to be inviscid and ideal, such that P_g is spatially uniform and $P_g V = nRT$, where n is the number of moles in cluster of volume V. For simplicity, we take linear phase equilibria, $P_g = KC_i$, in all perimeter sites i ($i = 1, N$). Bubble growth is dictated by the net mass transfer rate, $\frac{dn}{dt} = \sum_{i,j} J_{ij}$, where the sum is over all perimeter sites i and the liquid-occupied sites j adjacent to them. The diffusive flux is $J_{ij} = DA_{ij}\frac{(C_i - C_j)}{l_{ij}}$, where the area A_{ij} and the length l_{ij} pertain to pore throat ij. Mass influx ($\frac{dn}{dt} > 0$) results into either pressurization ($dP_g > 0$) or bubble growth ($dV > 0$). Pressurization is necessary to overcome the capillary barrier of a perimeter bond, which occurs when the capillary pressure is sufficiently large, $P_g - P_{l,j} > \frac{2\gamma}{r_{p,ij}}$, where $r_{p,ij}$ is the radius of the connecting bond and γ the interfacial tension. Upon penetration, the interface advances and occupies site j. A measure of the driving force is the capillary number, $Ca = \frac{JaDl^*\mu_l}{\gamma k}$, where l^* is a characteristic lattice spacing, k is permeability (which scales with the average throat size [49], r_p^*, as $k \sim r_p^{*2}$) and the characteristic velocity u^* is based on diffusion, $u^* = \frac{JaDl^*}{k}$. Note the difference with the conventional Ca in external displacements [64, 111]. An additional relevant parameter is the solubility constant $\alpha = \frac{RT}{M_w K}$, where M_w is the solute molecular weight.

To characterize bubble growth requires that the cluster pattern and its rate of growth be determined. Growth in the bulk or in an effective porous medium is compact and obeys the scaling [70, 84, 97] $R \sim t^{1/2}$. In a random porous medium we expect percolation at sufficiently small sizes and viscous fingering at larger sizes.

2.2 GROWTH PATTERNS

2.2.1 Percolation

The cluster will follow a percolation pattern, if perimeter bonds are invaded "one-at-a-time", such that the largest perimeter bond is always invaded first. These rules are the same with invasion percolation, except that here invasion occurs from an internal, rather than an external source. The following conditions must apply for percolation: (i) Immediately preceding and during pressurization, all interfaces reside in converging pore geometries. (ii) During filling, only "one-site-at-a-time" is invaded, the simultaneous penetration of another throat not being possible. Condition (i) is always statisfied, since liquid and gas pressures are spatially uniform (no flow) during pressurization. Condition (ii) depends on the viscous pressure drop. During filling of a partly occupied site m, the capillary pressure in the site is small, $P_g \sim P_{l,m}$. Simultaneous penetration at another location l is not possible if $P_g - P_{l,l} \leq \frac{2\gamma}{r_{p,l}}$, namely if the pressure difference between the two sites is small. At the percolation boundary, the pattern ceases being pure percolation due to the viscous pressure drop, which is in turn related to mass transfer. We shall denote by R^p the cluster radius of gyration when this is reached and proceed for its estimation as follows.

During percolation, growth occurs from one site only (say m) (although mass transfer to the cluster is to all perimeter sites), thus the pressure field is set by the velocity of that site. The latter can be estimated from mass balance, $v_m \sim \frac{RT}{bP_\infty} \sum_{i,j} J_{ij}$ where b denotes a length, $b = 2\pi h r_s^*$ in 2-D and $b = 4\pi r_s^{*2}$ in 3-D, where h is the thickness in 2-D and r_s^* a typical site radius. To calculate the mass flux, we must solve a problem of quasi-static diffusion in a Euclidean space, bounded internally by a fractal interface. Following Ref. [12], this flux equals the mean-field result

$$\sum_{i,j} J_{ij} \sim 2\pi h D R^p \left.\frac{\partial C}{\partial r}\right|_{r=R^p} = \frac{2\pi h D(C_0 - C_i)}{ln\frac{R_e}{R^p}} \quad \text{or} \quad \sum_{i,j} J_{ij} \sim 4\pi D(C_0 - C_i)R^p \qquad (15)$$

in the two geometries, respectively, where R_e denotes the outer boundary in 2-D. The velocity follows directly,

$$v_m \sim \left(\frac{\alpha JaD}{r_s^*}\right) \frac{1}{ln\frac{R_e}{R^p}} \quad \text{or} \quad v_m \sim \left(\frac{\alpha JaD}{r_s^*}\right)\left(\frac{R^p}{r_s^*}\right) \qquad (16)$$

in the two geometries, respectively. For a conservative estimate of the percolation limit we calculate the pressure drop across a distance that scales with R^p. To describe viscous flow in a pore, we

take Poiseuille's law. Then, the flow problem involves solving the Laplace equation subject to the velocity at site m given from (16). As before, we will use a mean field approach (see also a related study [63]). We obtain,

$$\Delta P_v \sim \frac{v_m \mu_l r_s^\star}{k} ln \frac{R^p}{r_s^\star} \quad \text{or} \quad \Delta P_v \sim \frac{v_m \mu_l r_s^{\star 2}}{k} \left(\frac{1}{r_s^\star} - \frac{1}{R^p} \right) \sim \frac{v_m \mu_l r_s^\star}{k} \tag{17}$$

Then, substitution of (16) gives the final results

$$\Delta P_v \sim \frac{JaD\alpha\mu_l}{k} \frac{ln \frac{R^p}{r_s^\star}}{ln \frac{R_c}{R^p}} \quad \text{or} \quad \Delta P_v \sim \frac{JaD\alpha\mu_l}{k} \frac{R^p}{r_s^\star} \tag{18}$$

in the two geometries, respectively.

We next define the percolation limit by requesting [63] that variations, ΔS, in the gas saturation due to penetration of more than one sites as a result of viscous forces are negligible: $\left| \frac{\Delta S}{S} \right| = \epsilon \ll 1$. From percolation, this is equivalently expressed as $\left| \frac{\Delta S}{S} \right| \sim (p - p_c)^{-1} \Delta p$, where p is the percolation probability and p_c the percolation threshold. In capillary-controlled displacements, p is related to the pore throat size distribution $\alpha_p(r_p)$ via $p = \int_{r_p}^{\infty} \alpha_p(r) dr$, hence $\Delta p \sim \alpha_p(r_p) \Delta r_p \sim \frac{\Delta r_p}{\sigma r_p}$, where σ is a dimensionless measure of the variance of $\alpha_p(r_p)$. To relate Δr_p to ΔP_v, we note that variations in liquid pressure equal those in capillary pressure, $\Delta P_v \sim \Delta P_c$. The latter can be related to variations in the occupied pore sizes, $\Delta P_c = \frac{2\gamma \Delta r_p}{r_p^2}$. Next, we identify the cluster extent with the cluster correlation length, thus $\frac{R^p}{l^\star} \sim \xi \sim (p - p_c)^{-\nu}$, where ν is the correlation length exponent, 1 to $\frac{4}{3}$ in 2-D and to 0.88 in 3-D. Then, we replace variations in p by variations in r_p, and substitute the above to find the results

$$\left(\frac{R^p}{l^\star} \right)^{\frac{1}{\nu}} \left(\frac{ln \frac{R^p}{r_s^\star}}{ln \frac{R_c}{R^p}} \right) \frac{\alpha r_p^\star Ca}{\sigma l^\star} \sim \epsilon \quad \text{or} \quad \left(\frac{R^p}{l^\star} \right)^{\frac{1}{\nu}+1} \frac{\alpha r_p^\star Ca}{\sigma r_s^\star} \sim \epsilon \tag{19}$$

in 2-D or 3-D geometries, respectively. Equation (19b) is analogous to the expression that delineates the percolation limit in external displacements [63]. Clearly, the radius at the percolation limit decreases as Ca increases, namely as Ja or D increase.

2.2.2 Viscous Fingering

As the cluster size increases, the pattern eventually departs from percolation. To infer its characteristics, Li and Yortsos [70] performed a linear stability of the equivalent problem in an effective

porous medium (or a Hele-Shaw cell). In the absence of capillarity, the growth posesses the Mullins-Sekerka instability of solidification [59, 83], which here also happens to coincide with the viscous fingering instability. As a result, we expect a limiting pattern of the DLA type at sufficiently large sizes. This was confirmed with numerical simulations (see below). To delineate the pattern boundary, R^{vf}, we proceed as in the previous. Now, however, we request that variations in the capillary pressure are small compared to the viscous pressure drop between adjacent sites, $\Delta P_c \ll \Delta P_v$. For the latter, we take

$$\Delta P_v \sim \frac{v_m \mu_l r_s^*}{k} ln2 \quad \text{or} \quad \Delta P_v \sim \frac{v_m \mu_l r_s^*}{2k} \tag{20}$$

and after substitution of v_m, we obtain

$$\left(\frac{1}{ln\frac{R_c}{R^{vf}}}\right)\left(\frac{\alpha Ca}{\sigma}\right) \sim \epsilon^{-1} \quad \text{or} \quad \left(\frac{R^{vf}}{l^*}\right)\left(\frac{\alpha Cal^*}{\sigma r_s^*}\right) \sim \epsilon^{-1} \tag{21}$$

in the two geometries, respectively. Large values of Ca result in promoting a pure DLA growth pattern at smaller cluster sizes.

We used the numerical simulator in 2-D geometries (Li and Yortsos [73]), to test the validity of the two limits. Simulations were performed in square lattices of variable sizes, but not larger than 50x50, due to computational limitations. First, the mean-field results for quasi-static mass transfer were tested. Fig. 28 shows a plot of the total net mass flux to a percolation cluster as a function of the cluster size. Good agreement with the theory is found provided that the computational domain is large (here equal to 200x200) and the cluster size sufficiently large, but not too large for the boundary to affect the radial symmetry. Plotted in Fig. 29 are numerical results for R^p and R^{vf}, where only quasi-static diffusion was considered (the simulator can also account for convection and transients [73]). The qualitative trend of the results is consistent with the theory. However, due to the small size of the computational domain (50x50), which gives rise to substantial finite-size effects, a quantitative agreement is difficult to be ascertained. The cluster must be large enough for meaningful percolation statistics, yet small enough compared to the outer boundary for the mean-field theories to be valid. We expect a better agreement as the size increases to at least 200x200 (compare with Fig. 28). The transition from percolation to DLA is illustrated in Fig. 30, which illustrates cluster growth under conditions of percolation (Fig. 30a) or viscous (Fig. 30b) control.

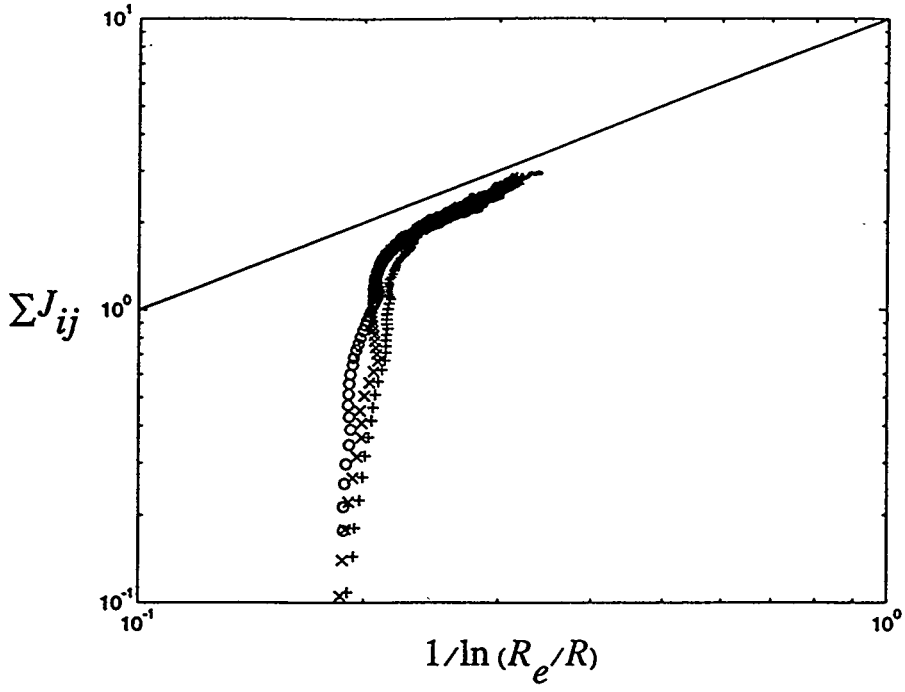

Figure 28: Total net flux to a percolation cluster under quasi-static diffusion. The solid line is the theoretical slope (eqn. 15).

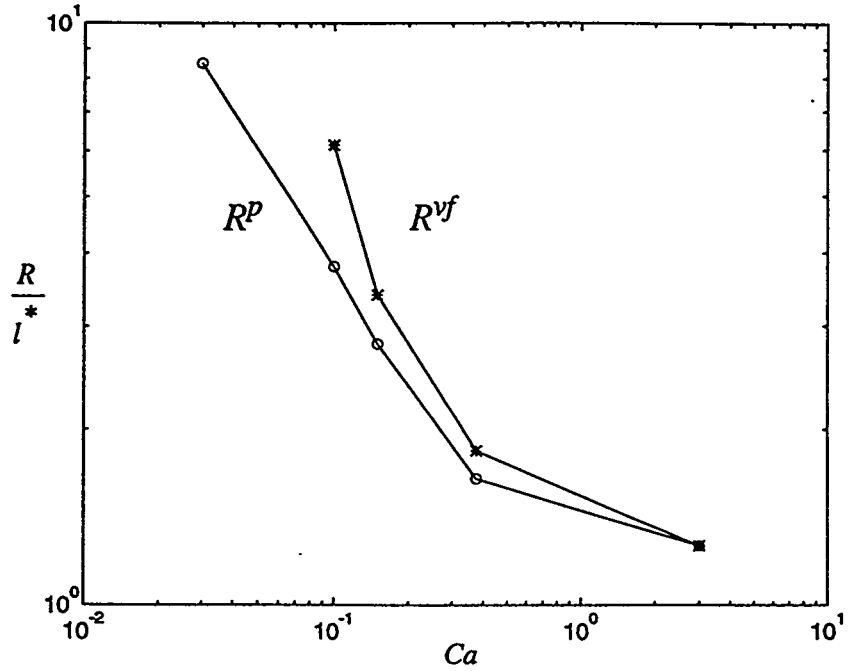

Figure 29: Percolation and viscous fingering boundaries from pore network simulations in a 50x50 square lattice. The solid line is a guide to the eye.

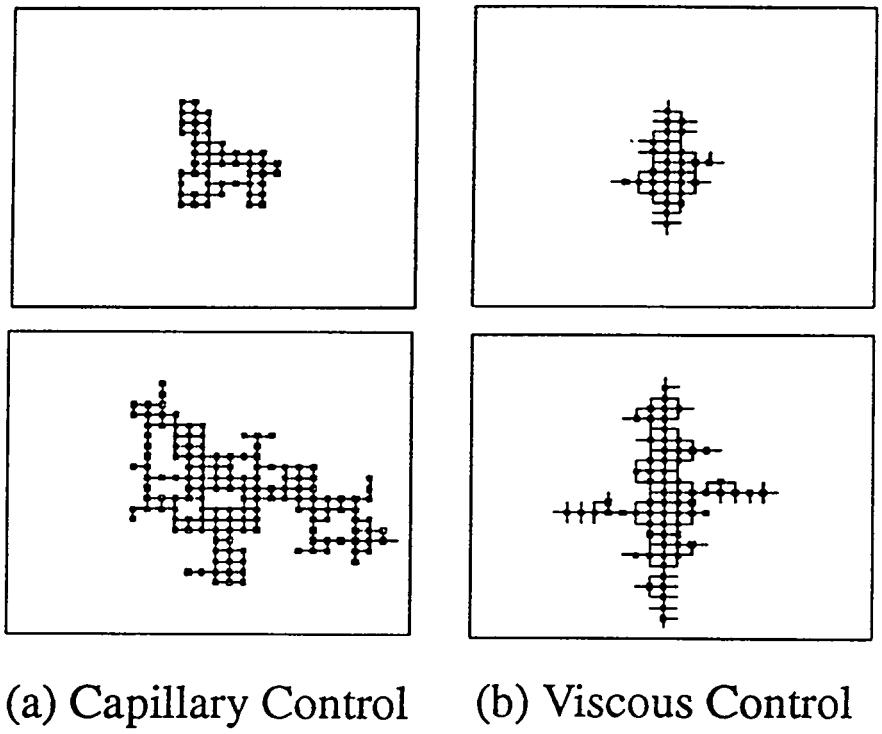

Figure 30: Typical sequence of gas cluster growth under conditions of: (a) Capillary control (Ca= 0.00001); (b) Viscous control (Ca= 0.1).

2.3 RATES OF GROWTH

From the above, rates of bubble growth can be calculated. If N_g is the number of sites occupied by the gas cluster and V_s the average site volume, we have $V_s \frac{dN_g}{dt} = v_m b$, where N_g is related to the radius R_g via $N_g \sim \left(\frac{R_g}{l^*}\right)^{D_f}$ and D_f is the fractal dimension of the cluster. Substitution from (2) yields the results

$$\left(\frac{R_g}{l^*}\right)^{D_f}\left[1+D_f ln\frac{R_e}{R_g}\right] \sim \frac{\alpha b Ja D D_f}{V_s r_s^*}t \quad \text{or} \quad \left(\frac{R_g}{r}\right)^{D_f-1} \sim \frac{(D_f-1)}{D_f}\frac{\alpha b l^* Ja D}{V_s r_s^{*2}}t \qquad (22)$$

in the two geometries, respectively. The two scalings should be contrasted to the classical for growth in the bulk, $R_g^2 \sim t$. As a result of its ramified structure, the cluster grows faster than in its effective medium analogue (for example, $R_g \sim t^{\frac{2}{3}}$, for the 3-D case in either the percolation or the viscous fingering limits).

All these scalings rely on the assumption of quasi-static mass transfer. For growth in the bulk this is equivalent to the condition $Ja \ll 1$. In the general case, however, this condition becomes [73] $Jat^{\frac{3-D_f}{D_f-1}} \ll 1$. Thus, contrary to the compact cluster ($D_f = 3$) the validity of the quasi-static approximation in fractal patterns ($D_f < 3$) is time-dependent. To check its validity when R^p and R^{vf} are reached we substitute in (19) and (21) the results from (22) to obtain $Ja^{1-\frac{\nu}{\nu+1}(3-D_f)} \ll 1$ and $Ja^{1-\frac{D_f(3-D_f)}{D_f-1}} \ll 1$, respectively. Since $D_f \sim 2.5$ in both patterns, the two conditions are still equivalent to the condition for bulk growth, $Ja \ll 1$.

2.4 CONCLUSIONS

We conclude that during single bubble growth in a porous medium the following regimes develop in succession: a short duration early-time regime, where finite size effects dominate, the growth is still compact and the effective medium scaling applies; a percolation regime ($R_g \leq R^p$); a transition to a viscous fingering regime ($R^p \leq R_g \leq R^{vf}$); and a DLA regime ($R^{vf} \leq R_g$). In the absence of convection, the corresponding rates of growth are different than the classical. Effects of convection are under study.

3 VISUALIZATION AND SIMULATION OF IMMISCIBLE DISPLACEMENT IN FRACTURED SYSTEMS USING MICROMODELS: II. IMBIBITION

M. Haghighi and Y.C. Yortsos

3.1 Introduction

Steam injection is a potentially effective method for the recovery of heavy oil from reservoirs. There are large accumulation of heavy crude and tar sands subject to steam injection in certain parts of the world, especially in western Canada, central Venezuela and in California and Utah in U.S.[87]. Steam injection can also be used to recover light crude much more effectively than waterflooding [87]. Naturally fractured reservoir may contain 25-30% of the world supply of oil [92]. Thus, steam injection in fractured reservoirs has a high potential importance in oil production.

Unfortunately, the understanding of steam injection in fractured systems is currently based mostly on phenomenology and typically consists of applying a double porosity formalism to steam simulators [16] [47] [61]. Most of these simulators use capillary imbibition as a mechanism for the exchange of fluids between the matrix blocks and the fracture network. Such a purely numerical approach offers little to further our insight into the process. A reasonable alternative is to conduct experiments in model geometries that mimic fractured systems. Glass micromodels can be constructed to mimic there. In this research, steam injection experiments in these models was conducted.

Since steam is non-wetting when in the vapor phase, but becomes wetting when condensed, steam injection involves both drainage and imbibition mechanisms in addition to the temperature effects on displacement and phase change. Therefore, to understand its effects the mechanisms isothermal displacement in fractured systems must first be studied. For this, based on visualization experiments we developed theories for both drainage and imbibition. A pore network simulator was also used to compare the experimental results and confirm the theory. Previously, we reported results on drainage processes [39]. In this report, we shall present our findings on imbibition. Steam displacement will reported in future reports.

3.1.1 Literature Review on Immiscible Displacement in Fractured Systems

Immiscible displacement in disordered porous media proceeds by different mechanisms, depending on the nature and history of the displacement (drainage or imbibition, primary or secondary process). These mechanisms have been clearly elucidated in recent years, notably by Lenormand who conducted careful experimental studies in micromodel geometries [65]. The local displacement mechanics are not expected to change when a fracture-matrix system is considered. Thus, primary displacements will proceed by a frontal advance of the menisci, the conditions for which vary depending on whether the process is drainage or imbibition, the latter including the possibility of flow along the surface roughness. Secondary imbibition will involve in addition film flow, film thickening and snap-off, resulting at low rates in displacements different than frontal. In a fracture-matrix system, or in a system containing a streak of high permeability, the presence of fractures (or high permeability streaks) adds an element of large-scale correlation. These large scale features affect the composite process and introduce important flow rate effects.

Mattax and Kyte [77] who studied imbibition in fractured water-drive reservoirs, experimented with a single matrix block and studied the effect of the matrix block size to predict the recovery behavior for a reservoir matrix block from an imbibition test on a core sample. They introduced the following scaling equation

$$t_d = t\sqrt{\frac{k}{\phi}}[\frac{\sigma}{\mu_w L^2}] \tag{23}$$

They also introduced the concept of a "critical rate", in connection with water advance in fractured-matrix reservoirs. This was defined as the rate for which the water advance level in the fracture is the same to the water level in the matrix. For rates less than the critical, the water level in the matrix is above that in the fractures. Thus, all the recoverable oil will be displaced from the matrix block before the water in the fractures reaches the top of the block. Inversely, at rates greater than the critical, the water level in the fracture moves ahead of the water in the matrix and the matrix block is completely surrounded by water before imbibition is completed.

Eka and Ershaghi [30] considered gas injection in naturally fractured reservoirs. This process was simulated using a mathematical model that included both gravity and capillarity forces. They concluded that recovery of oil from low permeability matrix block can be improved by temporarily shutting in production wells when the gas-oil ratios are high. Labastie [58] discussed the capil-

lary continuity between the matrix blocks during the gravity drainage in fractured reservoirs. He showed both experimentally and numerically that the oil recovery by a gravity drainage process in a naturally fractured reservoir strongly depends on the total height and capillary continuity. Rossen and Shen [90] proposed pseudo-capillary pressure curves for both the matrix and fracture to represent gravity drainage mechanism, which they used in a dual porosity simulator.

In theoretical studies on displacements in fractured systems, the main emphasis has been on deriving some representation of the matrix imbibition rate, either by solving an appropriate initial boundary value problem or by introducing various simplifying assumptions. For example, Aronofsky et al. [2] defined a simple exponential relation between recovery and time for a single matrix block due to water invasion in fractured reservoirs. de Swaan [22] presented a theory in which the matrix blocks downstream are exposed to a varying water saturation resulting from the water imbibition upstream blocks. He used as a convolution integral a solution in terms of a known solution with a unit-step boundary condition proposed by Aronofsky et al. [2].

In the first visualization study in fractured systems, Handy and Datta [41] provided visual evidence of water imbibing in an artificially-fractured sandstones and in a heterogeneous sand pack. In the case of fractured sandstone, they observed that the water moves preferentially through the fracture, due to the low capillary pressure, while in the heterogeneous sand pack water imbibes into the fine sand because of capillary forces stronger than in the coarse sand. As rates increased, the water was seen to move preferentially through the more permeable regions. Handy [40] proposed a rate equation for imbibition and discussed the validity of the use of the diffusion equation with a nonlinear diffusion coefficient as a model for imbibition. Babadagli [3] conducted a series of forced imbibition experiments in model fractured sandstones, visualized by CT scanning, which demonstrated that effective relative permeabilities of the composite system (fracture and matrix) are strong functions of flow rate and the properties of the matrix and fracture, such as matrix permeability and fracture aperture.

3.2 Imbibition

Imbibition is among the processes that may be involved in steam displacement in fractured systems. Imbibition mechanisms in the presence of fractures have not adequately been studied in the past. Previous work was concentrated on experiments with core or on simulation using a double porosity

simulator. Notably lacking are flow visualization using transparent 2-D micromodels and simulation of the matrix-fracture interaction. In this chapter, our objective is to provide a better insight on the recovery mechanisms in fractured systems during forced and free imbibition (both primary and secondary). To achieve this goal, pore level and larger scale visualization were first performed in a glass micromodel of a fracture-like structure, and a parametric experimental study of the effects of capillary number, mobility ratio, and gravity was undertaken. Next, we developed a simplified theory to predict the observed mechanisms. Subsequently, a pore network simulation of primary and secondary imbibition was used in order to compare the experimental results with the numerical output, and provide more details of the process.

3.2.1 Experiments

The experimental set-up in this chapter is the same as that for drainage. We used both triangular and square pattern micromodels. The values of the network and fracture parameters are shown in Table 8.

Table 8: Micromodel characteristics

Network	Square	Triangular
Length	11.2 cm	12.5 cm
Width	5.7 cm	7.5 cm
Number of squares	51×26	75×45
Maximum bond width	0.1 cm	0.04 cm
Minimum bond width	0.04 cm	0.04 cm
Average bond width	0.07 cm	0.04 cm
Fracture width	0.2 cm	0.2 cm
Fracture depth	0.018 cm	0.01 cm
Network depth	0.009 cm	0.01 cm

Forced experiments were carried out at constant rate by the use of a syringe pump. A video camera with a close-up kit provided the desired visualization. The front movement were also recorded under a microscope for clearer visualization. The following four fluid pairs were used in

the experiments:

1. Distilled water-air.
2. Distilled water-kerosene.
3. Distilled water-heavy mineral oil.
4. Distilled water-Dutrex 2621 (a synthetic oil, product of Shell Company with a measured viscosity of 10000 cP at 25°C).

In all experiments, kerosene and mineral oil were dyed with Fat Red 7B, and water was dyed with either Methylene Blue or Fluorescein. We used the measured value of 70 dynes/cm for the interfacial tension of water-air, and the approximate value of 35 dynes/cm for all water-oil systems.

3.2.2 Forced Primary Imbibition

Primary imbibition is the displacement of a non-wetting fluid by a wetting fluid in the absence of prewetting. Systematic primary imbibition experiments were carried out for each fluid pair at four different capillary numbers (Table 9).

In this set of experiments, we used the micromodel with triangular pore pattern, of coordination number 6. It was found that in experiments with water displacing air, and for a capillary number 2×10^{-6} and lower, the water invaded the matrix first. At the pore level, both in the inlet of the model and in the matrix, two different and simultaneous mechanisms were clearly observed: 1- Water flow along the roughness of the walls (Figures 31-36); 2- Meniscus movement (Figures 37-39). The flow of water along the surface roughness causes accumulation of water on the walls (Figures 31 and 32). When sufficient accumulation on one wall only, the radius of curvature of the interface increases, until it touches the opposite wall pore and adjacent channel are invaded instantaneously. When there is sufficient accumulation of water on walls, only the channel is filled. At capillary numbers below 2×10^{-8}, both mechanisms were at work (Figure 33 and 34), resulting into a rough shaped front (Figure 35). However, at capillary numbers above 2×10^{-7}, only the first mechanism was operating and no channel filling was observed; thus, the water invaded the network in a frontal movement that proceed line by line (Figure 36). Both these mechanisms are in agreement with earlier studies [65]. At the capillary number of 2×10^{-5}, water invaded the fracture at the same

Table 9: Conditions for forced primary imbibition experiments

Fluid Pair	Displacing Fluid Viscosity (cP)	Mobility Ratio	Volumetric Rate (cc/min)	Capillary Number
Water-Air	1	0.018	0.00052	2×10^{-8}
"	"	"	0.0052	2×10^{-7}
"	"	"	0.052	2×10^{-6}
"	"	"	0.52	2×10^{-5}
Water-Kerosene	1	"	0.00052	4×10^{-8}
"	"	1.50	0.0052	4×10^{-7}
"	"	"	0.052	4×10^{-6}
"	"	"	0.52	4×10^{-5}
Water-Mineral oil	1	100	0.00052	4×10^{-8}
"	"	"	0.0052	4×10^{-7}
"	"	"	0.052	4×10^{-6}
"	"	"	0.52	4×10^{-5}
Water-Dutrex	1	10000	0.00052	4×10^{-8}
"	"	"	0.0052	4×10^{-7}
"	"	"	0.052	4×10^{-6}
"	"	"	0.52	4×10^{-5}

time that invaded the matrix. In this regime, we observed meniscus movement only in which the viscous forces dominate the capillary forces. It follows, therefore, that a critical capillary number exists, where viscous forces are equal to capillary forces. In such cases, fracture and matrix are invaded at the same time. In our experiment, this critical capillary number lies between 2×10^{-5} and 2×10^{-6} for a water-air system (Figure 37).

While the water-air experiments showed indeed that the wetting phase preferentially invades the matrix block, this was not observed for a water-oil primary imbibition. At a capillary number lower than 4×10^{-6}, only the fracture was invaded. At higher values of the capillary number, water started to also invade the matrix similarly to drainage processes. Figures 38 and 39 show water-kerosene and water-Dutrex at a capillary number of 4×10^{-6}. At these experiments, water moves through the fracture only. We believe that this is due to the change of wettability in the micromodel. When the glass is first exposed to the it, the micromodel is contaminated with polar compounds existing in oil [19]. These components tend to adsorb on the micromodel roughness and render them oil-wet and the process turns out to be like drainage. For future work, it is recommended, as a solution of this problem, to use non-oil fluids such as air-mercury, or to perform imbibition tests using an oi l-wet model.

3.2.3 Secondary Forced Imbibition

Next, we considered secondary imbibition, in which the wettability was preserved by preventing any oil contact with the surface of the micromodel because of prewetted conditions. In secondary imbibition, the model was first saturated with water. Then, the non-wetting phase was injected at capillary number values greater than 10^{-5} (in excess of the critical value) in order to displace most of the wetting phase. This regime causes the least amount of trapping although trapped wetting phase still remains. Obviously, the precise way drainage has taken place substantially affect the subsequent mechanism of secondary imbibition. This set of experiments pertained to an initial drainage at relatively high capillary numbers. Here, the resulting residual water films were not interconnected. This has significant effects on the secondary imbibition. Table 10 shows the various parameter values used in the different runs.

During the experiments involving the fluid pair water-air, water invades the matrix block following a mechanism different than for the case of primary imbibition. Now, the displacement is

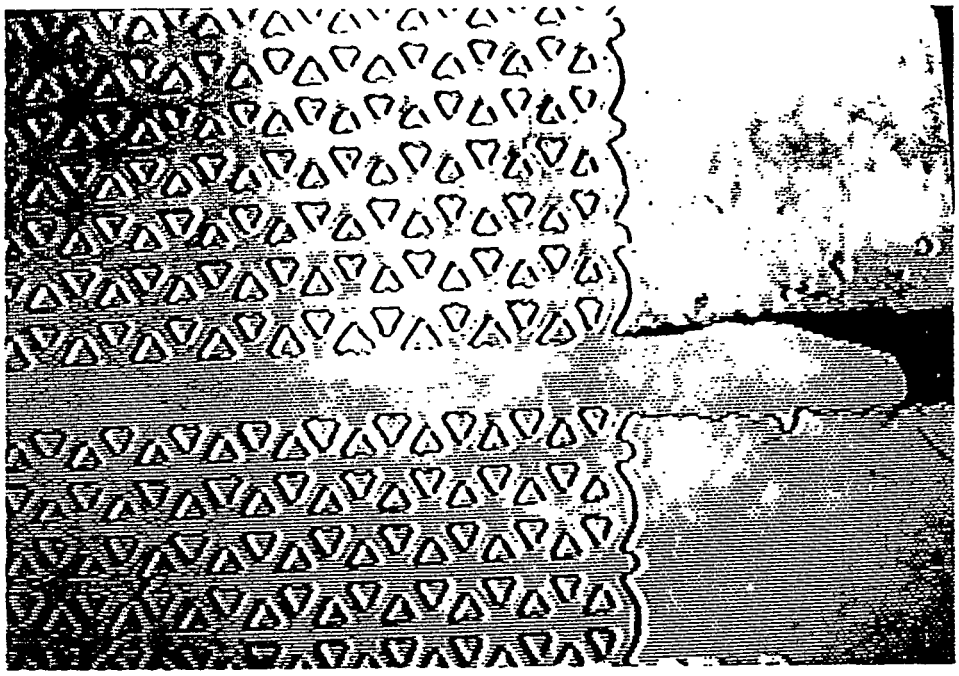

Figure 31: Primary imbibition (water-air) showing roughness flow.

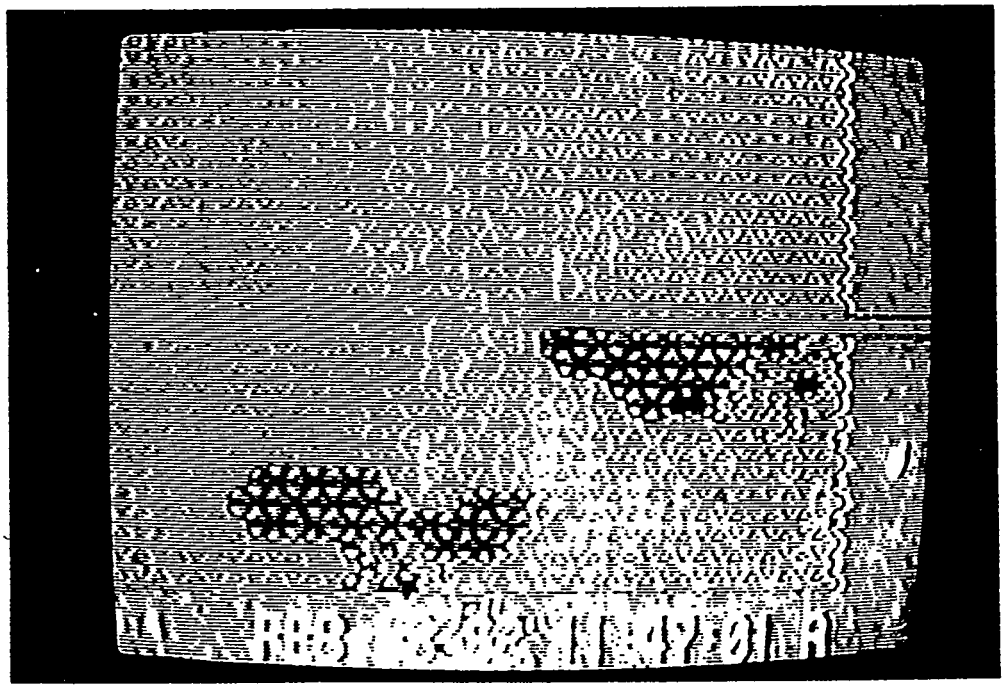

Figure 32: Primary imbibition (water-air) $Ca = 2 \times 10^{-8}$, showing discontinuous invasion of the model through roughness flow.

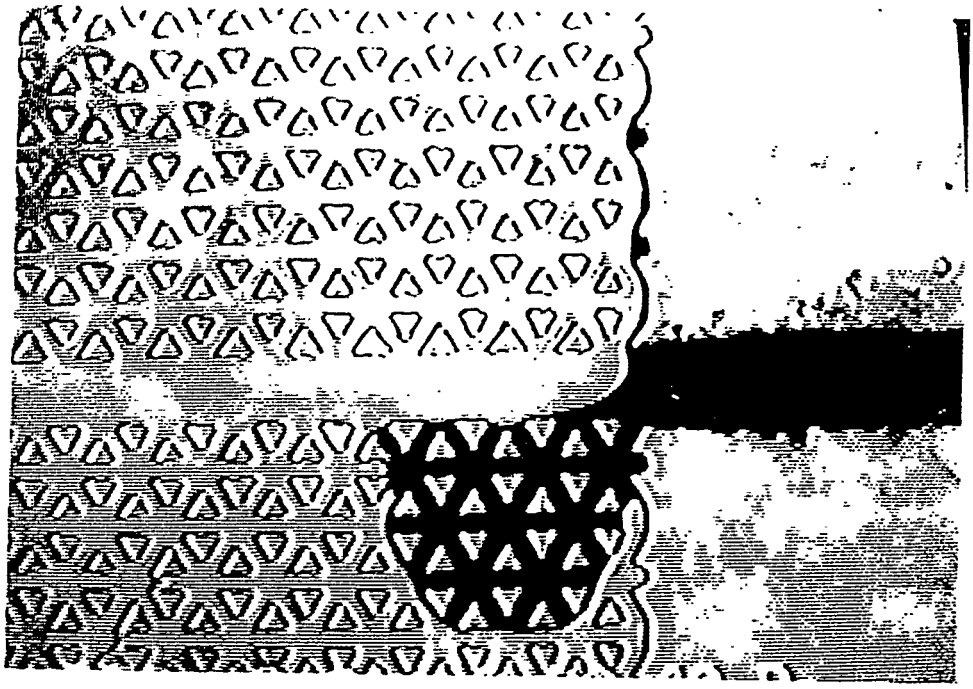

Figure 33: Primary imbibition (water-air) at $Ca = 2 \times 10^{-8}$, showing both pore invasion and channel filling (snapshot 1).

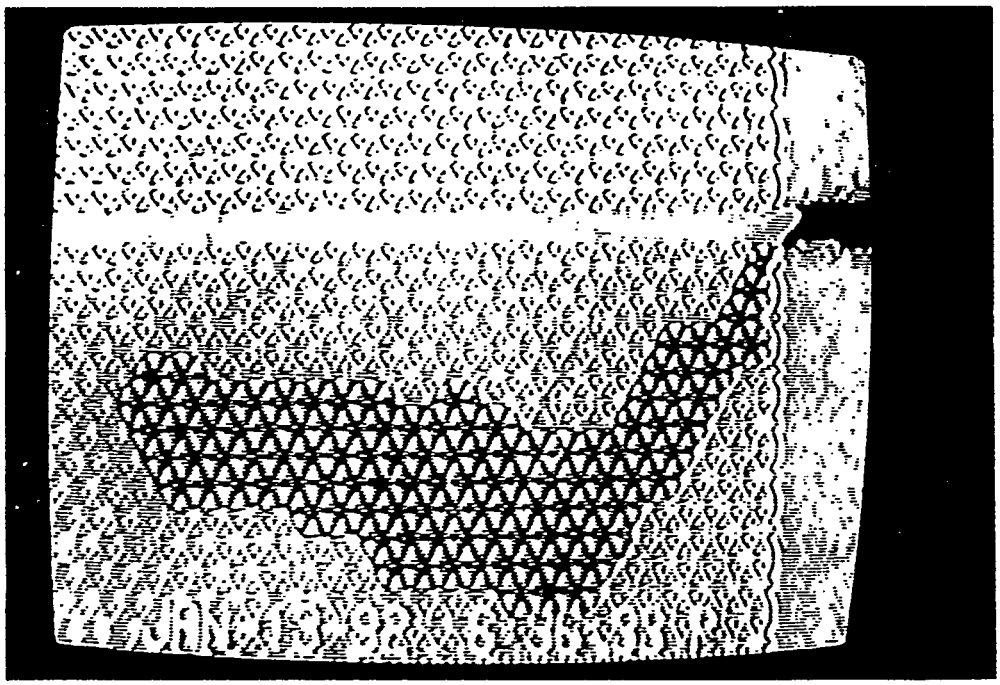

Figure 34: Primary imbibition (water-air) at $Ca = 2 \times 10^{-8}$, showing both pore invasion and channel filling (snapshot 2).

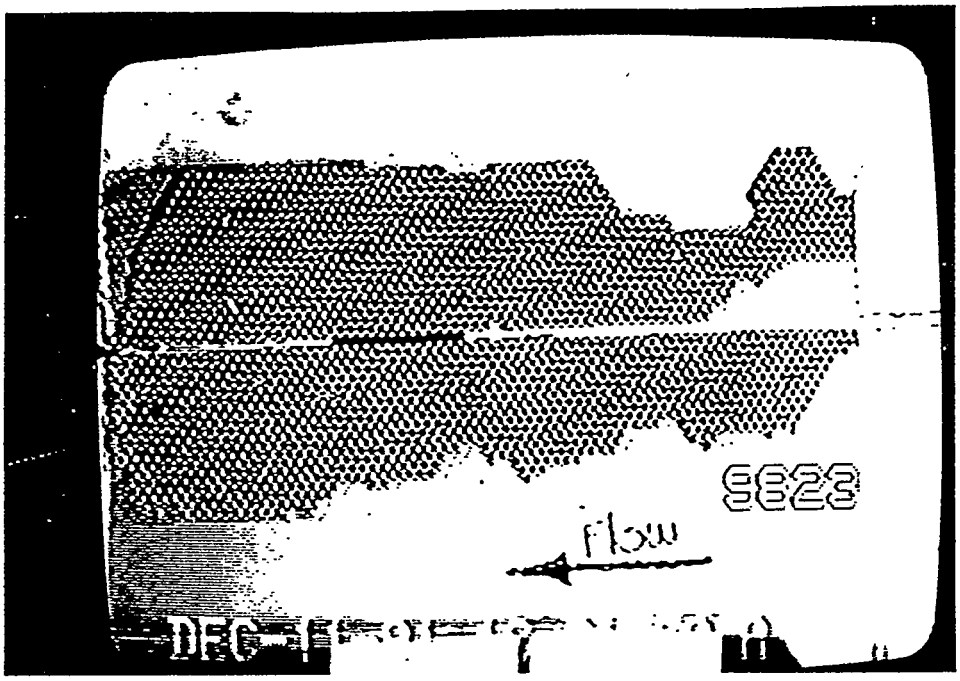

Figure 35: Primary imbibition (water-air) at $Ca = 2 \times 10^{-8}$ (snapshot 3).

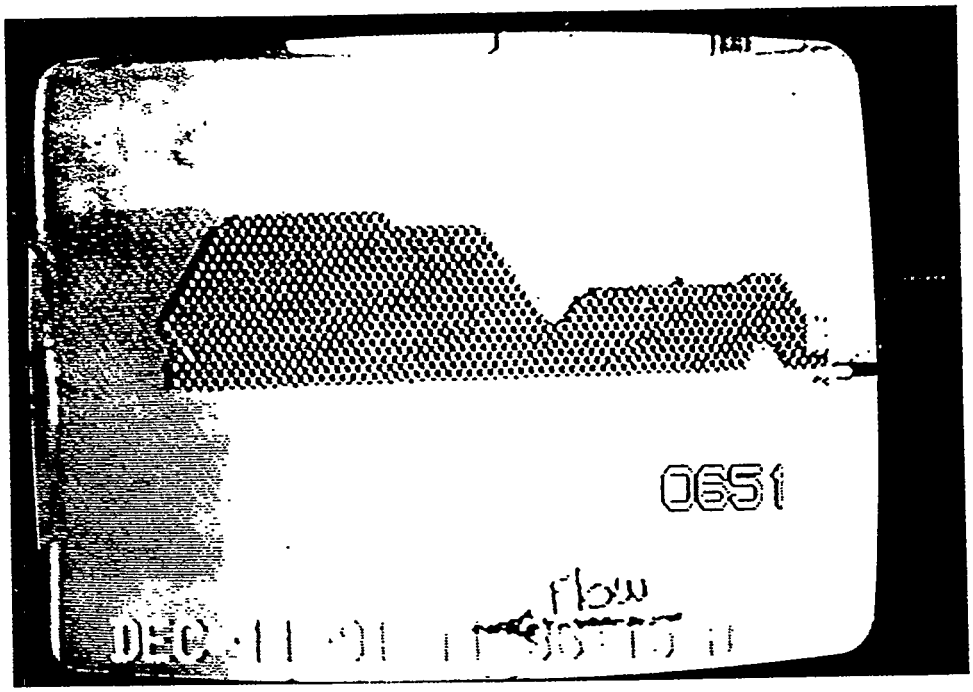

Figure 36: Primary imbibition (water-air) at $Ca = 2 \times 10^{-7}$.

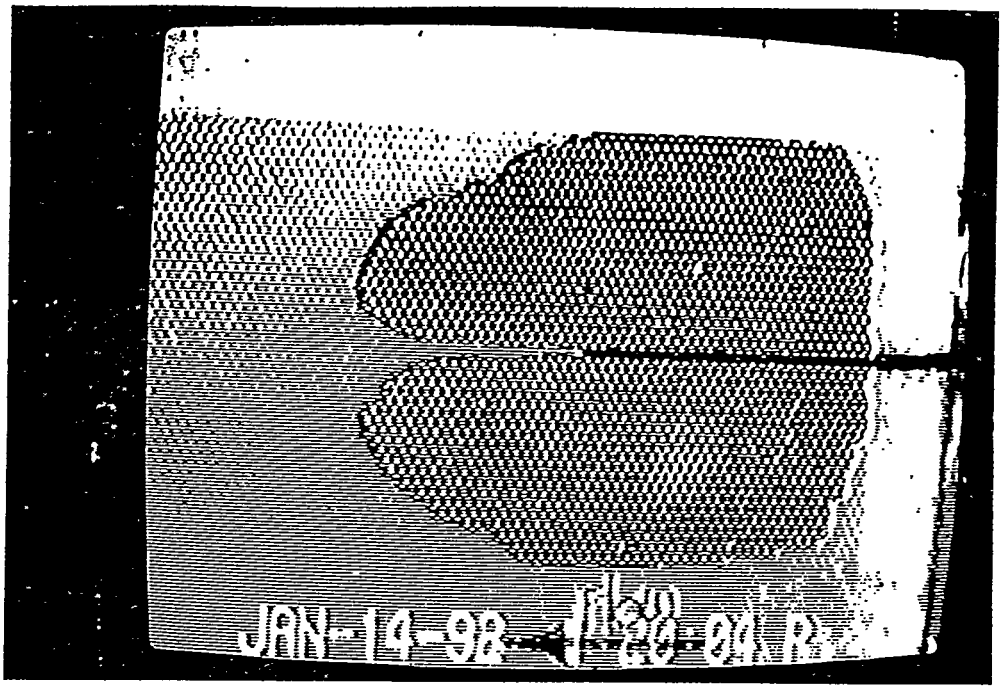

Figure 37: Primary imbibition (water-air) at $Ca = 2 \times 10^{-5}$, showing simultaneous invasion of the fracture and the matrix.

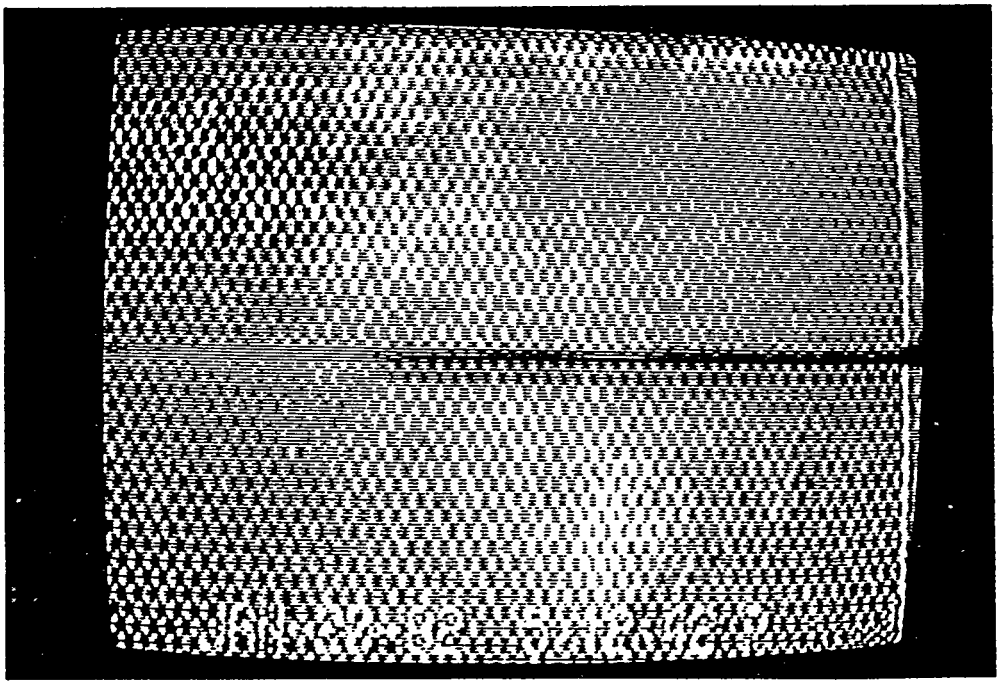

Figure 38: Primary imbibition (water-kerosene) at $Ca = 4 \times 10^{-6}$, showing that water moves through the fracture only.

Table 10: Conditions for secondary imbibition experiments

Fluid Pair	Displacing Fluid Viscosity (cP)	Mobility Ratio	Volumetric Rate (cc/min)	Capillary Number
Water-Air	1	0.018	0.00052	2×10^{-8}
"	"	"	0.0052	2×10^{-7}
"	"	"	0.052	2×10^{-6}
"	"	"	0.52	2×10^{-5}
Water-Kerosene	1	"	0.00052	4×10^{-8}
"	"	1.50	0.0052	4×10^{-7}
"	"	"	0.052	4×10^{-6}
"	"	"	0.52	4×10^{-5}
Water-Mineral oil	1	100	0.00052	4×10^{-8}
"	"	"	0.0052	4×10^{-7}
"	"	"	0.052	4×10^{-6}
"	"	"	0.52	4×10^{-5}
Water-Dutrex 2621	1	10000	0.00052	4×10^{-8}
"	"	"	0.0052	4×10^{-7}
"	"	"	0.052	4×10^{-6}
"	"	"	0.52	4×10^{-5}

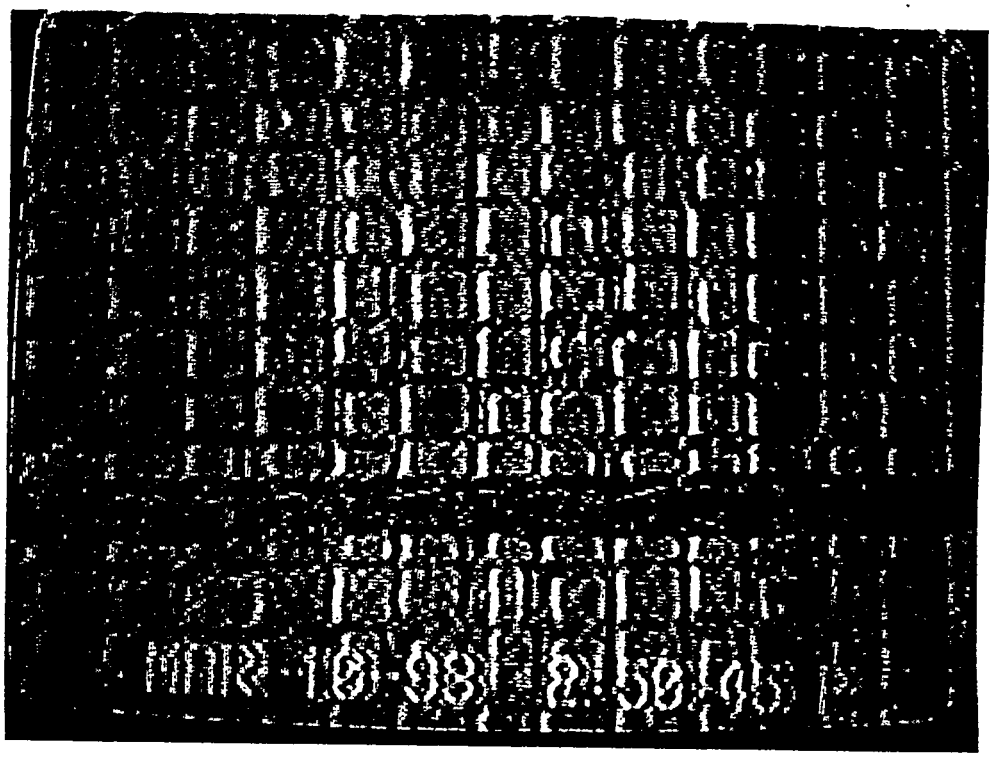

Figure 39: Close-up of primary imbibition (water-Dutrex) at $Ca = 4 \times 10^{-6}$, showing that water moves through the fracture only.

a succession of rapid invasion jumps that occur along the existing water films, left behind at the conclusion of primary drainage (Figures 40 and 41). This mechanism operates at low capillary numbers. At higher values, the typical meniscus displacement of the previous process was also observed.

For the experiments involving the fluid pair water-kerosene, secondary imbibition mechanism similar to the water-air system was observed at the capillary number 4×10^{-6} (Figures 42 and 43). Water was found to enter the fracture first. Then, the matrix block was invaded with a chain of rapid jumps as soon as the injecting water started to communicate with the previous water film along the roughness of the network. Oil was trapped in the pores, while adjacent channels were occupied with water at the conclusion of the snap-off process. At capillary number values lower than 10^{-6} this mechanism was not observed. Rather all water were found to enter the fracture first, and then pores adjacent to the fracture started to be invaded slowly (Figures 44 and 45). We attribute this lack of spontaneous imbibition to the lack of connectivity between the residual water films.

In the experiments with heavy oil, where the mobility ratio was higher than 100, water moves to the fracture first. However, before water breakthrough in the fracture, it also invaded the matrix. We will analyze this process later in theory section. The mechanism of displacement both in the pore throat and in the fracture is a slow, uniform meniscus movement. In these experiments, we observed that if a relatively heavy oil is used for drainage, the water film left behind is apparently very thin, such that spontaneous imbibition will not take place. However, as it is shown in Figures (46-49), secondary imbibition is a very slow process. For example, in water displacing heavy mineral oil, the complete imbibition requires about 100 pore volumes of water injection. Also, as shown in Figures 47-49, because of the slowness of the process, at lower capillary numbers, we experience a higher displacement efficiency.

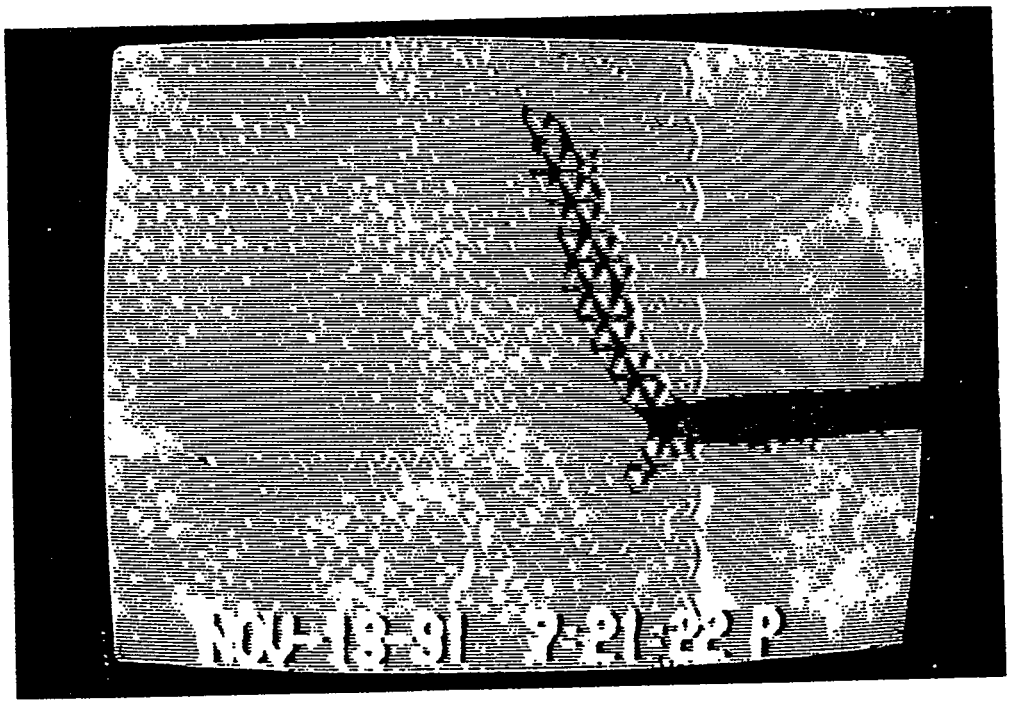

Figure 40: Secondary imbibition (water-air) at $Ca = 2 \times 10^{-8}$ (snapshot 1).

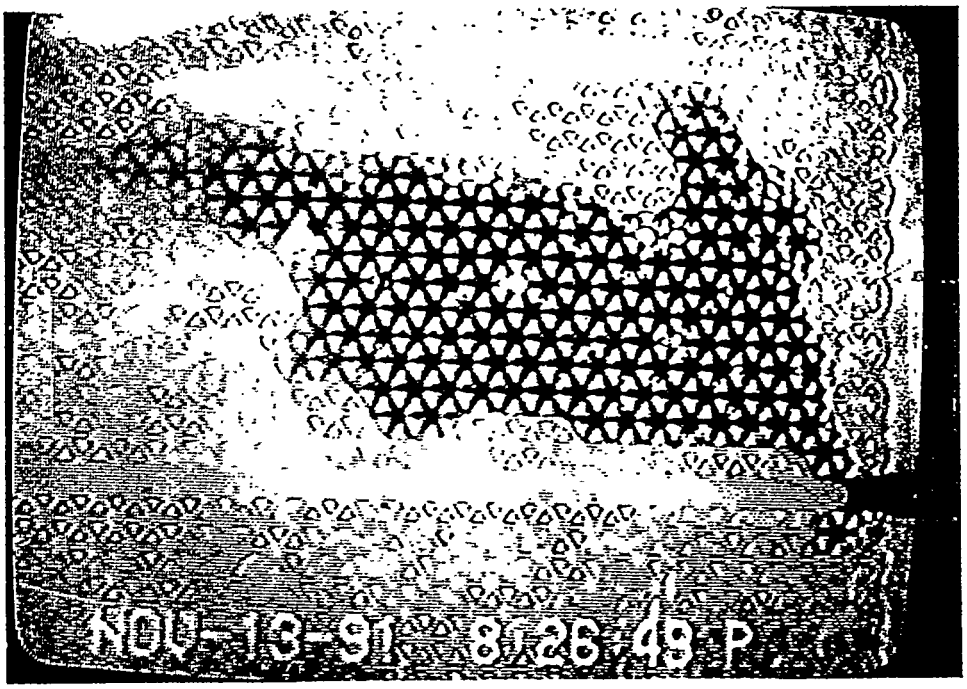

Figure 41: Secondary imbibition (water-air) at $Ca = 2 \times 10^{-8}$ (snapshot 2).

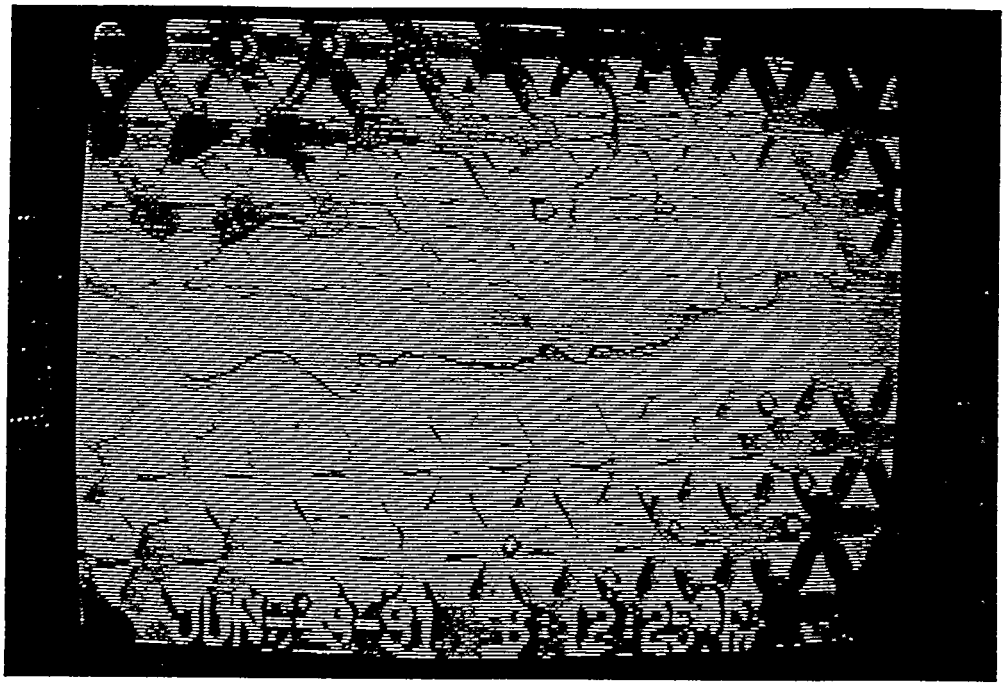

Figure 42: Secondary imbibition (water-kerosene) at $Ca = 4 \times 10^{-6}$ (snapshot 1).

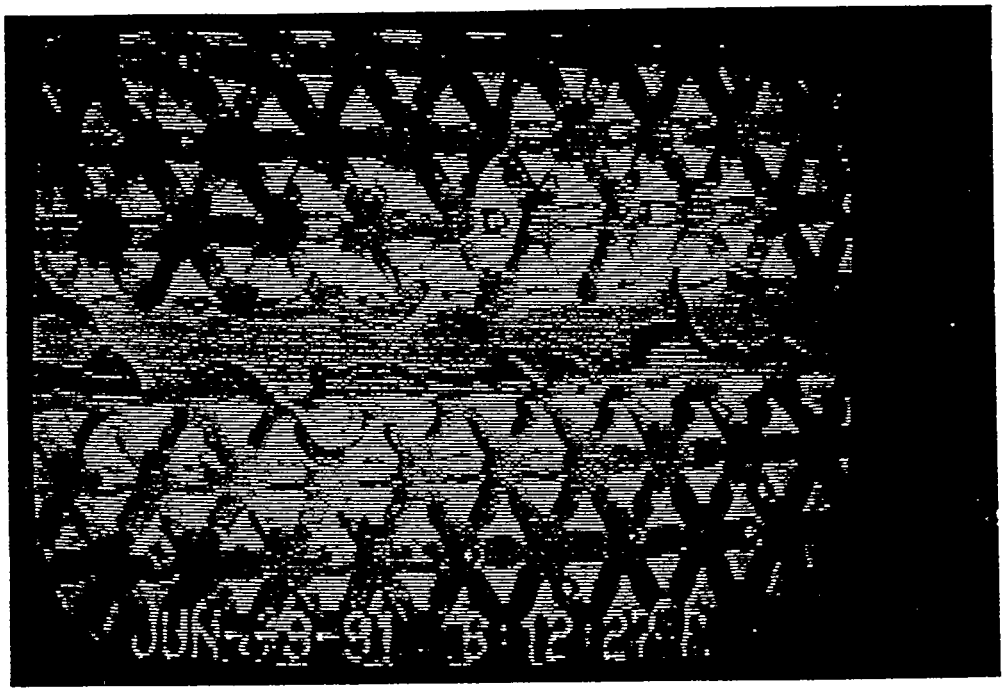

Figure 43: Secondary imbibition (water-kerosene) at $Ca = 4 \times 10^{-6}$ (snapshot2).

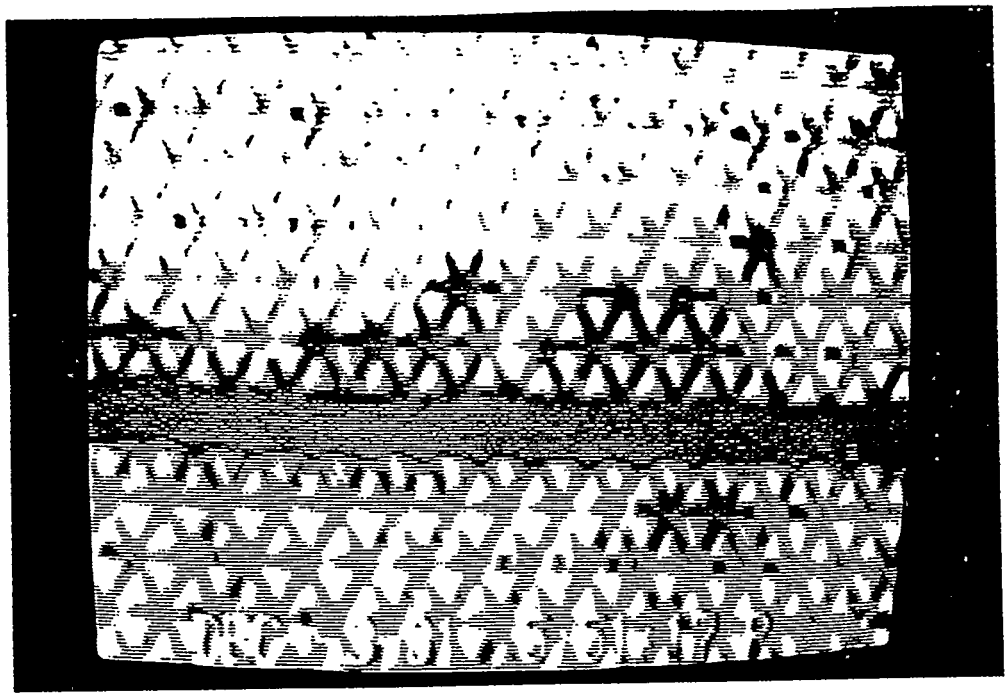

Figure 44: Secondary imbibition (water-kerosene) at $Ca = 4 \times 10^{-7}$.

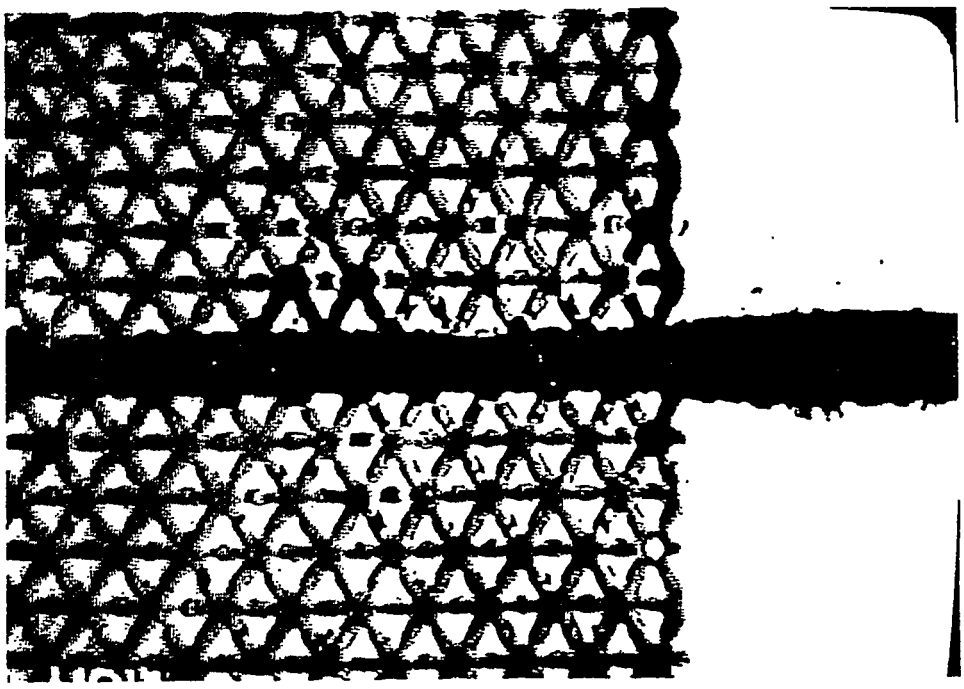

Figure 45: Secondary imbibition (water-kerosene) at $Ca = 4 \times 10^{-8}$.

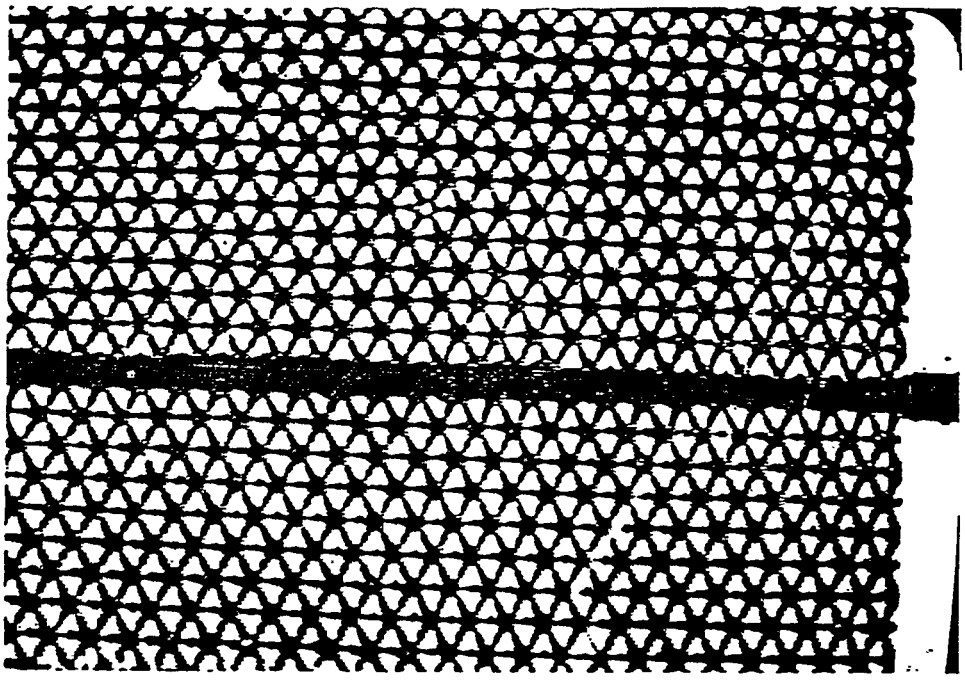

Figure 46: Secondary imbibition (water-heavy oil) at $Ca = 4 \times 10^{-8}$.

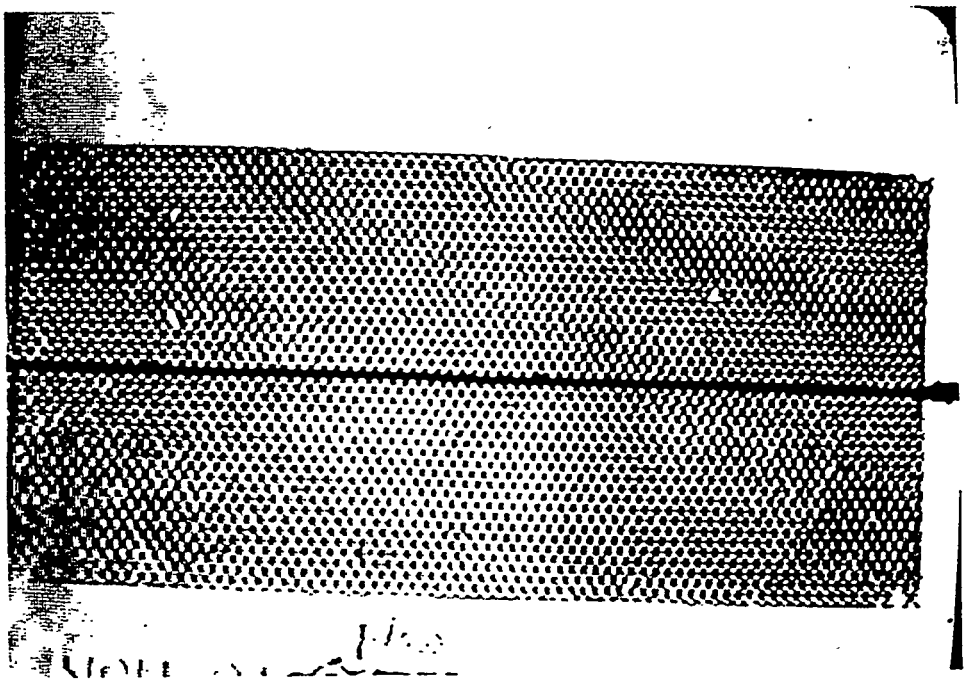

Figure 47: Secondary imbibition (water-heavy oil) at $Ca = 4 \times 10^{-7}$.

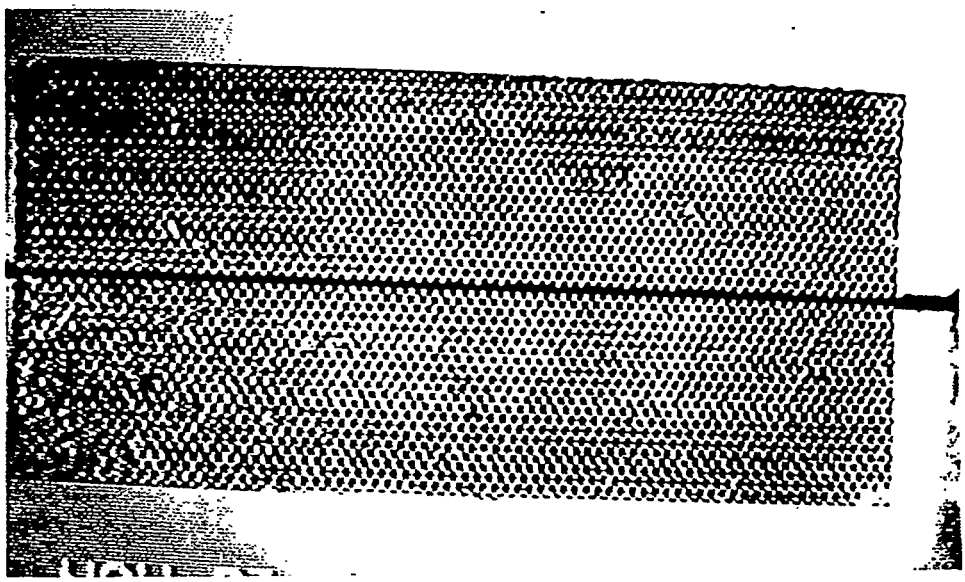

Figure 48: Secondary imbibition (water-heavy oil) at $Ca = 4 \times 10^{-6}$.

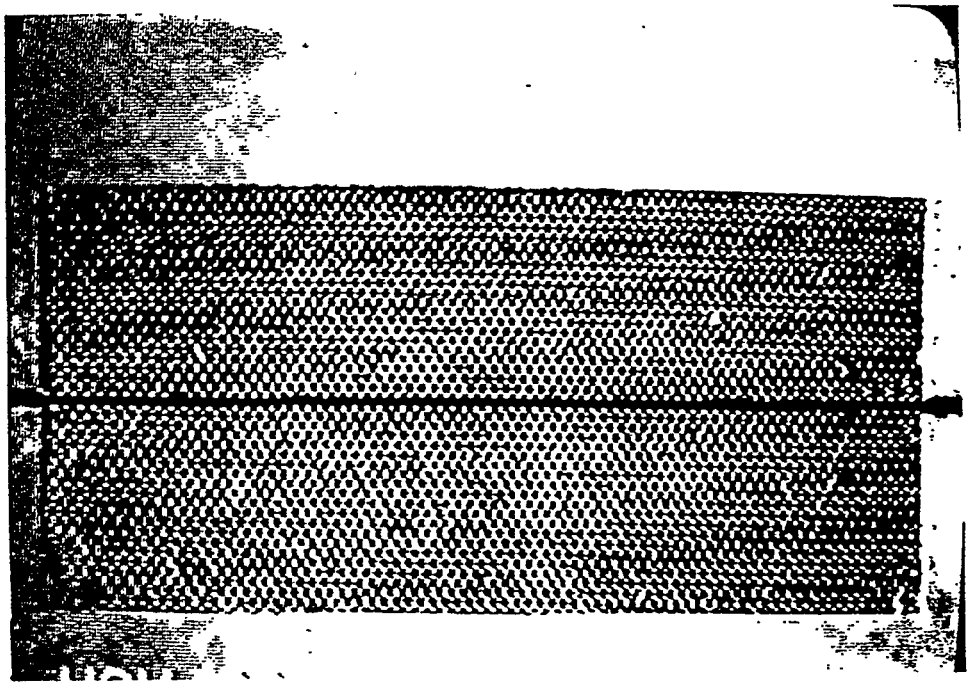

Figure 49: Secondary imbibition (water-heavy oil) at $Ca = 4 \times 10^{-5}$.

3.2.4 Free Imbibition

Free imbibition was experimented with water-air system. Dyed water was introduced to the clean and dry micromodel through a plastic tubing connected to a pipette. To prevent any gravity force resulting from the water column in the pipette at the beginning of the experiment, the plastic tubing was closed, and the water vertical level in pipette was balanced with the level of the micromodel. Then, the tubing was opened and water moved into the model. Since the inlet of the model is connected to the fracture, water movement was stopped at the inlet due to the capillarity of the fracture (Fig.50). Thus, it was necessary to raise the water level in the pipette by a few millimeters to provide a small gravity force to overcome the capillary pressure at the inlet and to start invasion into the network. After invasion started, the pipette was lowered to its original level. Water invaded the network by the capillary forces only. The Fracture was also invaded; however, the water front in the network was always a head of that in the fracture (Figures 51-53).

At the beginning, this test was observed to occur rapidly, but later it becomes a slow displacement. The mechanism is similar to the exponential decay of water saturation versus time proposed by Aronofsky et al. [2].

Later in this chapter, the numerical simulation of this process will be compared with the experiment.

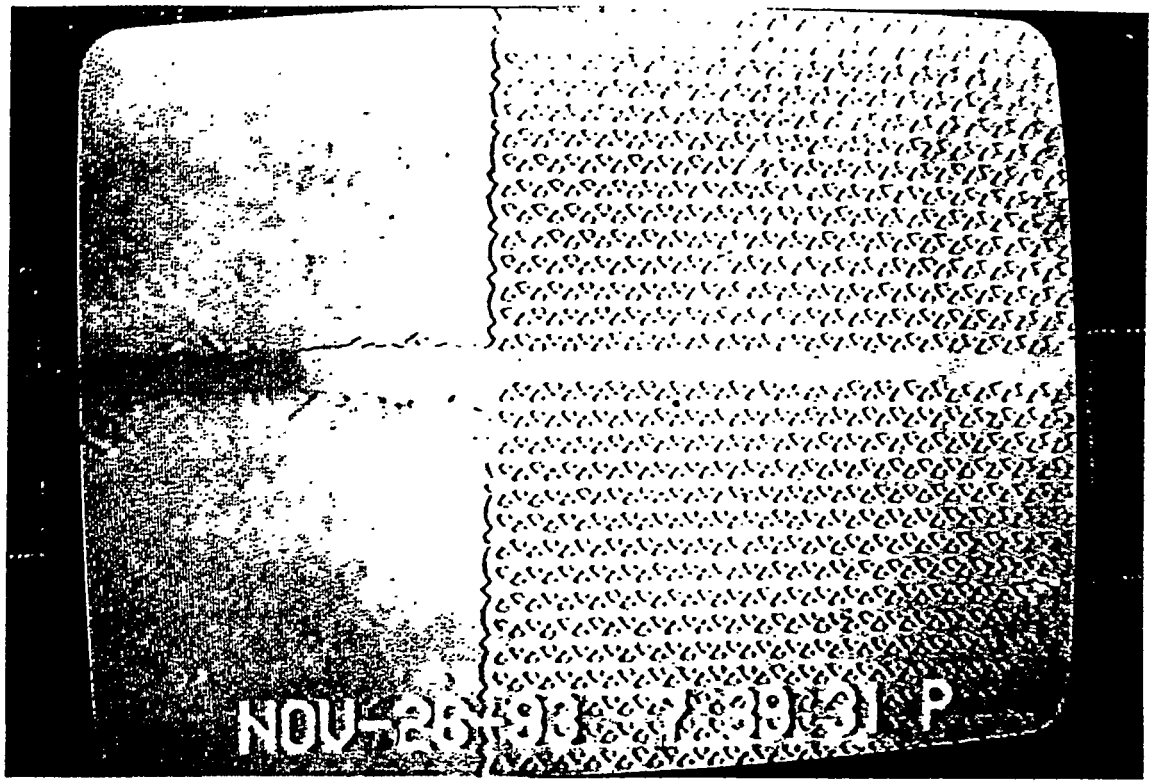

Figure 50: Free imbibition (water-air) (snapshot 1).

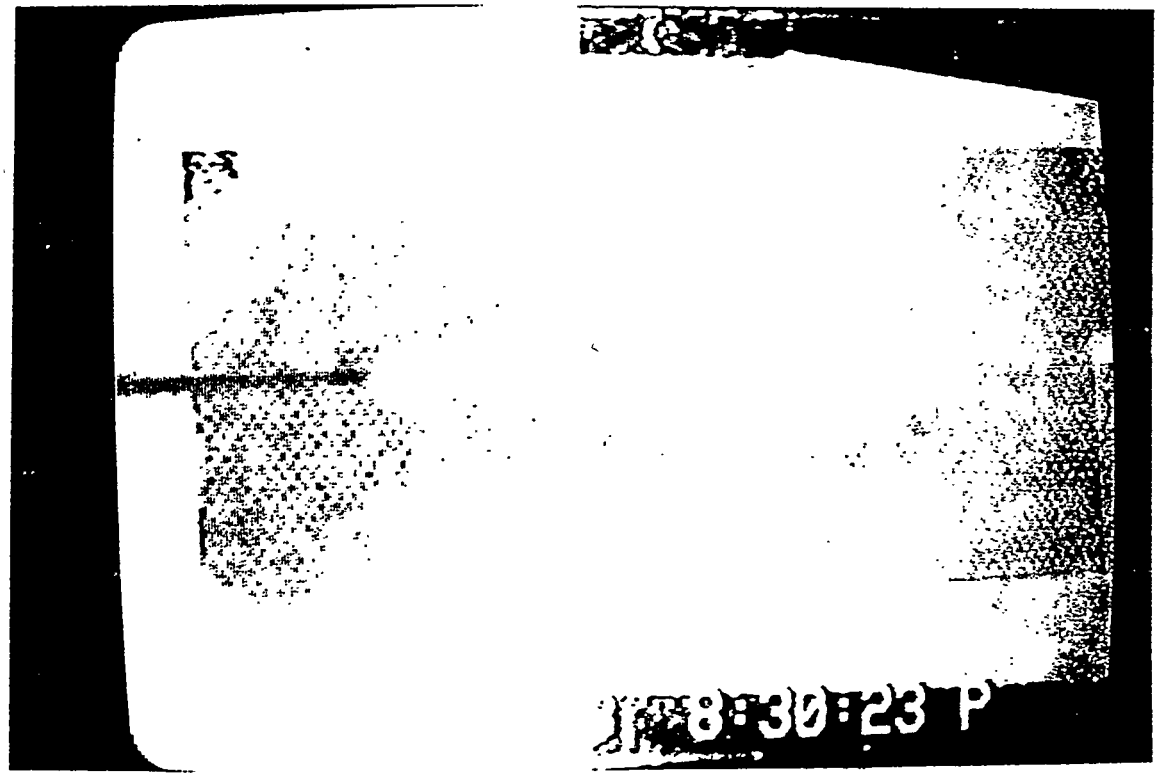

Figure 51: Free imbibition (water-air) (snapshot 2).

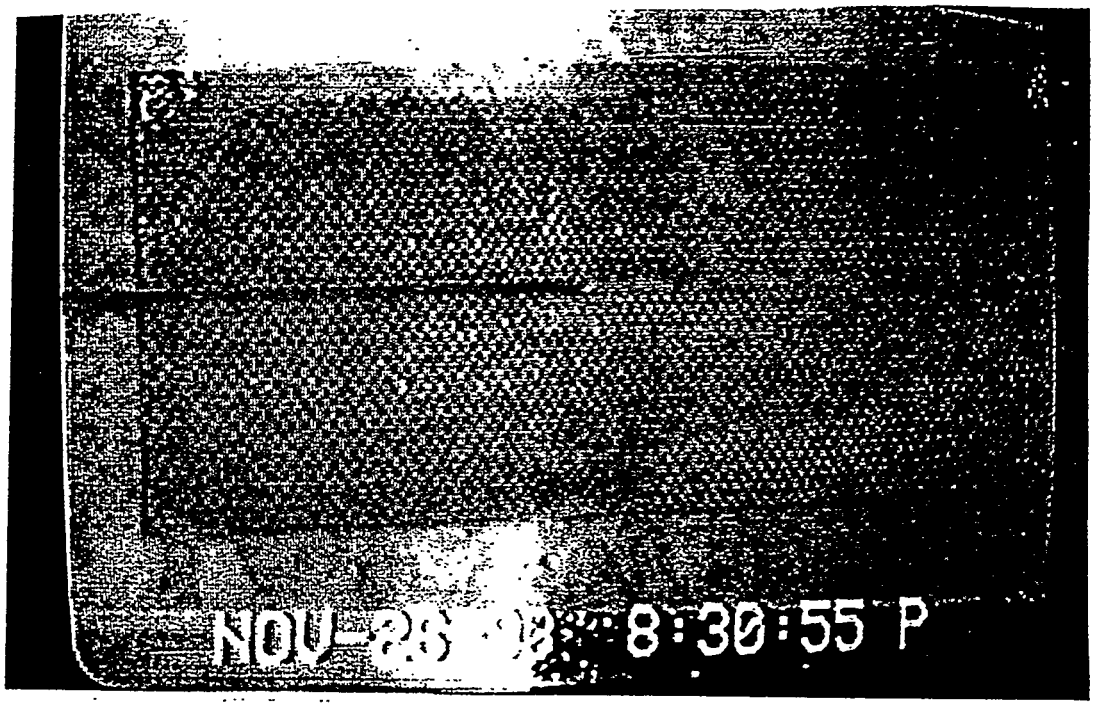

Figure 52: Free imbibition (water-air) (snapshot 3).

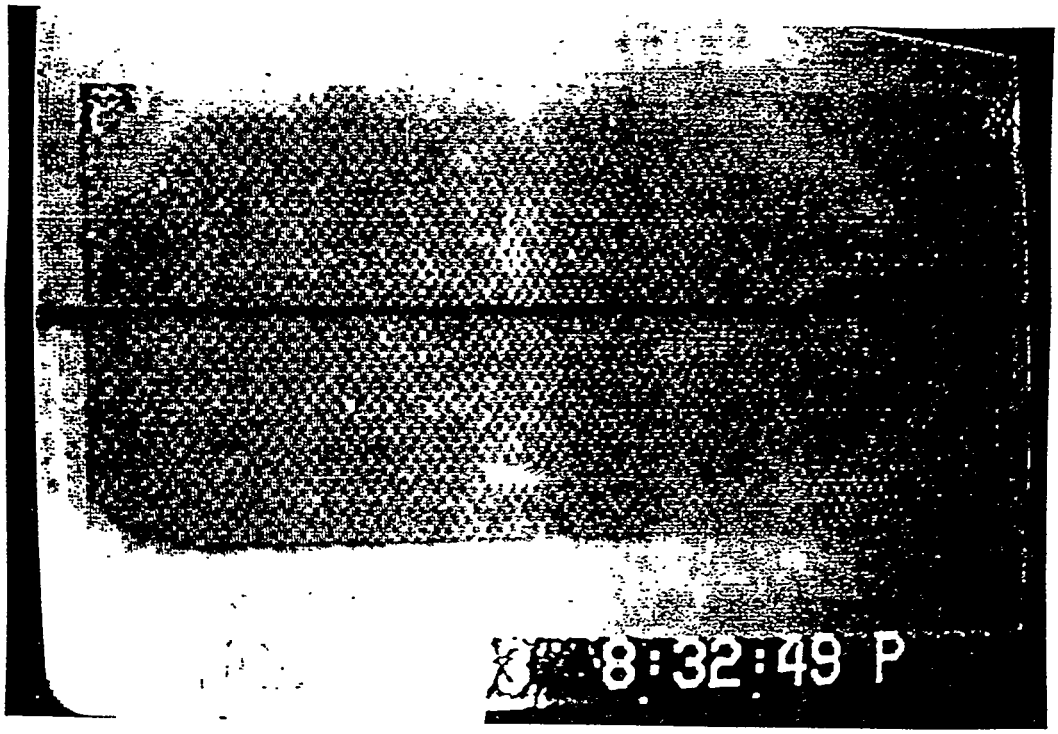

Figure 53: Free imbibition (water-air), (snapshot 4).

3.2.5 Gravity Effects

The next set of experiments investigated effects of gravity in water displacing kerosene following two different geometrical configurations, one with the micromodel tilted at a small angle with respect to horizontal, and another with the model rotated to the gravity vector (vertical cross-section). The water was not dyed in this set of experiments. All experiments were carried out at a capillary number of 4×10^{-6}.

In the first configuration we probed effects of formation dip. Water was injected from the bottom (updip) or from the top (downdip). For updip injection, a flat and stable displacement front with small size oil entrapments were observed (Figure 54). In contrast, for downdip injection, the density difference acted to destablize the front resulting into an unstable fingering mechanism with large size oil entrapments (Figure 55). Fingers in the fracture was more developed than in the matrix.

In the second configuration we examined effects of gravity override. The injected water flowed downwards towards the bottom of the model. Figure 56 shows the process at steady state.

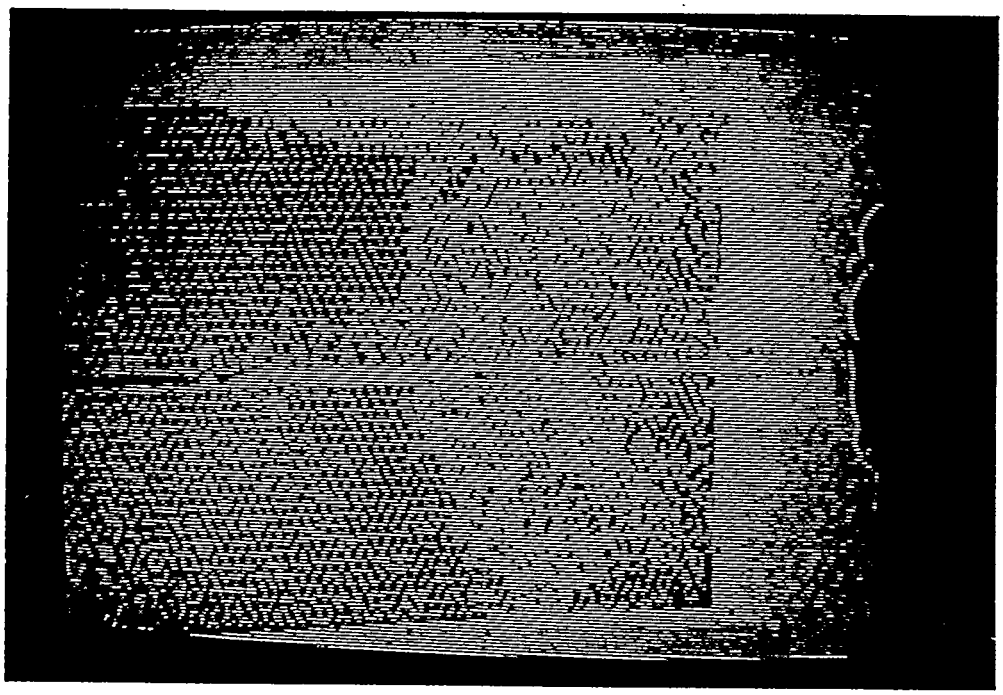

Figure 54: Updip water injection.

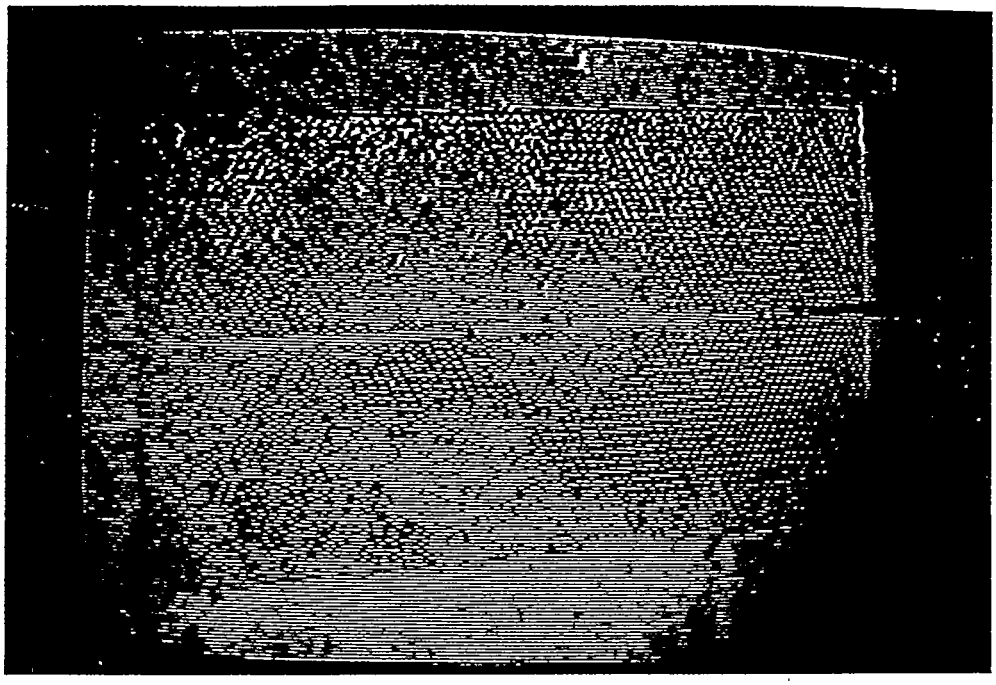

Figure 55: Downdip water injection.

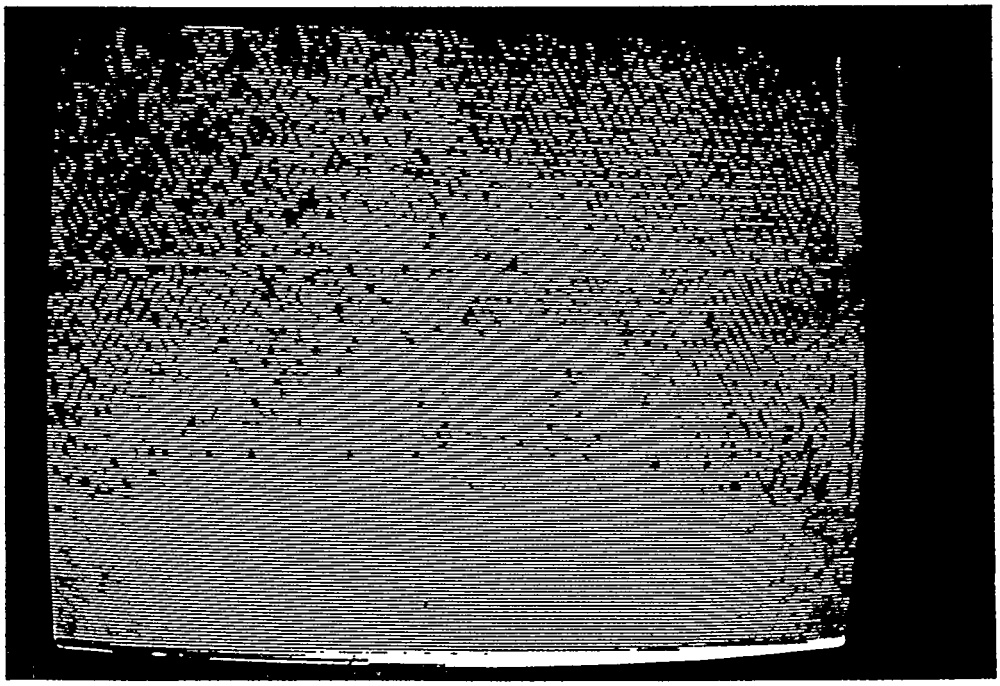

Figure 56: Water injection in a vertical cross-section.

3.2.6 Theory

In the previous section, we experimentally visualized forced primary imbibition with water displacing air (mobility ratio of 0.018). If the capillary number is sufficiently small , all injected fluid initially flows along the roughness of walls of the pore network. At higher injection rates, the wetting fluid flows at the bulk of pore network without any fracture penetration. At higher rates, the fracture is also invaded, but the front in the network is ahead of that in the fracture. Finally, when the injection rate is raised above to a critical value, the front of the wetting fluid in the fracture travels faster than that of the network. For the case of water displacing oil at any capillary number, both fracture and matrix are invaded provided that the mobility ratio is greater than one. Therefore, it seems that there exist two critical capillary numbers, one for the start of penetration in the fracture ($M \ll 1$), and another for which the wetting fluid in the fracture is the same to that in the matrix (any mobility ratio).

To calculate the first critical capillary number for the start of penetration in the fracture ($M \ll 1$), the pressure drop at the inlet must be equal to the capillary pressure in the fracture (Fig. 57),

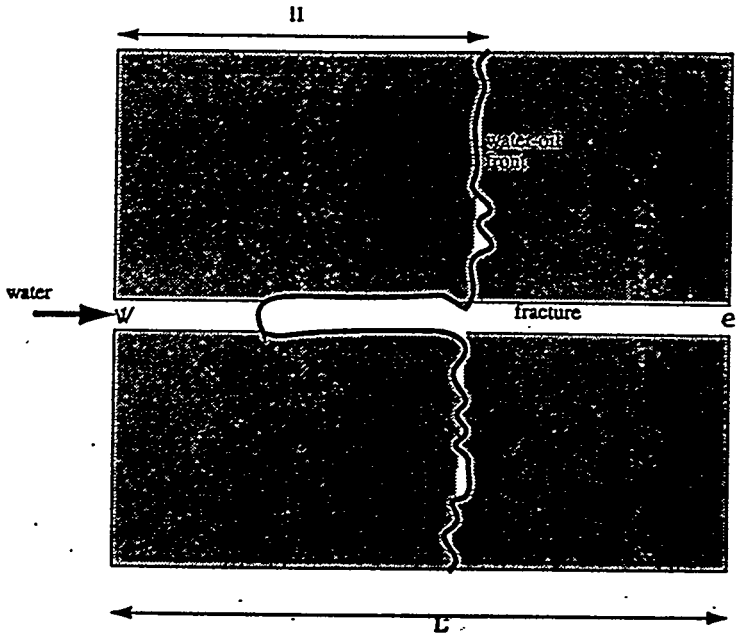

Figure 57: Schematic of fluids distribution after fracture penetration.

$$P_e - P_w = \frac{2\sigma}{r_f} \tag{24}$$

where σ is interfacial tension and r_f is the fracture radius. Application of Darcy's law for both wetting and non-wetting phases in the matrix gives

$$P_w - P_{wf} = \frac{q\mu_w l_1}{k_m k_{rw}} \tag{25}$$

and

$$P_{nwf} - P_e = \frac{q\mu_{nw}(L - l_1)}{k_m k_{rnw}} \tag{26}$$

where q is fluid velocity, μ is viscosity, k_m is matrix permeability, k_r is relative permeability and we used subscripts w, nw and f to denote wetting, non-wetting and front. In addition, at the displacement front in the network, the capillary pressure relationship exists

$$P_{wf} - P_{nwf} = -\frac{2\sigma}{r_m} \tag{27}$$

where r_m is the average pore radius of matrix. By combining equations (25),(26), (27) and substitution into the condition for the critical capillary number, $P_e - P_w = \frac{2\sigma}{r_f}$, we obtain

$$2\sigma(\frac{1}{r_m} - \frac{1}{r_f}) = \frac{q}{k_m}[\frac{(L - l_1)\mu_{nw}}{k_{rnw}} + \frac{l_1\mu_w}{k_{rw}}]. \tag{28}$$

Since $M \ll 1$, μ_{nw} can be neglected compared to μ_w, and using the capillary number definition $Ca = \frac{q\mu}{\sigma}$, equation (28) gives the critical value

$$Ca^* = \frac{2k_m}{L}(\frac{1}{r_m} - \frac{1}{r_f}) \tag{29}$$

By assumption, r_f is much greater than r_m, thus $\frac{1}{r_f}$ can be neglected compared to $\frac{1}{r_m}$, hence

$$(Ca^*)_1 = \frac{2k_m}{Lr_m} \tag{30}$$

Equation (30) suggests that for $M \ll 1$, the fracture penetration depends on the geometric properties of matrix, more permeable and shorter matrix block causing earlier fracture penetration for the same fluids and injection rate.

To calculate the critical capillary number for which the displacement front in the matrix is the same as that in the fracture, the pressure drop in the fracture should be equal to pressure drop in

the matrix. The pressure drop in the matrix is

$$P_w - P_e = \frac{q\mu_w l}{k_m} + \frac{q\mu_{nw}(L-l)}{k_m} - \frac{2\sigma}{r_m} \tag{31}$$

while the pressure drop in the fracture is

$$P_w - P_e = \frac{q\mu_w l}{k_f} + \frac{q\mu_{nw}(L-l)}{k_f} - \frac{2\sigma}{r_f}. \tag{32}$$

At the entrance ($l = 0$) equating the right side of equations (31) and (32) gives

$$\frac{Lq\mu_{nw}}{\sigma} = \frac{2(\frac{1}{r_m} - \frac{1}{r_f})}{(\frac{1}{k_m} - \frac{1}{k_f})}. \tag{33}$$

By substitution of the capillary number $Ca = \frac{q\mu}{\sigma}$ and the viscosity ratio $M = \frac{\mu_{nw}}{\mu_w}$ into (33) and making the assumption that $\frac{1}{k_f}$ and $\frac{1}{r_f}$ can be neglected compared to $\frac{1}{k_m}$ and $\frac{1}{r_m}$, respectively, the second critical capillary number will be obtained

$$(Ca^*)_2 = \frac{2k_m}{r_m ML} \tag{34}$$

Thus, this critical capillary number depends on the geometric properties of matrix *and* the viscosity ratio. For capillary number less than the above value, the wetting fluid front in the matrix is ahead of that in the fracture; inversely, at capillary numbers greater than the critical value, the wetting fluid moves ahead of the wetting fluid in the matrix. We compared the above critical capillary number with the Mattax and Kyte [77] experiments, they carried out a water-drive on a fracture-matrix system and found the critical rate to be $3"/day$. Their experiment was performed on a 1.9-md sandstone with a porosity of 9.1 percent, viscosity of water 0.9 cP, viscosity of oil 2.7 cP, and interfacial tension of 35 $dynes/cm$. The length of the sample was 3 inches. Based on the above data, the capillary number is calculated to be 2.3×10^{-8}. In turn, the critical capillary number from equation (34) using the Katz and Thompson formula [50] for the permeability calculation is computed to be 0.5×10^{-8}. Although both numbers are in the same order of magnitude, we should note that in deriving the theoretical formula, gravity was not considered, while in Mattax and Kyte experiment, the water was injected at the bottom of the sample. Thus, the actual capillary number is higher than the theoretical. Comparison of the theoretical expressions with our network simulation and the micromodel experiments are discussed in the following section.

3.2.7 Simulation

To compare experimental and theoretical results with a numerical simulation, we used two different pore network simulation for imbibition developed by Xu in Ref. [15]; one for primary imbibition which does not consider film flow or snap-off mechanisms, and another for secondary imbibition which accounts for film flow and snap-off which are two mechanisms that occur in secondary imbibition. In the absence of film flow simulation of imbibition is similar to drainage with the exception that the capillary pressure is calculated based on the pore instead of the bond radius, and the condition for invading the adjacent bond is $p_i + p_{cij} > p_j$, where p_{cij} is the capillary pressure between adjacent bonds i and j. We recall that the corresponding condition for drainage is $p_i > p_{cij} + p_j$. We used both constant flow rate and constant pressure boundary conditions. With a constant flow rate boundary, we were able to compare the numerical simulation with the forced primary imbibition experim ents. The constant pressure boundary, free imbibition can be simulated. In simulation of imbibition with film flow, which simulates secondary imbibition, Xu in Ref. [15] modified the conditions used by Lenormand [66]. The pressure field is calculated based on Poiseuille's law using an SOR method for both the bulk zone and the film region. According to Lenormand et al. [66], when there is corner flow in non-circular cross-section channel, an unstable state of interface is reached when the meniscus at the two adjacent corners join and snap-off occurs. For a rectangular throat with side x and y, snap-off will happen when $p_c = \frac{2\sigma}{r}, (r = min(x, y))$. In our simulation, it is assumed that snap-off develops when the film covers the circle, in a condition similar to a square shape throat. Fore pore filling, Lenormand et al. [66] categorized $Z - 1$ mechanisms for a network with coordination number of Z. For example, they defined mechanism $I1$ as that when pore is surrounded by $Z - 1$ filled bonds, $I2$ when a pore is surrounded by $Z - 2$ filled bonds, etc.. The pore filling conditions for the circular bonds and spherical pores are as follows:

$$p_{I1} = p_{nw} - p_w = \frac{2\sigma}{r_p} \tag{35}$$

and

$$p_{I2} = p_{nw} - p_w = \sigma(\frac{0.15}{r_t} + \frac{1}{r_p}) \tag{36}$$

Only one event occurs based on the pressure condition at any time step. If more than one event can happen, the pore which takes less time, first starts to fill and the time step increment is set

accordingly. At high flow rates, the rate of fluid injected into the system is more than that by which films which can absorb; therefore, a frontal drive will prevail similar to drainage. Further details on the simulator are available in [114].

We first run the simulator to simulate forced imbibition (absence of film flow) with the same pore structure and flow parameters used in the experiments. The simulations with the results from the corresponding experiments are shown in Figures 58-60. In this set, we used the square pattern micromodel in order to compare results with network simulations.

Figure 58 shows water displacing air in the micromodel and corresponding simulations for a capillary number 1.8×10^{-5}. In this experiment, water moves only in the matrix and no penetration in the fracture is observed (the corresponding capillary number is below the critical capillary number for the start of penetration in the fracture). The network simulation of the experiment show a that except for a few pores, the fracture is also not penetrated, and a generally good match with the experiments is obtained. In Figure 59, the water injection rate is increased for to a capillary number of 5.4×10^{-5}. As shown on the left side of Figure 59, the fracture is now penetrated; however, the water front in the fracture is always behind the water front in the matrix. The simulation of this experiment, shown on the right side, also indicates fracture penetration as well. The critical capillary number for the start of invasion in the fracture was calculated to be 1.08×10^{-5}. From both simulation and experiment, this number must be between 1.8×10^{-5} and 5.4×10^{-5} which was the same order of magnitude as the calculated. Figure 60 shows experiment and corresponding simulation for a capillary number of 5.4×10^{-4}. In this experiment fracture and matrix were penetrated at the same time showing that the capillary number has exceeded its second critical value. Recall that the latter was define

d as that dictating competition between the front in the fracture and that in the matrix, and for our experiment was calculated as 5.4×10^{-4}. The interactions between fracture and matrix in the experiment and the simulation were generally well matched, and it is shown that the critical capillary number derived is applicable both for experiments and simulations.

Subsequently, we run simulations for secondary imbibition namely by considering film flow and snap-off mechanisms. Figures 61-64 show the simulation results. In this set of figures, the left side shows the beginning of the process, the right side shows the steady state condition reached; invaded pores are shown with open circles, filled bonds following snap-off events are shown with

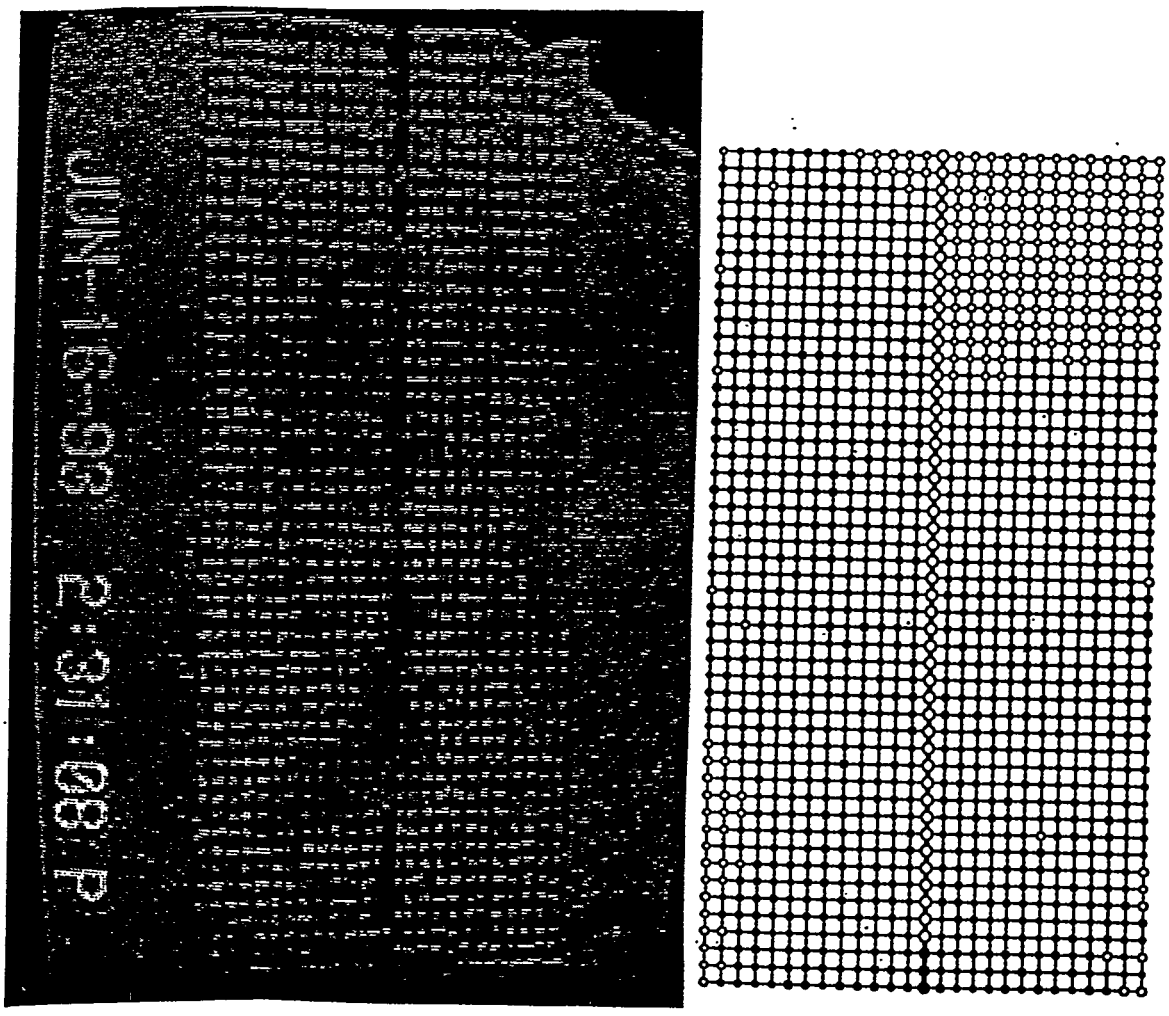

Figure 58: Comparison between experimental and numerical results for water-air, $Ca = 1.8 \times 10^{-5}$.

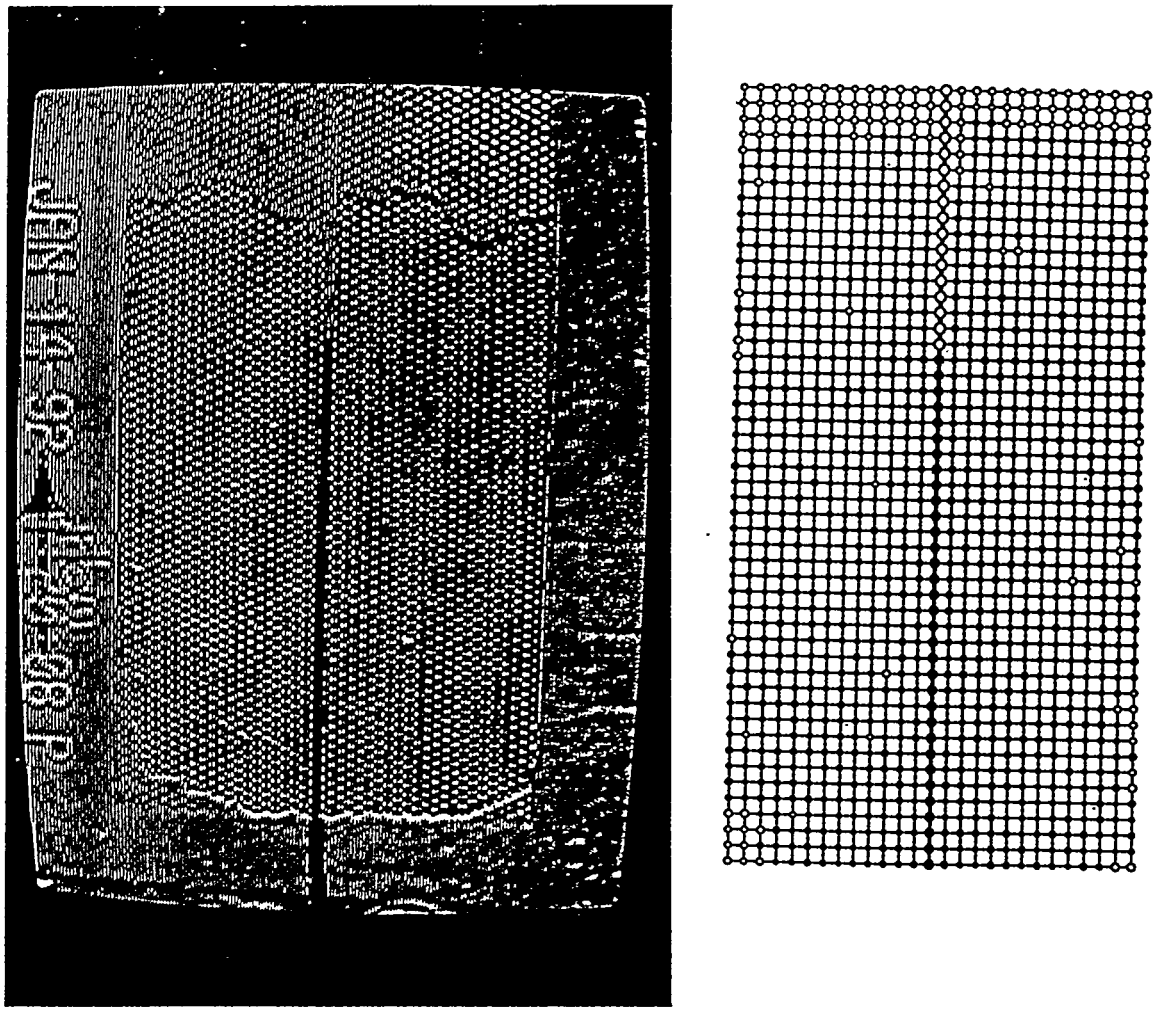

Figure 59: Comparison between experimental and numerical results for water-air, $Ca = 5.4 \times 10^{-5}$.

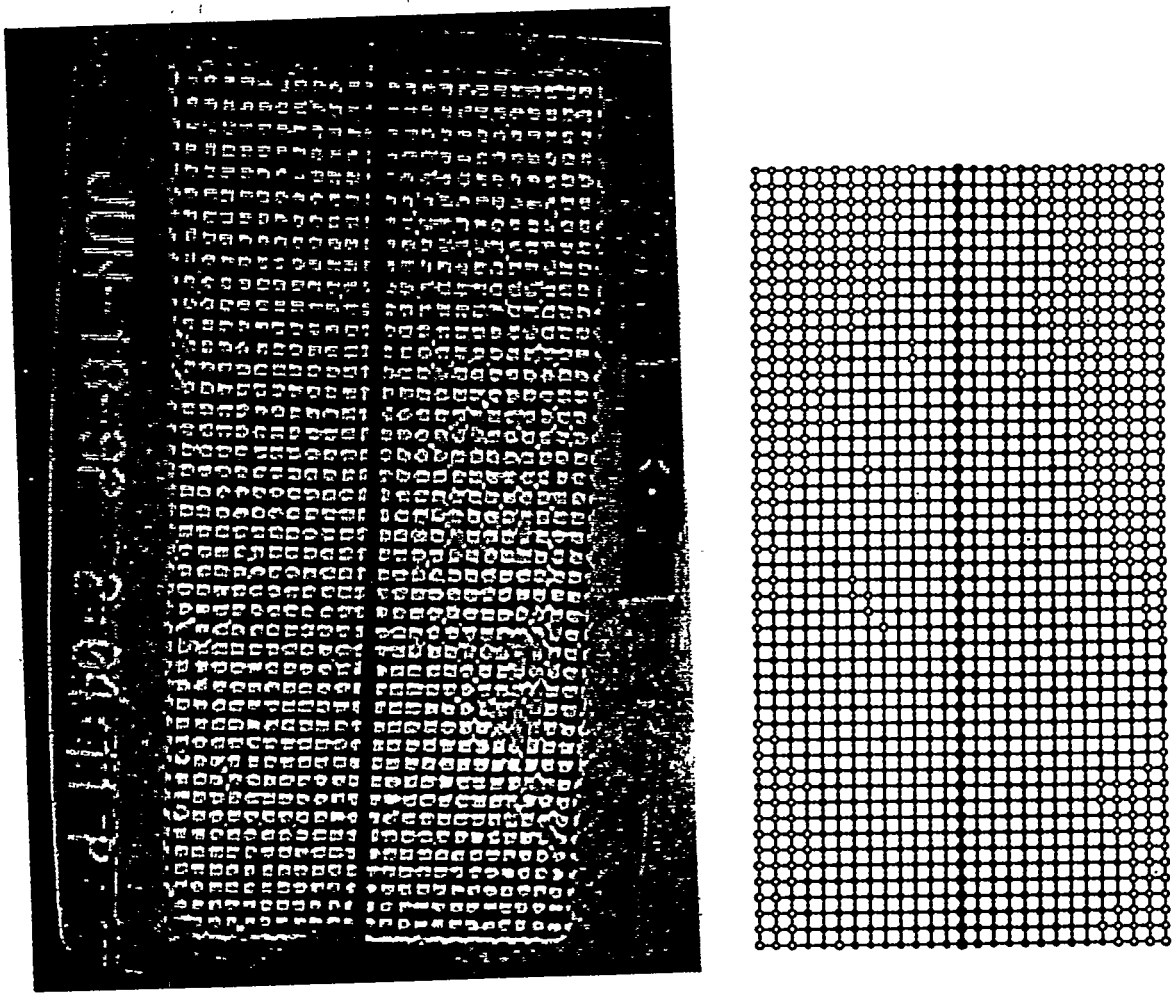

Figure 60: Comparison between experimental and numerical results for water-air, $Ca = 5.4 \times 10^{-4}$.

dashes. First we examined the low capillary number 5.4×10^{-8}. Film flow and snap-off are the dominant mechanisms under this condition (Figure 61). The capillary number was next increased to 1.8×10^{-6}, and the results are shown in Figure 62. Now, in addition to film flow, we have pore filling mechanisms as well; however, the fracture is practically not invaded. Then, the simulation was run at $Ca = 5.4 \times 10^{-6}$ (Figure 63). In this case, the fracture starts to be invaded; however, at steady state, the full fracture penetration was arrested. This result is comparable to a previous set (Figure 59) at $Ca = 5.4 \times 10^{-5}$ where film flow did not take place. Because of the order of magnitude difference between the two results, this is supporting the fact that in the experiments a film flow mechanism did not exist. The final run is at a capillary number of 5.4×10^{-5}. At these conditions, pore filling is the dominant mechanism. This is similar to a previous set (Figure 60) at $Ca = 5.4 \times 10^{-4}$. Comparison between the two indicates that if there is film flow, the start of the fracture invasion, and the competition between displacement fronts in the fracture and the matrix occur sooner.

In another set of simulations, the imbibition in the water-oil pair was studied. A network of size 60×20, with fractures in the side of the model is considered. Here, injection is through the entire inlet-face. The viscosity ratio is 100, while bond and pore radii of the fracture are five times larger to those in the matrix. The pore radius is ten times the bond radius. No film flow is assumed. The critical capillary number (when the front in the matrix and the fracture are the same) was 0.67×10^{-4} (Figure 65). The calculated value from equation (34) is 0.12×10^{-4}, which is a relatively good match despite the simplifications in deriving the formula. Then, the simulator was run for the same network, but with a bond radius one half of the previous. Now, the resulting critical capillary number becomes 0.75×10^{-6} (which is $\frac{1}{16}$ smaller of the previous). This is expected from Eq. (34), which shows that both cross section area and matrix permeability are proportional to the second power of the bond radius. This indicates that the critical capillary number is proportional to matrix permeability. We also run the simulator for different lengths and viscosity ratios and found the critical capillary number to be inversely proportional to the length and viscosity ratio. This set of simulations confirmed the proposed relationship (Eq. 34) for the critical capillary number. Finally, simulator was run for a different mobility ratio. Figure 66 shows the effect of viscosity ratio on the critical capillary number. At mobility ratio values higher than one, the slope obtained is close to 1. At mobility ratio values smaller than one, on the other hand, the effect of the mobility

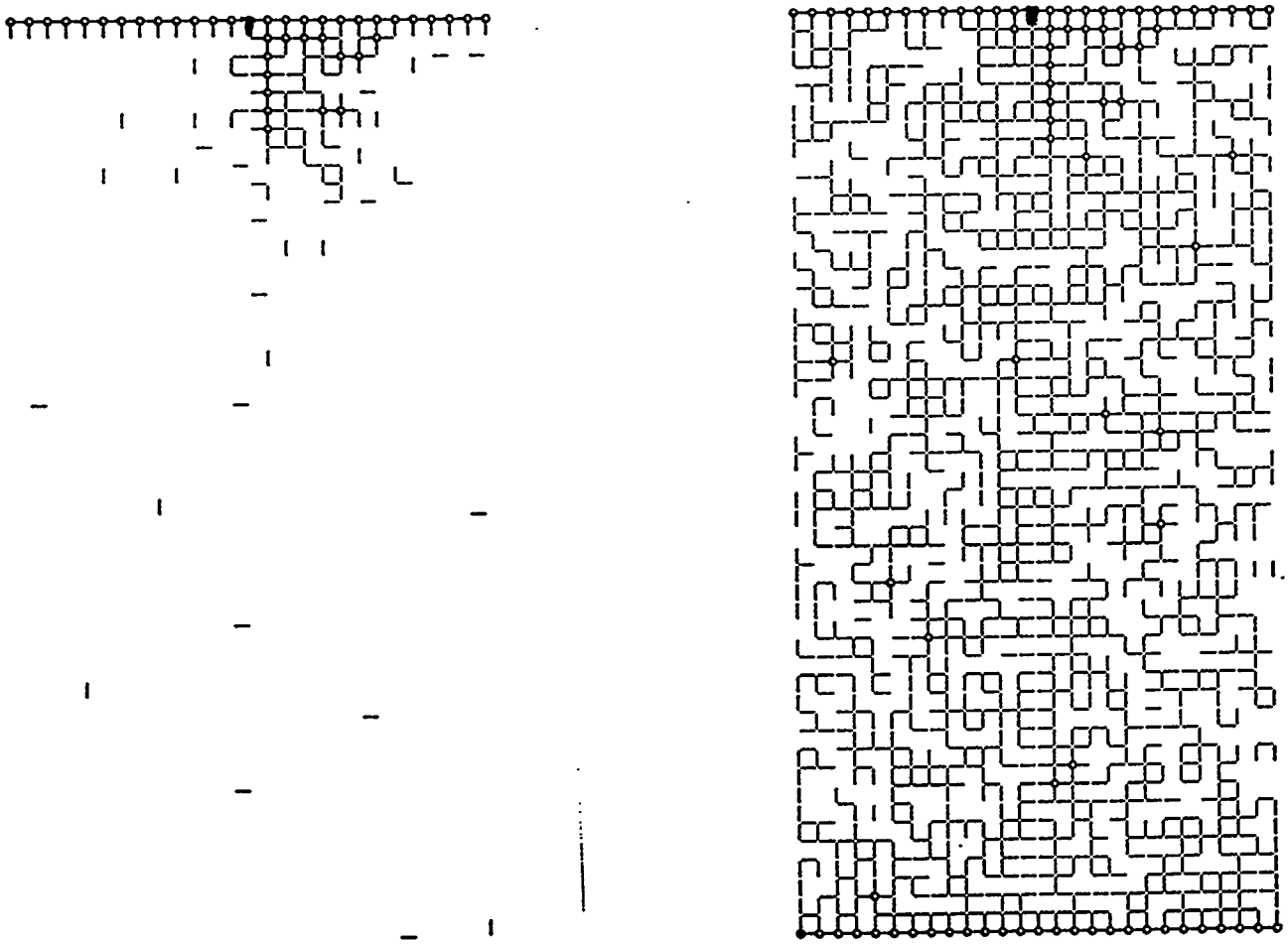

Figure 61: Numerical simulation of secondary imbibition (water-air) $Ca = 5.4 \times 10^{-8}$ (left: early time, right: steady state).

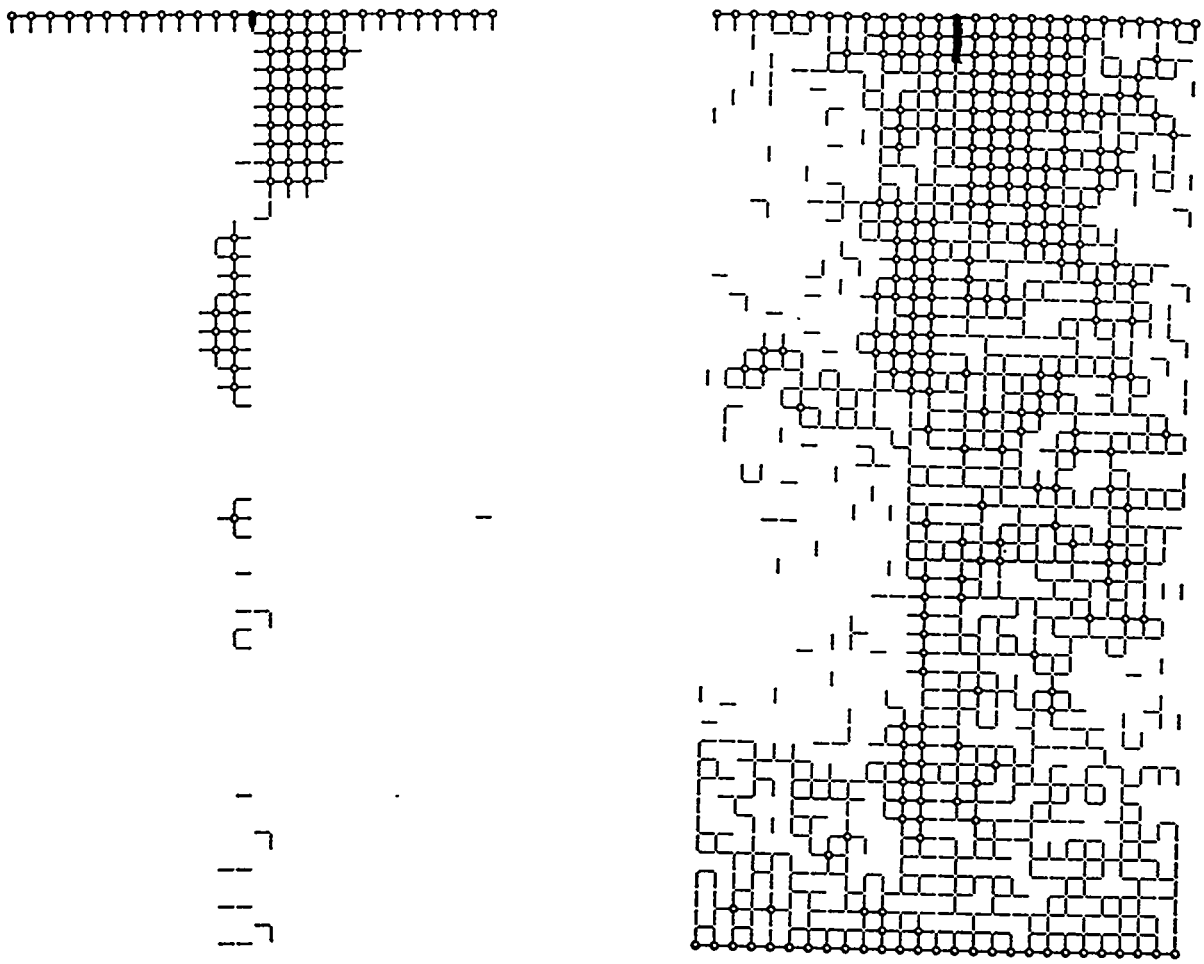

Figure 62: Numerical simulation of secondary imbibition (water-air) $Ca = 1.6 \times 10^{-6}$ (left: early time, right: steady state).

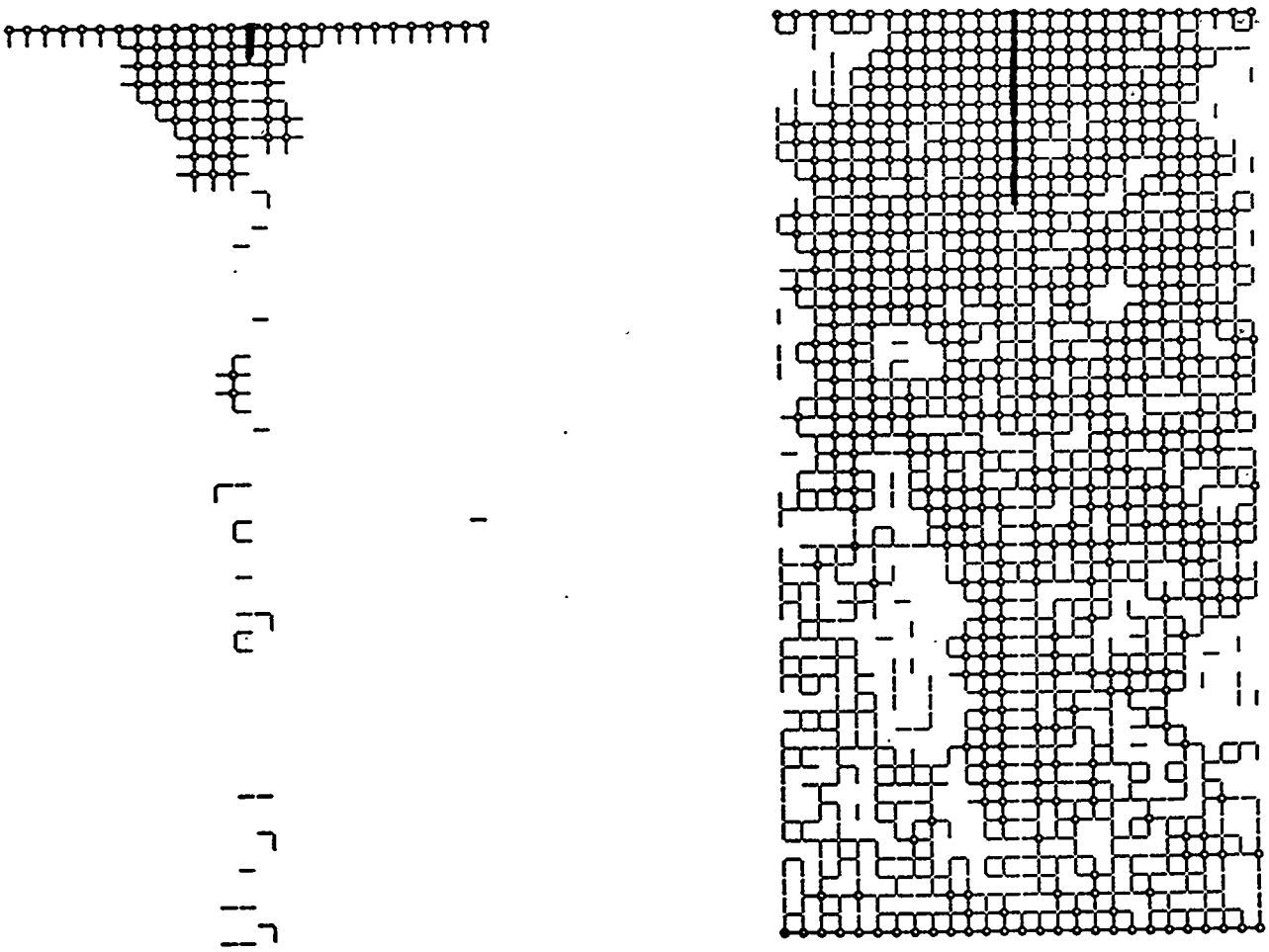

Figure 63: Numerical simulation of secondary imbibition (water-air) $Ca = 5.4 \times 10^{-6}$ (left: early time, right: steady state).

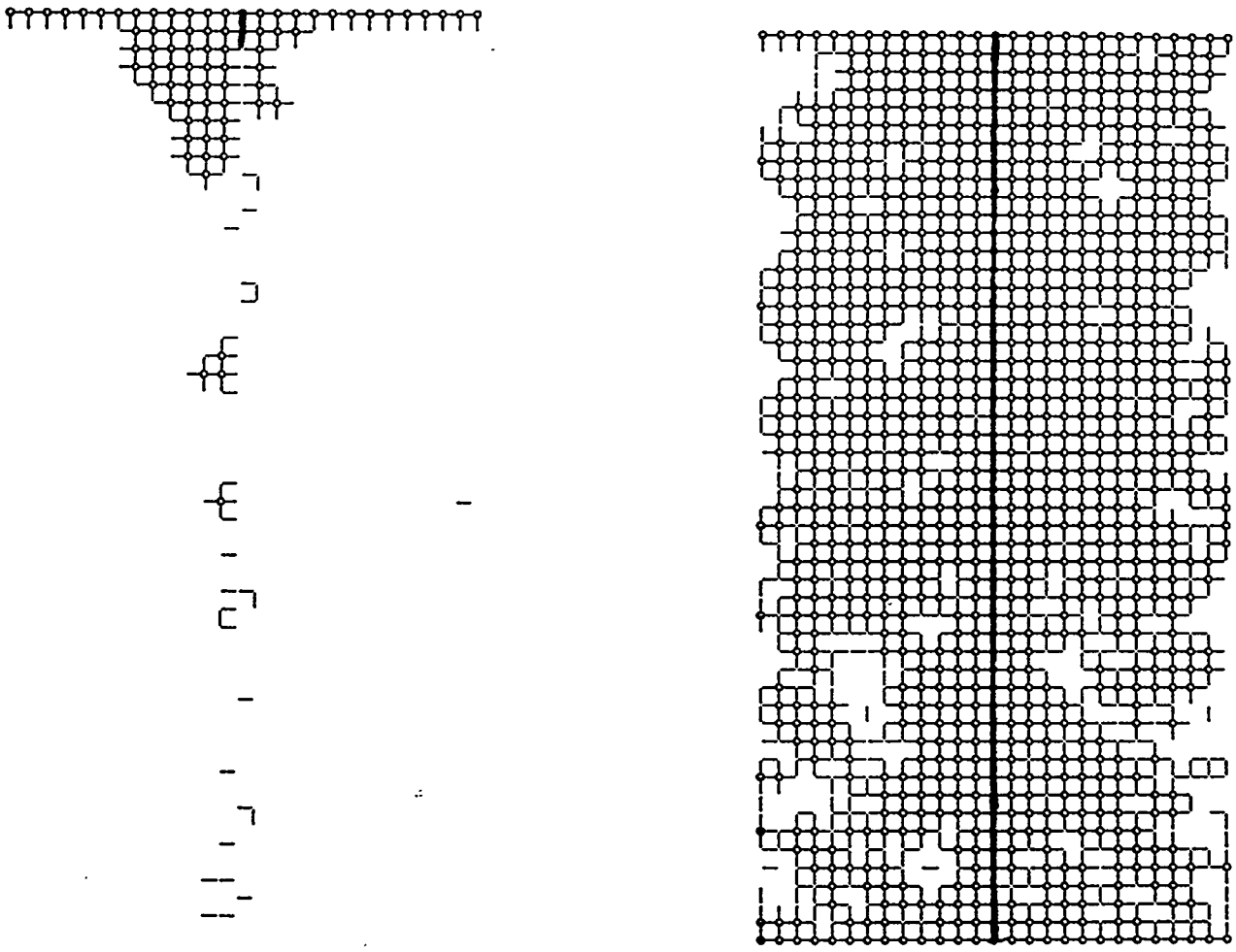

Figure 64: Numerical simulation of secondary imbibition (water-air) $Ca = 5.4 \times 10^{-5}$ (left: early time, right: steady state).

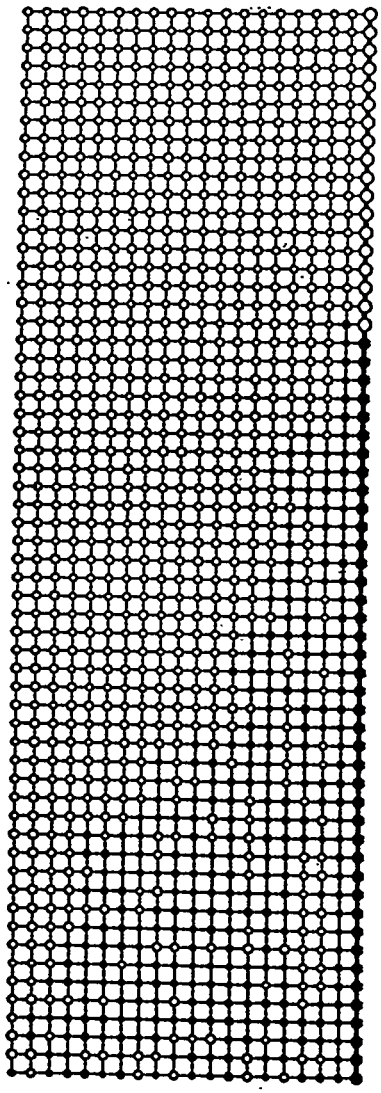

Figure 65: Numerical simulation of primary imbibition (water-air) $Ca = 0.67 \times 10^{-4}$, $M = 100$.

ratio on the critical capillary number is relatively small. This figure actually confirms the inverse proportionality of the first critical capillary number on mobility ratio, and shows that the second capillary number is almost independent of the mobility ratio.

Finally, we simulate water-air free imbibition experiment. Now, the boundary condition was changed from constant flow rate to constant pressure, and we set both inlet and outlet pressure to be atmospheric. The primary imbibition simulator was used. Figure 67 shows four snapshots of the results obtained. Similar to the experiment, water moves into the matrix first and no substantial trapping is observed. When substantial matrix invasion develops, water starts to invade the fracture as well. We note that the water saturation versus time curve for this simulation is linear. Aronofsy et al. [2] findings predict an exponential curve. The two, of course, are consistent at early times. Possible reasons for discrepancy are the assumption of no film flow and snap-off mechanisms in this simulation.

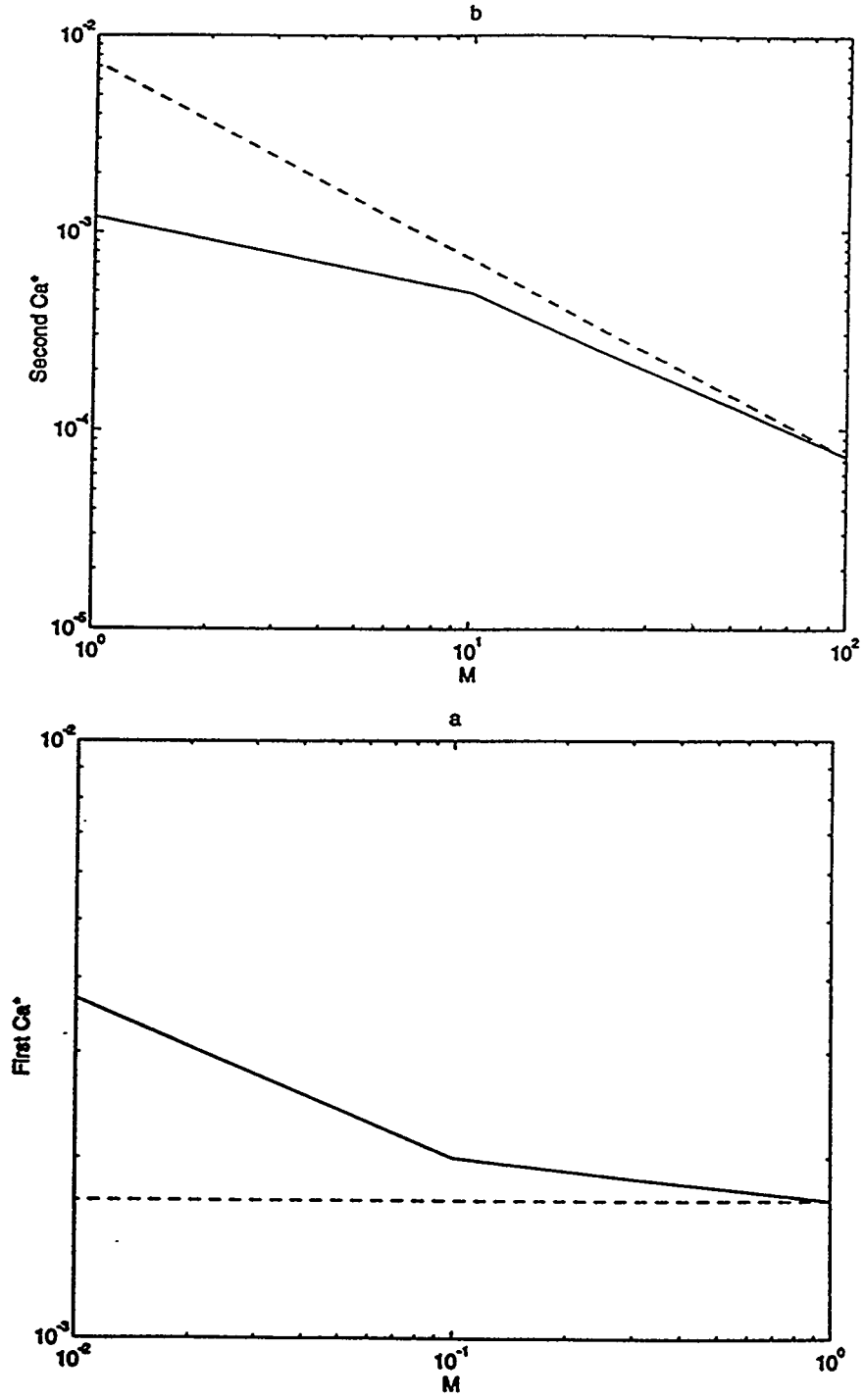

Figure 66: Dependence of the critical capillary number (open circles) on viscosity ratio for primary imbibition (the solid line is a guide to the eye). Theoretical predictions are shown as dashed curves.

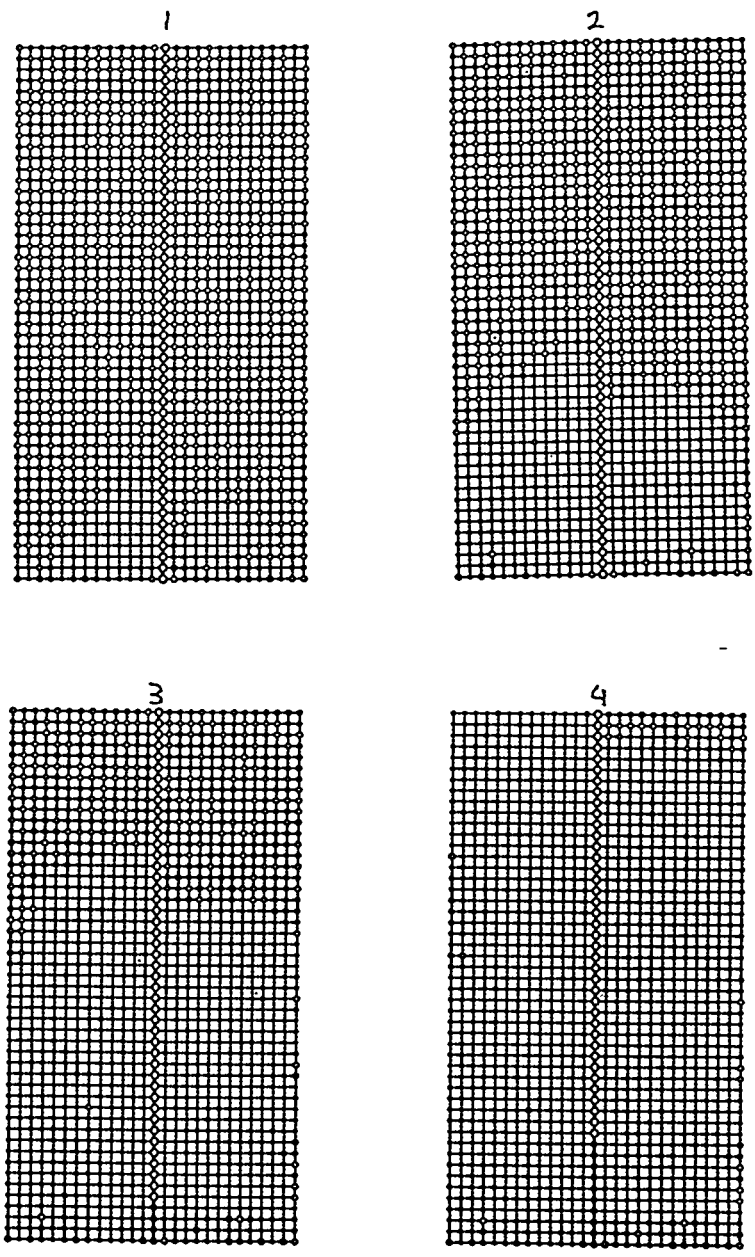

Figure 67: Numerical simulation of free imbibition (water-air). Four consecutive snapshots.

4 CAPILLARY PRESSURE OF ANISOTROPIC POROUS MEDIA

B. Xu and Y. C. Yortsos

4.1 INTRODUCTION

Anisotropy is the dependence of the magnitude of certain properties of a substance on the direction of measurement. In the case of crystals and fluids, anisotropy is an intrinsic property. In the case of porous media, the anisotropy of permeability has been studied thoroughly in terms of tensors [28]. But by the same reasoning, the capillary pressure function which is closely related to permeability should also have direction-dependence in anisotropic media. As far as can know, this problem has not been studied so far. It is the objective of this chapter to study the effects of anisotropy on capillarity by using percolation approach in network modeling [34].

Percolation in anisotropic networks has been studied by some researchers with emphasis on percolation characteristics, such as the universality of critical exponents. These works have been done using ordinary percolation, in which different occupancy probabilities are used in different directions, their ratio specified as anisotropic ratio (p_x/p_y). Yoon and Lee [117] studied the conductivity exponent (t) as a function of the anisotropic ratio in the range from 0.1 to 10. The exponent t relates the conductivity to probability p by the power-law relation

$$\sigma \sim (p - p_c)^t \tag{37}$$

These authors found that in the above range t varies from 1.67 to 1.08, compared to the isotropic value of 1.30. Other researchers have done some work on the scaling of conductivity [42][101], while some others studied the properties of the infinite cluster at anisotropic conditions [51]. However, no work has been published using invasion percolation with emphasis on the capillary behavior. In this chapter, we report preliminary results on this subject.

To model the process we consider an anisotropic network, consisting of two (2-D) or three (3-D) different pore (or bond) size distributions in the anisotropic directions (low (L) and high (H)), respectively. We recall that the pore size is related to the permeability by the relation $r \sim \sqrt{k}$. These distributions can be selected solely as to overlap or not to overlap with one another. In the case of overlap, we can further differentiate as wide, narrow or very narrow overlap, depending on the overlap range. In all cases, the (L) size distributions are the same, and uniform (in the range

of [0.6, 1.4]). The (H) distributions vary for different overlap conditions: in the case of no overlap, it it in the range [1.8, 4.4]; for wide overlap, in the range [0.9, 2.1]; for narrow overlap, in the range [1.29, 3.01] and for very narrow overlap, in the range [1.38, 3.22]. Trapping rules are included in the simulations which are based on standard invasion percolation.

4.2 RESULTS AND DISCUSSION

In the analysis, we discuss 2D and 3D network simulations, with or without overlap in the different directions.

4.2.1 2D Networks Without Overlap

We consider drainage in square networks where the displacing phase is injected from the sides facing high or low permeabilities (k), respectively. Injection at an angles with respect to the main direction was also considered. Figures 68 (a) to (e) give the capillary pressure curves corresponding to injection at 0° (high k direction (H,L)), 30°, 45°, 60° and 90° (low k direction (L,H)) angles. The curves are different depending on the injection angle. They suggest the existence of anisotropy in capillarity, which should be contrasted to the common practice of using a single P_c curve in anisotropic porous media. Injecting along the high k direction (0°) produces a low P_c curve, while injecting along the low k direction (90°) gives a high P_c curve, as expected. Injecting at an angle other than 0° or 90° gives a composite P_c curve, similar to the P_c curve in a composite medium with two permeability values suggested by Yortsos et al [120]. The jump links the low P_c curve plateau corresponding to 0° to the higher plateau corresponding to 90°. The jump varies with the angle, from 0° (no jump) to 30° (jump at $S_{nw} \sim 40\%$) to 45° (jump at $S_{nw} \sim 20\%$), 60° (jump at $S_{nw} \sim 8\%$) to 90° (jump at $S_{nw} \sim 0\%$). This will be analyzed next.

Figure 69 shows the displacement patterns for different injection angles. What is obvious is that the patterns are qualitatively different, especially for 0° and 90°, the intermediate angles possessing some similarities in the general shapes but different in size. For 0° angle injection (Figure 69(a)), the injection direction (from top to bottom) coincides with the large bond direction (high k in vertical). Since all bonds in the high k direction are larger than those in the low k direction, the invading phase proceeds along the large bond columns (connected to the outlet) only, with no interaction between different columns taking place. This is like a percolation in a 2D network

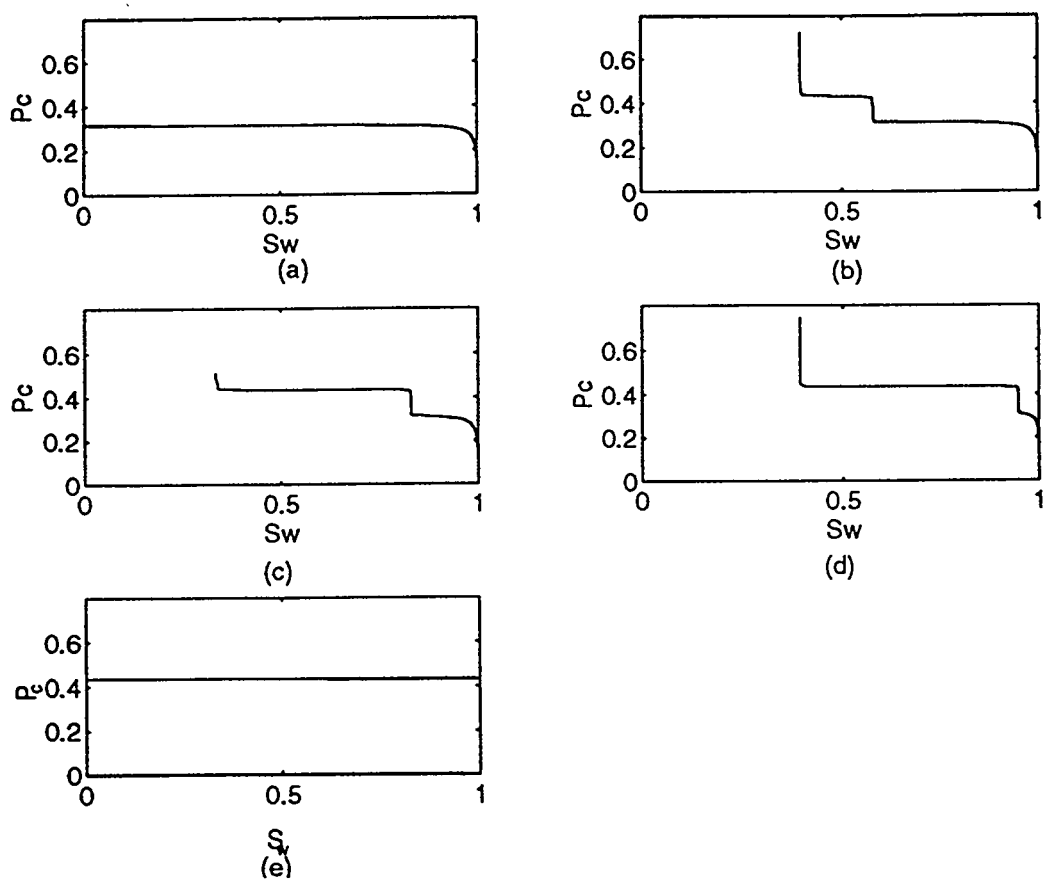

Figure 68: Capillary pressure curves for 2D, without size overlap for injection at different angles (a) 0°, (H,L) (b) 30° (c) 45° (d) 60° (e) 90°, (L,H).

with coordination number $Z = 2$, resulting in a percolation threshold $p_c = \int_{r_c}^{r_{max}} \alpha(r)dr = 1$ and $r_c = r_{Hmin}$, which means that the capillary pressure plateau $P_{cplateau} = \frac{2\gamma}{r_{Hmin}}$. Injecting at angle of 90° (from top to bottom) (Figure 69(e)), the nw phase first needs to penetrate a bond in the small k distribution (vertical). This first step raises the P_c to a value corresponding to the largest bond in the low permeability direction (r_{Lmax}). Once one node in this row is occupied, the large bonds in the transverse direction makes it easy to fill that entire row immediately. This process is repeated in the next row, thus the process advances row by row. This is a percolation process in a 2D network with $Z = \infty$ or NY for finite network and resulting in a $p_c = 0$ and $r_c = r_{Lmax}$, which means that $P_{cplateau} = \frac{2\gamma}{r_{Lmax}}$. When injecting at an angle to the high k direction (from top left corner), the situation is more complicated. As Figures 69(b), (c) and (d) show, the invading front first advances horizontally (the high k direction) from the inlet line, resulting into a low P_c plateau corresponding to the one in 0° angle injection. When the columns connected to the inlet are either filled or trapped, the non-wetting phase must move downwards, which is the low k direction, thus raising P_c to a high plateau corresponding to the one in 90° angle injection during which there is only one pore-filling. This results in the P_c jump. As long as $r_{Hmin} > r_{Lmax}$, a P_c jump appears.

Looking at the occupancy pattern, it can be seen that the saturation S^*_{nw} at which the jump happens has some dependence on the number of sites that are connected to the inlet through large horizontal bonds. There is one critical row where the non-wetting phase starts to proceed downwards through a vertical, small size bond. This is the lowest row connected to the injection line. Two situations can be identified: (a) injection angle $\theta < \pi/4$ and (b) $\theta \geq \pi/4$. For $\theta < \pi/4$, we can divide the range connected to the injection line into two regions, A and B, as shown in Figure 70. When $\theta \geq \pi/4$, only one region of rows that are connected to inlet is present and it acts like region A. Before the invading phase is forced into the small vertical bonds, region B is always completely filled, however region A is not and may contain trapped phase, once the row that separates regions A and B is filled completely. An analysis reveals that the saturation of the invading phase before the P_c jump given by

$$S^*_{nw} = \begin{cases} 1 - \frac{1}{2}(2 - S_{nwA}) \tan\theta & \theta < \pi/4 \\ \frac{1}{2} S_{nwA} \cot\theta & \theta \geq \pi/4 \end{cases} \tag{38}$$

where S_{nwA} is the invading phase saturation in range A when it traps all the remaining wetting

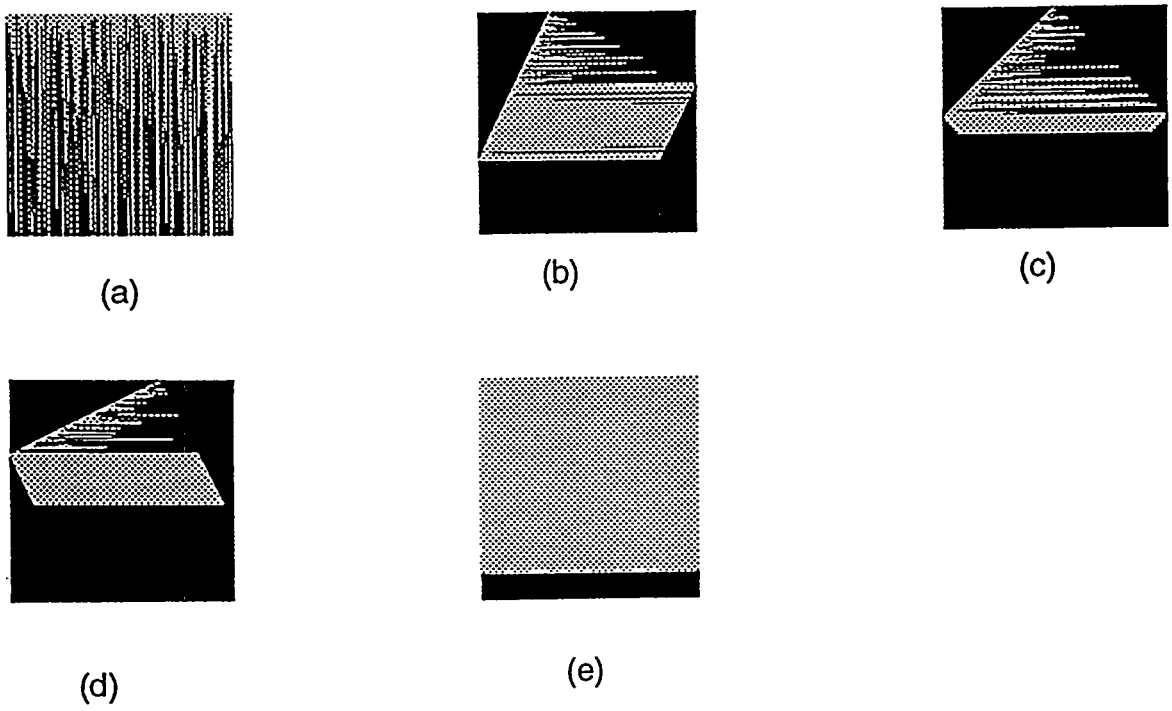

Figure 69: Invasion patterns corresponding to Figure 68.

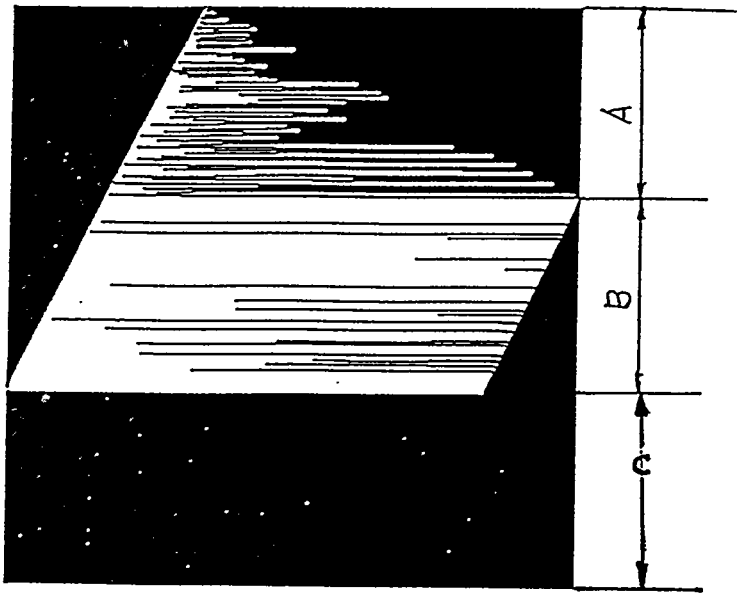

Figure 70: Schematic of the invasion regions for 2D injecting at an angle, without overlap.

phase. If we take S_{nwA} to be constant for different angles θ, then S_{nw}^* is monotonically decreasing with θ. This was confirmed in our simulations.

What is the property of the maximum saturation in range A, S_{nwA}? Is it size-dependent? Repeated runs with different realizations suggested that S_{nwA} may be distributed for finite size networks. So Monte Carlo simulations with a large number of realizations were carried out at $\theta = 30°$ for different sizes of square networks ($N = 100, 200, 300, 400$) to study its statistics. Figure 71 shows the distribution. Analysis of these data for different network sizes shows that as the network size increases, the standard deviation of the distribution of S_{nwA} decreases monotonically, and so does its mean, as plotted in Figure 72 and Figure 73. We may infer that when network size is large enough, S_{nwA} will converge to a small value, in which case P_c curves are reproducible.

The irreducible (trapped) wetting phase saturation (S_{wir}) at the end of displacement was found to be zero for $\theta = 0°$ and $90°$. Invasion occurs by rows (piston-like) or by columns, but finally it displaces all initial fluid. On the other hand, for $\theta = 30°$ and $60°$, S_{wir} is in the range of $35 \sim 40\%$ while for $\theta = 45°$, S_{wir} is about 30%. Thus, injection at an angle leaves a trapped wetting phase.

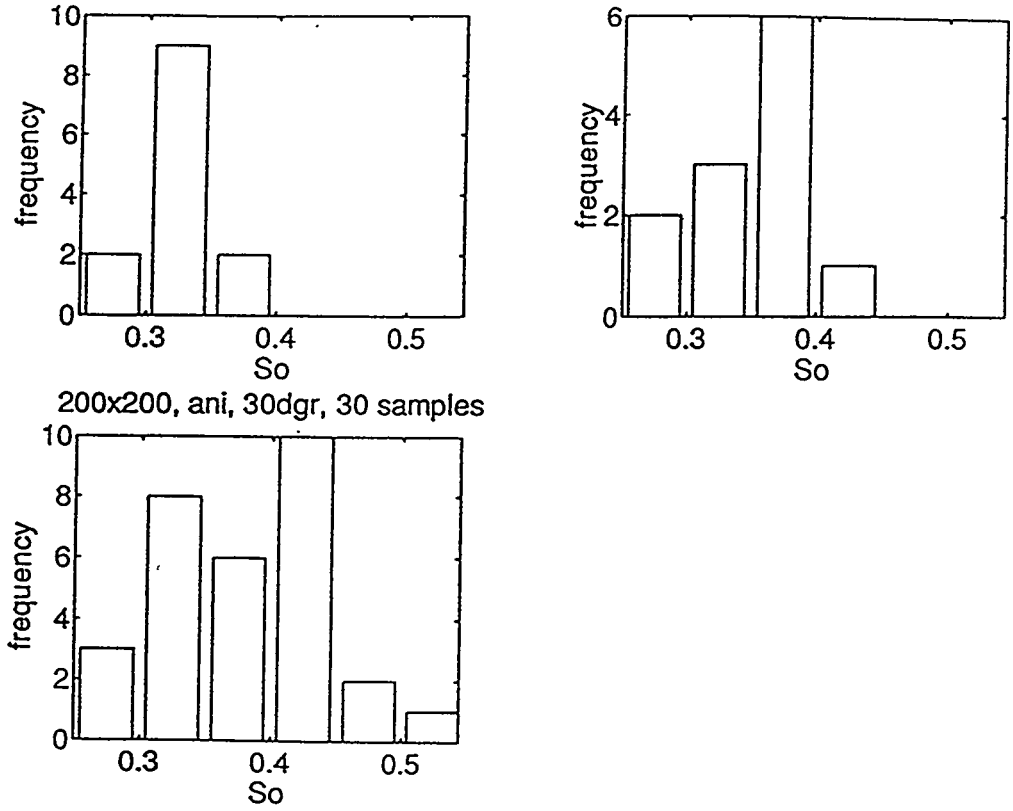

Figure 71: Statistics of S_{nwA} for injection at 30°, without overlap.

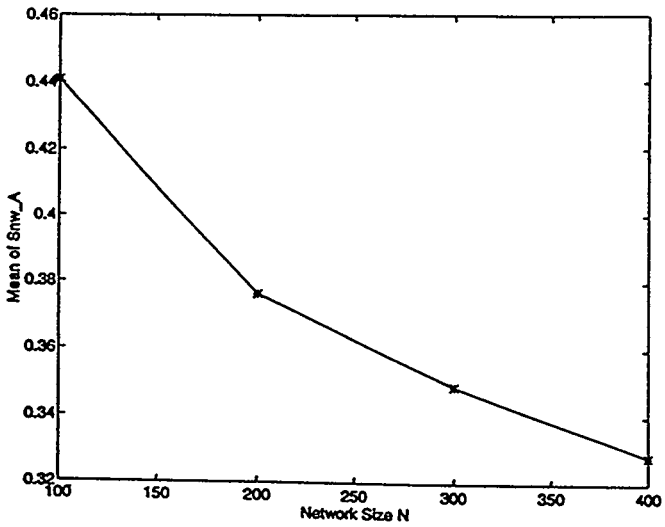

Figure 72: Mean of S_{nwA} as defined above vs network size.

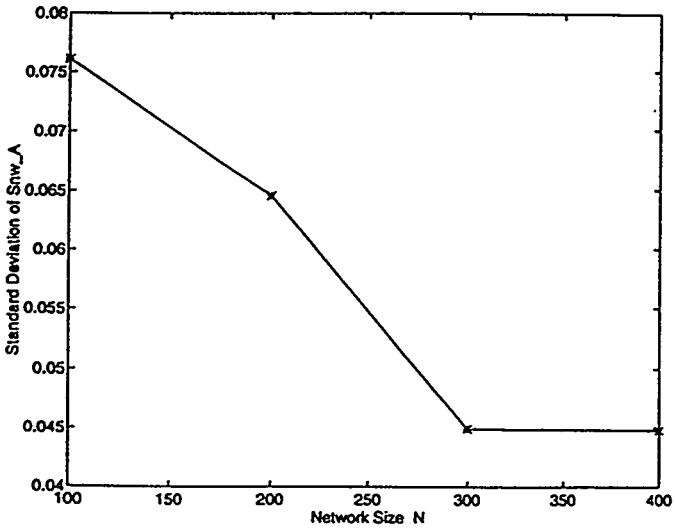

Figure 73: Standard deviation of S_{nwA} vs network size.

4.2.2 2D Networks With Overlap

When bond sizes in the two directions overlap, the effect can be significant in 2D. To make the overlap effects clear, three levels of overlap were studied, wide overlap, narrow overlap and very narrow overlap. Figures 74, 75 and 76 show the capillary curves for different overlap conditions at different injection angles. What is clear is that in all P_c curves, regardless of degree of overlap, the P_c jump observed in the non-overlapping cases disappears completely. All P_c curves for a given overlap condition have the same P_c plateau value. The only difference is in the irreducible wetting phase saturation. S_{wir} has the same trend as in the no-overlap cases, i.e., 0° and 90° injections have the lowest S_{wir}, 45° injection has a little higher, and 30° and 60° injections have the highest S_{wir}.

Further examining the plateau P_c values, we found that for wide overlap, the P_c plateau corresponds to a bond radius around $r = 1.2$, which is the middle value of the overlap range [0.9, 1.4] of the two distributions [0.6, 1.4] and [0.9, 2.1]. For the other two overlap conditions (narrow and very narrow), the P_c plateaus correspond to to their overlap ranges, respectively. With an increase in the overlap degree, the irreducible wetting phase saturations increase.

Figures 77, 78 and 79 show the different angle occupancy patterns for the three different overlap conditions. Comparing with the no-overlap Figure 69, it is clear that with overlap degree increases,

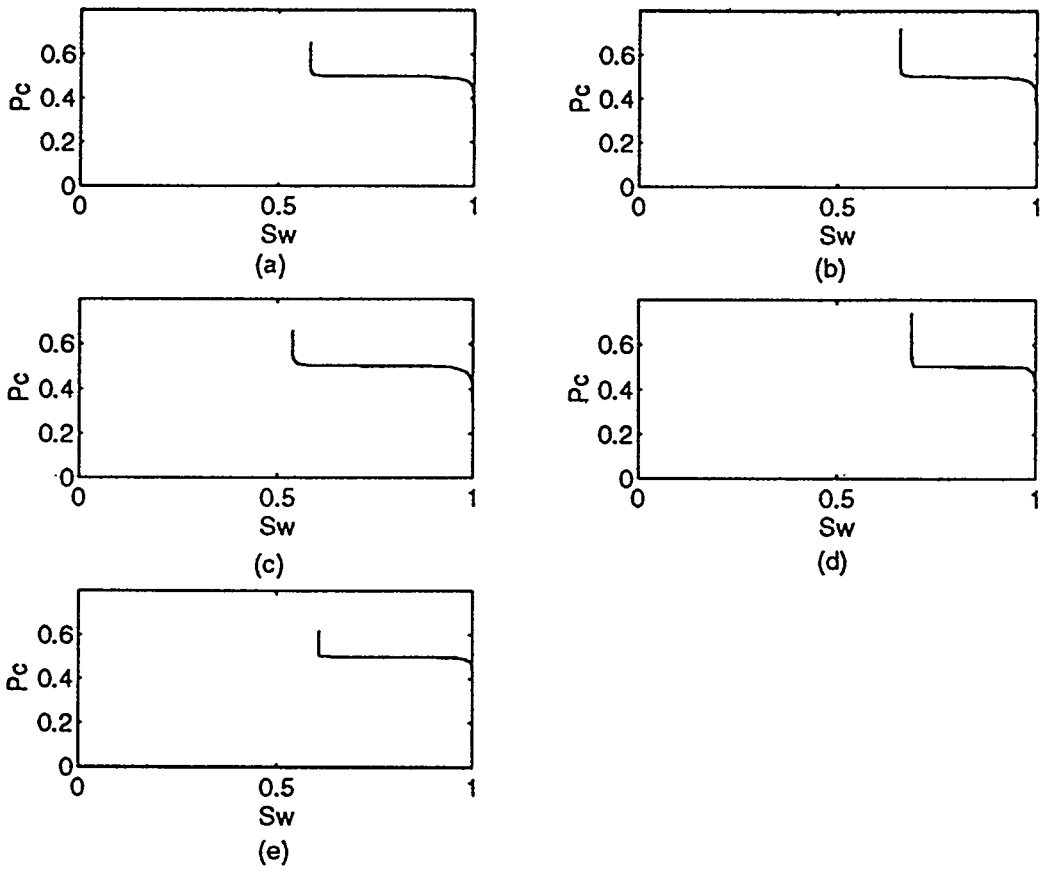

Figure 74: Capillary pressure curves for 2D, with wide size overlap; (a)-(e) refer to Figure 68.

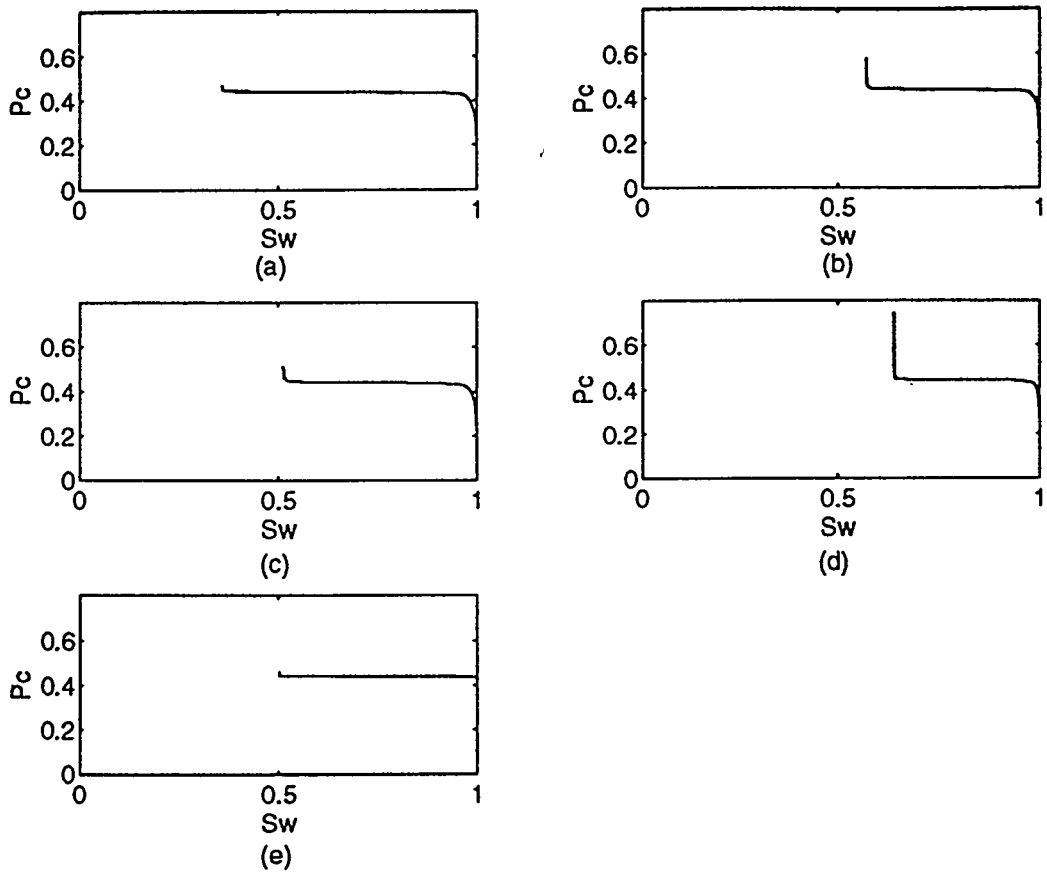

Figure 75: Capillary pressure curves for 2D, with narrow size overlap; (a)-(e) refer to Figure 68.

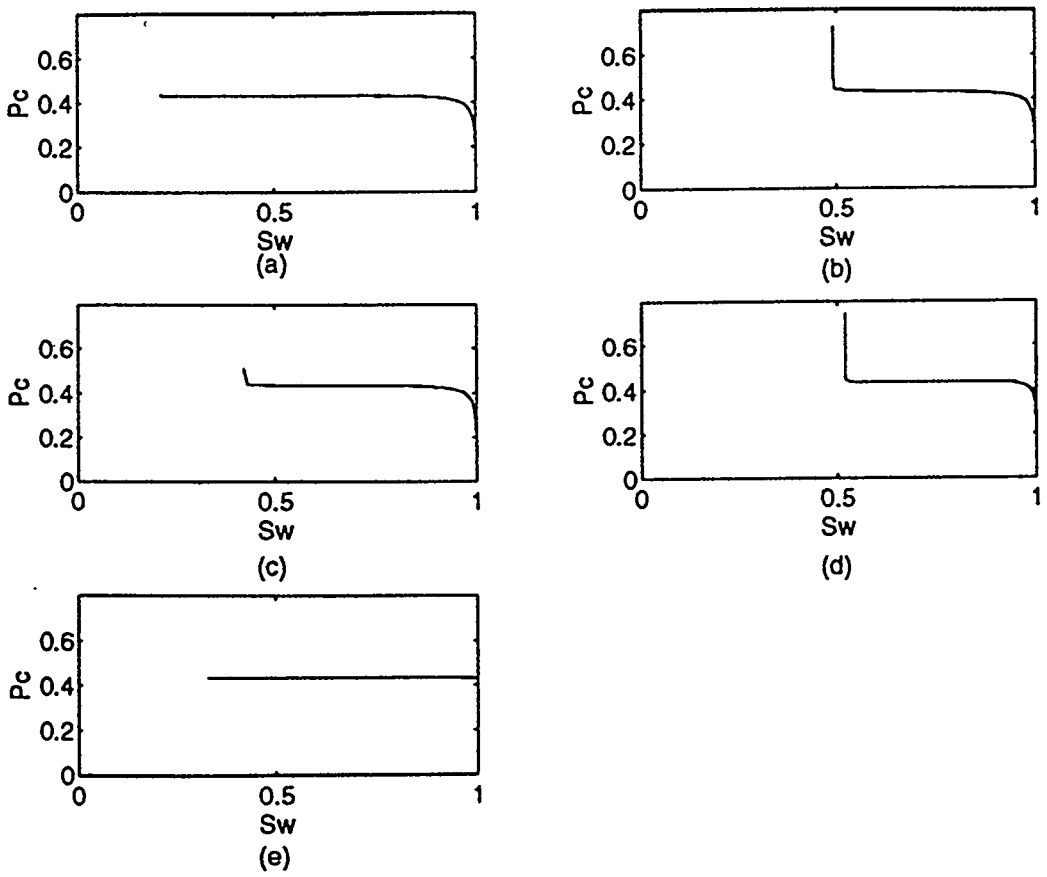

Figure 76: Capillary pressure curves for 2D, with very narrow size overlap; (a)-(e) refer to Figure 68.

the invasion branching increases. These can be explained as follows. With no overlap, each column advances independently. If there is overlap, at some point, the available to the front bonds in the high direction could be smaller than a transverse bond. Then branching occurs. This is what we see on the occupancy patterns for very narrow overlap. This branching causes more sites to be trapped and eliminates the P_c jump. From the no-overlap analysis, we already know that the high P_c plateau corresponds to r_{Lmax}, while the low P_c plateau corresponds to r_{Hmin}. Since $r_{Lmax} < r_{Hmin}$ in the no-overlap situation, we have the P_c jump. Now, with overlap, $r_{Lmax} > r_{Hmin}$ and the jump disappears. We note that these invasion patterns are very different from the isotropic ones. Their behaviors need to be analyzed further.

For comparison, we also show the use of equal size distributions and for different injection angles. Figure 80 shows the curve observed for 2D square network. Here we also obtained different curves, with main difference in the irreducible saturation but little difference in P_c plateau values, as obtained in the wide overlap cases. Figure 81 shows occupancy patterns. Injecting at an angle not coinciding with principal directions (or bond directions) caused more trapping. This is of course a result of the 2D square lattice which is an isotropic.

4.2.3 3D Networks Without Overlap

We consider, next, a 3-D and simple cubic network. We take the injection direction always parallel to an anisotropic (L,H) surface, the third direction having a distribution equal to one of the others (either high or low).

When no overlap exists, the capillary pressure results are similar to 2D. Figure 82 shows P_c curves for a (L,H,L) distribution, while Figure 83 shows P_c curves for a (L,H,H) distribution, with the first two directions in the plane parallel to the injection direction. It is clear that distinct P_c curves appear for different injection angles and jumps in P_c are involved, just as in 2D. The third direction does not contribute to the capillary pressure curve of the invading fluid. Take injection at an angle as an example. No matter what the permeability in the third direction is (L or H), before the invading phase can penetrate the low permeability bond at the lowest row connecting the inlet (refer in Figure 69 to the line separating ranges A (or B) and C), P_c has to be raised to a higher value. This is the same situation as in 2D where a P_c jump occurs.

The difference with 2D geometries lies in the fact that the irreducible wetting saturation at the

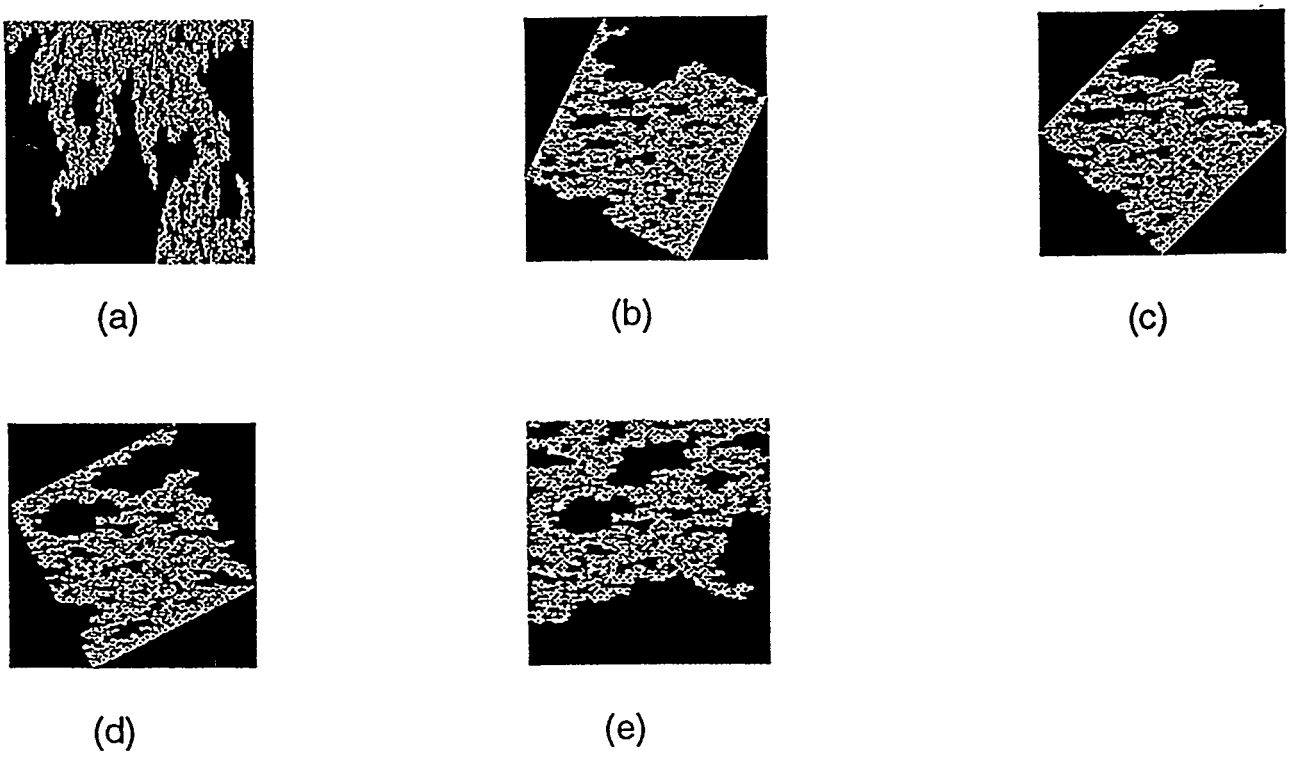

Figure 77: Invasion patterns corresponding to Figure 74, with wide overlap; (a)-(e) refer to Figure 68.

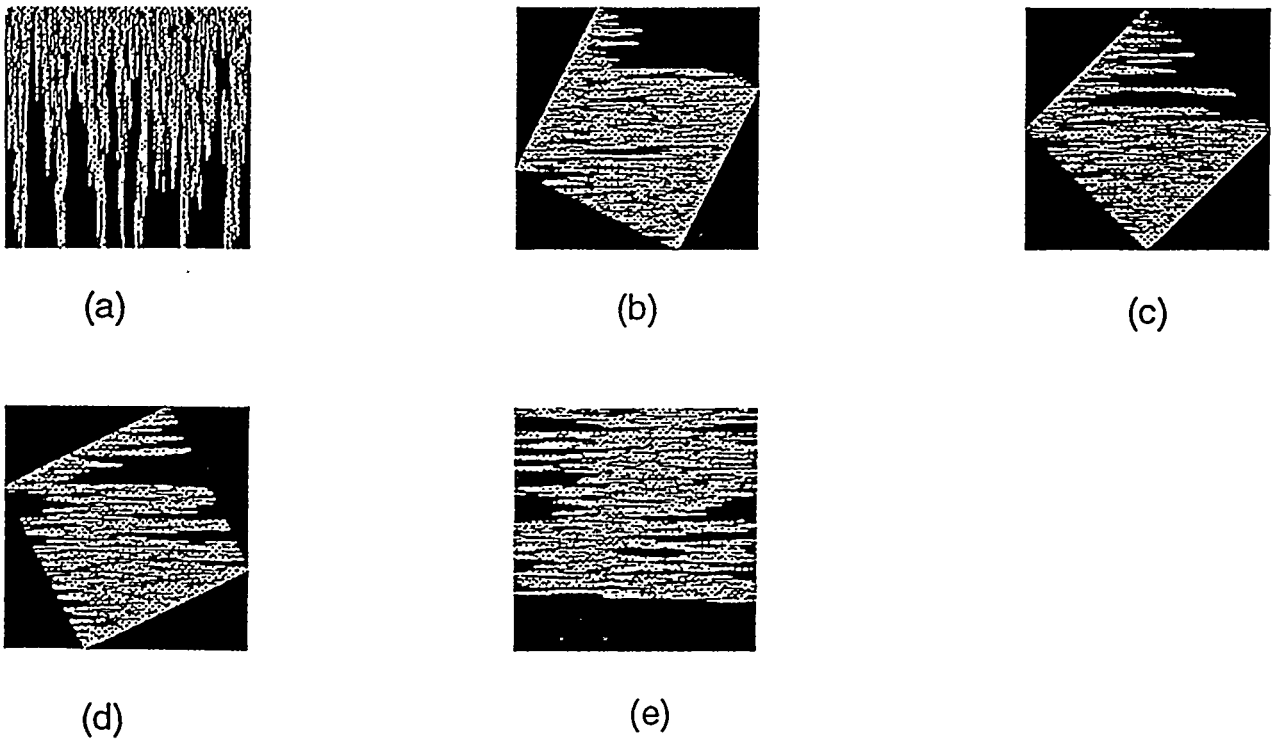

Figure 78: Invasion patterns corresponding to Figure 75, with narrow overlap; (a)-(e) refer to Figure 68.

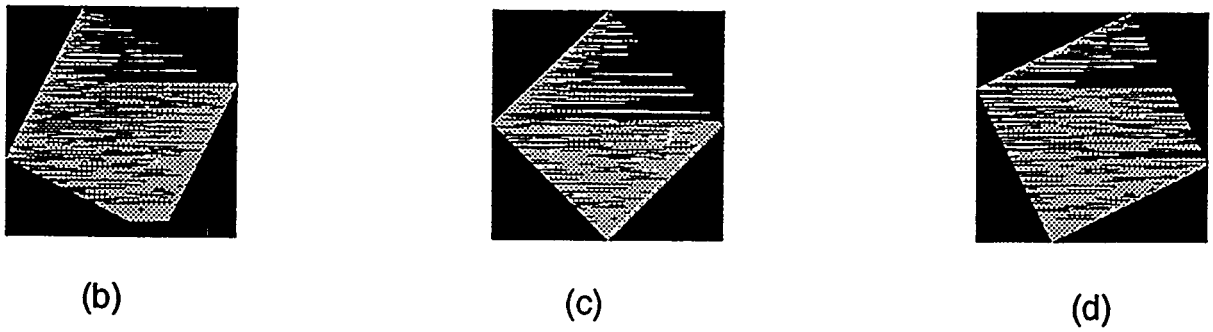

Figure 79: Invasion patterns corresponding to Figure 76, with very narrow overlap; (a)-(e) refer to Figure 68.

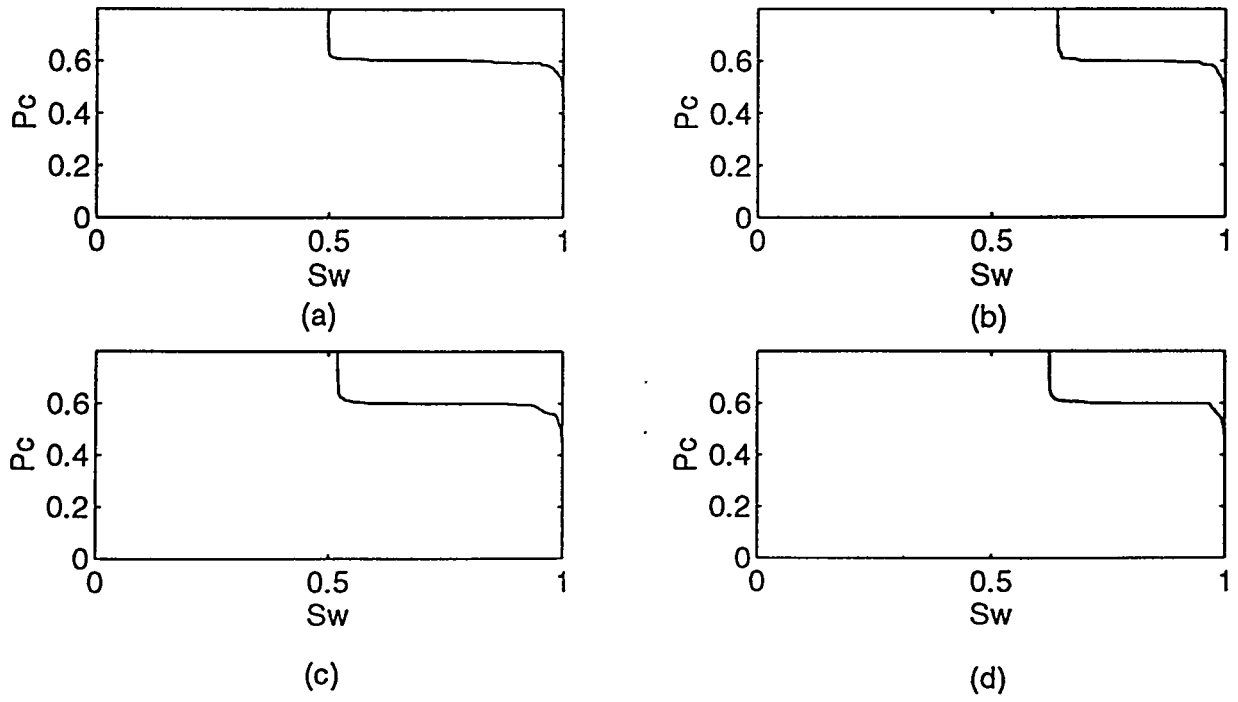

Figure 80: Capillary pressure curves for 2D, full overlap; (a)-(e) refer to Figure 68.

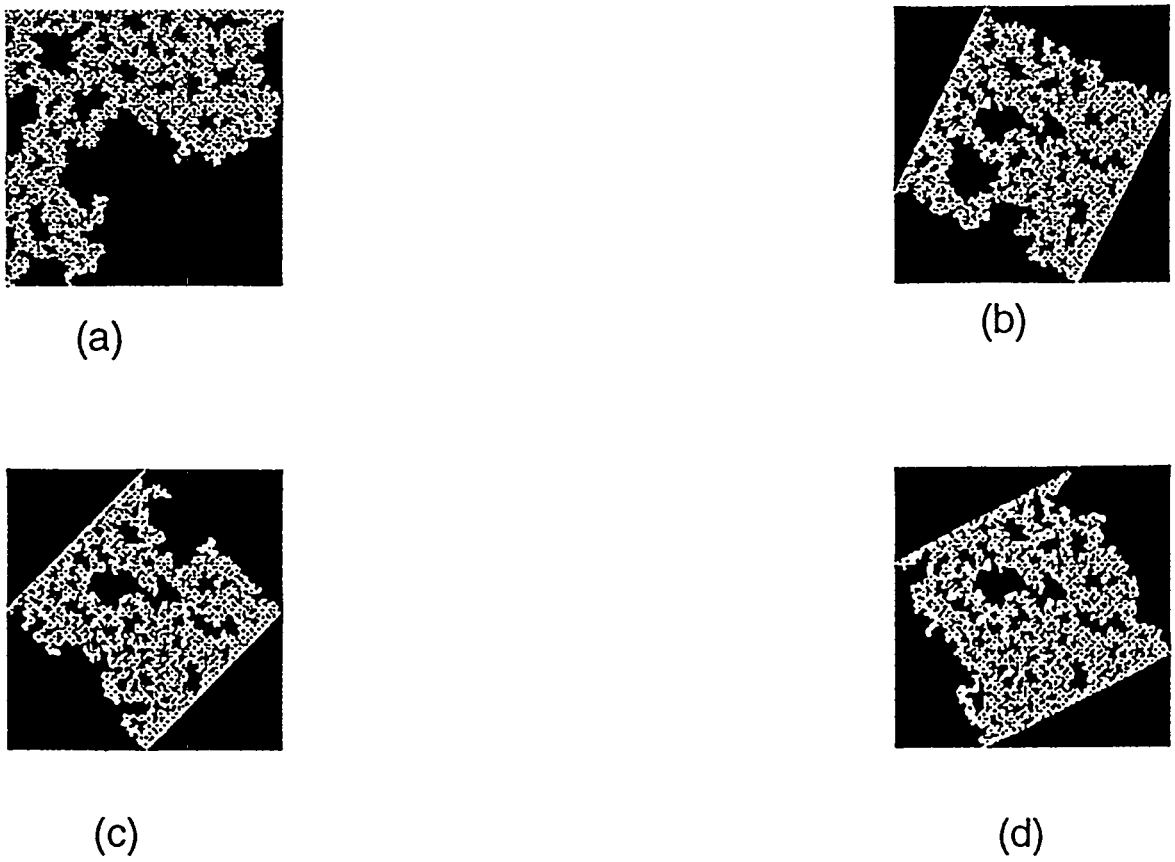

Figure 81: Invasion patterns corresponding to Figure 80; (a)-(e) refer to Figure 68

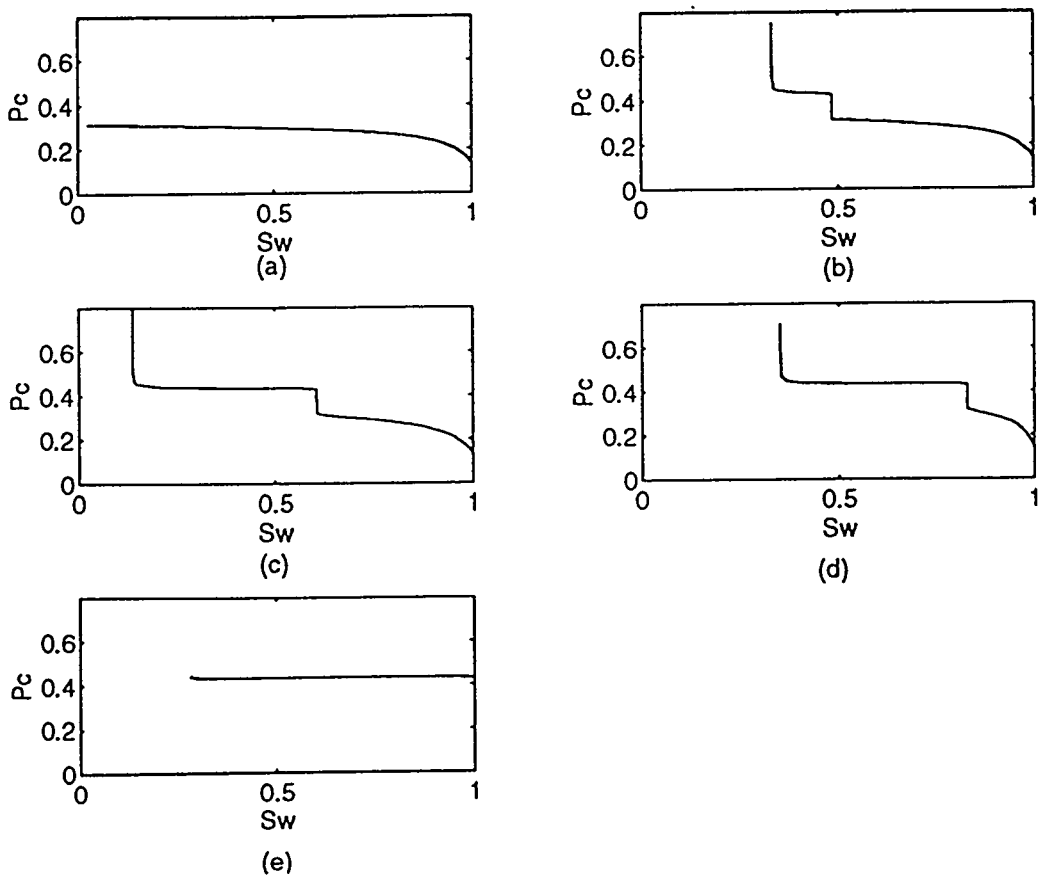

Figure 82: Capillary pressure curves for 3D (L,H,L) without overlap; (a)-(e) refer to Figure 68.

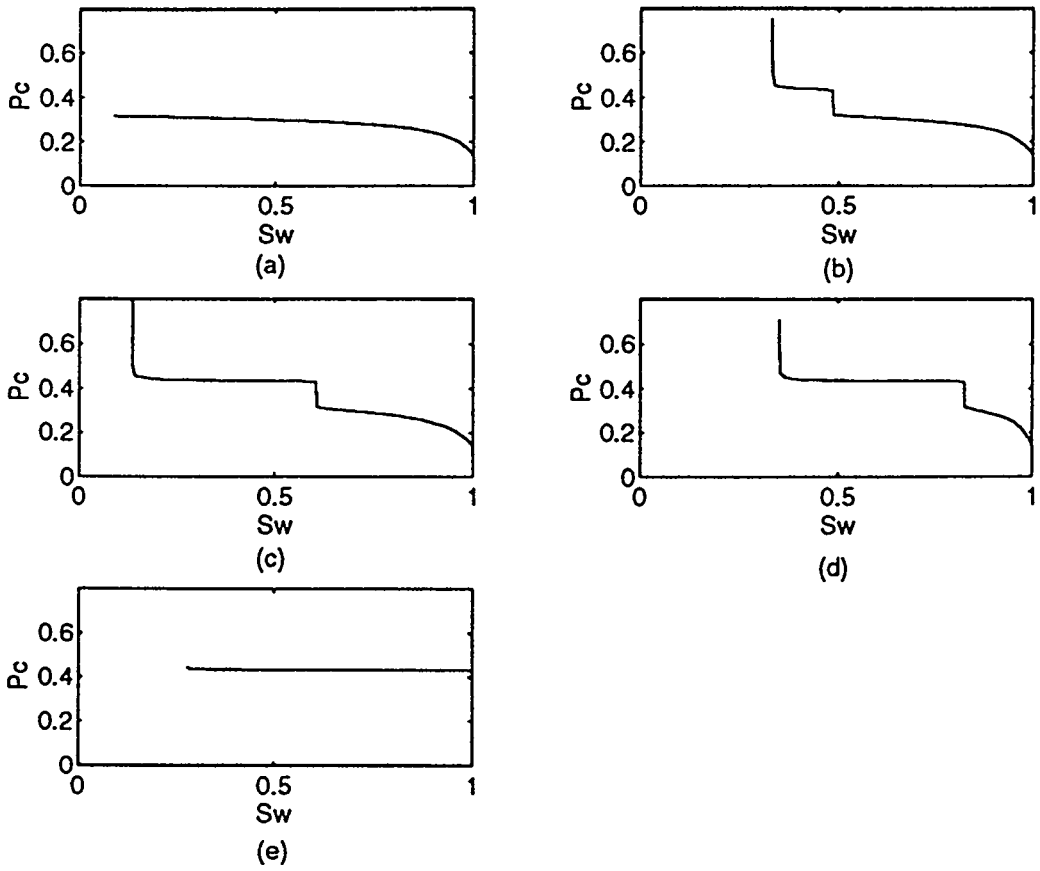

Figure 83: Capillary pressure curves for 3D (L,H,H) without overlap; (a)-(e) refer to Figure 68.

90° injection (LHL or LHH) is no longer zero, as in 2D, as the third direction introduces some trapping.

4.2.4 3D Networks With Overlap

When overlap in the two kinds of distribution (L and H) exists, we expect, according to 2D results, the step-like P_c phenomena should disappear and the P_c curves at different injection angles to make much less difference. We report on P_c curves of the type (LHL) and (LHH). Figures 84 and 85 show the corresponding P_c curves for different angles of each case, respectively. We can see that the (LHL) case agrees with the 2D results: the step disappears and the P_c curves at different angles become much alike, except for the long transition part before the plateaus. This transition part shortens as the rotation angle increases, just like the jump position varies with the angle of injection.

In the (LHH) case, on the other hand, we observe the step-like P_c curves. The various curves for different angle injection look quite similar to the ones with no overlap at all (refer to Figure 68 for 2D, Figure 83 for 3D), and even the jump positions obey the rule of no-overlap, namely that as the angle increases, the jump occurs earlier. What happens if we increase the overlap range? Could the jump disappear? Several simulations were run with different overlap ranges for $\theta = 30°$, as shown in Figure 86. It is clear from this Figure that as overlap range increases, the jump amplitude gradually decreases, but stays non-zero for a wide range of overlap. We explain this behavior below.

Denote the high k direction in the anisotropic surface as x, the low k direction as y and the third direction as z (L or H). Each xy plane would look like the one in Figure 69. The flow will tend to move preferably in the x direction. In the (LHL) cases, the invasion along the x direction proceeds by columns and eventually will meet the low end of the high k distribution which is smaller than the high end of the low k distribution in y and z; thus it will branch into y and z bonds. This makes for a high P_c and no jumps. In (LHH) cases, however, though we have (LH) anisotropy in the xy plane, the plane in xz is isotropic, and both directions have high permeability. According to 2D bond percolation, each xz plane can percolate at the mean bond size (for narrow overlap, $r_{Hmeam} = 2.15$). This is the low P_c plateau before a P_c jump. When regions A and B (Figure 70 corresponding to xy plane) are completely filled or trapped, a y direction small bond must be penetrated, which raises the P_c to a value corresponding to $r_{Lmax} = 1.4$. Thus, a P_c jump

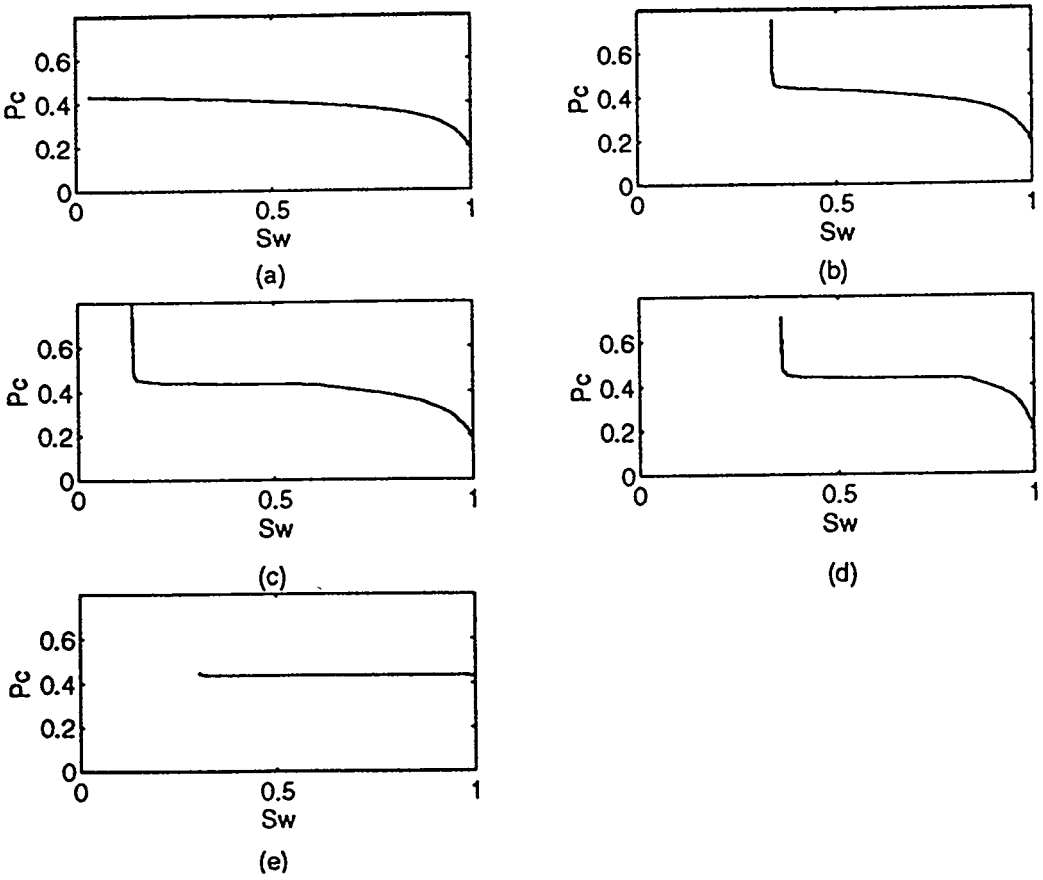

Figure 84: Capillary pressure curves for 3D (L,H,L) with narrow size overlap; (a)-(e) refer to Figure 68.

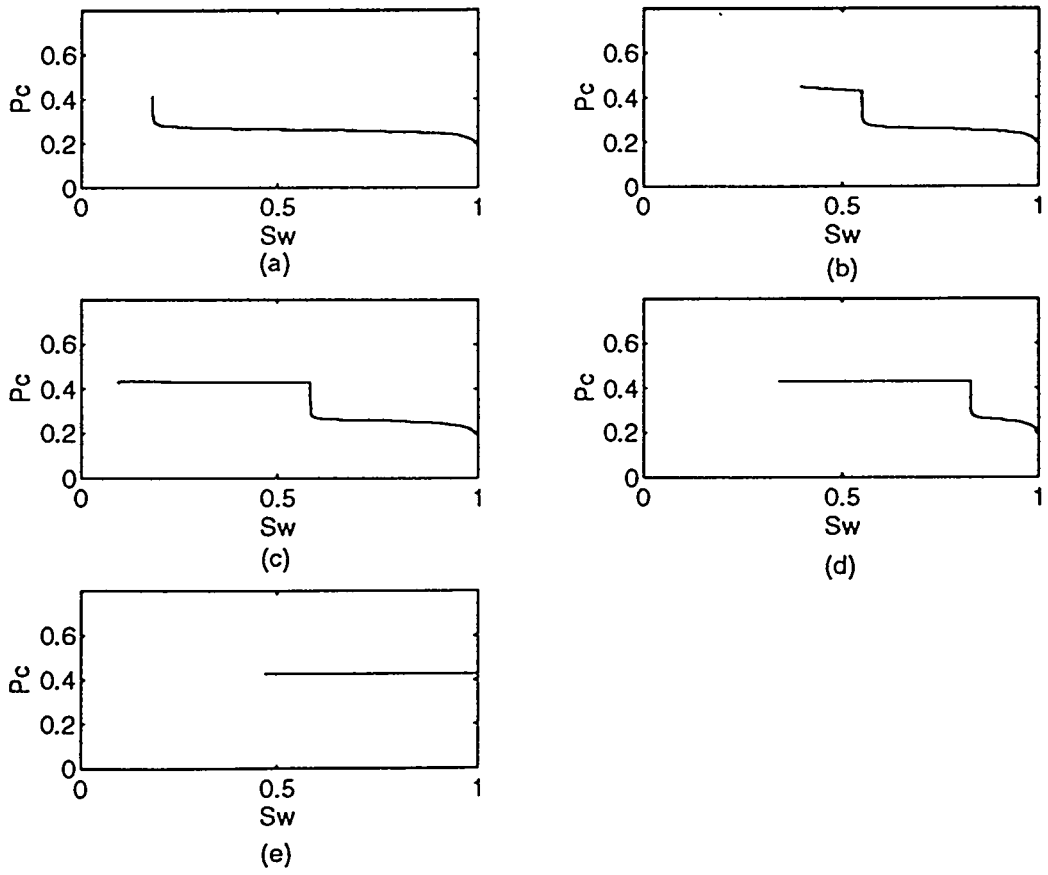

Figure 85: Capillary pressure curves for 3D (L,H,H) with narrow size overlap; (a)-(e) refer to Figure 68.

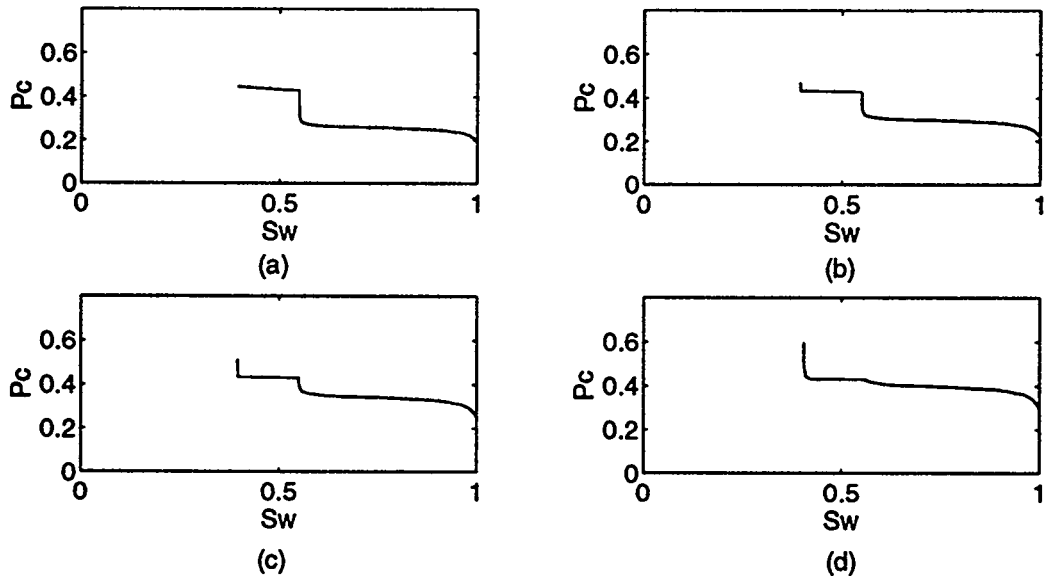

Figure 86: Capillary pressure curves for 3D (L,H,H) at 30° angle injection with different size overlap. High k size ranges are: (a) [1.2, 2.8] (b) [1.29, 3.01], narrow overlap (c) [1.05, 2.45] (d) [1.38, 3.22], very narrow overlap (e) [0.9, 2.10]

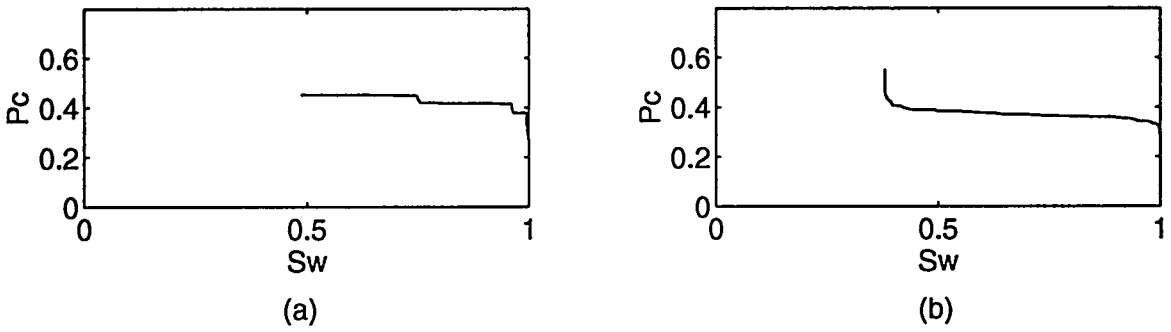

Figure 87: Capillary pressure curves for 2D layered system: (a) injection parallel to the layers (b) injection perpendicular to the layers.

is observed. This jump decreases as the overlap range increases or as r_{Lmax} approaches r_{Hmean}. When $r_{Lmax} = r_{Hmean}$, and for large enough networks (to avoid finite size effect), the jump will disappear.

4.2.5 2D Layered System

We also studied another anisotropic configuration – a 2D layered system. Each row is a layer with one different and randomly distributed mean, with the two direction bonds on this layer having the same mean. We inject from a direction perpendicular or parallel to the layers. Figure 87 shows corresponding P_c curves. The two are different from each other, with the one corresponding to injection perpendicular to the layers having many small steps (jumps), while the one at injection parallel to the layers having a smooth S shape.

4.3 CONCLUSIONS

The above study of capillary invasion in 2D and 3D anisotropic porous media shows that anisotropic porous media do have distinct anisotropic capillary pressure curves. The following conclusions can be stated:

1. Without size distribution overlap in different directions, P_c curves are intrinsically different with a jump varying with the injection angle.

2. With size overlap for either 2D or 3D (LHL) cases, the only major difference is in the irreducible wetting phase saturation. Even porous media with identical size distributions in the two directions exhibit this property when injecting at different angles.

3. With size overlap for 3D (LHH) cases, the P_c step-like jumps still persist. This shows that even with overlap, the anisotropic capillary pressure difference still holds strong.

4. Invasion percolation patterns under different overlap conditions need to be studied further.

5 BOUNDARY EFFECTS IN THE NUMERICAL SIMULATION OF MISCIBLE DISPLACEMENT

Z.M. Yang and Y.C. Yortsos

5.1 INTRODUCTION

Miscible displacements are common in enhanced oil recovery processes. The corresponding flow regimes can be viscous fingering, dispersion, gravity bypassing or channelling depending on the dominance of the particular controling factors.

Viscous fingering is mainly present under conditions of unfavourable mobility ratio and weakly heterogeneous porous media. Dispersion usually sets in very heterogeneous permeable media but without long-range correlations. Gravity bypassing is due to the significant density difference between displaced and displacing fluids. Channelling is mainly due to the result of fluid displacement in media with long-range correlations and strong heterogeneity arising from geological deposition and diagenesis.

Vertical flow equilibrium (VFE) is an asymptotic condition for fluid displacement [115]. Under the VFE concept, the total potential difference in the transverse direction can be ignored and the pressure only changes in the longitudinal direction. Using the VFE concept, the mathematical description can be greatly simplified to facilitate analysis and application. The factor $R_L = (L/H)\sqrt{k_v/k_h}$ is a measure of the VFE condition [48],[118],[115], with $R_L \gg 1$ leading to VFE being good approximation.

In this section, we present numerical solution of the mathematical models of miscible displacement, both for the full model (pressure and concentration) and for the VFE model (concentration only). The major difficulty in solving the convective-dispersive equations of predominantly convective behaviour is numerical dispersion and numerical oscillation. The use of stable low-order difference scheme causes large amounts of numerical dispersion, which may smear out the physical front. While the use of conventional high-order difference schemes may cause numerical oscillation near the concentration front. These problems can be solved by using the Total Variation Diminishing (TVD) method with flux limiter, which is a dynamic weighting between lower and higher order difference schemes, depending on the local flow condition. As a result, high accuracy can be

reached without causing numerical oscillation at the concentration fronts.

Flow regimes can be identified by plotting mixing zone length vs. time or by plotting transversally averaged concentration vs. appropriate time-spatial coordinates (x/t or $(x-ut)/\sqrt{t}$). It was found in our simulations that the use of the physically reasonable no-flow boundary condition at the top and bottom boundaries may result in finger-like flow near the boundaries when the system approach vertical flow equilibrium (VFE) condition. We call this a "boundary effect". It is essentially due to the use of Darcy's law at the boundaries and becomes significant when the system approaches the VFE condition and the porous media have no strong heterogeneity. Due to the contamination caused by this problem, it may limit the use of no-flow boundary condition when the system approaches VFE. The use of periodic boundary conditions may eliminate this problem.

The viscous instability problem of both miscible and immiscible displacements have been numerically simulated by many researchers at conditions far away from VFE [31],[17],[10]. In their results, the boundary effect is not clear. Some authors use periodic boundary conditions, thereby avoiding this problem [88],[122]. Miscible displacement at VFE condition has also been simulated [57]. However, the results are available for strong heterogeneity condition ($V_{DP} \geq 0.5$) and do not show this boundary effect either. Waggoner et al show results at VFE condition [48], where a clear boundary effect can be observed, although the problem is not discussed.

In this section, the condition and reason of this effect are discussed. It is shown that this effect will be severe when the system approaches VFE, viscous forces are dominant and the porous media are weakly heterogeneous.

5.2 MATHEMATICAL MODEL AND NUMERICAL SOLUTION

Under the assumption of first-contact miscible displacement and incompressible fluids, the full model of the process can be described by a mass conservation equation of solvent along with the total volumetric conservation equation and Darcy's law. The dimensionless form of the model is as follows:

$$\phi\frac{\partial C}{\partial t} + \nabla\cdot(\vec{V}C) = \nabla\cdot(D\nabla C) \tag{39}$$

$$\vec{V} = -\frac{K}{\mu}(\nabla P - \rho\vec{g}) \tag{40}$$

$$\nabla\vec{V} = 0 \tag{41}$$

The shape factor R_L is an indicator of the approximation to VFE condition [48],[118],[115]. As long as R_L is greater than a certain value, VFE will be a good approximation to the displacement process from a practical point of view. When the asymptotic analysis is applied, a much simplified mathematical model can be derived as shown below in dimensionless form

$$\frac{\partial C}{\partial t} + \frac{\partial (uC)}{\partial x} + \frac{\partial (wC)}{\partial y} = N_{TD} \frac{\partial^2 C}{\partial y^2} \tag{42}$$

where:

$$u = \frac{\kappa \lambda}{\int_0^1 \kappa \lambda dy} \tag{43}$$

$$w = -\int_0^y \frac{\partial u}{\partial x} dy \tag{44}$$

Initial and boundary conditions are as follows:

$$C(x, y, 0) = 0 \tag{45}$$

$$C(0, y, t) = 1 \tag{46}$$

$$\frac{\partial C}{\partial x}|_{x=1} = 0 \tag{47}$$

$$F|_{y=0} = F|_{y=1} = 0 \tag{48}$$

where $F = wC - N_{TD} \frac{\partial C}{\partial y}$ is the total flux including convection and dispersion. $F = 0$ for no-flow or closed boundary condition, but $F \neq 0$ for periodic boundary condition. Under the VFE condition. the pressure term in Eq.(42) has been cancelled. As a result, Eq.(42) is much simpler than the complete miscible displacement model (Eq.(39) to Eq.(41)), which will be appropriate for simulating viscous fingering details at much less computational costs.

As mentioned, the major numerical problem for solving the convective-dispersive equation of dominating convective nature (Eq.(39) and Eq.(42)) is numerical dispersion and oscillations near concentration fronts [60],[32]. First order difference schemes for the convective term will give stable results, but, unfortunately, with large numerical dispersion. The increase of gridblock resolution will decrease numerical dispersion. However it is not feasible to decrease it to an acceptable level from a practical point of view. Higher order difference schemes often result in oscillations near the concentration fronts although numerical dispersion problem can be ignored. At the present stage, the most appropriate numerical method is the TVD flux Limiter scheme, which is the dynamic

weighting between lower and higher order difference schemes depending on the local flow conditions [9],[106]. By means of this method, a high accuracy can be reached without causing numerical oscillations at concentration fronts. The difference schemes are as follows:

For the time derivative, a first-order implicit scheme is applied

$$\frac{\partial C}{\partial t} \doteq \frac{C^{n+1} - C^n}{\Delta t} \tag{49}$$

For the convective term, the explicit TVD flux limiter scheme is defined

$$\frac{\partial (uC)}{\partial x} \doteq \frac{u^n_{i+1/2} C^n_{i+1/2} - u^n_{i-1/2} C^n_{i-1/2}}{\Delta x} \tag{50}$$

$$C^n_{i+1/2} = C^n_i + \frac{1}{2}\varphi(r_i)(C^n_{i+1} - C^n_i) \tag{51}$$

where, the gradient ratio is given as

$$r_i = \frac{C^n_i - C^n_{i-1}}{C^n_{i+1} - C^n_i} \tag{52}$$

Various flux limiters are used by different authors, but all of them are located in the second-order region [116]. Van Leer's flux limiter is applied here, where the flux limiter function can be difined as:

$$\varphi(r_i) = max\left\{ 0, min(2, \frac{r_i + |r_i|}{1 + r_i}) \right\} \tag{53}$$

The diffusion terms in Eq.(39) and Eq.(42) are discretized by standard central difference scheme. The difference equations obtained are solved simultaneously by an LSOR method. The results prove to be accurate when comparing numerical solutions with analytical solutions of a rectangular wave and a Buckley-Leverett problem (Figure 88 and Figure 89).

5.3 RESULTS AND DISCUSSIONS

5.3.1 Boundary Disturbance Problem

Viscous fingering is a flow instability which occurs when a less mobile oil is displaced by a more mobile agent ($M > 1$), mainly in porous media without long-range correlations and strong heterogeneity. Otherwise, dispersion and channelling dominate. Due to viscous fingering, the sweep efficiency is low and oil production is poor. The detail of viscous fingering flow can be traced by means of high resolution numerical modelling in which the fingering is triggered by disturbing the injection condition or the permeability field. The fingering that develops depends on the strength

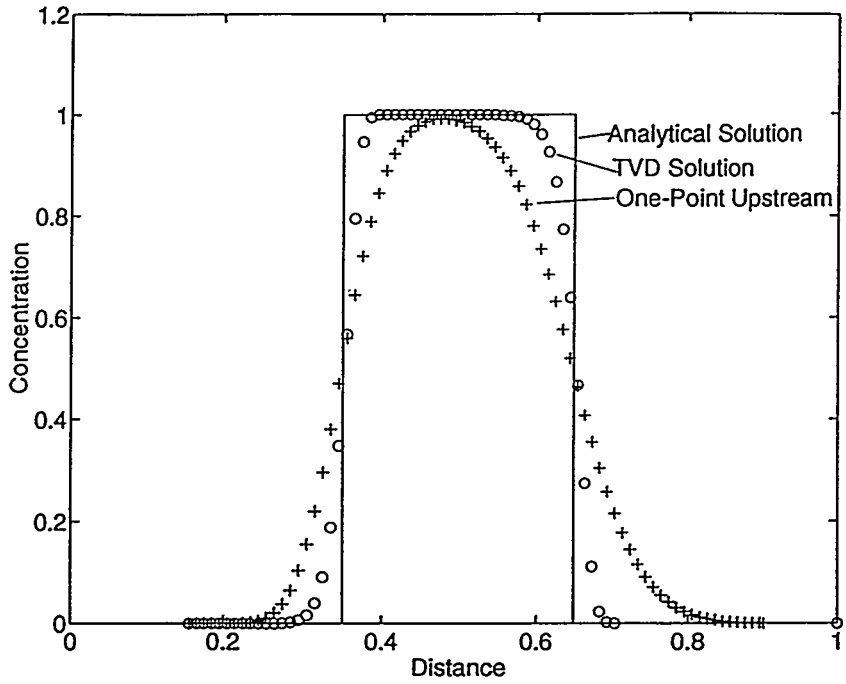

Figure 88: Comparison of numerical and analytical solutions for a rectangular wave.

of viscous instability. It was observed that the enforcement of no-flow boundary condition at top and bottom boundaries causes finger-like disturbance near the boundaries when the process approaches VFE. This disturbance is not significant when the system is far away from VFE, but becomes severe when the system approaches VFE. The possible factors influencing the boundary disturbance problems are shape factor R_L (the scale of the problem and the strength of transverse mixing), mobility ratio M (the strength of viscous instability) and the reservoir heterogeneity factor V_{DP} (the relative importance of viscous force and dispersion due to heterogeneity). The numerical simulation results obtained are discussed below.

Figure 90 shows the effect of the shape factor on this boundary effect. All concentration profiles are at time $0.3PV$ of injection, correspond to an unstable mobility ratio ($M = 10$), both for the full model and the VFE model. Clear viscous fingers are obtained and evident boundary effects are observed. When R_L is small ($R_L \leq 10$), the boundary effect is not significant. However, when the system approaches VFE condition ($R_L > 10$), the finger-like boundary effect becomes severe.

Figure 91 and Figure 92 show the ratio of transverse velocity to transmissibility for $R_L = 1$

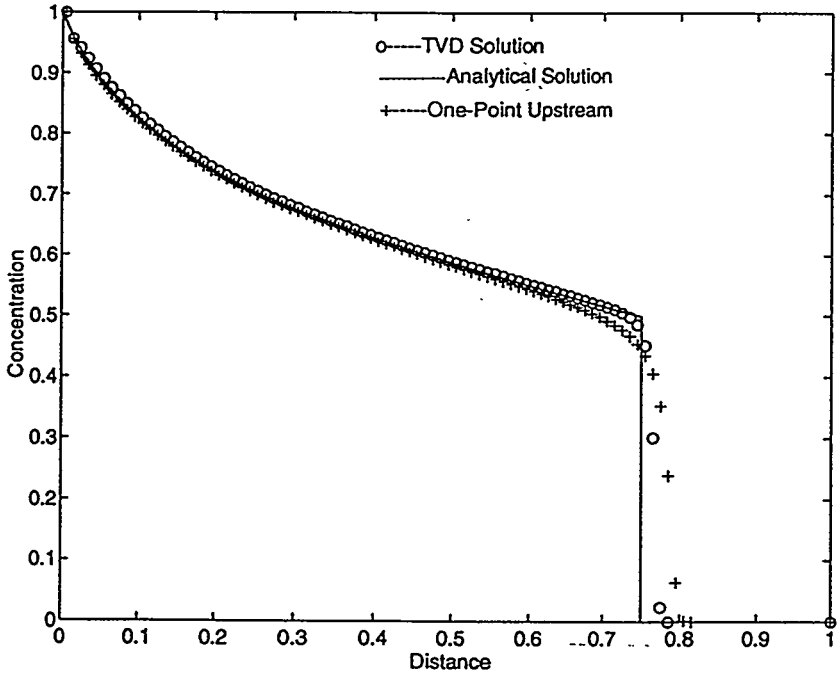

Figure 89: Comparison of numerical and analytical solutions for the Buckley-Leverett problem.

and $R_L = 10$, respectively. It is clear that there are zones with gradually increasing transverse velocity near the top and bottom boundaries if the no-flow boundary conditions are enforced. In a viscous finger, the transverse pressure gradients (and the transverse velocity) at the main part of the finger are closed to zero, flow into and out of a finger mainly occuring at the tip and base parts of the finger [109]. This no-flow condition prevents the finger from disapearing due to the mixing between the inner region (high concentration) and outside region (low concentration) [109]. Thus, the low transverse velocity zone near the boundaries is similar to a finger zone. Due to this similarity, the mathematical model automatically treats this boundary region as a finger-like region, thus causing a boundary disturbance problem. In other words, the boundary effect is due to the development of a viscous instability. When the system is away from VFE condition (R_L small), the contrast of transverse velocity values are small and this boundary problem is not significant (see Figure 91). This may be the reason why no publication mentions this problem, as most publications on numerical simulation of viscous fingering are for the systems away from VFE. On the other hand, when the system approaches VFE condition (R_L large), the increasing mixing in

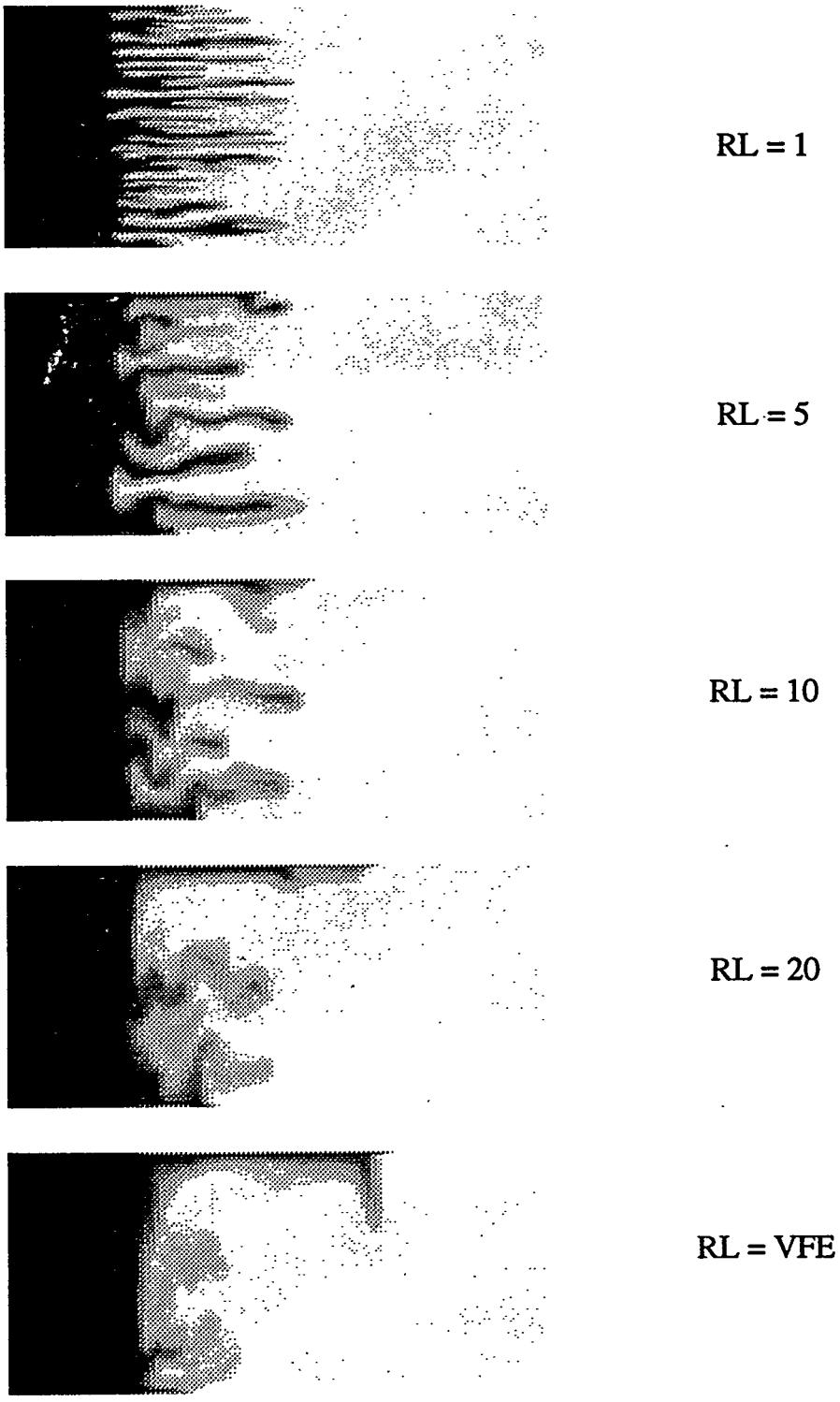

Figure 90. Effect of shape factor RL on the boundary effect (M=10, VDP=0.05.)

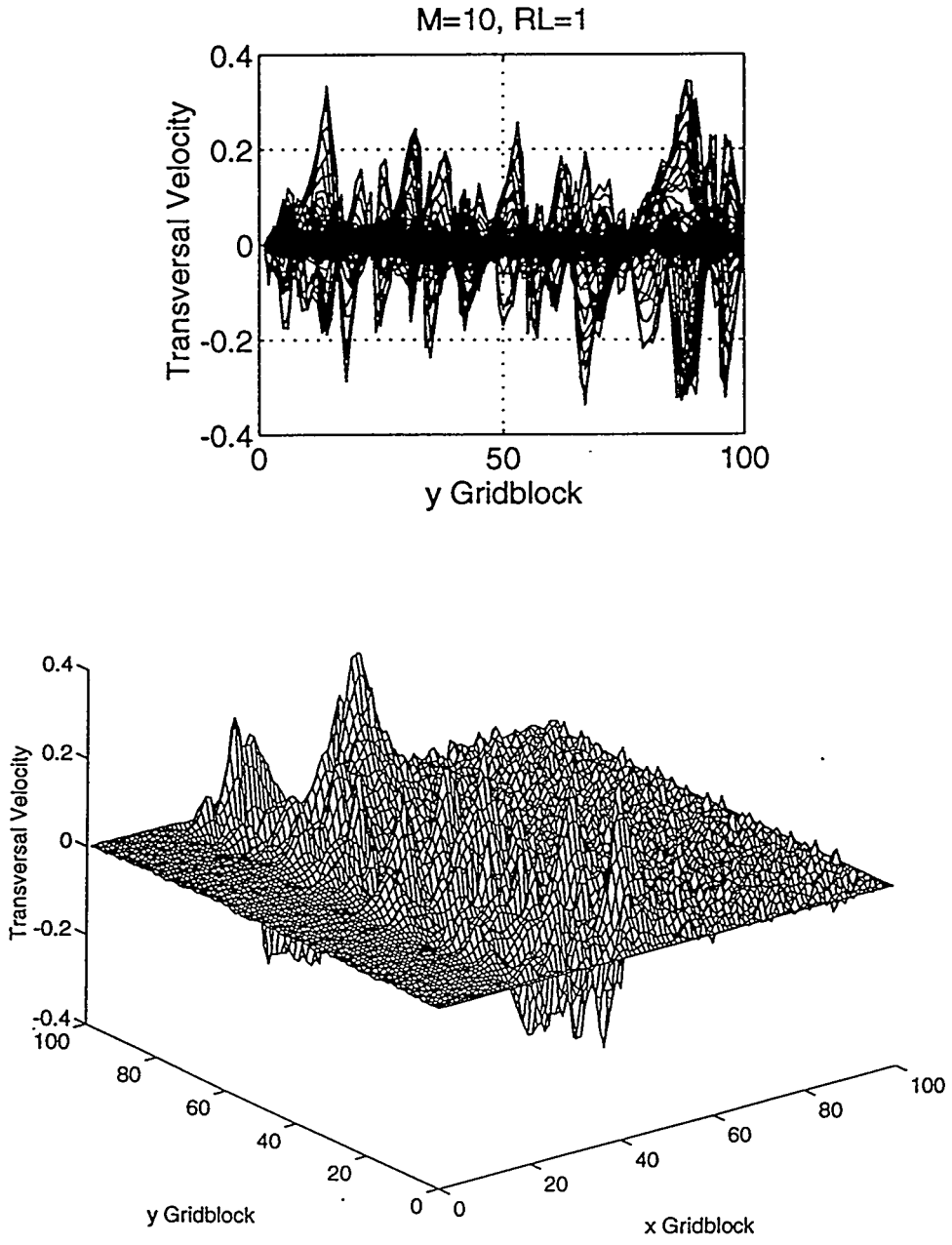

Figure 91: Transverse velocity distribution (no-flow boundary, $V_{DP} = 0.05$).

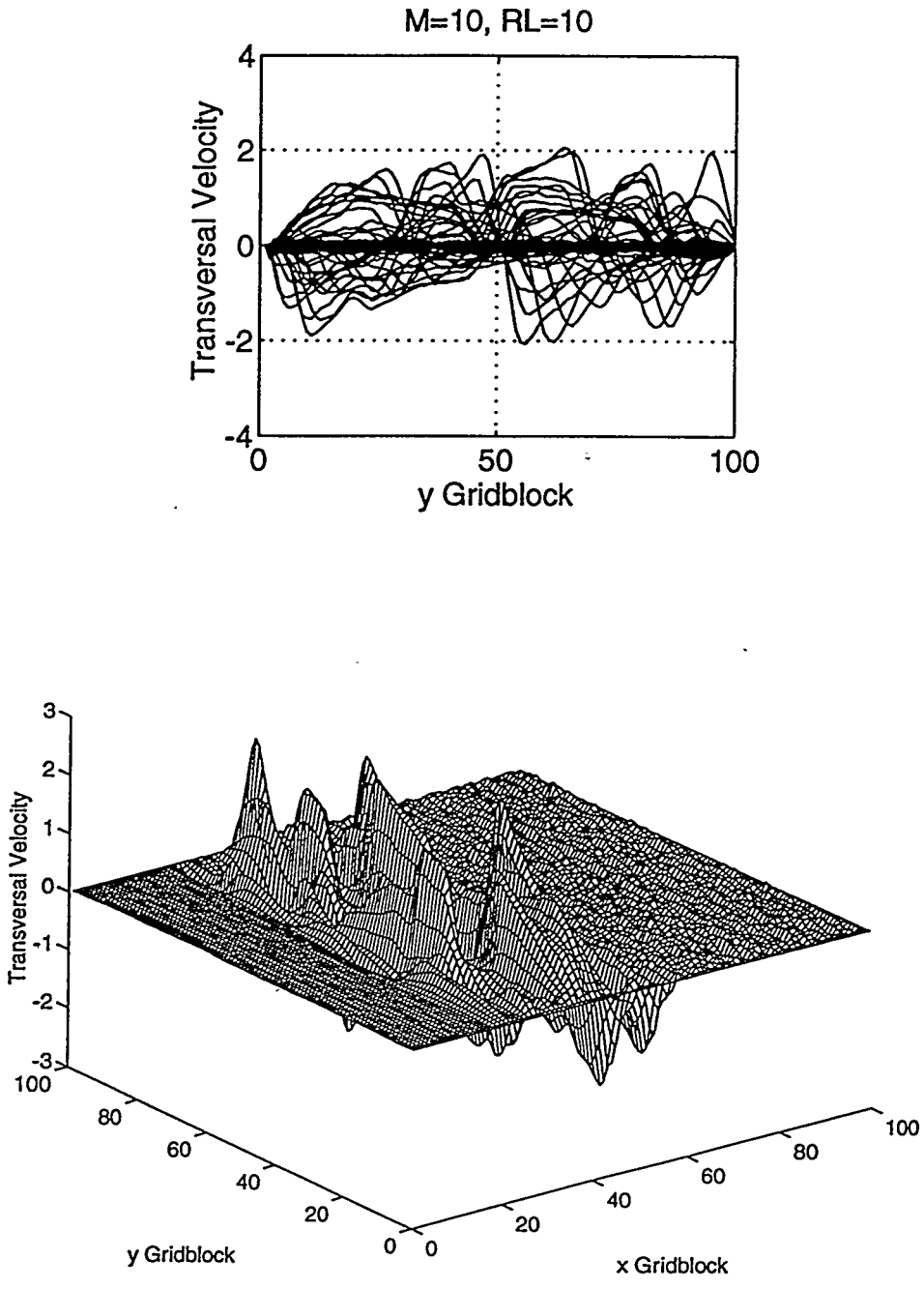

Figure 92: Transverse velocity distribution (no-flow boundary, $V_{DP} = 0.05$).

the transverse direction gives rise to a strong contrast of the transverse velocity, a strong boundary disturbance, therefore an inscreasing boundary effect (see Figure 92).

Figure 93 shows the influence of mobility ratio on this boundary effect, with mobility ratios of 3, 10 and 50. When R_L is small, the boundary disturbance is not significant as mentioned before. When R_L is large, the boundary disturbance effect gets severe. It is evident that for the same shape factor, the boundary disturbance increases with an increase in the mobility ratio. This is the result of the stronger viscous instability at high mobility ratios.

All of the above results are for weak heterogeneity ($V_{DP} = 0.05$), where viscous forces dominate. Figure 94 shows the effect of increasing heterogeneity. When the heterogeneity is increased ($V_{DP} = 0.5$), the relative importance of viscous force decrease and dispersion due to heterogeneity increases. As a result, both viscous fingering and finger-like boundary disturbance shrink. Because the boundary effect is similar to the viscous fingering, it mainly appears at conditions of dominating viscous force. On the other hand, when the system is at strong heterogeneity, the influence of viscous force decrease, both fingering and boundary disturbance decrease and dispersion will get stronger.

Although both mobility ratio and reservoir heterogeneity contribute to the degree of boundary effect, the shape factor R_L is the fundamental controling factor to the problem. It is only when the system approaches VFE conditions that the boundary effect becomes significant.

5.3.2 Periodic Boundary Conditions

Because of the profile contamination caused by the boundary effect, the viscous fingering characterization when a system approaches VFE could not be appropriately obtained from numerical simulation results with no-flow boundary condition. To overcome this problem, we may use periodic boundary conditions. The use of periodic boundary condition implies that in a representative part of a reservoir, the flow into (or out of) the top boundary is equal to the flow out of (or into) the bottom boundary. With a periodic boundary condition, there is no evident boundary as the boundary region is not different from the inner region. As a result, the boundary disturbance problem can be avoided. With the use of a periodic boundary condition, the transverse velocity w can be expressed as

$$w = -\int_0^y \frac{\partial u}{\partial x} dy + \frac{\int_0^1 \frac{1}{\kappa\lambda} \int_0^y \frac{\partial u}{\partial x} dy' dy}{\int_0^1 \frac{1}{\kappa\lambda} dy} dy \tag{54}$$

$M = 3, R_L = 10$

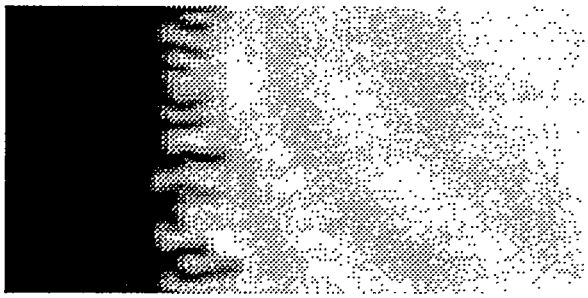

$M = 3, R_L = VFE$

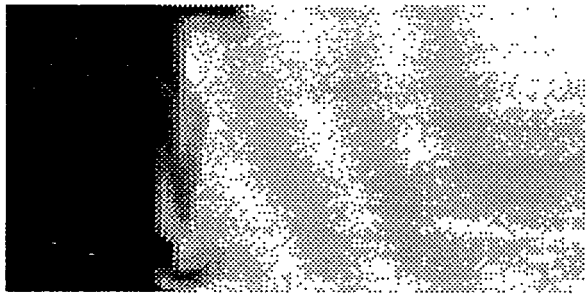

$M = 10, R_L = 10$

$M = 10, R_L = VFE$

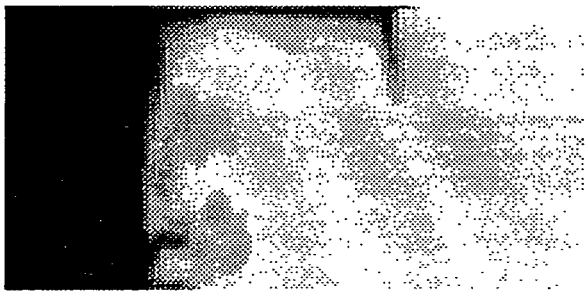

$M = 50, R_L = 10$

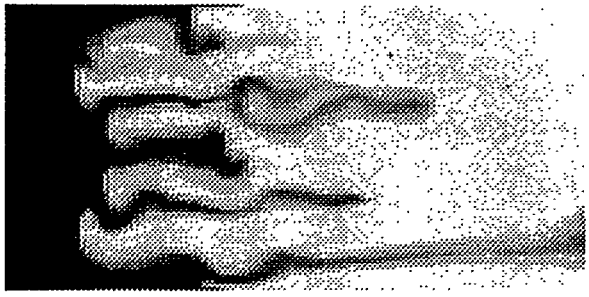

$M = 50, R_L = VFE$

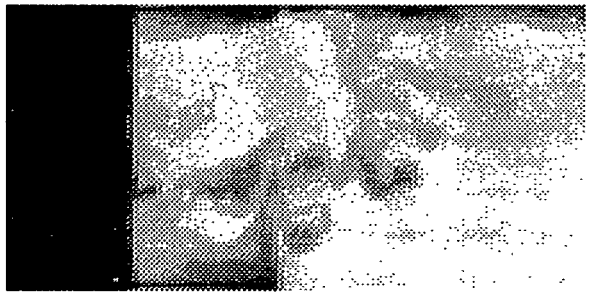

Figure 93: Effect of mobility ratio on boundary effect ($V_{DP} = 0.05$).

$V_{DP} = 0.05, R_L = 10$

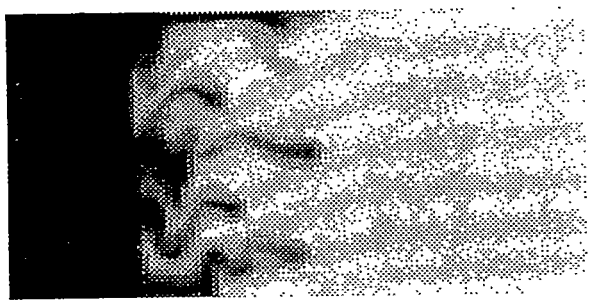

$V_{DP} = 0.50, R_L = 10$

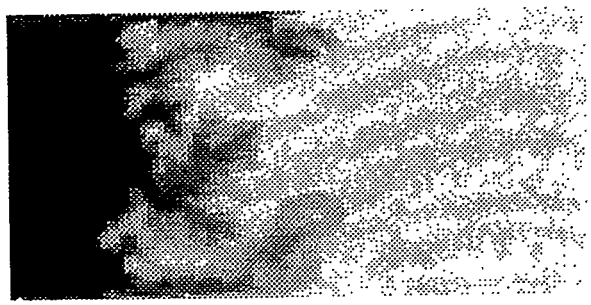

$V_{DP} = 0.05, R_L = 20$

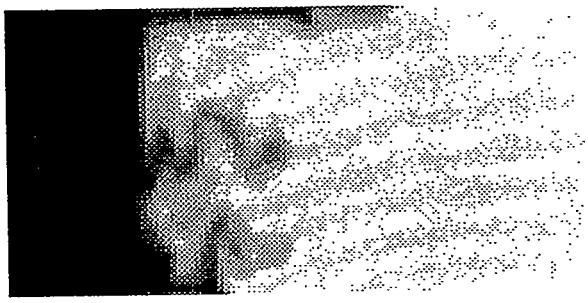

$V_{DP} = 0.50, R_L = 20$

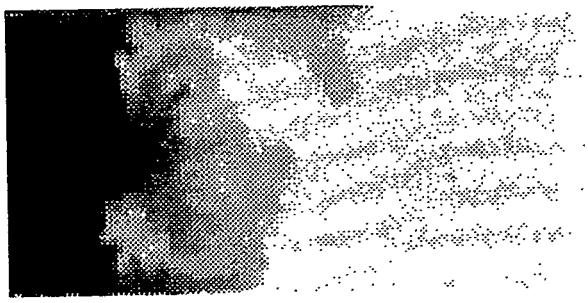

$V_{DP} = 0.05, R_L = VFE$

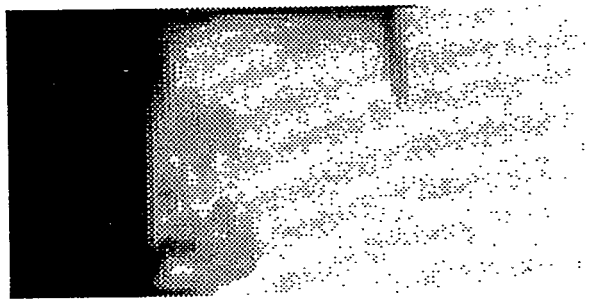

$V_{DP} = 0.50, R_L = VFE$

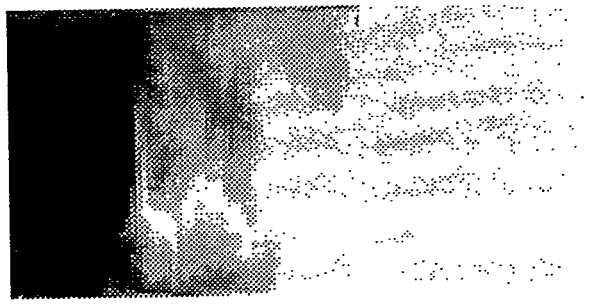

Figure 94: Effect of heterogeneity on boundary effect ($M = 10$).

Figure 95 shows the concentration profile obtained for a periodic boundary condition. It is evident that the boundary disturbance problem (Figure 90) does not occur here. Figure 96 shows a plot of the transverse velocity. Compared with the no-flow boundary condition, there is not a gradual increasing zone of transverse velocity. As a result, the use of periodic boundary condition allow us to avoid the boundary disturbance problem. By this method, the viscous fingering behaviour at VFE condition can be studied and applied to field simulation.

5.4 CONCLUSIONS

Based on the numerical simulation results obtained, it is observed that when the viscous force is dominating and the system approaches VFE condition, the enforcement of no-flow condition at the top and bottom boundaries gives rise to a boundary effect, which limits the application of numerical simulation at the above said condition. This effect is caused by the development of viscous instability. It can be remedied when periodic boundary conditions are applied. This will help the application of numerical simulation when viscous force is dominating and the system is at VFE conditions.

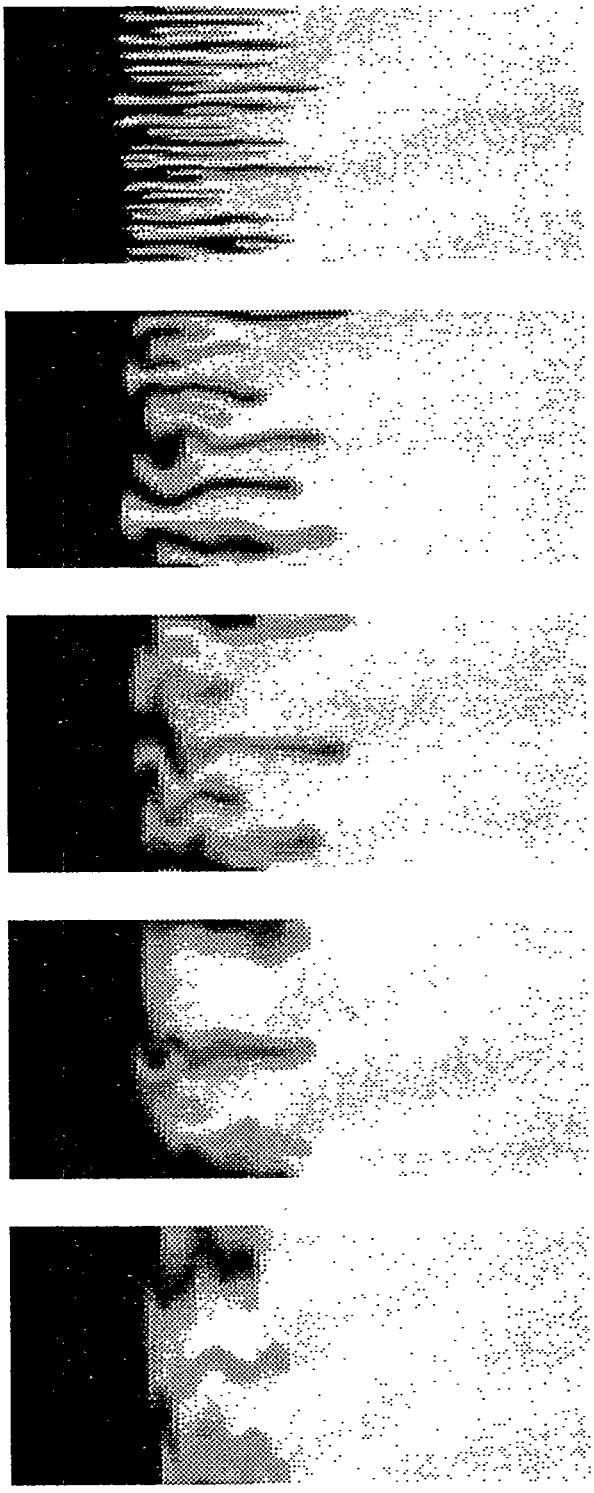

Figure 95. Results of a periodic boundary condition (M=10, VDP=0.05.)

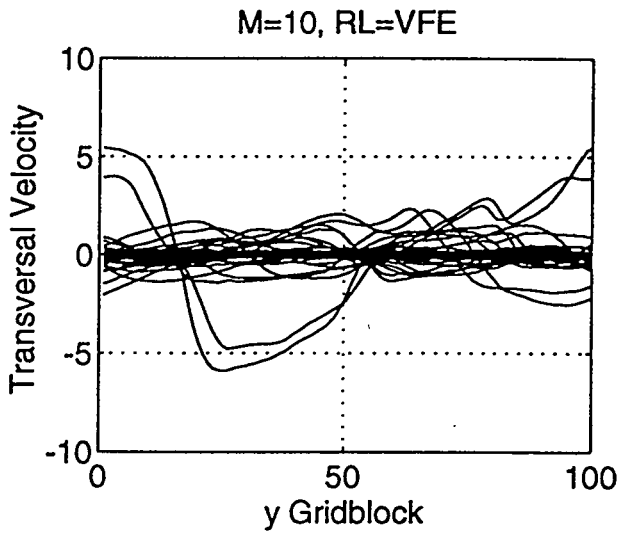

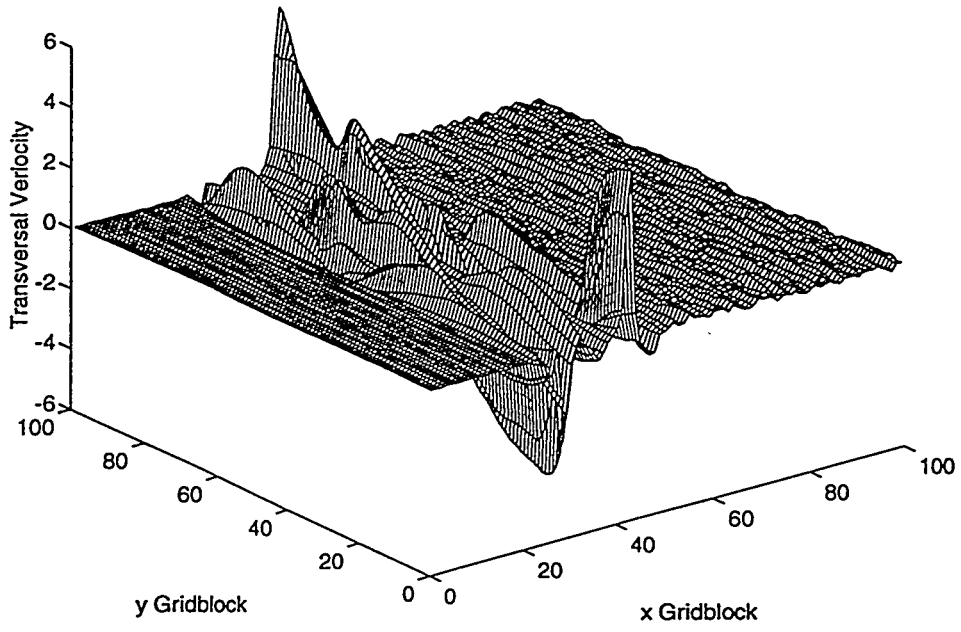

Figure 96: Transverse velocity distribution (periodic boundary condition, $V_{DP} = 0.05$).

6 ASPECTS OF BINGHAM PLASTICS DISPLACEMENT IN POROUS MEDIA

C. B. Shah and Y. C. Yortsos

6.1 INTRODUCTION

Heavy crude oils and tar sands are becoming important energy sources as conventional oil deposits become depleted. Heavy crude oils are found worldwide, but predominantly in USA, Canada, Russia and Venezuela. These are typically petroleum and petroleum-like liquids or semi-solids naturally occurring in porous media [83]. At reservoir flow conditions, heavy crudes have a gas-free viscosity in the range of 100-10000 cp and they often behave as Bingham plastics. Heavy oils are traditionally characterized by a low Hydrogen-to-Carbon ratio and consist of mixtures of oils, resins and asphaltenes [96]. They also generally contain high level of contaminants, such as sulfur, nitrogen and various metals, which tend to accumulate in the heavy asphaltene fraction.

Laboratory tests and rheological studies have indicated that some heavy oils at reservoir conditions display non-Newtonian flow behavior. Based on his studies on bitumen and heavy oil Dealy [24] indicated that there was a mild degree of intramolecular and intermolecular aggregation between longer asphaltene molecules, with a reversible de-aggregation at low shear rates resulting in a viscosity decrease. Recently, Poon and Kisman [86] indicated that mixtures of heavy oil and water with a small amount of sand behave as non-Newtonian and offered possible explanations for shear thinning and shear thickening. Bitumen and heavy oils were found [24, 86] to be pseudoplastic, dilatant or Newtonian depending on temperatures and shear rates. However, a definitive explanation for the non-Newtonian rheology of some heavy oils is not available in the literature. In many heavy oil reservoirs in the Soviet Union it has been reported that their rheological behavior may be approximated as a Bingham fluid, possessing a nonzero yield stress [5]. In such fluids, flow takes place only after the applied pressure gradient exceeds a certain minimum value. Other examples of such flow in porous media include foam, ground water flow in certain clayey soils, drilling and hydraulic-fracturing fluids, which can also be approximated as Bingham plastics [113].

Despite their importance, there is a limited understanding of single- and multi-phase flow of Bingham plastics in porous media. Most of the existing studies are phenomenological and consist of solving effective continuum equations. For example, Wu et al. [112, 113] have investigated the

transient flow of Bingham fluids in porous media, including single- and multi-phase flow, using an *ad-hoc* extrapolation of the single-capillary expressions for Bingham flow. The immiscible displacement of Bingham plastics by a Newtonian fluid (for example in relation to heavy oil production by waterflooding) is another process of practical interest. Nonetheless, not many studies have been undertaken to explore the micromechanics of such processes at a more fundamental level and to relate flow phenomena at different scales. Such studies are necessary not only for single-phase but also for multi-phase flow problems. The single-phase flow of Bingham plastics was discussed in earlier DOE report [98].

To provide a better insight on this problem, we present in this section a pore level simulation of immiscible displacement of Bingham plastics. We have used a network model to represent the porous media and simulated the displacement of Bingham plastics by a Newtonian fluid in a drainage process. Flow patterns were obtained for different values of the yield stress and injection rates and characterized in relation to that of Newtonian displacement [68]. Throughout the analysis, the important assumption is made that the fluid rheology corresponds to flow in capillaries of uniform cross-section. We expect this assumption to be valid at very low flow rates, but to become progressively restrictive at higher rates when the converging-diverging geometry of the porous media dominates the macroscopic characteristics of the flow. In subsequent, we also present immiscible displacement experiments involving Bingham plastics in Hele-Shaw cells and glass bead packs.

6.2 RHEOLOGICAL ASPECTS

The production of heavy crude oil is also sometimes associated with a small amount of suspended sand [86] particles and other solids like asphaltene. The rheology of such fluids does not follow simple Newton's law of viscosity and is much more complicated. These characteristics of heavy oil or bitumen suspensions and emulsions can play a significant role in the design of pumps, pipelines and other processing and production equipments. There have been numerous studies on the rheological behaviour of such fluids both in petroleum and in the chemical engineering literature. A recent review on the rheology of heavy oil and bitumen was presented by Poon and Kisman [86]. It was generally found that these fluids follow either pseudoplastic or dilatant behavior depending on the temperatures and shear rates. The extent of water emulsion and sand affect the rheological characteristics. In general, a mixture of heavy oil (or bitumen) and water with a small amount of

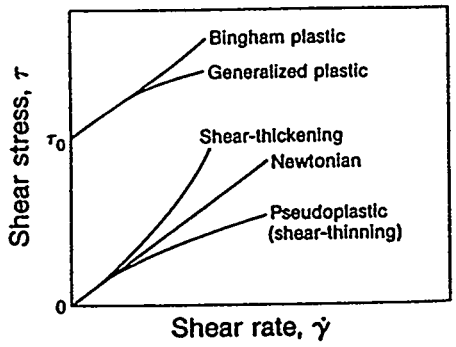

Figure 97: Classification of Bingham Plastics Based on Shear Stress-Shear Rate Behavior.

suspended sand particles behaves as a non-Newtonian fluid at low temperatures. Dealy [24] studied the effect of asphaltene content on the rheological behavior of bitumen. The high-molecular-weight asphaltene fraction in bitumen and heavy oil is responsible for non-Newtonian rheological behavior. The molecular interpretation of such non-Newtonian behavior, as described in [24], is mainly attributed to the intramolecular and intermolecular aggregation and deaggregation of asphaltene molecules. Some heavy oils also exhibit the rheology of Bingham plastics [5]. The mobilization of such fluids requires application of sufficient pressure gradient such that the characteristic yield stress of the fluid is exceeded. The efficient recovery of such fluids from underground reservoirs is generally difficult.

Chaffey [13] reported on the rheology of suspensions, such that Brownian motion and van der Waals steric and electrostatic interactions are negligible at high shear rates, while inertial and deformation, elastic or by surface tension, are negligible at low rates. The rheology of suspensions is influenced by factors like the volume fraction of solid in liquid, the particle arrangements, the distribution of particle sizes and the interparticle forces governing the microstructure [13]. A detailed review on the applications of computer simulations to dense suspension rheology is presented by Barnes et al. [6]. The rheological behavior of non-Newtonian suspensions is system-dependent,

where the liquid is subject to effects due to repulsive forces between the particles, shear-rate dependent osmotic pressure, shear-induced inhomogeneities and particle migration [6]. These effects would make a general rheogram for a suspension somewhat doubtful. Recent computer simulations based on non-equilibrium molecular dynamics (NEMD) are being developed in order to accommodate all the above mentioned effects [80]. NEMD was originally introduced for calculations of Newtonian viscosity, but recently it has been applied to non-Newtonian material, such as polymer melts, slurries etc. [80].

A Bingham plastic is a special type of non-Newtonian fluid which exhibit a finite yield stress at zero shear rate. Also Bingham plastics can be characterized as the extreme case of pseudoplasticity. They are distinguished from Newtonian, and other types of non-Newtonian fluids, by the fact that it requires a finite value of shear stress to initiate flow. Figure 97 shows a schematic of the rheological behavior of Bingham and generalized plastics. Bingham plastics can be represented by following Bingham model [7]

$$\tau = \tau_o - \mu_p \dot{\gamma} \tag{55}$$

where τ and $\dot{\gamma}$ are shear stress and shear rate respectively and τ_o and μ_p are two Bingham model parameters, the yield stress and the plastic viscosity respectively. The plastic viscosity is defined as the shear stress in excess of the yield stress that will induce unit rate of shear. For values of shear stress larger than τ_o, the resistance to the shear caused by the tendency for the particles to build a structure fails completely, facilitating shearing flow to begin. For some practical applications with fluids with yield stress, the plastic viscosity, μ_p, is dependent on shear rate. Such fluids are known as generalized plastics and can be characterized by the Herschel-Bulkley model [1].

6.3 BINGHAM PLASTIC DISPLACEMENT

6.3.1 NUMERICAL SIMULATION

An important practical application of Bingham plastic displacement in porous media is in the case of the recovery of heavy oil by waterflooding. The physics of displacement of such fluids at pore level are not well understood. For an insight, we carried out network calculations at the pore level and obtained displacement patterns under different conditions. A network model of randomly sized

bonds connected by randomly sized nodes was used to model such immiscible displacement in a drainage process. We have used the following standard assumptions for the simulation purpose [68]: (i) Volume calculations apply to pore bodies only, the pressure drop occurring in pore throats. (ii) Throats are filled by either invading or displaced fluids, while bodies may contain both fluids. (iii) The capillary pressure in a throat is inversely proportional to the tube radius, while the capillary pressure drop in a node is negligible. (iv) Inertial and gravity effects are neglected.

In the simulations, we considered the drainage of a wetting Bingham plastic by injecting a non-wetting Newtonian fluid through a face of the network, at a constant injection rate with no-flow boundary conditions applied on the lateral boundaries. The pressure at the outlet face in kept constant. Initially, the network is occupied by a Bingham plastic and the expression for the flow of Bingham plastic in each bond connecting adjacent nodes i and j of the network is given by [7]

$$q_{ij} = \frac{\pi {R_{ij}}^4}{8\mu_o l_{ij}}(1 - \frac{4}{3}(\frac{\tau_o}{\tau_{R_{ij}}}) + \frac{1}{3}(\frac{\tau_o}{\tau_{R_{ij}}})^4)\Delta P_{ij} = g_{ij}(P_i - P_j) \text{ when } \tau_{R_i} > \tau_o, \tag{56}$$

and by

$$q_i = 0 \text{ when } \tau_{R_i} < \tau_o \tag{57}$$

where P_i is the nodal pressure, R_{ij} and l_{ij} denoting radius and length of the capillary respectively.

The pressure field in the network is calculated by applying mass balances at each node as described in the simulation of the single-phase flow [98]. The non-wetting fluid cannot enter a bond unless the pressure difference across that bond exceeds a threshold pressure P_c, given by Laplace law

$$P_c = \frac{2\gamma}{R_{ij}} \tag{58}$$

where γ is the interfacial tension. Hence, a particular bond is invaded if there is no trapping and the capillary pressure condition is satisfied. Once the bond is invaded by a Newtonian fluid, the governing flow equation in the bond changes to Poisseuille's law

$$Q_{ij} = \frac{\pi R_{ij}^4 (P_i - P_j)}{8\mu L_{ij}} = g_{ij}(P_i - P_j) \tag{59}$$

where μ is the viscosity of the Newtonian fluid. In the subsequent steps for pressure calculation, the same iterative method is applied, except that we use a combination of the flow equations (56), (57) and (59) depending on the type of the fluid present in each bond of the network. For maintaining a constant injection rate through the network, the following mass balance at the inlet face must be solved

$$\sum_{k=1}^{M} g_k(P_{in} - P_k) = Q \tag{60}$$

where P_{in} is the pressure at the inlet face, P_k is the pressure at the nodes adjacent to the inlet nodes and Q is the prescribed constant flow rate. P_{in} is calculated iteratively until convergence is reached. The node saturation is updated at each timestep using (59). In time Δt the node saturation $S_i(t)$ increases as follows

$$S_i(t + \Delta t) = S_i + \Delta t V_i \sum_j Q_{ij} \tag{61}$$

where V_i is the volume of node i. The time interval Δt is taken such that only one node is filled at each time step. During the next time step, the calculations are repeated and the pressure fields determined. We typically used a network of small size 25×25.

6.3.2 RESULTS AND DISCUSSIONS

Computer simulation of immiscible displacement in a drainage process was carried out in network-like porous media of a wide bond size distribution [0.01-1.99]. This process is characterized by the two dimensionless numbers [68], the capillary number Ca

$$Ca = \frac{q\mu}{\gamma} \tag{62}$$

and the mobility ratio M

$$M = \frac{\mu}{\mu_o} \tag{63}$$

In the present problem, however, there exists an additional dimensionless number, which we define as the *Bingham number*

$$N_B = \frac{q\mu}{\tau_o k^{1/2}} \tag{64}$$

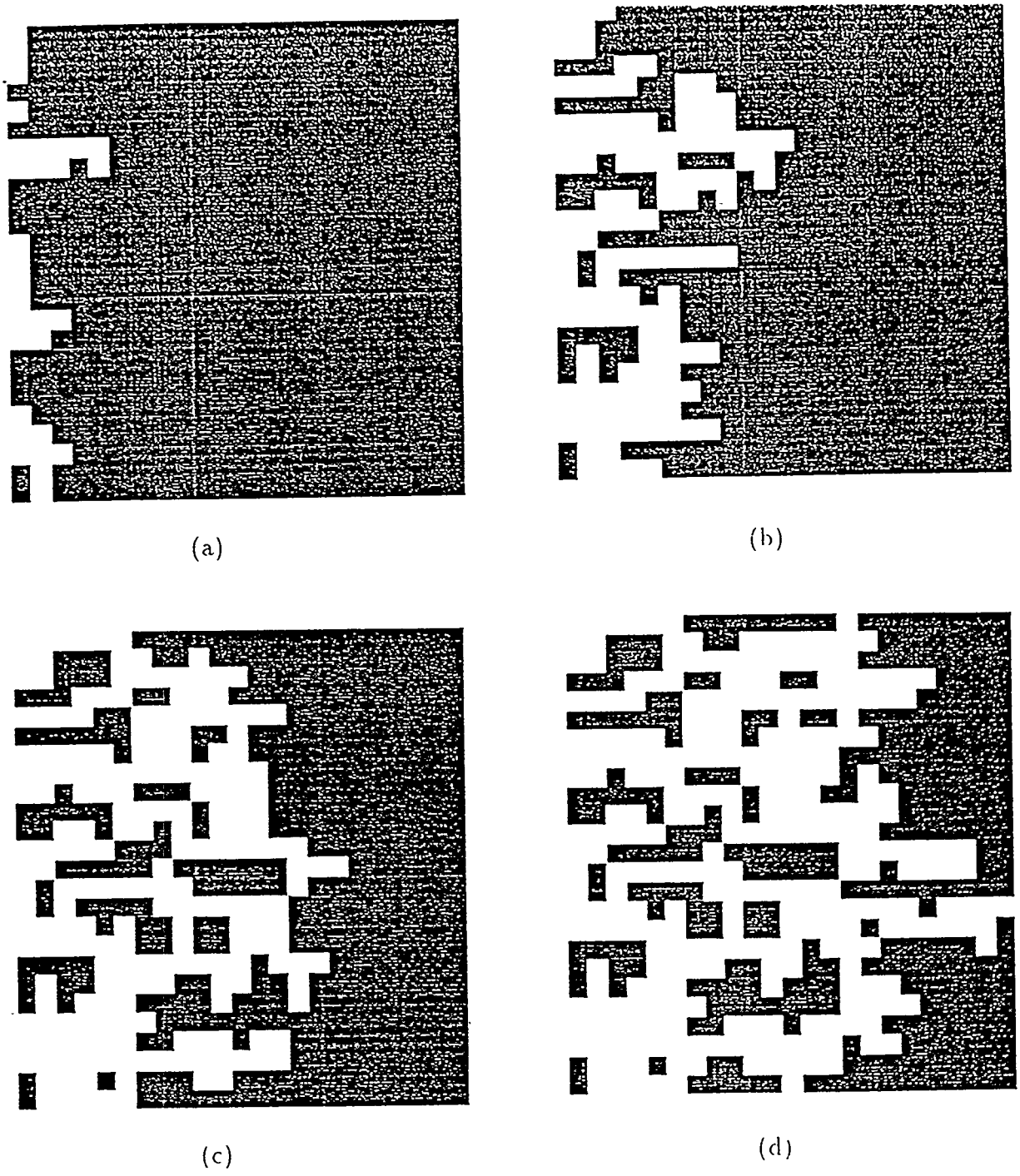

Figure 98: Snapshots of Immiscible Displacement for τ_o=0 $dyne/cm^2$ (N_B= ∞) in the Absence of Capillarity.

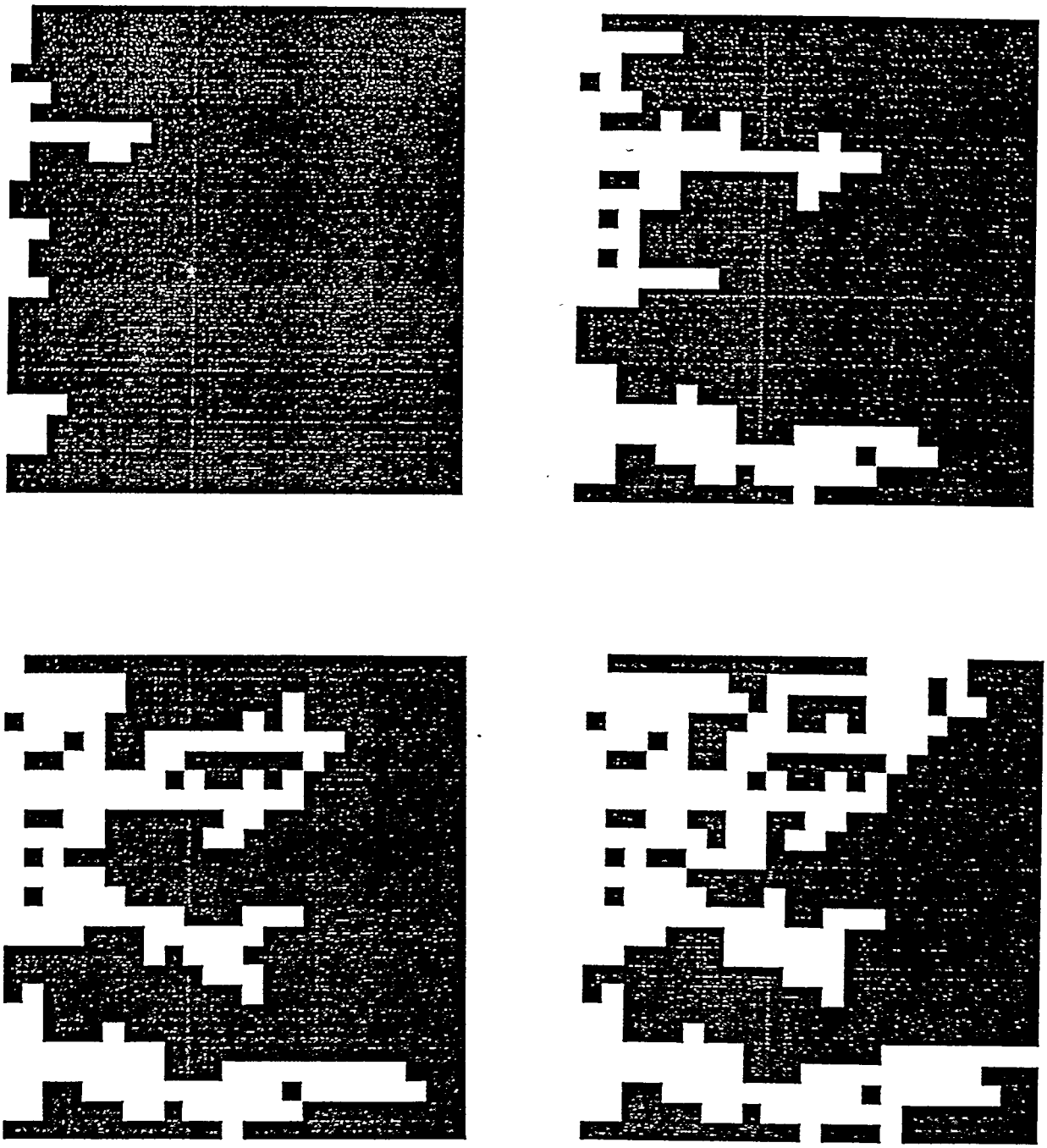

Figure 99: Snapshots of Immiscible Displacement for τ_o=175 $dyne/cm^2$ (N_B= 0.018) in the Absence of Capillarity.

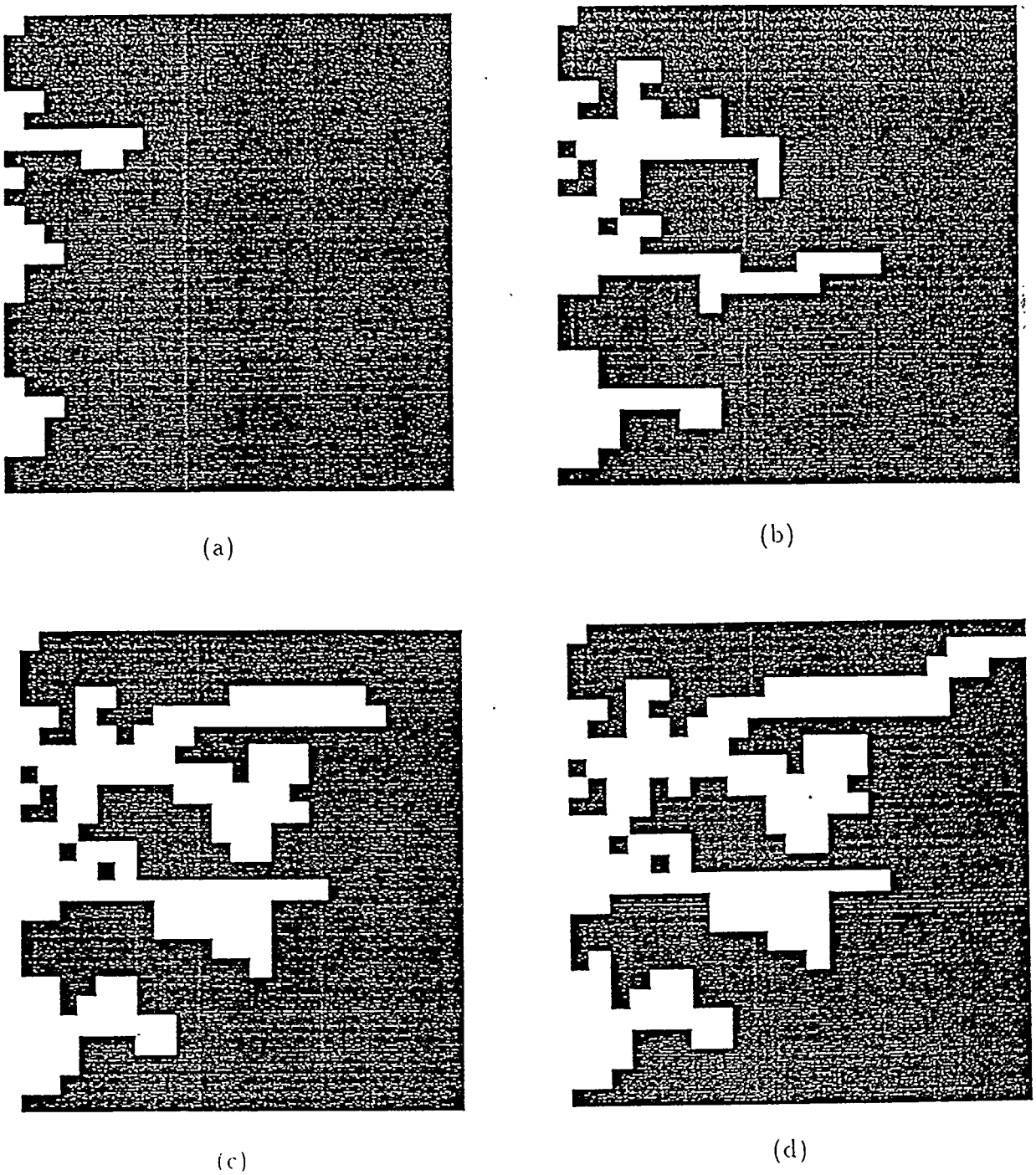

Figure 100: Snapshots of Immiscible Displacement for τ_o=300 $dyne/cm^2$ (N_B= 0.01) in the Absence of Capillarity.

where k is the single-phase permeability. We shall characterize all the patterns to be obtained below in terms of these three numbers.

The first set of simulations probed the high Ca region, where effects of capillarity are negligible. Here we studied the effect of yield stress (N_B). Figure 98 shows displacement patterns at four different times for the case of two Newtonian fluids ($\tau_o = 0$), for a unit mobility ratio (M=1). Because of the disorder in the porous media, a small degree of dispersion is expected. As we increase the value of yield stress to 175 $dyne/cm^2$, ($N_B = 0.018$), however, a somewhat different pattern emerges as shown in Figure 100. The pattern resembles, although it is not identical to, a viscous fingering pattern. We identify a greater degree of dispersion that is similar to viscous fingering and the bypassing of a sizable portion of the initial fluid in place. Figure 99 shows displacement patterns at a higher value of τ_o (=300 $dyne/cm^2$, $N_B = 0.01$). The displacement has all the characteristics of an unstable displacement at large M, with pronounced fingering and large stagnant regions. The flow pattern, however, is not identical to a DLA pattern. Here the mechanism is somewhat different. Because of the distribution of pore sizes, the Bingham plastic flows only in such pores, where the yield stress value can be exceeded and flow can take place. Bonds that cannot flow due to large yield stress requirements behave effectively as having infinitely large viscosity, while those that contain flowing fluid have an effective viscosity that decreases as the flow rate through them increases, thereby moderating somewhat the "fingering" tendency.

The second set of simulations was conducted to investigate the sensitivity of the displacement to regions where capillarity dominates. Figure 101 shows patterns obtained at a value of Ca equal to 2.0×10^{-5} for a unit mobility ratio and for different values of the Bingham number. The first pattern at zero yield stress (infinite N_B) has many of the characteristics of a percolation pattern, namely the existence of trapped regions and a ramified structure as expected. As the yield stress increases, however, additional trapping is observed (Figure 102, where $N_B = 1.0 \times 10^{-4}$). This pattern is certainly not the same with percolation, as in addition to capillarity the yield stress requirement needs to be exceeded for the occupancy of any bond. Here, the important difference from the typical percolation problem is that regardless of how small Ca is, viscous effects enter the problem *de facto*, as certain bonds behave with effectively an infinite viscosity. The analysis of this interesting regime is currently in progress. Although we have not examined the sensitivity to the viscosity ratio M, we expect a sensitivity similar to that for the Newtonian case.

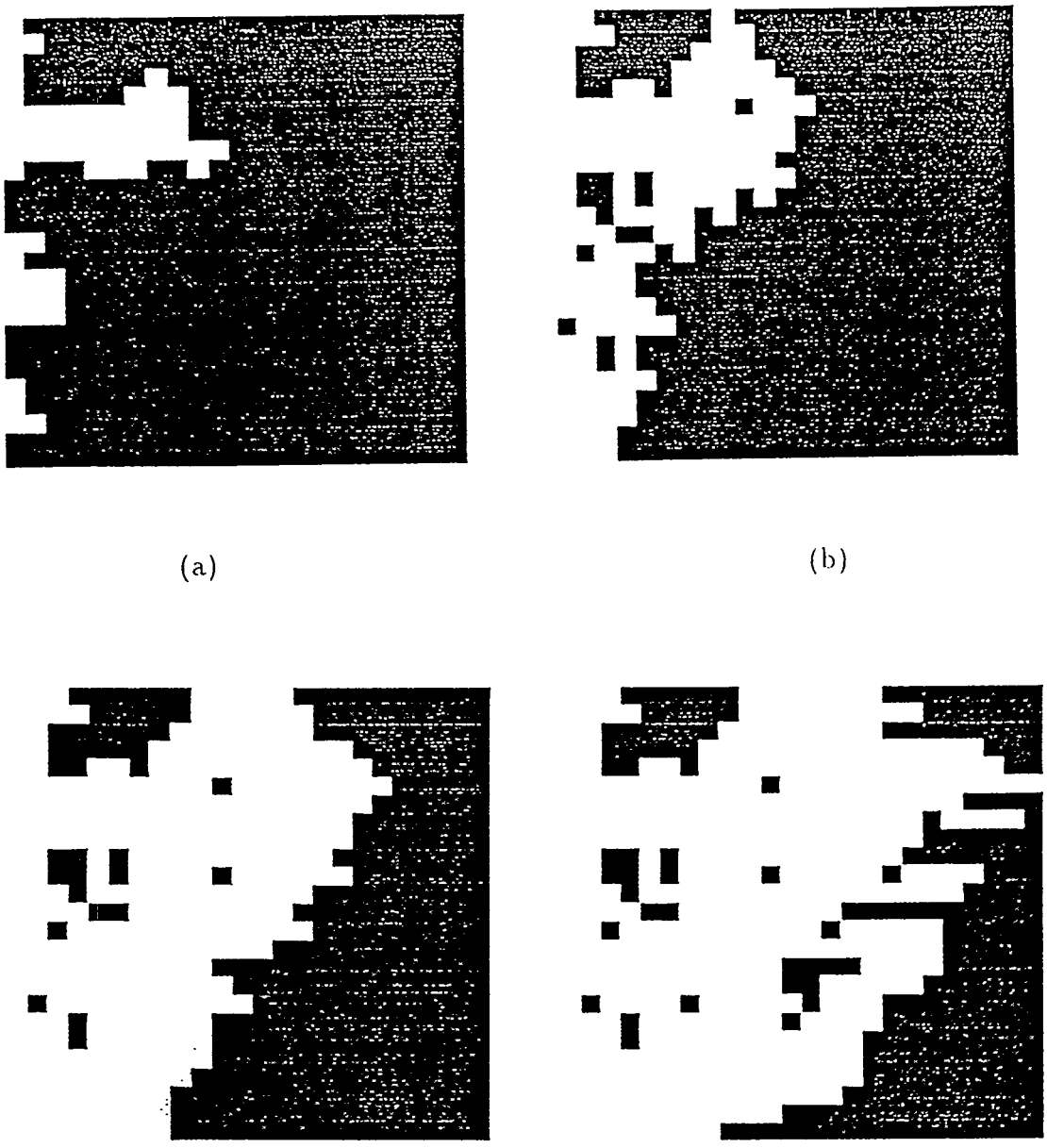

Figure 101: Snapshots of Immiscible Displacement for τ_o=0 (N_B= ∞ and Ca=2.0 $\times$ 10^{-5}).

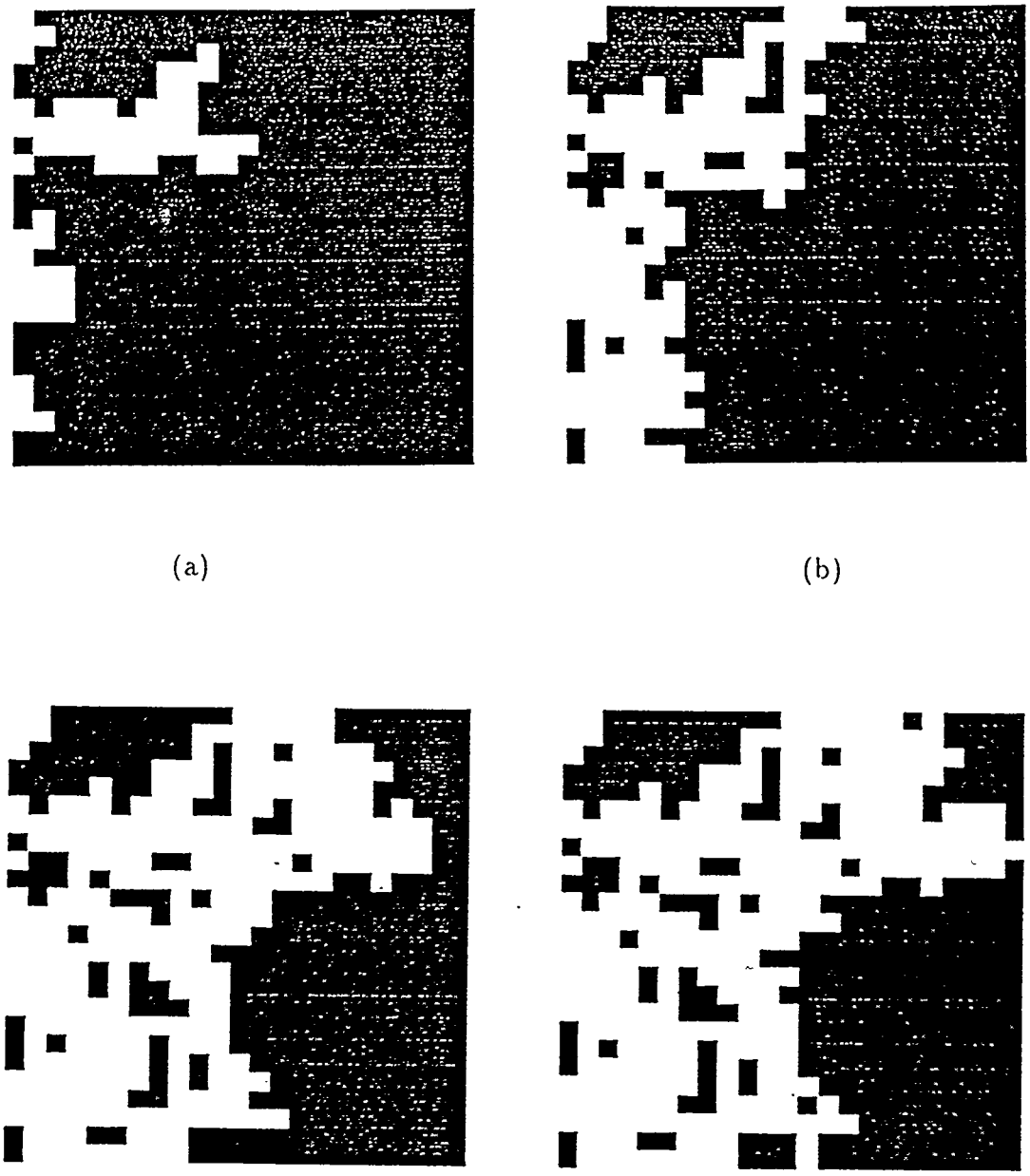

Figure 102: Snapshots of Immiscible Displacement for τ_o=300 (N_B= 1.0×10^{-4} and Ca=2.0×10^{-5}).

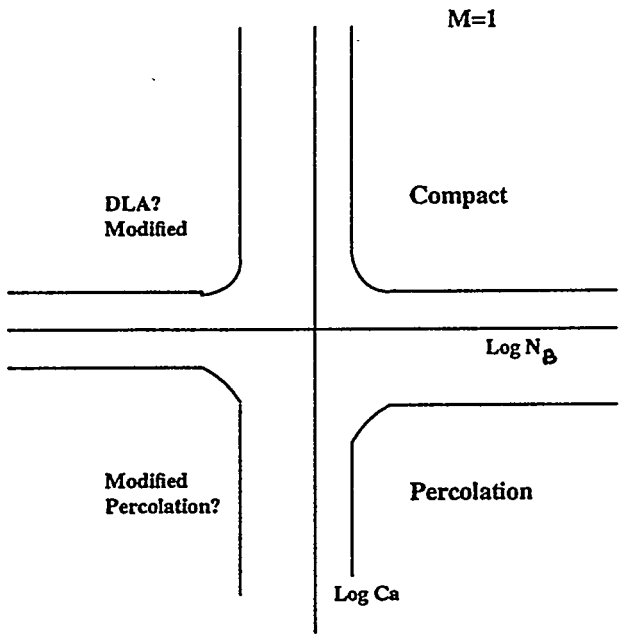

Figure 103: Phase Diagram for Bingham Plastic Displacement.

The behavior of the overall process can be summarized in a phase diagram similar to that Newtonian displacements, as described by Lenormand et al. [68]. Now, however, a third coordinate expressing variations in the Bingham number, N_B, needs to be introduced (Figure 103). In our study we have only probed the case $M = 1$. In such a diagram (Figure 103), we expect the following: For large N_B, a compact pattern at large Ca and a percolation pattern at low Ca. For small N_B, we expect a viscous-fingering-like pattern at large Ca and a new percolation type pattern at small Ca. The particular patterns, their limiting boundaries and the effect of M are currently under study. However, the general result can be stated that the efficiency of the displacement decreases as the yield stress increases.

6.4 FLOW VISUALIZATION

6.4.1 BACKGROUND

The randomness and complicated geometry of the porous media make the problem of flow complicated and mathematically difficult in some cases. Experiments with real porous media are also not very illustrative in terms of understanding the pore level phenomena, particularly in the case of immiscible fluids. To overcome this difficulty, flow visualization experiments, using transparent Hele-Shaw cells, glass bead packs and glass micromodels have been successfully employed in reservoir engineering for many years [53]. Such geometries have been traditionally used two-dimensional flow in a porous medium, thus they lack important 3-D aspects. Nev they are of fundamental interest for establishing mechanisms.

A large amount of the visualization work has been done on simple immiscible displacements involving fluids which generally follow Newtonian rheology. A great deal of valuable information has been obtained regarding the various regimes, portrayed in the form of phase diagram using two dimensionless numbers, capillary number, and viscosity ratio [68]. Studies with micromodels, also for Newtonian fluids, have been very useful for researchers to understand pore-level flow processes in porous media. An excellent recent summary can be found in [44].

On the contrary, very little visualization work has been done where one or both the fluids are of non-Newtonian type. Nittmann et al. [81] reported immiscible displacement of non-Newtonian polysaccharide solution by water in a Hele-Shaw cell to characterize the structure of a viscous finger. Daccord et al. [20] carried out similar types of experiments using radial Hele-Shaw cells

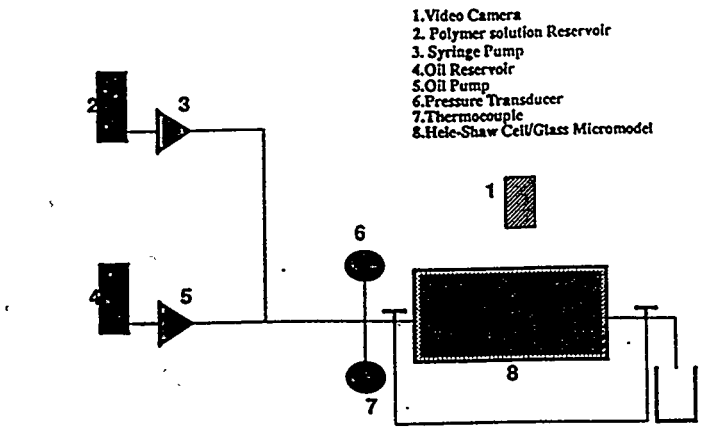

Figure 104: Schematic of the Experimental Unit

in order to avoid effects of boundary conditions. Stoneberger and Claridge [104] recently carried out miscible displacements involving shear-thinning fluids in a Hele-Shaw cell. In their study, they used two types of polymers (Xanflood and Pusher 1000) for making polymer solutions and carried out five experimental runs: (1) Newtonian fluids displacing Newtonian fluids with varying mobility ratio, M; (2) pseudoplastic fluids displacing Newtonian fluids; (3) pseudoplastic fluids displacing pseudoplastic fluids; (4) Newtonian fluids displacing pseudoplastic fluids; and (5) pseudoplastic graded banks displacing a Newtonian fluid. The purpose of the study was to device a method for the design of graded viscosity banks of pseudoplastic fluids in five-spot patterns for EOR processes. To the best of our knowledge there is no study reported where visualization experiments have been carried out using Bingham plastics in immiscible displacements. This has been undertaken here, with main objective of the visualization in Hele-Shaw cells and glass bead pack models. The study is expected to shed light on the displacement of heavy oils with finite yield stress.

6.4.2 EXPERIMENTAL APPARATUS

The Hele-Shaw cell was of dimensions 18 cm x 7.6 cm x 0.05 cm and consisted of two glass plates of 1/2 inch thickness. The pyrex glass plates were separated by a silicon rubber spacer. Two ports

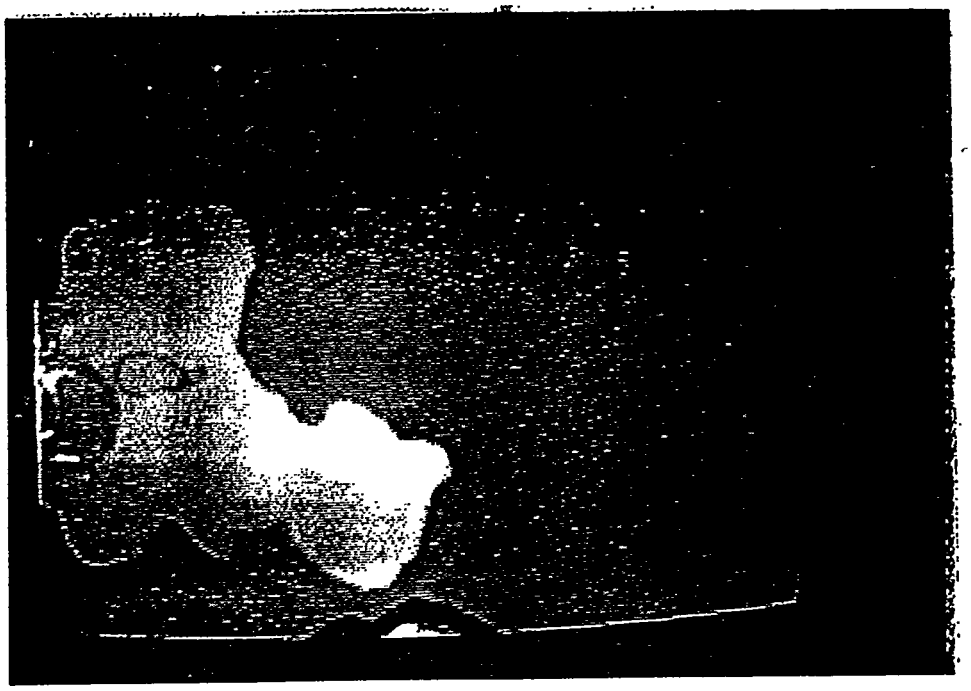

Figure 105: Displacement of Mineral Oil by Water at the rate of 2.3 cc/min in the Hele-Shaw Cell: Snapshot I

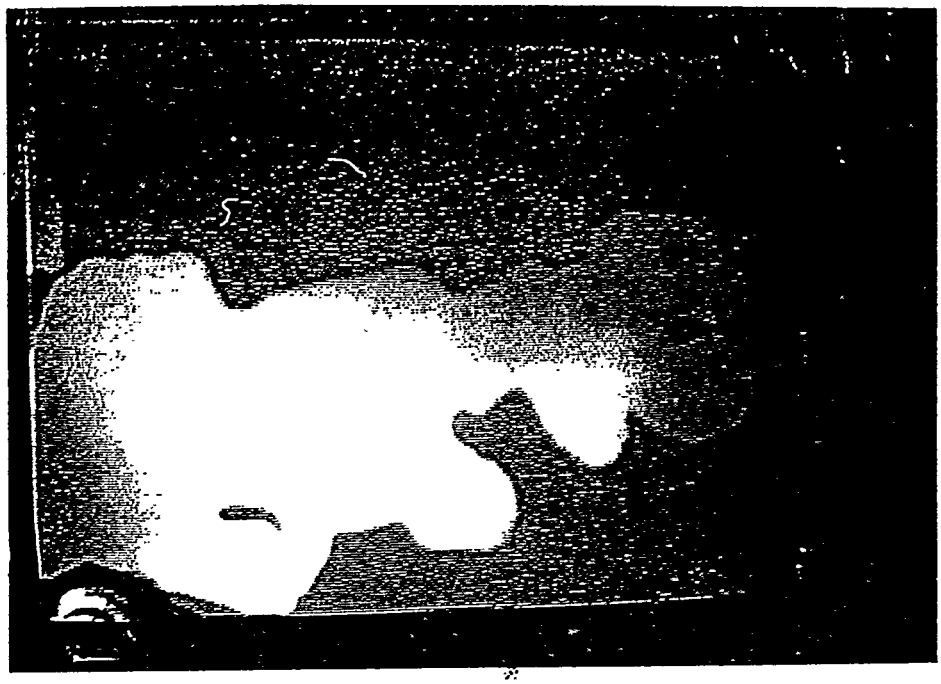

Figure 106: Displacement of Mineral Oil by Water at the rate of 2.3 cc/min in the Hele-Shaw Cell: Snapshot II

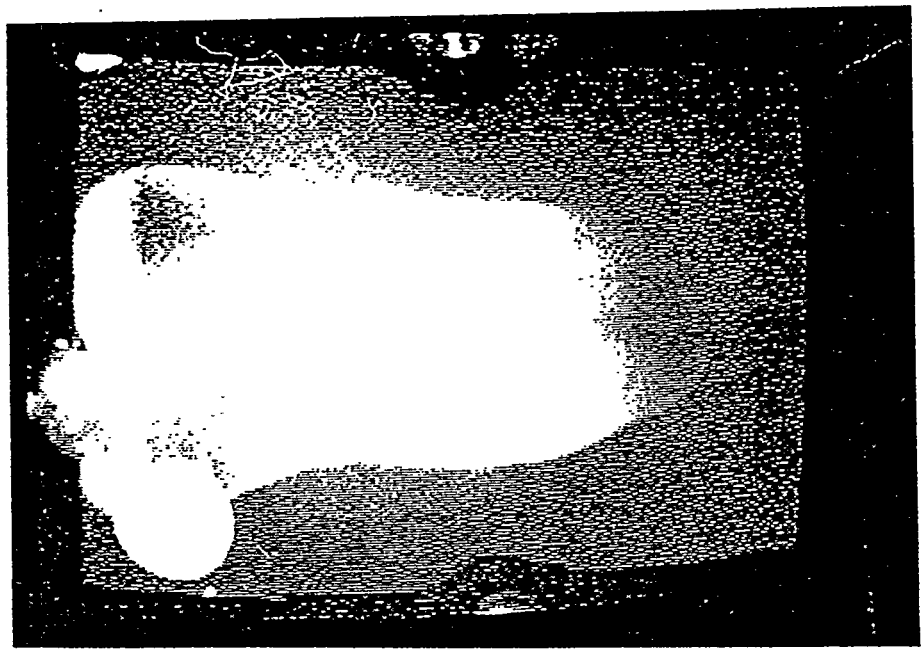

Figure 107: Displacement of Bingham Plastic (BP1) by Air at the rate of 3.08 cc/min in the Hele-Shaw Cell: Snapshot I

were provided on the top plate, one for injection, the other for production. A schematic of the experiment set up is shown in Figure 104 for both the Hele-Shaw cell and the glass bead pack. A syringe pump was used to provide constant displacement rate during the experimental runs. In the glass bead pack models, one layer of closely packed glass beads was sandwiched between two flat plates of same dimensions as used for Hele-Shaw cells.

6.4.3 EXPERIMENTAL FLUIDS

Two types of water-based mud were used for representing Bingham plastic rheology. They were supplied by Drilling Specialties Company, Oklahoma and their characteristic Bingham model parameters are reported subsequently. The Newtonian fluids consisted of kerosene, high viscosity mineral oil or air. Red dye was added to the kerosene and the mineral oil in order to visualize the interface movement clearly during the course of the experiments.

Actual flow conditions are not kn ıghout the path of water- based muds, but virtually all water-based muds that contain c. ın a quasi-Bingham plastic manner [21]. The slope of the straight-line portion of the stress-strain curve represents plastic viscosity and the intercept

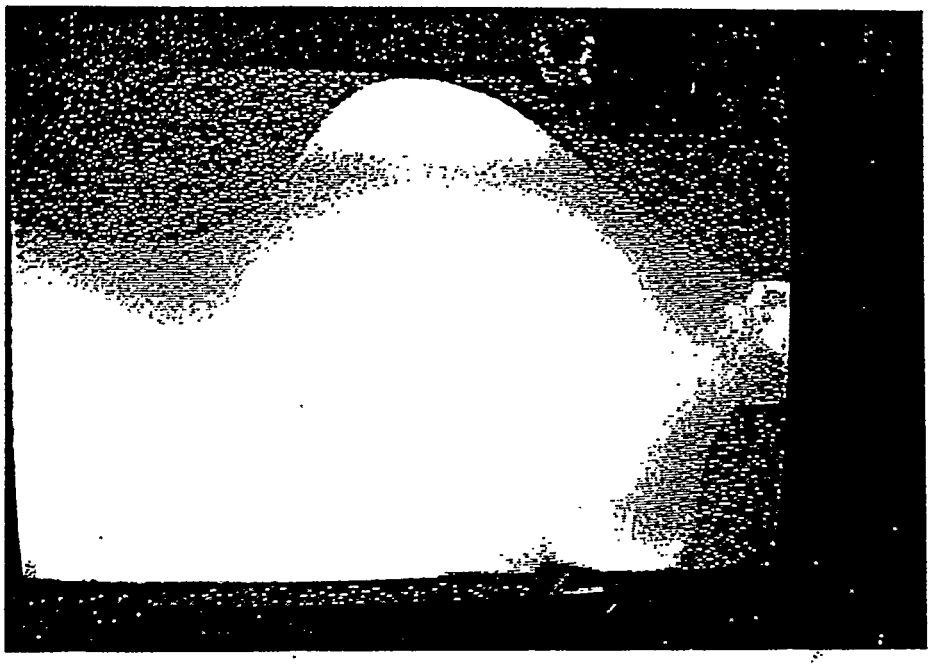

Figure 108: Displacement of Bingham Plastic (BP1) by Air at the rate of 3.08 cc/min in the Hele-Shaw Cell: Snapshot II

value at zero shear is the yield point. In a given mud system, a change in plastic viscosity usually represents a change in the solid content. Similarly, the yield point is an indication of interparticle attraction while the mud is moving. The water-based mud system will fairly represent the class of heavy oils which follow Bingham plastic rheology as these heavy oils contain suspended solid particles in terms of sand and asphaltene.

6.4.4 RESULTS AND DISCUSSIONS

We present some of the interesting experimental results for immiscible displacement of Bingham plastics both in the Hele-Shaw cell and the glass bead packs. We take as base case the displacement of heavy mineral oil (21CP) by water at the rate of 2.3 cc/min in the Hele-Shaw cell. In the subsequent pictures, taken from a still videotape, displacement is from left to right. As shown in Figures 105 and 106, water injection into high viscosity mineral oil leads into viscous fingering and tip splitting, as expected and reported in Newtonian displacement. In the colored pictures, red is the color of original oil, and bright white is water.

Figure 107 shows the initial part of the displacement for one Bingham plastic, BP1 (τ_o =

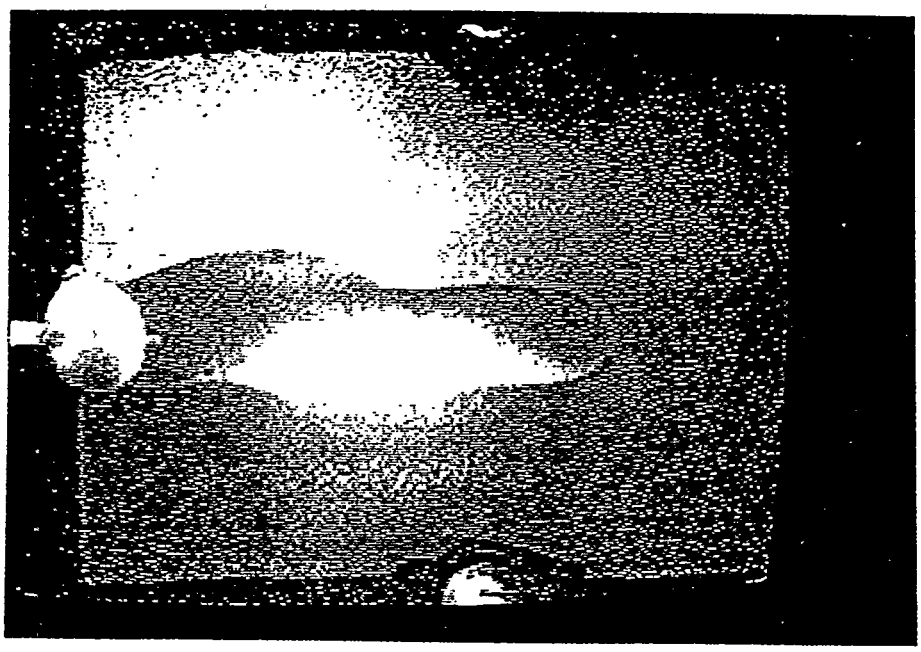

Figure 109: Displacement of Bingham Plastic (BP2) by Air at the rate of 3.08 cc/min in the Hele-Shaw Cell: Snapshot I

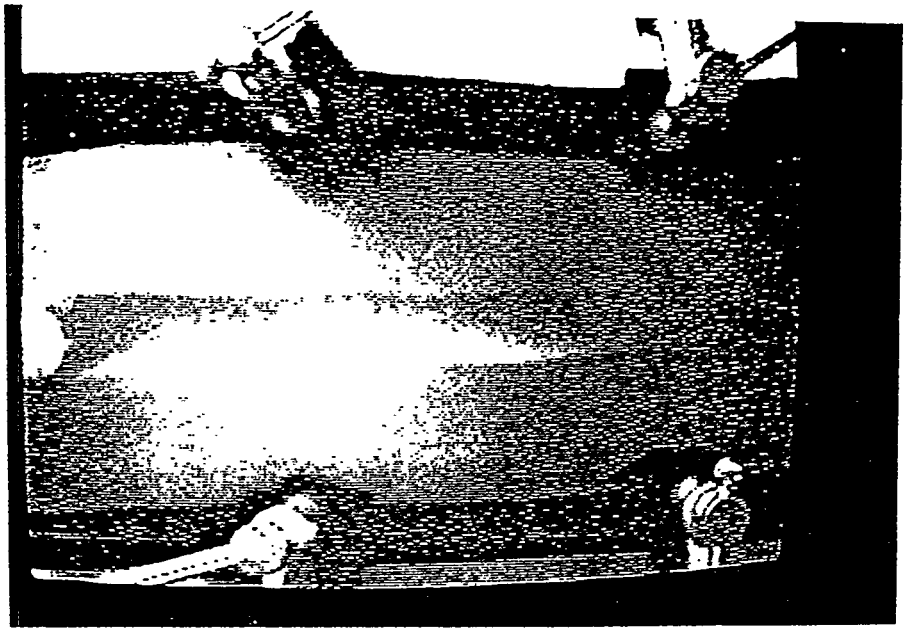

Figure 110: Displacement of Bingham Plastic (BP2) by Air at the rate of 3.08 cc/min in the Hele-Shaw Cell: Snapshot II

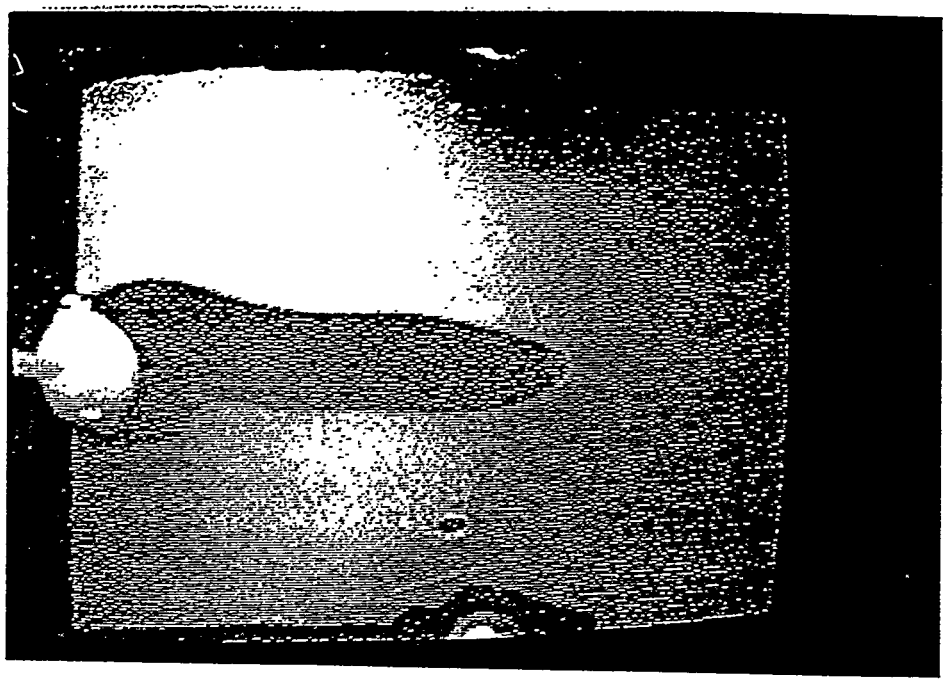

Figure 111: Displacement of Bingham Plastic (BP2) by Kerosene at the rate of 3.08 cc/min in the Hele-Shaw Cell: Snapshot I

$12lb/100ft^2, \mu_O = 13cp$) by air at 3.08 cc/min. In this Figure, brown is the color of BP1 and white is air. The air penetrates through BP1 as a finger and breaks through as shown in Figure 108. Figures 109 and 110 indicate the initial part of the displacement and breakthrough for the other Bingham plastic, BP2 ($\tau_o = 25lb/100ft^2, \mu_o = 19cp$) by air at the same flow rate as above. The fingering tendency not only remains but also this finger is smaller and sharper compared to that in the BP1 displacement. The finger penetrates through BP2 and rapidly breaks through leaving a large portion of the initial fluid in place. The displacement of BP2 was also carried out with kerosene and heavy mineral oil at the same flow rate of 3.08 cc/min. Figures 111 and 112 show colored pictures of the displacement patterns with kerosene injection, where we also observe one sharp finger flowing through BP2 and quickly breaking through. Similar results are also obtained from the immiscible displacement of BP2 by heavy mineral oil (Figures 113 and 114). The initial yield stress of Bingham plastic makes this displacement difficult even when viscosity ratio is almost unity.

The next set of results was obtained using glass bead-pack models for both BP1 and BP2 at the flow rate of 3.08 cc/min. In all subsequent colored pictures, brown represents the Bingham

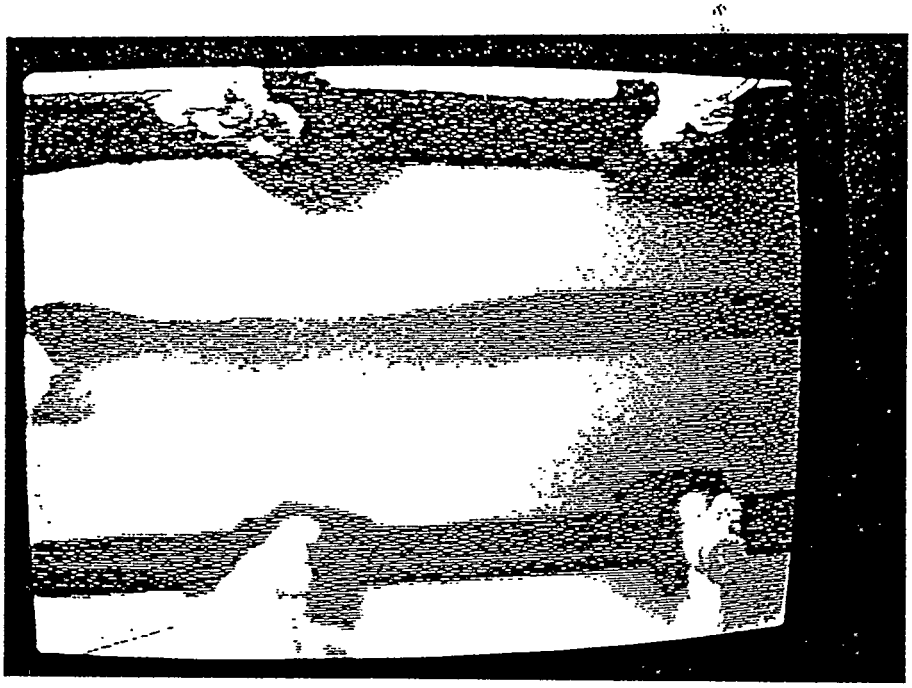

Figure 112: Displacement of Bingham Plastic (BP2) by Kerosene at the rate of 3.08 cc/min in the Hele-Shaw Cell: Snapshot II

plastics, and red the kerosene. Figure 115 shows the initial stage of the displacement of fluid BP1 where kerosene is advancing slowly through glass bead pack model. The pattern is developing quite similar to viscous fingering. The subsequent stages as shown in Figure 116 and 117 show such trend until breakthrough. The overall pattern as shown in Figure 117 resembles viscous fingering and the displacement is unstable. The interesting displacement results are obtained for fluid BP2 under the same displacement conditions. Figures 118 - 120 indicate such displacement at four different stages. As shown, a single sharp finger emerges right from the beginning of the initial displacement and penetrates through the high yield stress fluid BP2, leaving most of the initial fluids in place. Figure 120 shows one thin finger from the injection port to the production port through fluid BP2. The value of higher yield stress, τ_o makes the displacement difficult and the unrecoverable region in the glass bead-pack model is large in such cases [5].

6.4.5 COMPARISON WITH SIMULATIONS

To compare the experimental results for fluids BP1 and BP2 in the glass bead pack models, numerical simulations were subsequently carried out. The network model was used to represent the glass

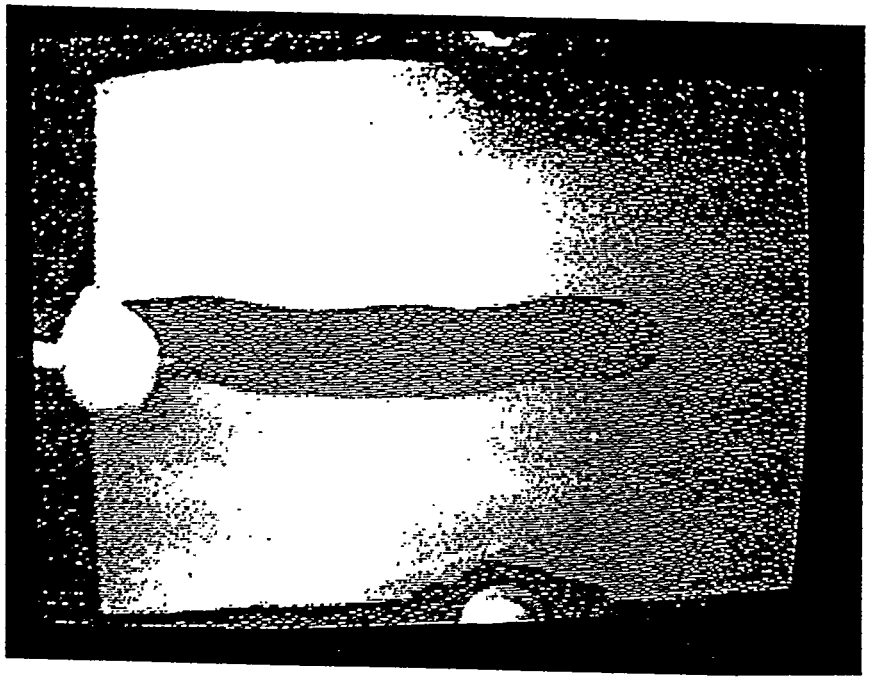

Figure 113: Displacement of Bingham Plastic (BP2) by Mineral Oil at the rate of 3.08 cc/min in the Hele-Shaw Cell: Snapshot I

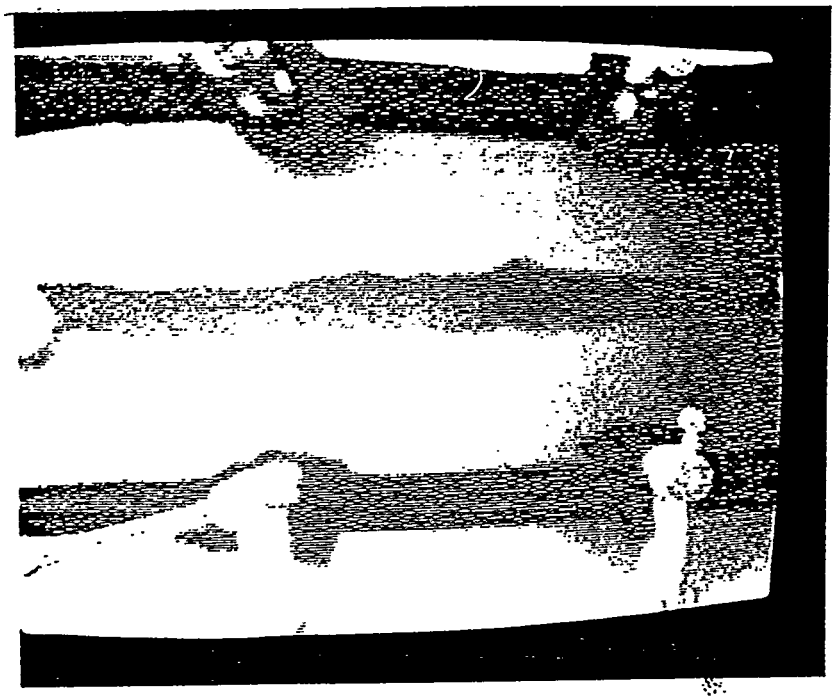

Figure 114: Displacement of Bingham Plastic (BP2) by Mineral Oil at the rate of 3.08 cc/min in the Hele-Shaw Cell: Snapshot II

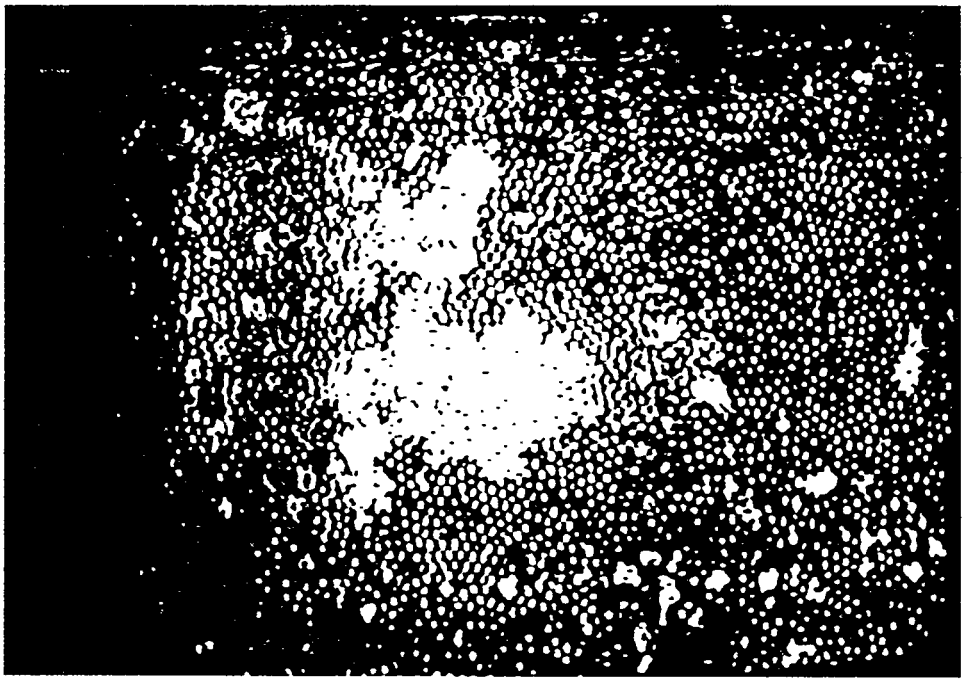

Figure 115: Displacement of Bingham Plastic (BP1) by Kerosene at the rate of 3.08 cc/min in the Glass Bead-Pack: Snapshot I

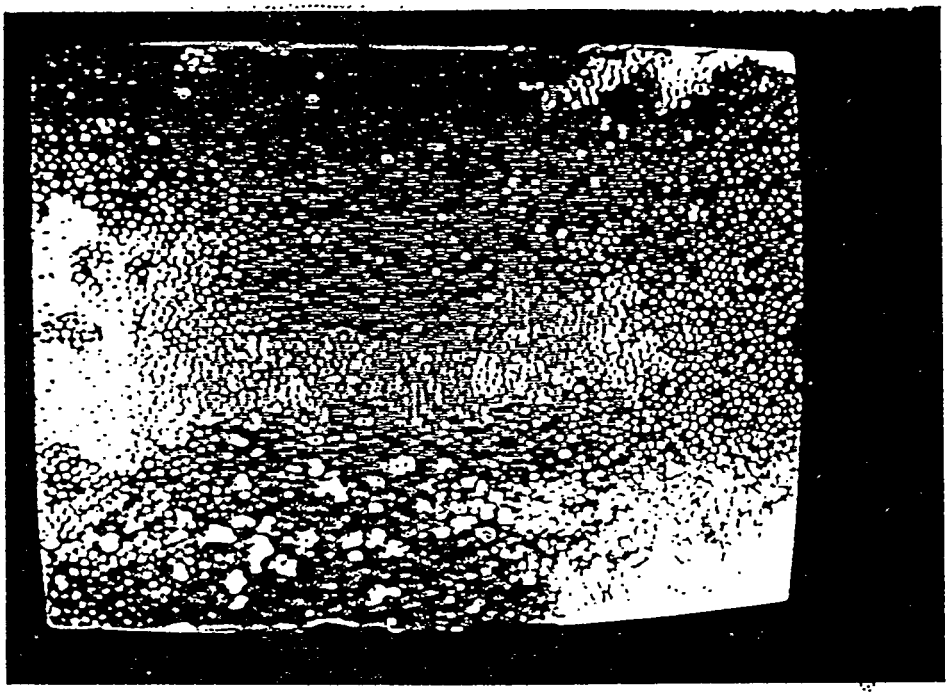

Figure 116: Displacement of Bingham Plastic (BP1) by Kerosene at the rate of 3.08 cc/min in the Glass Bead-Pack: Snapshot II

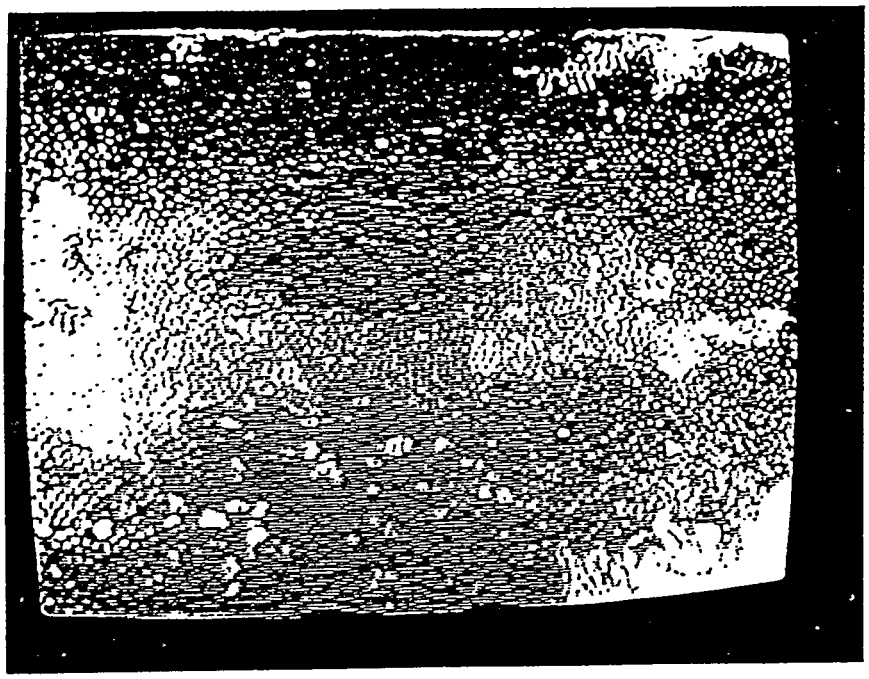

Figure 117: Displacement of Bingham Plastic (BP1) by Kerosene at the rate of 3.08 cc/min in the Glass Bead-Pack: Overall Pattern

bead-pack model, which is a simplification adopted to carry out the simulations. The simulation of immiscible displacement of Bingham plastics was carried out by injecting a Newtonian fluid using drainage process as described earlier in detail. The network size used for the simulation was 45 $\times$ 100 corresponding to the aspect ratio of glass bead pack models employed in the experimental work.

The comparison between experimental and numerical simulation results leads to a good agreement for both types of Bingham plastic fluids. Figure 121shows snapshots of numerical simulation results at two different stages for BP1. The patterns match quite well with the experimental results as shown in Figures 115 and 116. There is a tendency of trapping, bypassing and fingering in both cases. Similarly, Figure 122 indicates snapshots at two stages for fluid BP2. There is a relatively higher tendency of fingering and early breakthrough leaving large amounts of fluid BP2 in the network. These simulation results are in relatively good agreement with the experiments shown in Figures 118 to 120.

The important conclusion of this study is that with the higher yield stress of a Bingham plastic, there is a larger tendency of fingering and bypassing making the displacement difficult. Another

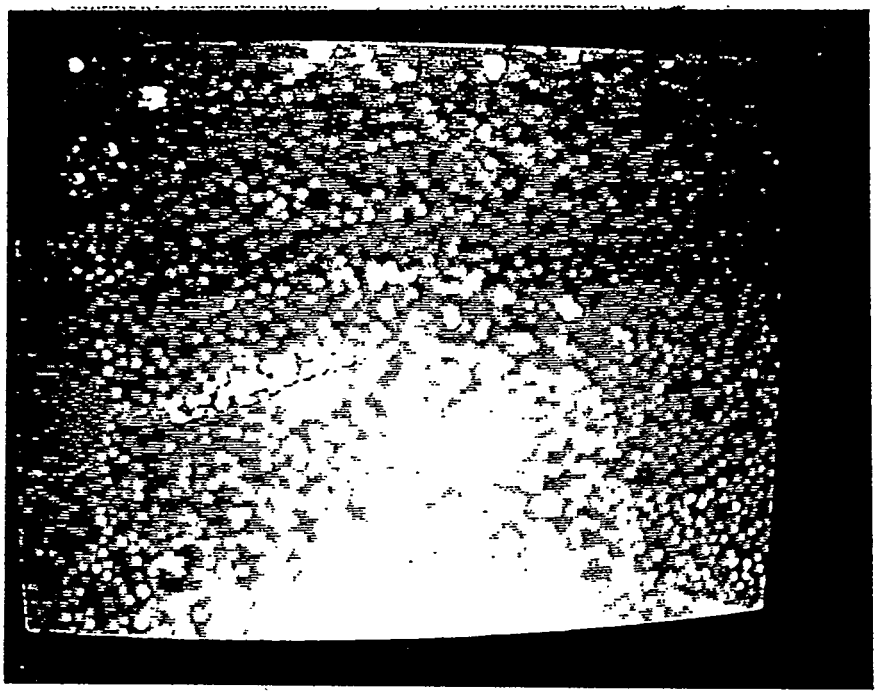

Figure 118: Displacement of Bingham Plastic (BP2) by Kerosene at the rate of 3.08 cc/min in the Glass Bead-Pack: Snapshot I

conclusion is that the relatively good agreement between the experiments and the simulations confirms the microscopic rules used in the network simulation. However, it is important to mention here that the rheological Bingham model used for drilling fluids may be simple and a more rigorous rheological model will be required to use for better agreement and understanding. Experiments involving actual heavy oils which follow Bingham plastic rheology will be more realistic and representative.

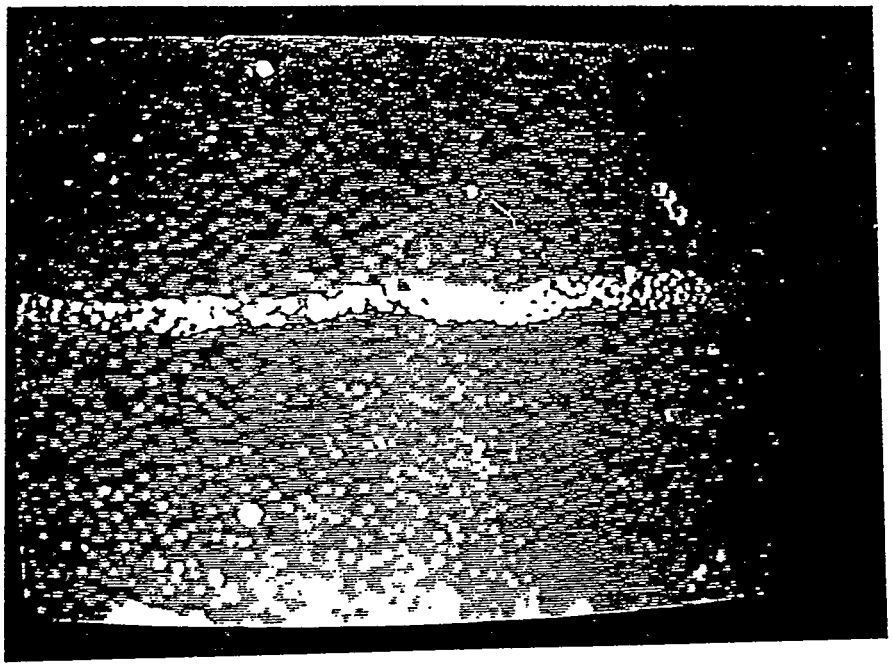

Figure 119: Displacement of Bingham Plastic (BP2) by Kerosene at the rate of 3.08 cc/min in the Glass Bead-Pack: Snapshot II

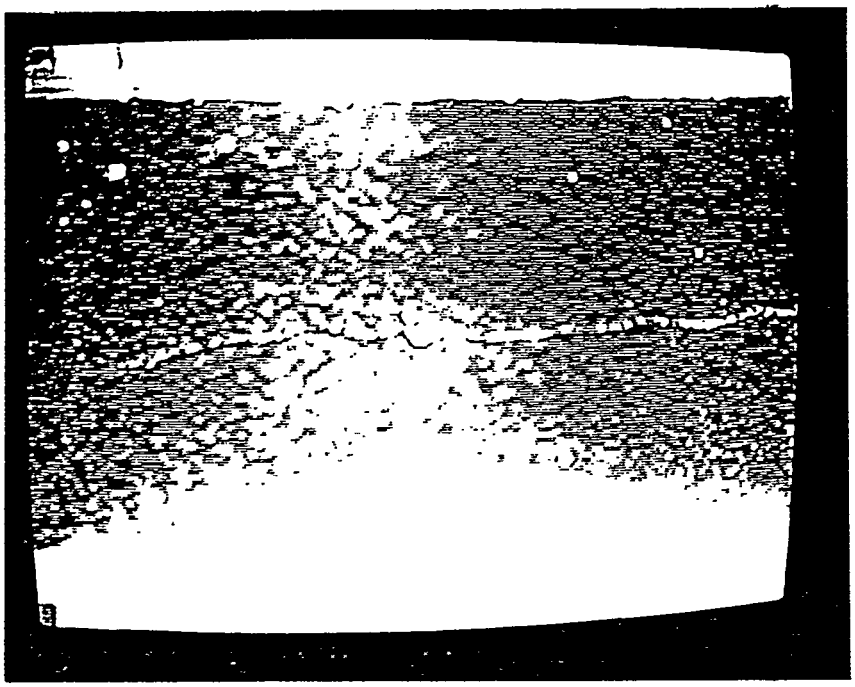

Figure 120: Displacement of Bingham Plastic (BP2) by Kerosene at the rate of 3.08 cc/min in the Glass-Bead Pack: Overall Pattern

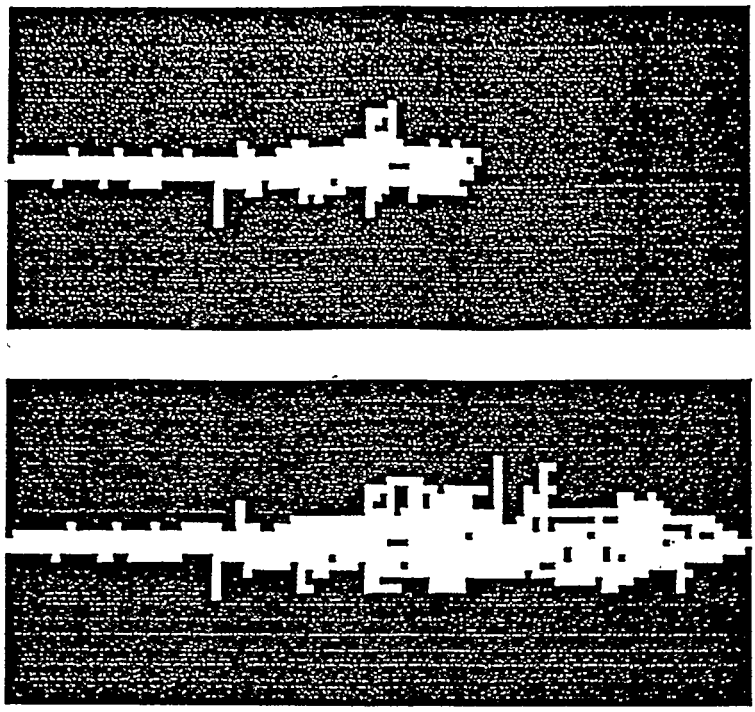

Figure 121: Numerical Simulations for the Displacement of Bingham Plastic (BP1) at the rate of 3.08 cc/min.

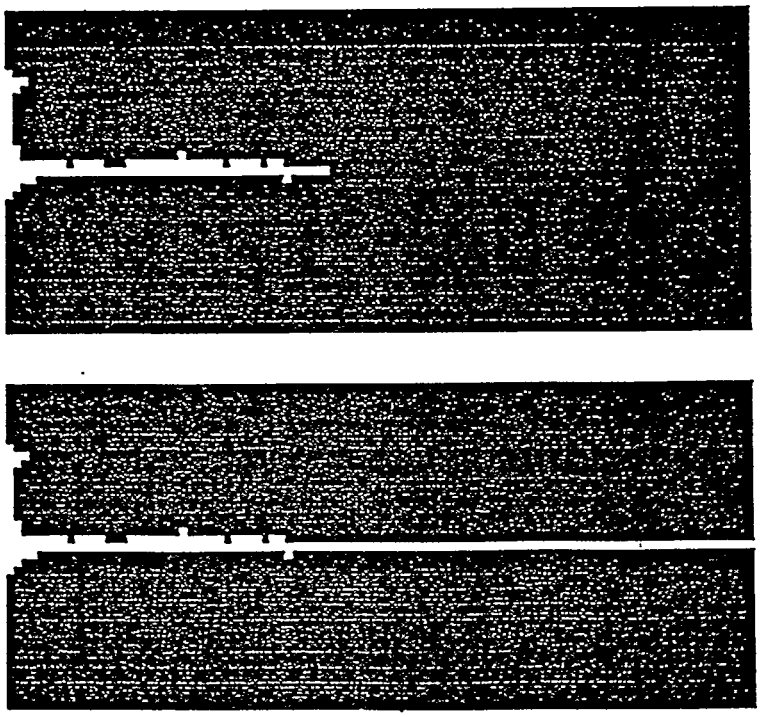

Figure 122: Numerical Simulation for the Displacement of Bingham Plastic (BP2) at the rate of 3.08 cc/min.

7 TRANSIENT AND STEADY STATE FOAM FLOW IN POROUS MEDIA

H. Kharabaf and Y. C. Yortsos

7.1 INTRODUCTION

Successful application of foam in EOR requires efficient numerical models, in addition to experimental data. Investigators working at different conditions, proposed various patterns for the foam flow. Mahmood and Brigham [76], summarized the behaviors to seven types: (1) Bubble flow, (2) Intermittent flow, (3) Plug flow, (4) Trapped-Gas flow, (5) Segregated flow, (6) Membrane flow, and (7) Tubular -Channel flow. Disagreements among the investigators shows the necessity of microscopic studies, for foam flow mechanism.

Laboratory data for the transient displacement of foam injection are not as many. Baghdikian and Handy [4] studied the transient behavior of simultaneous flow of gas and surfactant solution in consolidated porous media. Several of the factors that contribute to the foam generation were described. A systematic study of foaming with different fluid velocities and foam qualities provided extensive data for foam flow conditions. Two foam flow regimes, weak and strong foam were identified. Results indicated that in some cases an excessively large number of pore volumes of foam injection would be necessary to propagate foam deep into the reservoir. Higher gas injection velocities reduced the foam "incubation time" in their experiments. Many of these findings cannot be explained by existing theories.

Two main models of foam generation, the population balance and mechanistic model, have been suggested in the literature. Kovscek and Radke [55], recently presented a mechanistic foam simulator which incorporates a foam-bubble population balance with the traditional reservoir simulation equations, and solves for both transient and steady states. The proposed model depends heavily upon the foam texture. Kinetic expressions for lamellae generation and coalescence are saturation-dependent and trapping is a function of foam texture. The latter also affects the foam apparent viscosity. Relative simplicity and accuracy of the results in Kovscek and Radke's model can be

improved by more realistically determining the functional dependence of trapped-foam fraction.

In this work, two results are presented in transient foam flow behavior. First, we show a simple method to solve Kovscek and Radke's model. It provides an efficient way for simulating the displacement. Second, we use a network model to study the transient behavior of foam flow in porous media.

7.2 SIMPLE METHOD FOR SOLVING TRANSIENT FOAM FLOW

7.2.1 Model and Assumptions

Kovscek and Radke [55] developed the following model to describe transient foam flow in porous media. The model is based on standard form of equations for the mass balance of liquid and gas phase,

$$\frac{\partial(\phi\rho_w S_w)}{\partial t} + \frac{\partial(\rho_w u_w)}{\partial x} = 0 \,, \tag{65}$$

and

$$\frac{\partial(\phi\rho_g S_g)}{\partial t} + \frac{\partial(\rho_g u_g)}{\partial x} = 0 \,. \tag{66}$$

where, S_i, u_i and ρ_i represent the saturation, Darcy's velocity and, density of phase (i), respectively, and ϕ is the porosity of the medium. The gas phase is assumed to be nitrogen. Ideal gas law is considered. Gravitational and capillary effects are neglected.

Foam bubble density mainly controls the foam mobility. To include this effective parameter in the model, rates of convection, trapping, accumulation, generation and coalescence of the bubbles are included into the simulator by the following equation,

$$\frac{\partial[\phi(n_f S_f + n_t S_t)]}{\partial t} + \frac{\partial(n_f u_f)}{\partial x} = \phi S_g(r_g - r_c) \,, \tag{67}$$

where n_f is the bubble density (bubble number per unit volume of the medium), t and f denote trapping and flowing fractions of foam and, r_g and r_c refer to the generation and coalescence rates of the bubbles per unit volume of the porous medium. The accumulation term embodies two terms corresponding to the rate of accumulation of flowing foam and the rate of trapping foam. Trapping

Table 11: Values of the parameters for transient foam injection model.

Reservoir Simulation		*Population Balance*	
parameter	*value*	*parameter*	*value*
K	$1.3\ \mu m^2$	k_1	$5.13E+5\ s^{1/3}.cm^{-13}$
ϕ	0.25	k^o_{-1}	$1.5\ E-3\ cm^{-1}$
g	3.0	S^*_w	0.26
k^o_{rw}	0.7	a	1/3
h	3.0	b	1.0
k^o_{rg}	1.0	α	$1.80\ E-6\ mPa.s.s^{-1/3}.cm^{10/3}$
S_{wc}	0.25	c	1/3
μ_w	$1.0\ mPa.s$	$X_{f,eq}$	0.1
μ_g	$0.018\ mPa.s$	β	$1.0\ E-3, cm^3$, 1.25

and flowing foam are assumed in equilibrium, where n_t equals to n_f, which in turn simplifies the equation (67) to

$$\frac{\partial(\phi n_f S_f)}{\partial t} + \frac{\partial(n_f u_f)}{\partial x} = \phi S_g(r_g - r_c)\ . \tag{68}$$

Darcy's law applies for the velocity of either phase,

$$u_i = \frac{k k_{ri}}{\mu_i}(-\frac{\partial P_i}{\partial x})\ , \tag{69}$$

where k, is the absolute permeability of the medium, and k_{ri}, μ_i, and P_i are the relative permeability, viscosity, and pressure of the phase i, respectively. In gas phase, μ_i is the effective viscosity of the foam given by,

$$\mu_f = \mu_g + \frac{\alpha n_f}{v_f^c} \tag{70}$$

α and c are parameters given in Table 11. The properties of shear thinning and texture dependence of foam viscosity are included in equation(70) by Friedmann et al. [36].

Snap-off is the dominant mechanism of foam generation in this model (although at higher gas velocities, Hirasaki [43] conjectures that lamellae division is more important). For snap-off,

the aqueous phase needs to be accumulated at the pore throat, while the number density of the bubbles depends on the gas velocity. Thus, the rate of generation is written as

$$r_g = k_1 v_f^a v_w^b \ , \tag{71}$$

where v_i represents the interstitial velocity of phase i ($v_i = u_i/\phi S_i$), a and b are power indices and k_1 is the generation rate constant (values are given in Table 11).

For the rate of coalescence the model takes

$$r_c = k_{-1}(S_w) v_f v_w \ , \tag{72}$$

where $k_{-1}(S_w)$ is a coalescence rate constant given by

$$k_{-1}(S_w) = k_{-1}^{\circ} \frac{1 - S_w}{S_w - S_w^*} \ , \tag{73}$$

S_w^* corresponds to critical capillary pressure P_c^* , and k_{-1}° is a constant. Finally, standard Corey exponent models are utilized for relative permeabilities,

$$k_{rw} = k_{rw}^{\circ} \overline{S_w}^g \ , \tag{74}$$

Because the majority of the gas phase is present as a trapped foam, its relative permeability is modified by the fraction of flowing foam (X_f) to be,

$$k_{rf} = k_{rg}^{\circ} [X_f (1 - \overline{S_w}]^h \ , \tag{75}$$

where in equations (74) and (75), k_{rw}°, k_{rg}°, g and h are constants.

A most important parameter in this model is the trapped foam fraction that controls the propagation and mobility of the foam, by affecting apparent viscosity and relative permeability of the gas phase. The trapped fraction of the foam X_t, is given by

$$X_t = \frac{S_t}{S_g} \ , \qquad (X_f = 1 - X_t = \frac{S_f}{S_g}) \ . \tag{76}$$

X_t is an unknown function of capillary pressure, aqueous phase saturation, pore geometry and pressure gradient. Thus far, X_t has only been measured experimentally [36, 37]. The flowing fraction of the foam is given by the following equation [56]

$$X_f = 1 - X_{t,max}(\frac{\beta n_t}{1+\beta n_t}) \ , \tag{77}$$

where β is another parameter and $X_{t,max}$ is the maximum trapped foam fraction. Table 11, lists all the constants and parameters needed for the above equations (from Ref. [56]).

Using a standard finite difference IMPES (Implicit Pressure Explicit Saturation) simulat' method and upstream weighting of the phase mobilities, the above equations may be solved for three variables of pressure, saturation and bubble density. Howewver, several numrical difficulties were encountered. To avoid unnecessary complications, we elected instead to proceed with a semi-analytical solution.

It is expected that because of the particular form of the model equations, a shock develops. We expect that following this shock a steady state solution develops. This will be used along with the front velocity to find the transient behavior of the foam flow in a one-dimensional core. This is a computationally efficient way to solve the equations without imposing any limitation.

At steady-state, the mass conservation and population balance equations reduce to

$$\frac{\partial u_w}{\partial x} = 0 \quad or \quad u_w = u_w^\circ = constant \ , \tag{78}$$

$$\frac{\partial(\rho_g u_g)}{\partial x} = 0 \tag{79}$$

or by employing the ideal gas law for the gas phase

$$P u_f = constant \tag{80}$$

and

$$\frac{\partial}{\partial x}(n_f u_f) = \phi S_g (r_g - r_c) \ . \tag{81}$$

Darcy's law gives two more equations (for either phase) that can be solved along with equations (80) and (81) to find the four unknowns P, S_g, u_f and n_f at any position at steady state.

In the unsteady state, the equations can be written in dimensionless form as

$$\frac{\partial S_w}{\partial t} + \frac{\partial u_w}{\partial x} = 0 \,, \tag{82}$$

$$\frac{\partial (PS_g)}{\partial t} + \frac{\partial (Pu_f)}{\partial x} = 0 \,, \tag{83}$$

and

$$\frac{\partial (n_f S_g)}{\partial t} + \frac{\partial (n_f u_f)}{\partial x} = S_g (r_g - r_c) \,. \tag{84}$$

Given that a shock develops we shall have

$$V_{F1} = \frac{dx_{F1}}{dt} = \frac{[u_f]}{[S_g]} = \frac{u_f^- - u_f^+}{S_g^- - S_g^+} \tag{85}$$

$$V_{F2} = \frac{dx_{F2}}{dt} = \frac{[Pu_f]}{[PS_g]} = \frac{P^- u_f^- - P^+ u_f^+}{P^- S_g^- - P^+ S_g^+} \tag{86}$$

$$V_{F3} = \frac{dx_{F3}}{dt} = \frac{[n_f u_f]}{[n_f S_g]} = \frac{n_f^- u_f^- - n_f^+ u_f^+}{n_f^- S_g^- - n_f^+ S_g^+} \tag{87}$$

where the brackets indicate difference between the values of the variables just before and right after the shock. Because of the particular initial conditions,

$$u_f^+ = n_f^+ = S_g^+ = 0 \tag{88}$$

We shall have

$$V_{F1} = \frac{u_f^-}{S_g^-} \tag{89}$$

$$V_{F2} = \frac{P^- u_f^-}{P^- S_g^-} = \frac{u_f^-}{S_g^-} \tag{90}$$

$$V_{F3} = \frac{n_f^- u_f^-}{n_f^- S_g^-} = \frac{u_f^-}{S_g^-} \tag{91}$$

For the shock condition to be satisfied we must have,

$$V_{F1} = V_{F2} = V_{F3} = \frac{dx_F}{dt} \tag{92}$$

Here, u_f^- and S_g^- will be determined by the steady state solution of the problem. If equation (80) is introduced into equation (92) at steady state reads

$$\frac{dx_F}{dt} = \frac{u_f^\circ}{P_s^-(x)S_{g,s}^-(x)} \tag{93}$$

where subscript s, denotes the steady state values. Then, the time required for the front to reach position x can be determined by the simple result

$$t = \int_0^x \frac{S_{g,s}^-(x)P_s^-(x)}{u_f^\circ}dx \tag{94}$$

The results of the simulation using the above simple method for the Kovscek and Radke's model [55] have been plotted in Figures 123 and 124. Figure 123 shows the history of pressure, saturation, foam number density and foam velocity variations, while figure 124 shows the profile of the same variables. Comparison between these figures and those of Kovscek and Radke (Figure 125) shows very good agreement.

Next, the simulator was used to check if it is possible to model Baghdikian and Handy's experiments [4]. These authors used two cores with dimensions $(1'' \times 4'')$ and $(2'' \times 10'')$, porosities 0.27 and 0.25, and absolute permeabilites 0.7 and 0.5 darcies, respectively. The Chevron chaser SD-1000 was used as surfactant, which is expected to have different generation or coalescence rates than the ones used in the simulation. A back pressure of about 790$[kPa]$ was used in the experiments. Gas and liquid velocities were much higher than in Kovscek and Radke's experiments (about 100 times).

Figure 126 shows the pressure history according to the experiment and the simulation. Gas and liquid velocities are 117 and 11.8 (ft/d), respectively. To obtain the needed order of magnitudes, rates of foam generation and coalescence were taken as 0.035 times lower and 10 times higher than the previous one, respectively.

It is apparent that, the predicted response cannot be adequately matched. Figure 127 shows

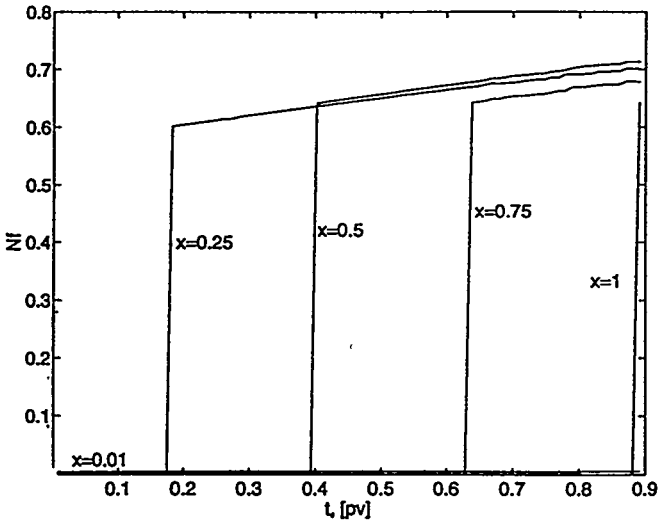

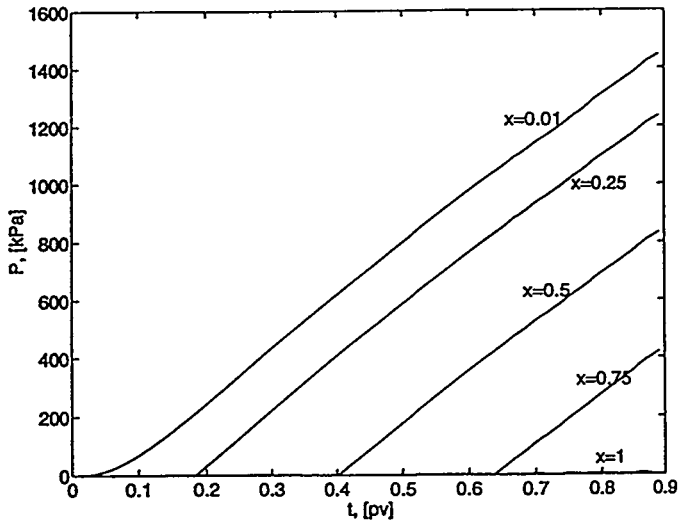

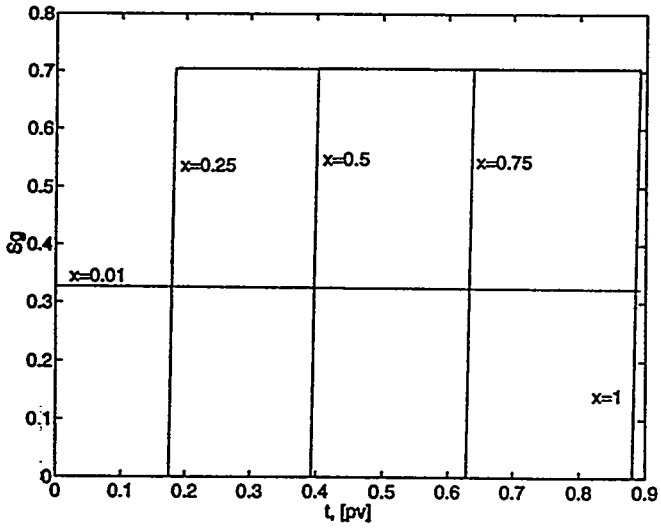

Figure 123: History of transient behavior of foam injection, using the semi-analytical solution.

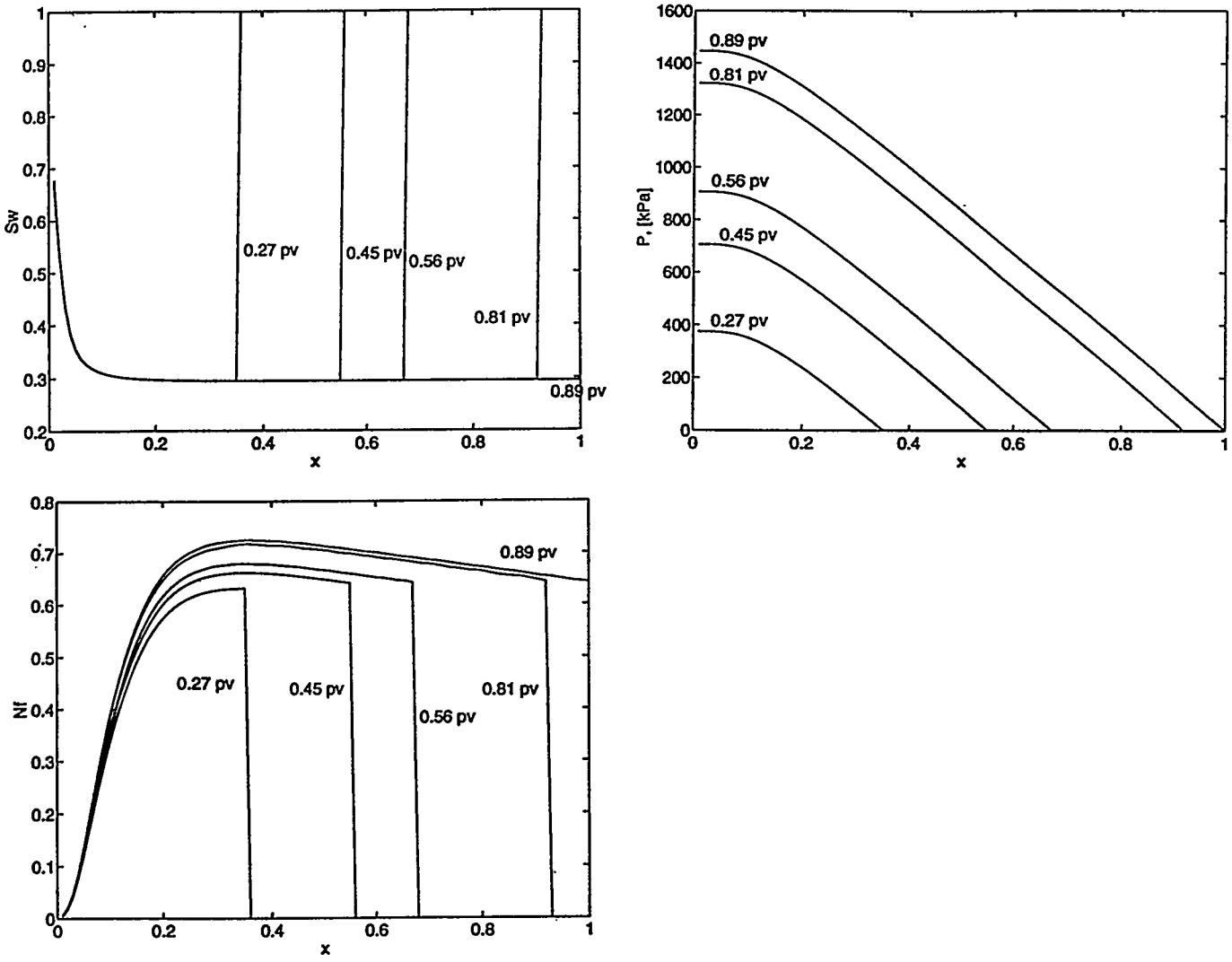

Figure 124: Profile of transient behavior of foam injection, using the semi-analytical solution.

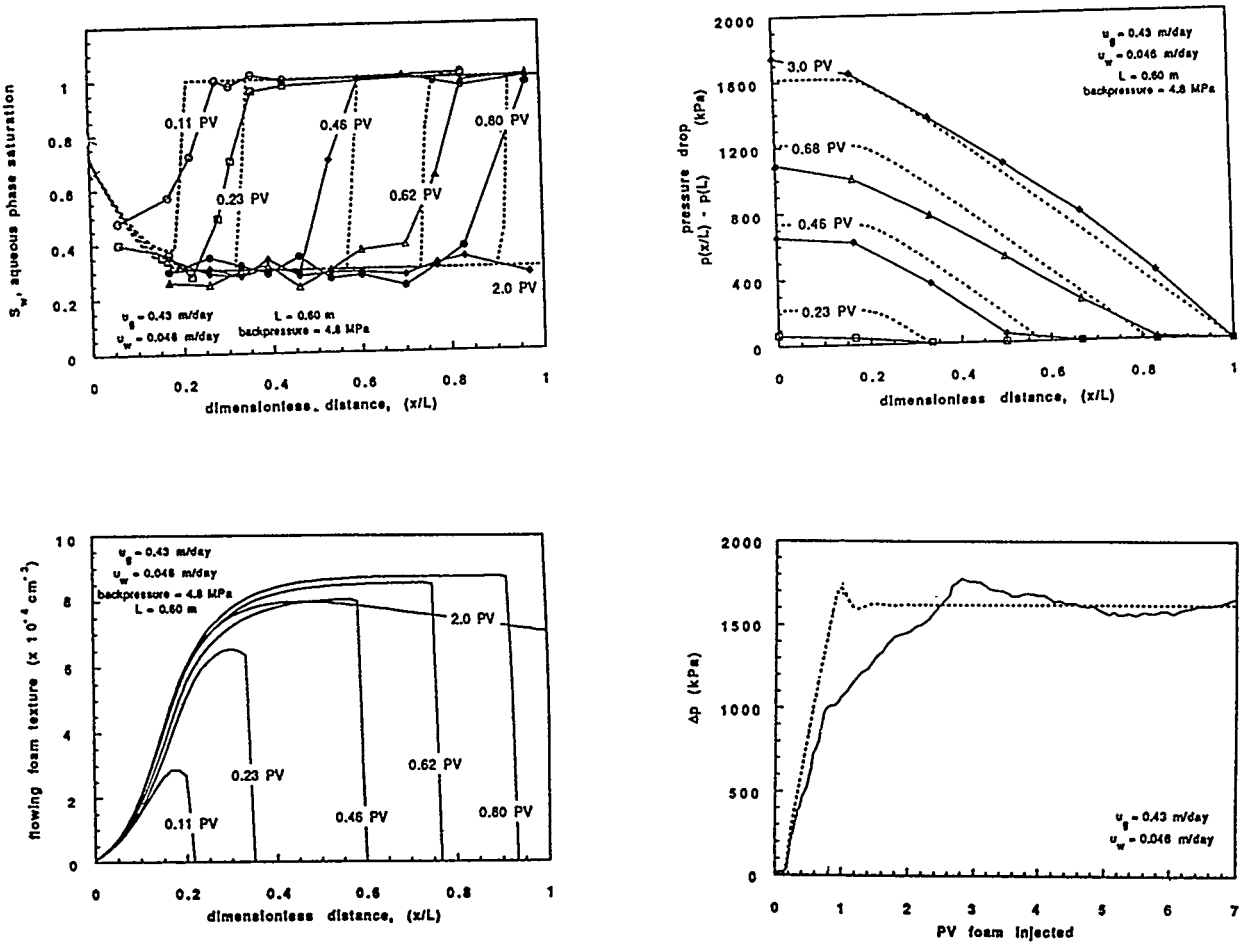

Figure 125: Experimental and model transient aqueous phase. (*a*) Saturation, (*b*) Pressure, (*c*) Flowing foam texture, and (*d*) Pressure drop history (from ref. [55]).

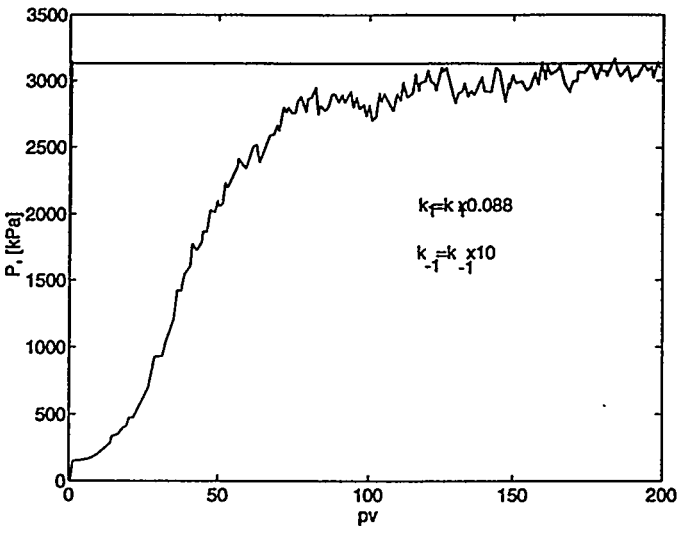

Figure 126: Model simulation (flat curve), and the experimental results of Baghdikian and Handy [4].

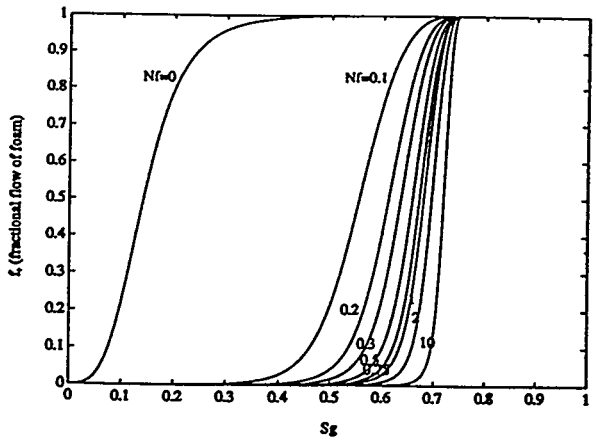

Figure 127: Fractional flow curves of foam at different foam textures with respect to gas saturation.

that u_f does not change drastically with respect to S_g as the foam density number increases from 0.1 to 1. Hence, the front velocity given by eq.(92) is almost constant. On the other hand in the experiments, gas and foam generation fronts have two different velocities, so that foam generation and propagation occur much later after the gas front has passed.

To attempt to simulate these experiments, it is necessary to introduce another parameter in the equations. Mathematically this may be done by employing a parameter λ in the population balance equation

$$\lambda \frac{\partial(n_f S_g)}{\partial t} + \frac{\partial(n_f u_f)}{\partial x} = S_g(r_g - r_c) \tag{95}$$

This will cause the foam generation front to propagate with a velocity other than the gas advancement front,

$$\frac{dx_{F,f}}{dt} = \frac{\bar{u_f}}{\lambda \bar{S_g}} \,. \tag{96}$$

Particularly, in order to make the foam generation front much slower than the gas front we will request

$$\lambda \gg \frac{\bar{u_f}}{\bar{S_g}} \tag{97}$$

By introducing this parameter the previous simpler method cannot be applied any longer. Nonetheless, we can distinguish in case $V_{F,f} < V_{F,g}$, three different regions: (a) $x \leq V_{F,f}t$, where variables have reached steady state, (b) $V_{F,f}t < x < V_{F,g}t$, a transition region, and (c) $x > V_{F,g}$, the initial state.

Figure 128 shows the gas saturation and foam number density profiles at different pore volumes of injection for $\lambda = 1, 2$ and 3. The three different regions have been specified in Fig. 129. Obviously, because of the continuity equation, the area under the saturation curve for the same pore volume of injection is equal for any value of λ.

Figure 130 shows the results for λ=200 along with the experimental data of Baghdikian and Handy. For this particular case, it is shown that there is relatively a good match. This propmt us to search for a physical meaning of the parameter λ. It certainly could not be as a result of surfactant adsorption, since adsorption requirement were satisfied (40 pore volume of surfactant

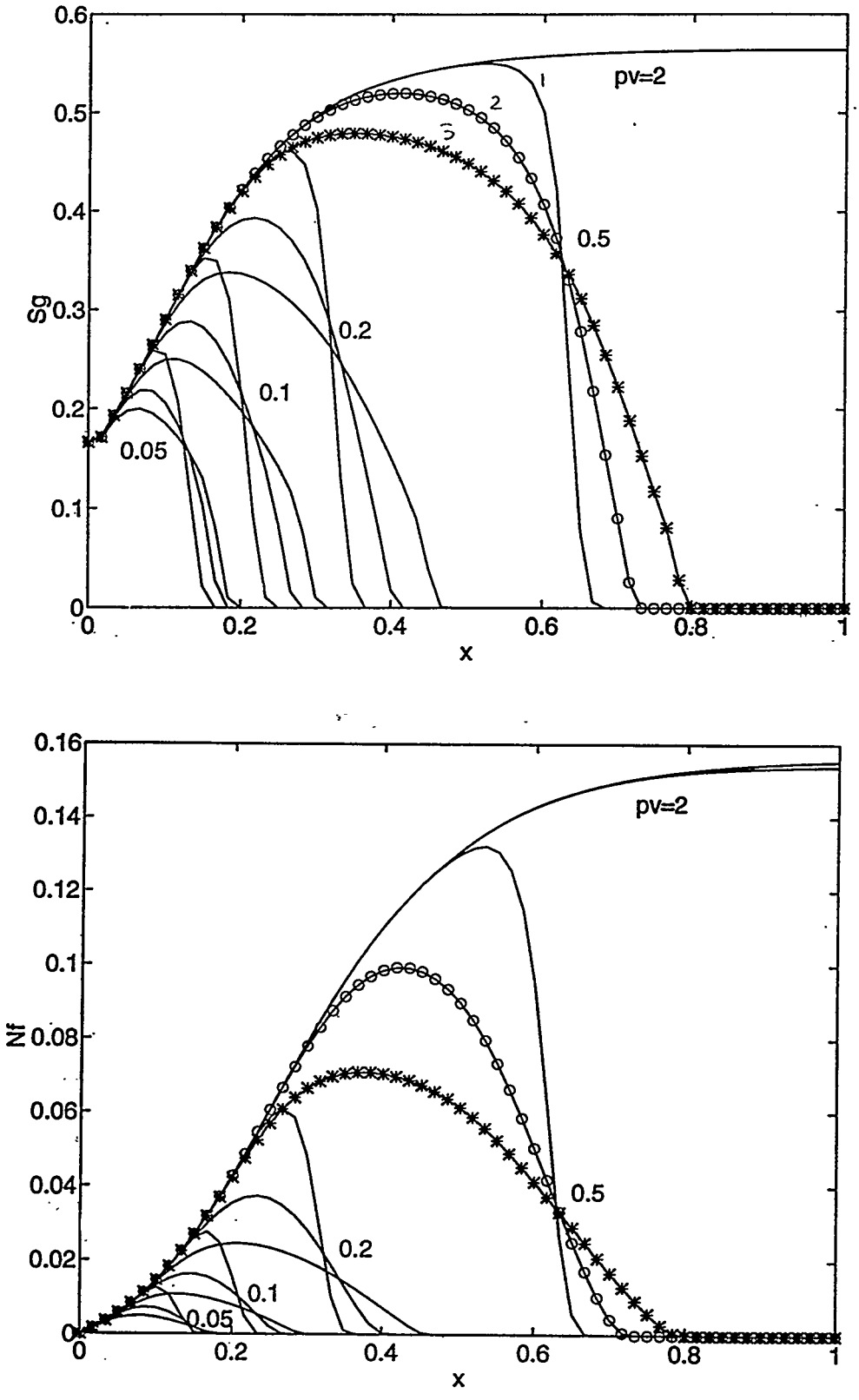

Figure 128: (*a*) Gas saturation and (*b*) Foam density profiles, for different values of λ.

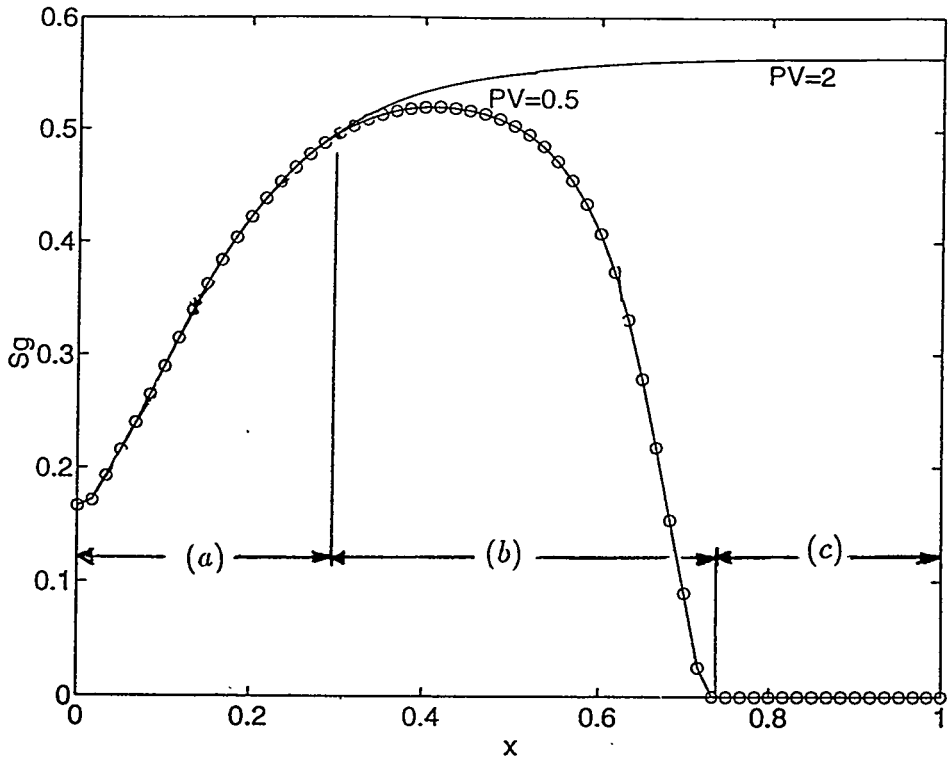

Figure 129: The three different regions: (a) $x \leq V_{F,f}t$, (b) $V_{F,f}t \leq x \leq V_{F,g}$, and (c) $x \leq V_{F,g}t$, for $\lambda = 2$.

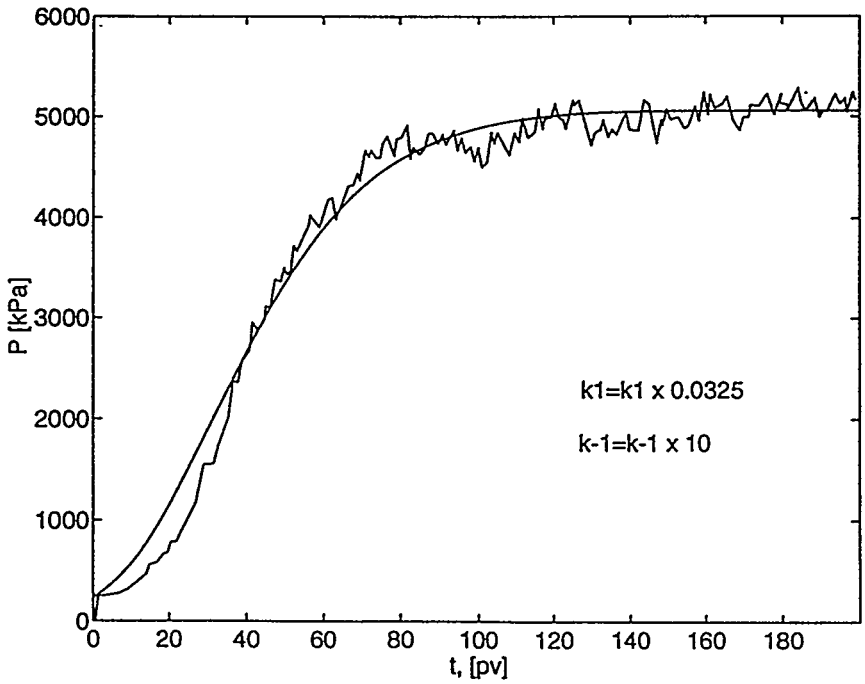

Figure 130: Model simulation result for $\lambda = 200$ (solid curve) and Baghdikian and Handy's data [4].

solution was injected to establish adsorption equilibrium) before the conduct of the experiment. It appears that there must be a different interpretation which needs to be considered.

It is possible that some of the assumptions made need to be changed. For example, if in simplifying eq.(67), one does not assume $n_f = n_t$, but take, instead,

$$n_f S_f + n_t S_t = n_f S_g X_f + n_t S_g (1 - X_f) = S_g (n_f X_f + n_t (1 - X_f)) \tag{98}$$

then, λ satisfies

$$n_f X_f + n_t (1 - X_f) = \lambda n_f \tag{99}$$

For any X_f, the desired λ, would follow from

$$\lambda = X_f + (1 - X_f) \frac{n_t}{n_f} \tag{100}$$

In other words, only by assuming different foam number density ratio of flowing and trapped foam it is possible to generate a value of λ which in turn, would have a significant effect on the results. To be able to proceed in this direction, a network model is necessary.

7.3 PORE NETWORK MODEL

In this section, pore network models will be employed to study transient foam flow in porous materials.

In these models, porous media are represented as two- and three-dimensional lattices of coordination number 4 and 6, respectively, with bonds and nodes representing pore throats and sites. For size distribution of either throats or sites, a Rayleigh distribution with different average radii ($\overline{r_i}$) has been used:

$$\alpha_i(r) = \frac{\pi r}{2\overline{r_i}^2} \exp[-\frac{\pi r^2}{4\overline{r_i}^2}] \tag{101}$$

where i denotes either throat or site, and $\overline{r_s} = 1.5\ \overline{r_t}$. Periodic boundary conditions are employed to reduce boundary effects.

The system is initially occupied by a surfactant solution. By injecting gas from one end, liquid can be displaced. As the pressure in the non-wetting fluid increases gradually, the largest accessible bond which has the lowest resistance and the following site are invaded first. Here, we shall neglect viscous or gravitational forces. However, trapping will be considered for liquid phase in either sites or bonds. In this way, lamellae can be generated by the Leave-behind mechanism. Snap-off is also possible during invasion. For simplicity, however, we neglect Lamellae-division. A Leave-behind mechanism occurs whenever pore throat trapping is permitted. Snap-off, which is only a function of pore geometry [14], occurs even in the absence of any surfactant, although the surfactant is stabilizing the generated thin liquid films. Snap-off is driven by the curvature difference between pore throats and pore bodies, which provides higher capillary pressure or lower liquid pressure at the throats, assuming uniform pressure over the gas phase. This draws more liquid towards the throat (via solid corners) and eventually generates a liquid film at the throat location. For this mechanism, the pore body-to-pore throat size ratio, called the *aspect ratio*, needs to be higher than some specific value, which is believed to be between 1.5-2.5, [68, 74, 78, 89].

In case there are sufficient lamellae generated by snap-off, the gas phase can become discontinuous. Continuing the displacement in such a case, may require to mobilize some lamellae first. For this, the pressure difference across the lamella needs to be higher than $4\gamma/r_{min}$ [91], where γ is the interfacial tension between wetting and non-wetting phases and r_{min} is considered to be equal to the pore throat radius, (r_t). This is almost twice the pressure difference between invading and defending phases for the same throat size.

By increasing the pressure of the injecting phase it is possible that before the next invasion can take place, one or more of the lamellae generated by either mechanism are mobilized. In such a case, it will be assumed that stretching will cause a lamella to break as soon as it moves out of the throat and reaches the next pore body. This allows a certain path which has the minimum resistance to open and invasion to take place. After this step, it is assumed that the surfactant solution can generate new lamella at the same throat. This process continues until foam breaks through.

7.3.1 Results and discussion

Results obtained from the pore network modeling are discussed in the following. Figure 131 shows schematically how invasion takes place in a 60×100 network, at different displacement times. Here, snap-off was assumed whenever the aspect ratio is greater than 1.5. One may notice three regions in the model. First, an invaded, stabilized region, which does not change as invasion takes place. Second, a transient section. This region does not grow and it keeps almost the same width as the displacement proceeds. And a third uninvaded region.

The intensity of pressure at each pore at a fixed time is depicted by increased brightness, the lightest color representing the highest pressure. Because liquid is interconnected all over the network, via corners and channels, but viscous forces have been neglected, the darkest regions show trapped or not-yet displaced liquid. This schematic is also a good representation of the system's saturation.

In this case, at breakthrough 76.6% of the throats contain lamellae (23% by snap-off and 53.6% by leave-behind). Notice, that in order for the gas path to be discontinuous, only snap-off is needed. However, after the path becomes disconnected, the lamellae generated by both mechanisms are important and it would be possible for each of them to be a part of the path which has the minimum resistance.

Figures 132 and 133 show the same simulation for the case when the condition for snap-off is that the aspect ratio exceeds 2 and 2.5, respectively. One of the differences between these figures is in the width of the transient front, which becomes wider as the critical aspect ratio becomes larger (less lamellae in the system). Also more trapping can be observed with similar trend. These result from a less frequent snap-off events. The total percentage of lamellae at breakthrough are about 35.2% and 21.7% where 25.8% and 11.5% of those are generated by snap-off, respectively. Even Leave-behind lamellae are less than in the previous case. It needs to be mentioned that the critical aspect ratio has only been used to generate different percentage of lamella in the system. Practically, the foam density can be a function of injection velocity, saturation, fractional flow of

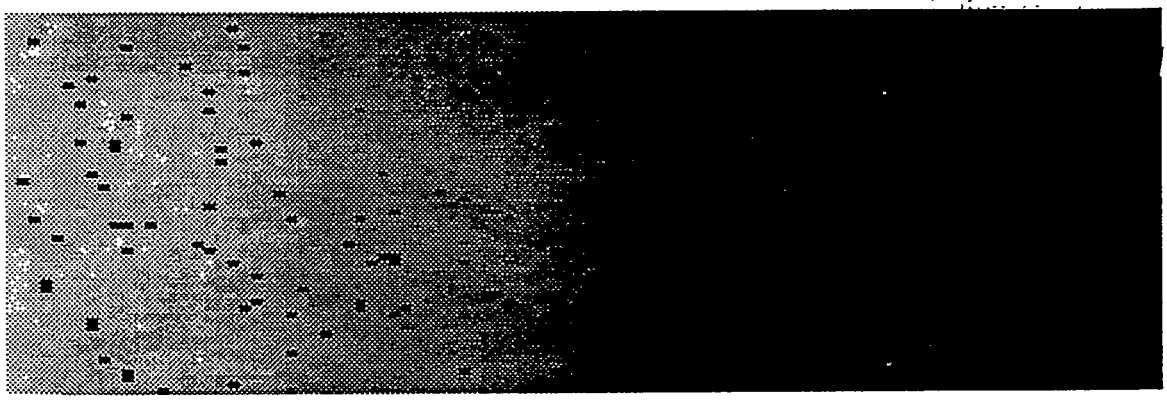

(a)

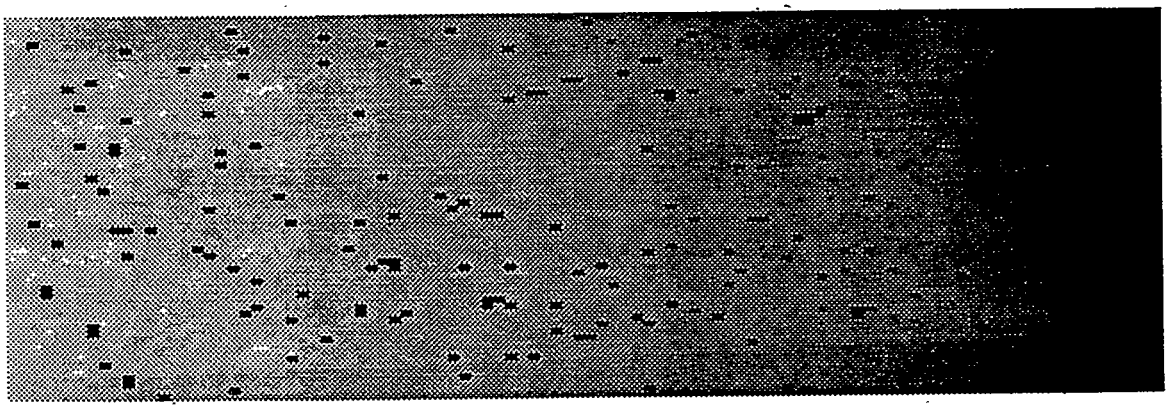

(b)

Figure 131: Displacement in a 60 × 100 network. Average front advancement at (*a*) $x = 0.5$, and (*b*) breakthrough. (Critical aspect ratio for snap-off, 1.5).

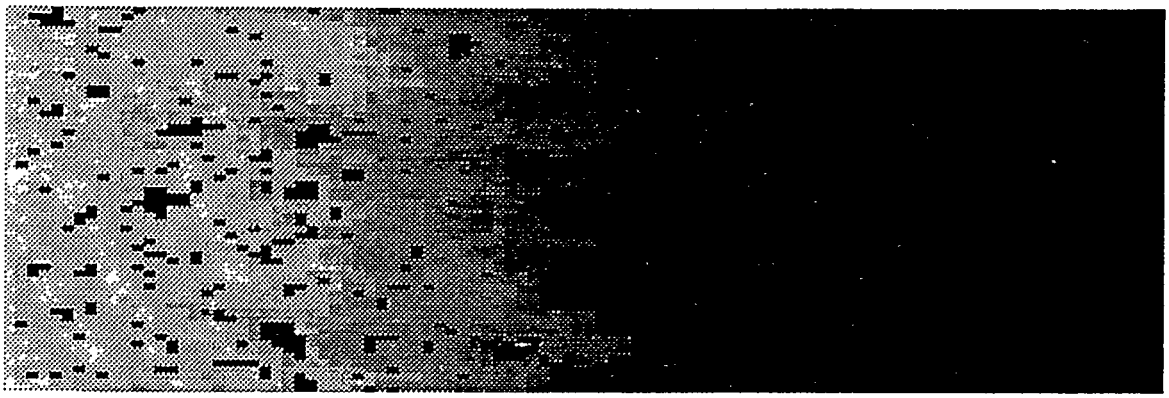

(*a*)

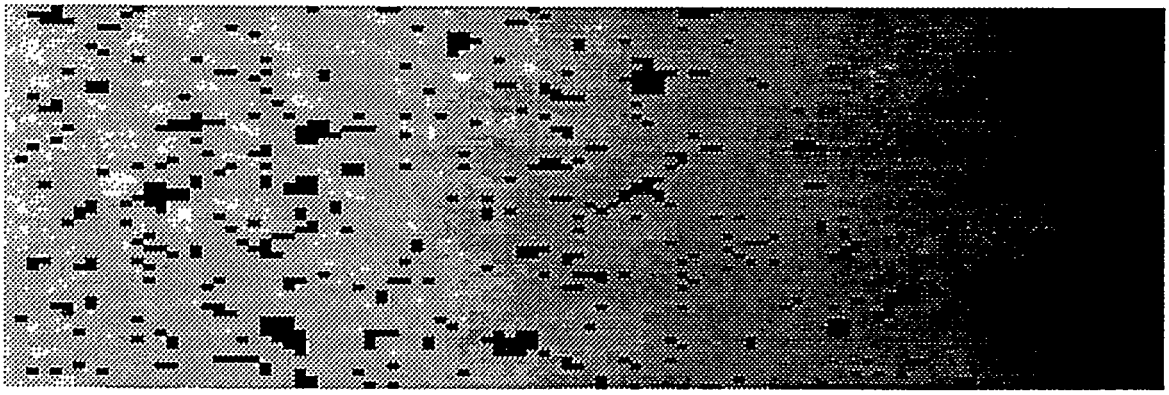

(*b*)

Figure 132: Displacement in a 60×100 network. Average front advancement at (*a*) $x = 0.5$, and (*b*) breakthrough. (Critical aspect ratio for snap-off, 2).

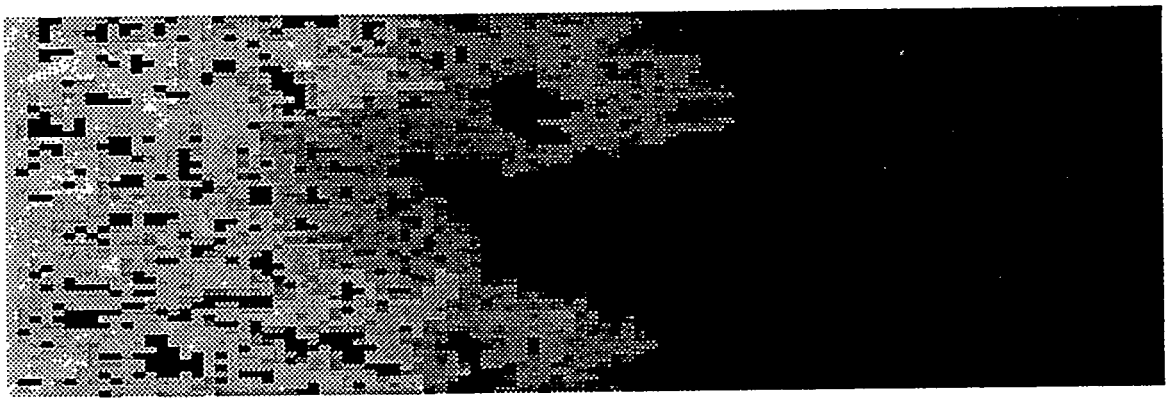

(*a*)

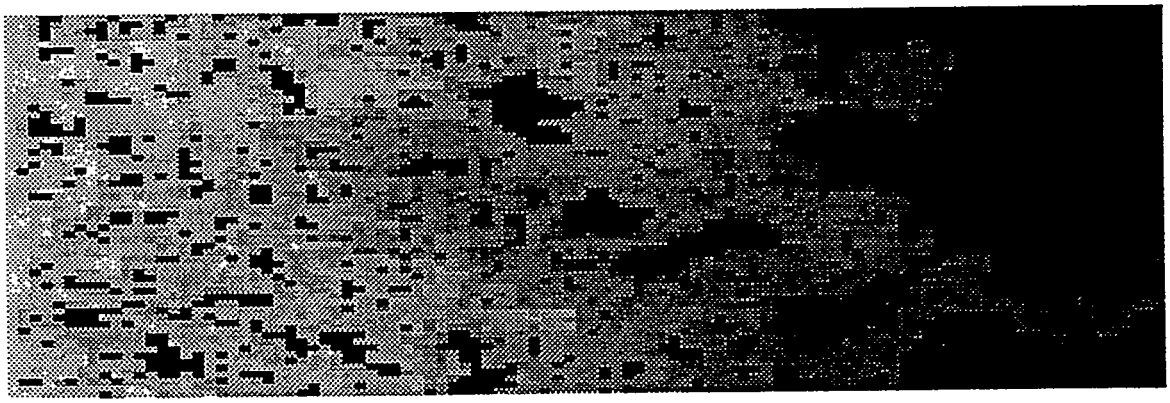

(*b*)

Figure 133: Displacement in a 60 × 100 network. Average front advancement at (*a*) $x = 0.5$, and (*b*) breakthrough. (Critical aspect ratio for snap-off, 2.5).

phases, etc.

Figure 134 shows the gas saturation, lamellae number density, (L_f, generated either by snap-off or both mechanisms), and pressure profiles in a 3-D ($20 \times 50 \times 20$) network with critical aspect ratio equal to 2. L_f has been normalized by the total number of throats on the same volume fraction of the system. For determining the pressure gradient, it is assumed that the average throat radius of the network is equal to $50(\mu m)$ and the bond length is $150(\mu m)$. The IFT was taken to be $30(mN/m)$.

Those results have a qualitative resemblance to other experimental and theoretical works. Figure 135 shows similar results for the case when the aspect ratio criterion for snap-off is 2.5. Further work is continuing on this problem.

7.3.2 Heterogeneous porous media

For simulating heterogeneous media, the pore network has been divided into two portions (of higher and lower permeability), with the top portion assigned to have a higher permeability (the average throats and sites of the top portion are two times larger than the bottom).

Figures 136 and 137 show schematically foam displacement within such media for two different critical aspect ratios. As the possibility of snap-off increases, the sweep efficiency in the lower permeability region increases. By contrast, when there is no snap-off, the sweep efficiency in the less permeable region is almost zero (Figure 138).

The network model proposed is capable of simulating some aspects of transient and steady state foam flow in porous media.

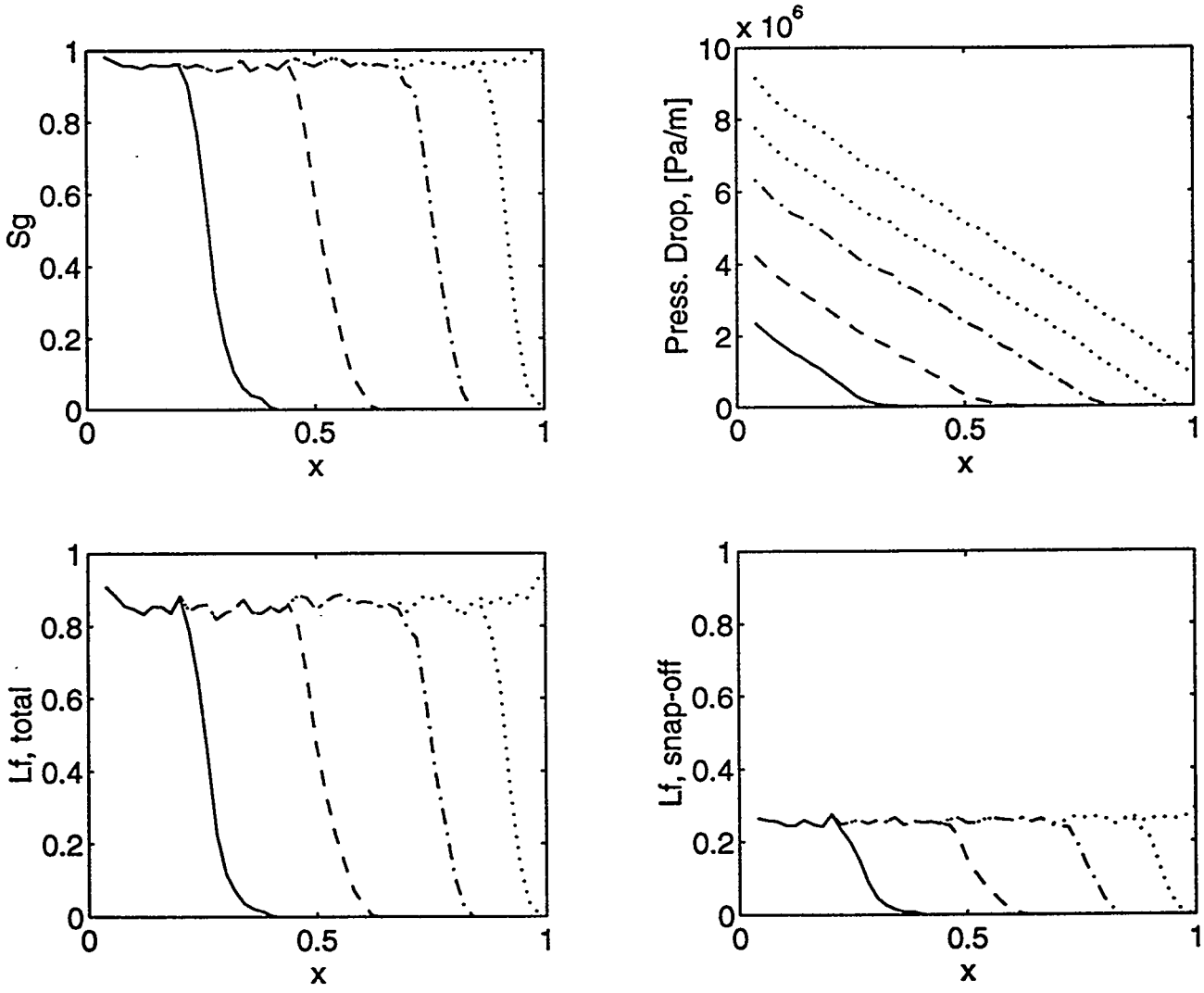

Figure 134: Profiles of (*a*) Gas saturation, (*b*) Pressure gradient, (*c*) Snap-off lamellae, and (*d*) Total lamellae at different times. Network size: $20 \times 50 \times 20$. (Critical aspect ratio, 1.5).

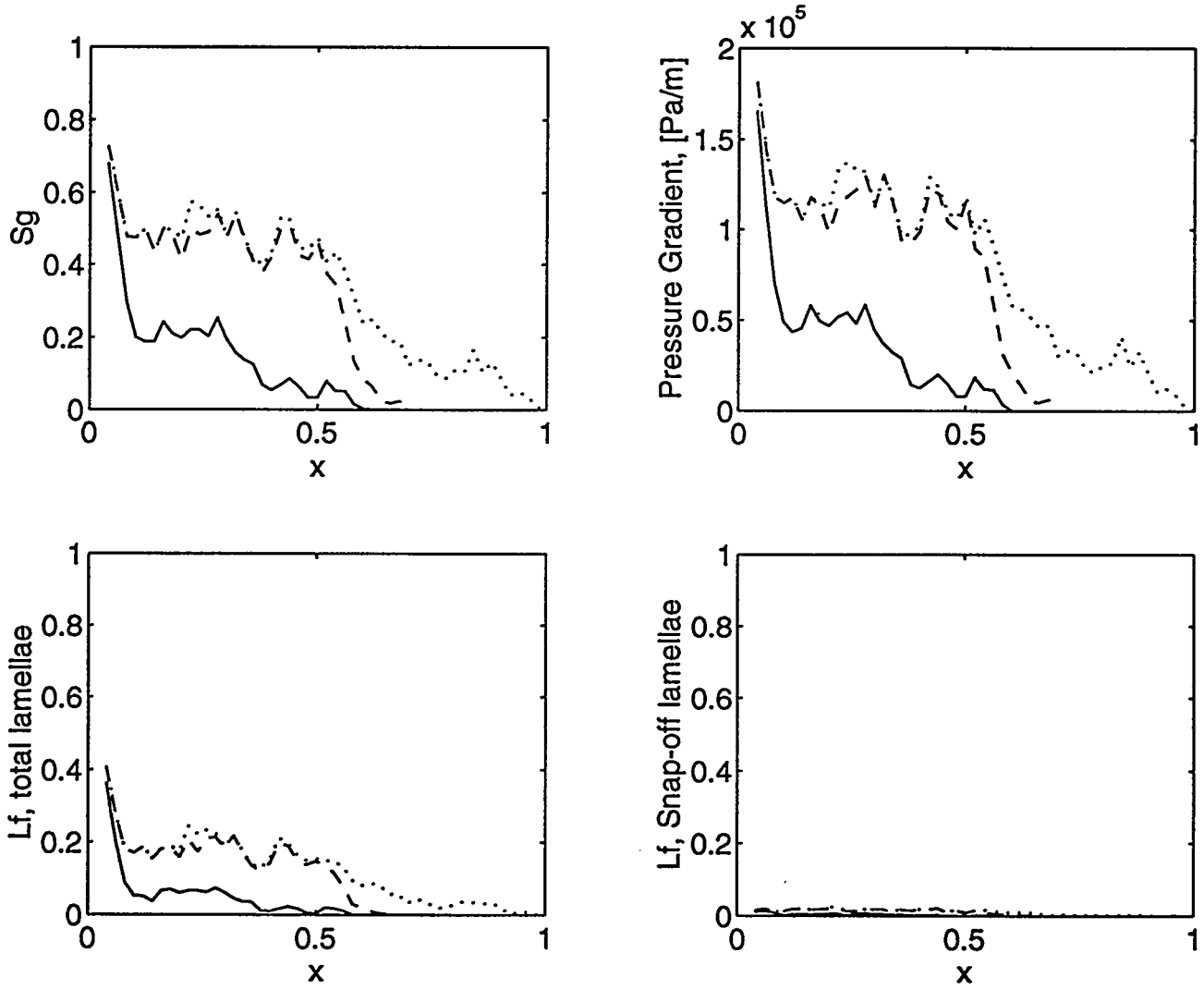

Figure 135: Profiles of (*a*) Gas saturation, (*b*) Pressure gradient, (*c*) Snap-off lamellae, and (*d*) Total lamellae at different times. Network size: $20 \times 50 \times 20$. (Critical aspect ratio, 2.5).

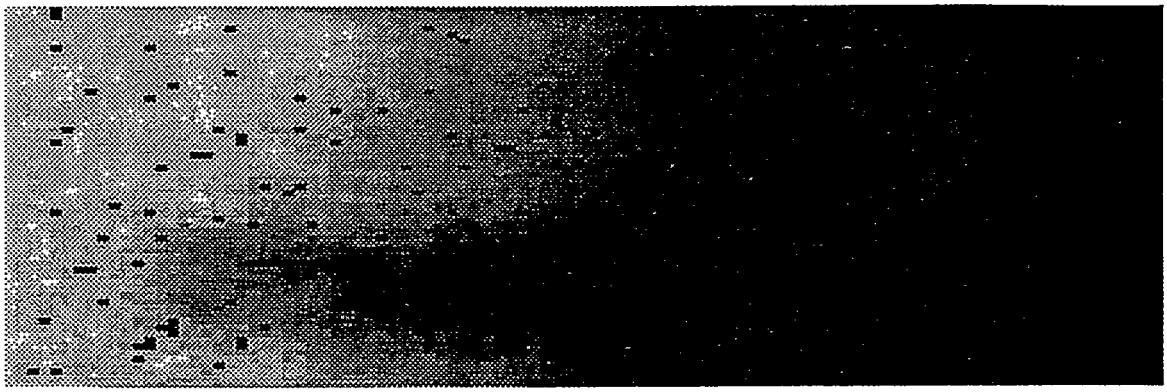

(*a*)

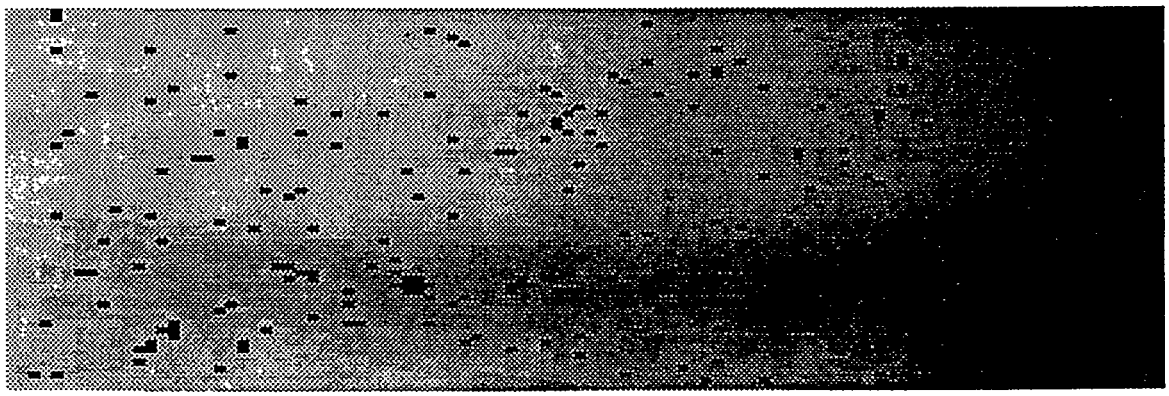

(*b*)

Figure 136: Displacement in a 60×100 network with the top part having a higher permeability. Average front advancement at (*a*) $x = 0.5$, (*b*) breakthrough. (Critical aspect ratio for snap-off, 1.5).

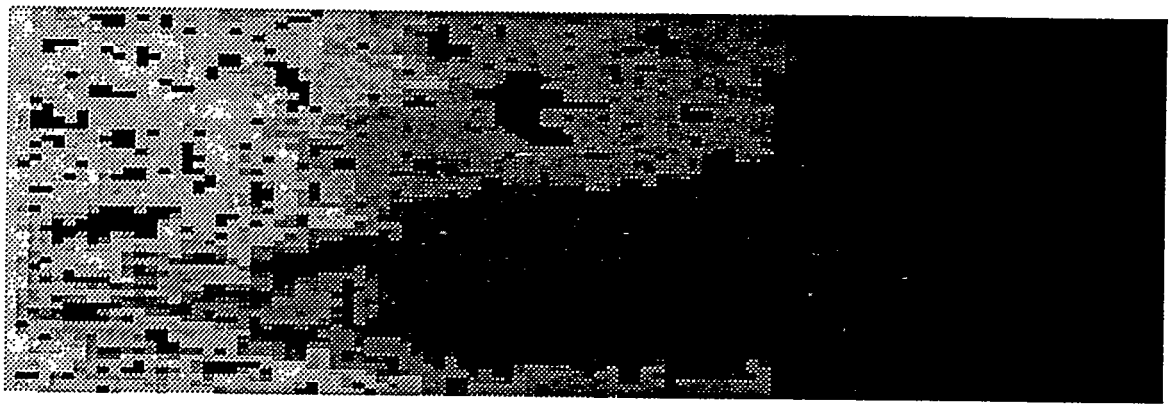

(*a*)

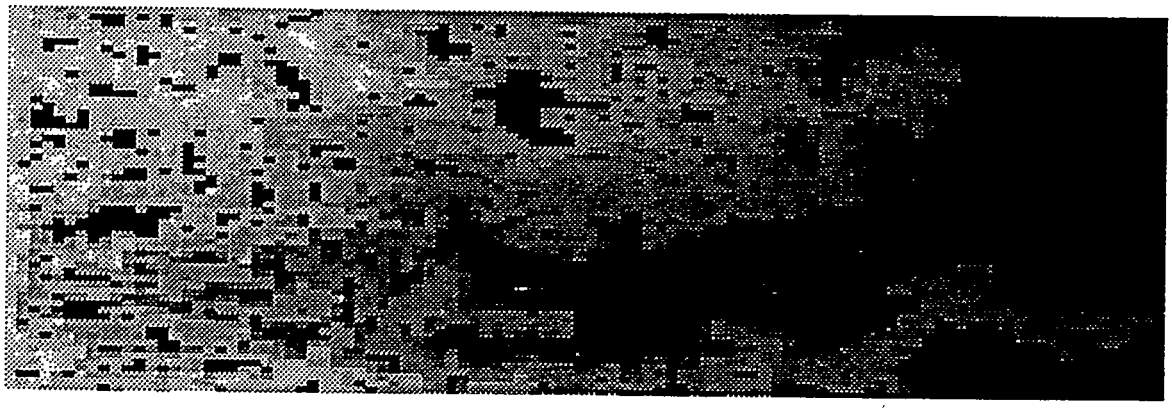

(*b*)

Figure 137: Displacement in a 60×100 network with the top part having a higher permeability. Average front advancement at (*a*) $x = 0.5$, (*b*) breakthrough. (Critical aspect ratio for snap-off, 2.5).

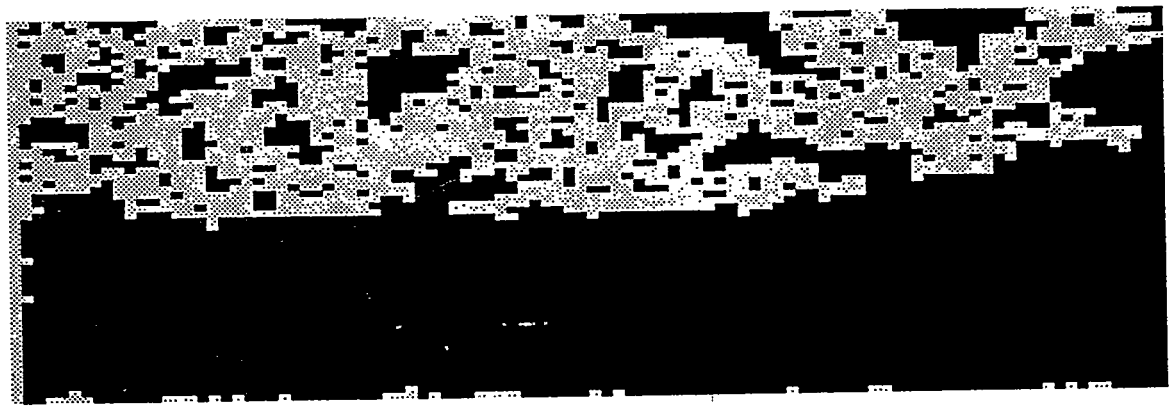

(*a*)

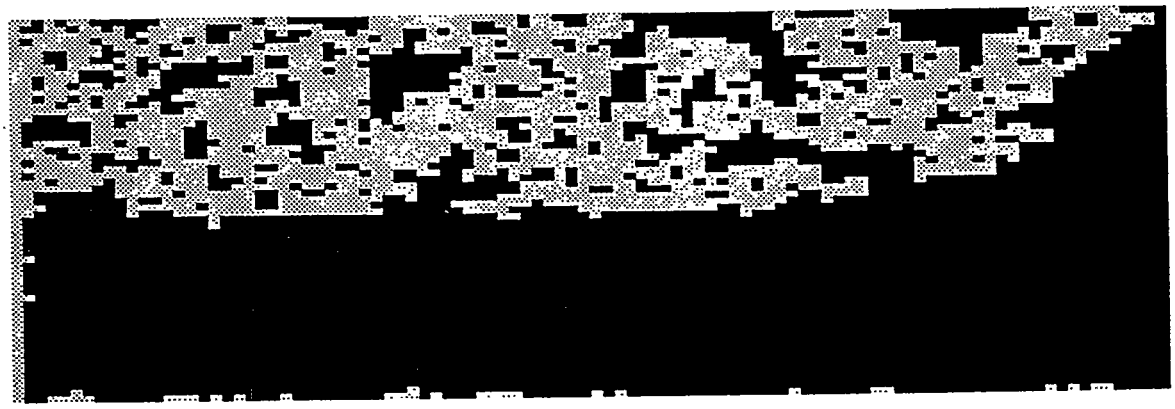

(*b*)

Figure 138: Displacement in a 60×100 network with the top part having a higher permeability. Average front advancement at (*a*) $x = 0.5$, (*b*) breakthrough. No snap-off lamellae.

References

[1] T. Al-Fariss and K. L. Pinder. *The Canadian Journal of Chemical Engg.*, 65:391, 1987.

[2] J.S. Aronofsky, L. Masse, and S.G. Natanson. *Trans, AIME*, 213:17, 1958.

[3] T. Babadagli. Ph.D. Dissertation, University of Southern California, 1993.

[4] S. Y. Baghdikian and L. L. Handy. DOE Annual Report, May 1991.

[5] G. I. Barenblatt, V. M. Entov, and V. M. Ryzhik. *Theory of Fluid Flows Through Natural Rocks.* Kluwer Academic Publishers, Netherlands, 1990.

[6] H. A. Barnes, M. F. EdWards, and L. V. Woodcock. *Chem. Engg. Sci.*, 42:591, 1987.

[7] R.B. Bird, Steward W.E., and Lightfoot E.N. *Transport Phenomena.* John Wiley and Sons, New York, 1960.

[8] N.E. Bixler and C.R. Carrigan. *Geophysical Res. Letters*, 13:42–45, 1986.

[9] M. Blunt and B. Rubin. *Journal of Computational Physics*, 102, 1992.

[10] M.J. Blunt and M.A. Christie. paper SPE 22613, Oct.6-9 1991.

[11] J.M. Buchlin. In Y. Corapcioglu and J. Bear, editors, *Proceedings NATO/ASI on Transport in Porous Media*, Pullman, WA., July 9-18 1989.

[12] M. E. Cates and T. A. Witten. *Physical Rev. A*, 35:1809–1824, 1987.

[13] C. E. Chaffey. *Colloid and Polymer Sci.*, 255:691, 1977.

[14] K. T. Chambers and C. J. Radke. *Capillary Phenomena in Foam Flow Through Porous Media*, chapter 6. Marcel Dekker Inc., New York and Basel, 1990.

[15] M. Chaouche, N. Rakotomalala, D. Salin, B. Xu, and Y.C. Yortsos. Paper SPE 26658 presented at the 68th SPE Annual Technical Conference and Exhibition, Houston, Texas, 1993, also *Chem.Eng.Sci.* (in press), 1994.

[16] W.H. Chen, M.L. Wasserman, and R.E. Fitzmorris. Paper SPE 16008 presented at the 1986 SPE Symposium on Reservoir Simulation, San Antonio, February 1-4, 1987.

[17] M.A. Christie. *SPE Reservoir Engineering*, pages 874–881, Aug. 1992.

[18] K. Cornwell, B.G. Nair, and T.D. Patten. *J. Heat Mass Transfer*, 19:236–238, 1976.

[19] F. F. Jr. Craig. *Monograph 3.* SPE, Richardson, TX, 1971.

[20] G. Daccord, J. Nittman, and Stanley H. E. *Phys. Rev. Lett.*, 56:4:336, 1986.

[21] H. C. H. Darley and G. R. Gray. *Composition and Properties of Drilling and Completion Fluids.* Gulf Publishing Company, Houston, 1988.

[22] de Swaan. *SPEJ*, 18:117, 1978.

[23] A. De Swaan. *J. Pet. Tech.*, page 907, 1981.

[24] J. M. Dealy. *The Canadian Journal of Chemical Engg.*, 57:677–683, 1979.

[25] V. Dhir and I. Cotton. *J. Heat Transfer*, 99:250–256, 1977.

[26] M. M. Dias and A. C. Payatakes. *J. Fluid Mech.*, 164:305–336, 1986.

[27] C. Doughty and K. Pruess. *Int. J. Heat Mass Transfer*, 31:79–90, 1988.

[28] F.A.L. Dullien. *Porous Media, Fluid Transport and Pore Structure.* Academic Press, New York, 1991.

[29] E.R.G. Eckert, R.J. Goldstein, A.I. Behbahani, and R. Hain. *Int. J. Heat Mass Trans.*, 28:1187–1196, 1985.

[30] A.S. Eka and I. Ershaghi. Paper SPE 10758, presented at the SPE California Regional Meeting, San Francisco, CA, 1982.

[31] B. Rubin et al. paper SPE 25234, Feb.28-Mar.3, 1989.

[32] J.R. Fanchi. *SPE Journal*, pages 143–151, Feb. 1983.

[33] I. Fatt. *Trans. AIME*, 207:144–159, 1956.

[34] I. Fatt. *Trans. A.I.M.E.*, 207:160, 1956.

[35] J. Feder. *Fractals.* Plenum Press, New York, 1988.

[36] F. Friedmann, W. H. Chen, and P. A. Gauglitz. *SPERE*, pages 37–45, 1991.

[37] J. V. Gillis and C. J. Radke. SPE 20519, presented at the 65th Annual Technical Conference, New Orleans, LA, Sept. 1990.

[38] E.E. Gomma and W.H. Somerton. In *Proc. SPE California Regional Meeting* , SPE Paper 4896-B, April 1974.

[39] M. Haghighi, B. Xu, and Y. C. Yortsos. *J. Collid Interface Sci.* (in press), 1994.

[40] L.L. Handy. *Trans. AIME*, 219:75, 1960.

[41] L.L. Handy and P. Datta. *Chevron California Research Center Report*, 1964.

[42] A. Hansen, E. L. Hinrichsen, and D. Stauffer. *Transport in Porous Media*, 11, 1993.

[43] G. J. Hirasaki. *JPT*, pages 449–456, 1989.

[44] G. M. Homsy. *Ann. Rev. Fluid Mechanics*, 19:271, 1987.

[45] E. B. Jr. Hunt and V. M. R. Berry. *AICHEJ*, page 560, 1956.

[46] David R. Lide (Editor in Chief). *Handbook of Chemistry and Physics.* CRC Press, 1993-1994.

[47] T.B. Jensen. Ph.D. Dissertation, Univ. of Wyoming, 1991.

[48] J.L. Castillo J.R. Waggoner and L.W. Lake. paper SPE 21237 (Feb. 17-20, 1991)., Feb. 17-20, 1991.

[49] A. J. Katz and Thompson A. H. *Phys. Rev. B*, 34:8175, 1987.

[50] A.J. Katz and A.H. Thompson. *Phys. Rev. B*, 34:8175, 1987.

[51] S. Kirkpatrick. *Reviews of Modern Physics*, 45, 1973.

[52] X. Kong, M. Haghighi, and Y. C. Yortsos. *Fuel*, 71:1462, 1992.

[53] J. Koplik. *J. Fluid Mech.*, 119:219–247, 1982.

[54] J. Koplik and T. J. Lasseter. *Chem. Eng. Commun.*, 26:285–295, 1984.

[55] A. R. Kovscek and C. J. Radke. paper presented at the DOE/NIPER Symposium on Field Application of Foams for Oil Production, Bakersfield, CA, Feb. 1993.

[56] A. R. Kovscek and C. J. Radke. DOE Topical Report, Oct. 1993.

[57] P.S. Ringrose K.S. Sobie, G.E. Pickup and J.L. Jensen. paper SPE/DOE 24140, April 22-24, 1992.

[58] A. Labastie. Paper SPE 20515 presented at the 65th SPE Annual Meeting, New Orleans, LA, 1990.

[59] J. S. Langer. *Rev. Mod. Phys.*, 52:1, 1980.

[60] D.D. Laumbach. *SPE Journal*, pages 517–531, Dec. 1975.

[61] B.Y.Q. Lee and T.B.S. Tan. Paper SPE 16009 presented at the 1986 SPE Symposium on Reservoir Simulation, San Antonio, February 1-4, 1987.

[62] R. Lenormand. *Physica*, 140A:114–123, 1986.

[63] R. Lenormand. *Proc. R. Soc. Lond.*, A423:159, 1989.

[64] R. Lenormand. *J. Phys.: Condens. Matter*, 2:SA79, 1990.

[65] R. Lenormand. *J. Phys. C.:Condens. Matter*, 2:SA79, 1990.

[66] R. Lenormand, E. Touboul, and C. Zarcone. *J. Fluid Mech.*, 189:165, 1988.

[67] R. Lenormand, E. Touboul, and C. Zarcone. *J. Fluid Mech.*, 189:165, 1988.

[68] R. Lenormand, C. Zarcone, and A. Sarr. *J. Fluid Mech.*, 135:337–353, 1983.

[69] X. Li. Ph.D. Thesis, May 1993, University of Southern California, Los Angeles, California.

[70] X. Li and Y. C. Yortsos. Submitted to *Phys. Fluids A*, 1993.

[71] X. Li and Y. C. Yortsos. Paper SPE 22589 presented at the 1991 Fall Meeting of the SPE, Dallas, TX, Oct. 6-9 1991.

[72] X. Li and Y. C. Yortsos. Submitted to *AIChEJ*, 1993.

[73] X. Li and Y. C. Yortsos. Submitted to *Chem. Eng. Sci.*, 1993.

[74] Y. Li and N. C. Wardlaw. *J. Colloid Interface Sci.*, 109:461–472, 1986.

[75] C. Lin and J. C. Slattery. *AIChE Journal*, 28(2):311–324, 1982.

[76] S. M. Mahmood and W. E. Brigham. No. SUPRI-TR-58, Stanford, CA, June 1987.

[77] C.C. Mattax and J.R. Kyte. *SPEJ*, 2:177, 1962.

[78] K. K. Mohanty, H. T. Davis, and L. E. Scriven. *SPERE*, pages 113–128, Feb. 1987.

[79] V. Nassehi, R. G. Holdich, and I. W. Cumming. *Trans IChemE*, 71:390, 1993.

[80] J. Nittman, Daccord G., and Stanley H. E. *Nature*, 314:141, 1985.

[81] Y. Ogniewicz and C.L. Tien. Porous heat pipe. in *Heat Transfer, Thermal Control and Heat Pipes*,(Edited by W.B. Olstad), 70, Progress in Astronautics (Series Editor M. Summerfield) 329-345, AIAA, New York. Presented as paper 79-1093, AIAA 14th Thermophysics Conf., Orlando, Florida, June 1979.

[82] E. Okandan. *Heavy Crude Oil Recovery, NATO ASI Series.* Martinus Nijhoff Publishers, The Hague, 1984.

[83] P. Pelce (ed). *The Dynamics of Curved Fronts.* Academic Pres, 1988.

[84] M.S. Plesset and A. Prosperetti. *Ann. Rev. Fluid Mech.*, 9:145–185, 1977.

[85] D. Poon and K. Kisman. *The Journal of Canadian Petroleum Tech.*, 31, No. 7:55–59, 1992.

[86] M. Prats. *Thermal Recovery.* SPE Monograph, Dallas, Texas, 1982.

[87] M. Prats. *Thermal Recovery.* SPE, Richardson TX, 1982.

[88] A. Rogerson and E. Meiburg. submitted to *Physics of fluid A*, April 1993.

[89] J. G. Roof. *SPE J.*, pages 85–90, March 1970.

[90] R.H. Rossen and E.I. Shen. Paper SPE 16982 presented at the 62nd SPE Annual Meeting, Dallas, TX, 1987.

[91] W. R. Rossen and P. A. Gauglitz. *AIChE J*, pages 1176–1188, Aug. 1990.

[92] A. M. Saidi. *Reservoir Engineering of Fractured Reservoirs: Fundamental and Practical Aspects.* Total Edition Presse, Paris, 1988.

[93] C. Satik. Ph.D. Dissertation, Univ. of Southern California, 1994.

[94] J. G. Savins. *Industrial and Engineering Chemisrty*, 61:19, 1969.

[95] G. Schubert and J.M. Straus. *J. Geophys. Res.*, 82:3411–3421, 1977.

[96] M. M. Schumacher. *Heavy Oil and Tar Sands Recovery and Upgrading.* Noyes Data Corporation, New Jersey, USA, 1982.

[97] L.E. Scriven. *Chem. Eng. Sci.*, 10:1–13, 1959.

[98] C. B. Shah and Y.C. Yortsos. *Aspects of Non-Newtonian Flow and Displacement in Porous Media.* Topical Report, DOE, Febuary 1993.

[99] T.M. Shaw. *Phys. Rev. Lett.*, 59:1671, 1987.

[100] R. Simon and F. J. Kelsey. *SPEJ*, pages 99–112, June 1971.

[101] A. Skal and I. Grebnev. *J. Phys.: Condens. Matter*, 4, 1992.

[102] C.H. Sondergeld and L. Turcotte. *J. Geophys. Res.*, 82:2045–2053, 1977.

[103] K. S.. Sorbie. von Karman Institute for Fluid Dynamics Lecture Series 1990-01, Modelling and Applications of Transport Phenomena in Porous Media, February 05-09, 1990.

[104] M. W. Stoneberger and E. L. Claridge. *SPE Res. Engg.*, November:1221, 1988.

[105] A.K. Stubos and J-M. Buchlin. in "Convective Heat and Mass Transfer in Porous Media", S. Kakac, B. Kilkis, F.A. Kulacki and F. Arinc Eds., NATO ASI Series E, Applied Sciences, Vol. 196, Kluwer Academic Publishers, 1991.

[106] P.K. Sweby. *SIAM J. Numerical Analysis*, 21, No.5:995–1011, 1984.

[107] J. Szekely and G.P. Martins. *Chem. Eng. Sci.*, 26:147–159, 1971.

[108] J. R. Thome. *Enhanced Boiling Heat Transfer.* Hemisphere Publishing Co., 1990.

[109] J.R. Waggoner and L.W. Lake. presented at the II Simposio Internacional sobre Recuperacion Mejorada de Crudo Trabajos Tecnicos, (Feb. 24-27, 1987), Maracaibo, Venezuela.

[110] D.E. White, L.J. Muffler, and A.H. Trusdell. *Econ. Geol.*, 66(1):75–97, 1971.

[111] D. Wilkinson and J. F. Willemsen. *J. Phys. A*, 16:3365–3376, 1983.

[112] Y. S. Wu, K. Pruess, and P. A. Witherspoon. *SPERE*, August:369, 1992.

[113] Y-S. Wu, K. Pruess, and P.A. Witherspoon. *Paper SPE 20051 presented at the 60th California SPE Regional Meeting.* April, 1990.

[114] B. Xu. Ph.D. Dissertation, Univ. of Southern California, anticipated Dec. 1994.

[115] Y.C.Yortsos. Paper SPE 22612, Oct. 6-9, 1991.

[116] H.C. Yee and R.F. Warming. *J. of Comp. Physics*, 57:327–360, 1985.

[117] S. Yoon and Sung-Ik Lee. *Physica*, 167, 1990.

[118] Y.C. Yortsos. The 3rd European Conference on the Mathematics of Oil Recovery, June 17-19, 1992.

[119] Y.C. Yortsos and M. Parlar. Paper SPE 19697 presented at the 64th Annual Technical Conf. and Exhibition of SPE, San Antonio, Texas,Oct. 8-11, 1989.

[120] Y.C. Yortsos, C. Satik, J.-C. Bacri, and D. Salin. *Transport in Porous Media*, 10, 1993.

[121] E. Yousfi, C. Zarcone, S. Bories, and R. C. Lenormand. *R. Acad. Sci. Paris*, 313, Series II:1093, 1991.

[122] W.B. Zimmerman and G.M. Homsy. *Phys. Fluids A*, 3(8), 1991.

☆U.S. GOVERNMENT PRINTING OFFICE: 1994 - 660-029/00041